VNIVERSITAT DE VALÈNCIA

Facultat de Física

Departament de Física Atòmica, Molecular i Nuclear

Institut de Física Corpuscular (UV-CSIC)

Search for radiative b-baryon decays and study of their anomalous photon polarization at LHCb

Luis Miguel García Martín

Directed by:

María Aránzazu Oyanguren Campos

Fernando Martínez Vidal

Doctorado en Física

Enero, 2020

Dra. MARÍA ARÁNZAZU OYANGUREN CAMPOS
Investigadora Doctora

Dr. FERNANDO MARTINEZ VIDAL
Catedrático de la UV

CERTIFICAN:

Que la presente memoria, «**Search for radiative b-baryon decays and study of their anomalous photon polarization at LHCb**», ha sido realizada bajo mi dirección en el *Departament de Física Atòmica, Molecular i Nuclear* de la *Universitat de València*, y constituye el trabajo de tesis doctoral de Luis Miguel Garcia Martin para optar al grado de Doctor en Física.

Y para que así conste, en cumplimiento con la legislación vigente, firmamos el presente certificado.

Firmado
Dra. María Aránzazu Oyanguren Campos

Firmado
Dr. Fernando Martinez Vidal

Declaration

This dissertation is the result of my own work, except where explicit reference is made to the work of others, and has not been submitted for another qualification to this or any other university.

Luis Miguel Garcia Martin

For nothing is truly complete until the day it is finally destroyed.
(and so will be for the SM)
— Brandon Sanderson, *Mistborn Trilogy*

Confía en tus pies.
— Arnau Brossa Gonzalo

七転び八起き
— Japanese proverb

かなし けど しょうがない
— Anonymous

Acknowledgements

This achievement has been made possible thanks to the contribution of many people. However, I would need another book the size of this one just to properly mention every single person I would like to. Foremost, I would like to express my gratitude to my advisors, Fernando Martinez and Arantza Oyanguren, for giving me the opportunity to start a PhD at IFIC. They have formed me as a Physicist. They have been the best possible directors, as they let me free without ever leaving me alone. They always had their door open for me, no matter how busy they were.

There are those who follow me more closely, in my everyday work: the IFIC squad. Thanks for receiving me with open arms when I reach Valencia for first time, and sharing so much. To the Celda 132 people, for the music and dancing on Fridays, the jokes, the dinners and the uncompleted calendar. I couldn't have asked for a better company in the office. Special thanks to LHCb people: Pablo, for being my "sensei" during my first steps in the PhD; Clara and then, Joan, who were my partners during the path; Carlos, our guide, who enlighten the path for us, for not to fall and unravel the great mysteries; Brij, with whom I love sharing experiences and stories that always were guarantied to be funny; Jose, who provided me with a different vision and discussions that helped me a lot; and Louis, who always had an answer for me in science, philosophy or even for jokes.

To the Bugei people, Shidoushi, Sensei, Senpai's and Kohai's. It was my way to blow off steam and start every day with a smile. To the Volleyball people, thanks for showing me a new passion, which I enjoyed a lot, specially, due to you.

A mis padres, por animarme a ser curioso, enseñandome las maravillas y secretos del mundo, sin importar lo cansados u ocupados que estuvieran. Especial mención a mi padre, a quien, siguiendo su lógica, un porcentaje de esta tesis le pertenece por la propiedad transitiva.

Al GDC, con cuyos integrantes compartí mucho y siempre formarán una parte de mi. Y así lo demostraré, gritando nuestro lema en las montañas mas altas.

Adri, quien ha sido mi amigo y entrenador durante el último año y con quien he compartido interesantes y divertidas conversaciones. Gracias a ti he tenido una via de escape adicional.

To Placido, to whom I consider my guide at CERN and who showed me a world of new entertainments. And thanks to the rest of the people I meet there: Africa, Dani, Arnau and Ana. Thanks to all of you, I really enjoyed my stay at CERN.

The days were sweeter thanks to all the workshop and conference organizers from which I have loot a piece of coffee break.

To the only beauty that never decay, the greatest treasure I could ever dream of finding: Marina. Who supported me in every single state I was, no matter if it was down, up or even upside down. I accomplished my part, now is your turn. In the meantime, you can call me Doctor.

Preface

This thesis is focused on the study of the rare radiative b-baryon decays $\Lambda_b^0 \to \Lambda\gamma$ and $\Xi_b^- \to \Xi^-\gamma$. As a first step, a search for these decays is performed using LHCb data in order to provide a measurement of their branching ratios. As a second step, the signal candidates are used to measure the photon polarization using the helicity formalism. This thesis presents the first measurement of the photon polarization in b-baryon decays using the $\Lambda_b^0 \to \Lambda\gamma$ decay channel, and the first study of the $\Xi_b^- \to \Xi^-\gamma$ decay.

The current theoretical framework of the particle physics, the Standard Model (SM), describes the properties of the known particles and their interactions with three of the fundamental forces (electromagnetic, weak and strong). However, the SM is unable to provide explanations for some observed phenomena and, thus, needs to be extended. This work aims to test some predictions of the SM, helping to point toward the direction wherein extensions of the model should be developed. Chapter 1 presents an overview of the SM and describes the helicity angular distributions used to measure the photon polarization.

The data used for this thesis have been collected by the LHCb detector. This detector was specifically designed to study the properties of decays of b- and c-hadrons. The LHCb detector is one of the four main experiments at the Large Hadron Collider (LHC) at CERN, a proton-proton (pp) circular collider operating at a center-of-mass energy of 13 TeV during the 2015-2018 period. The LHC and the LHCb detector are described in detail in Chapter 2.

The charged decay products of the particles originated in the pp collisions

are detected by the modules of the LHCb detector as energy deposit called hits. These hits need to be processed to provide the original path of the particles. This process is called tracking, and it is the first step in the reconstruction chain. The precise estimation of the tracking efficiency is crucial in order to provide accurate measurements. Methods relying on simulated data are very convenient, but are sensitive to simulation mismodeling. An innovative method to compute the tracking efficiency for long-lived particles using real data is presented in Chapter 3.

The reconstruction and selection of b-baryon decays is challenging due to the long lifetime (order 10^{-10} seconds) of the decay products. The selection criteria to achieve pure signal samples has been developed in this thesis. The reconstruction and selection procedures using the LHCb framework are described in Chapter 4.

The photon polarization can be extracted from the angular distribution of b-baryon decays. The precision achieved can be affected by several sources. The limited amount of signal candidates, the effect of the angular resolution, the acceptance, and the background contribution increase the uncertainty on the photon polarization measurement. A correct modeling of these effects is crucial in order to avoid any biases in the measurement. Photon polarization sensitivity studies are reported in Chapter 5.

The description of the analysis techniques and the results obtained are presented in Chapter 6. This includes the signal and background descriptions used in a mass fit, along with the expected signal yields and a validation of the procedure using toy experiments. The branching ratio of the $\Lambda_b^0 \to \Lambda\gamma$ decay channel is measured and the photon polarization extracted from the angular distribution of the signal candidates. A search for the $\Xi_b^- \to \Xi^-\gamma$ decay channel is also performed and an upper limit is set for its branching ratio. A study of the systematic uncertainties affecting the analyses is performed.

Lastly, the conclusions and prospects for the analysis performed in this thesis are reported in Chapter 7.

Contents

1 Introduction

1.1 The Standard Model

The current theoretical framework of particle physics, the Standard Model (SM) [1], was developed during the second half of the 20th century. The success of the SM has been overwhelming. Not only it was able to explain previous results, but it also made very accurate predictions which have later proven to match the experimental measurements. These predictions of previously unobserved phenomena include the properties of the weak interaction and the existence of the top quark, the tau neutrino, and the $W^{\pm}$, the Z and the Higgs bosons. The latter was recently discovered (2012) [2, 3] and completed the observation of the particles predicted by the model.

The SM is a relativistic Quantum Field Theory (QFT) [4], thus it describes the space-time as filled with different types of fields. The excitations of these quantum fields manifest as the elementary particles, and the interactions between the fields correspond to fundamental forces (electromagnetic, strong and weak). Within the model, the fundamental particles are divided into several categories and subcategories, as shown in Figure 1.1. The first categorization divides particles into fermions and bosons. The former are the building blocks of matter and are characterized by having a half-integer spin. Fundamental fermions are subdivided into quarks, capable of interacting through all fundamental forces, and leptons, which are not sensitive to the strong interaction. Quarks have fractional electric charge $+2/3|e|$, where $|e|$ is the fundamental positive electric charge, for up-type (u, c and t) while down-type quarks (d, s and b) have $-1/3|e|$. Neutral leptons are called neutrinos (ν_e, ν_μ and ν_τ) and negatively charged leptons are also

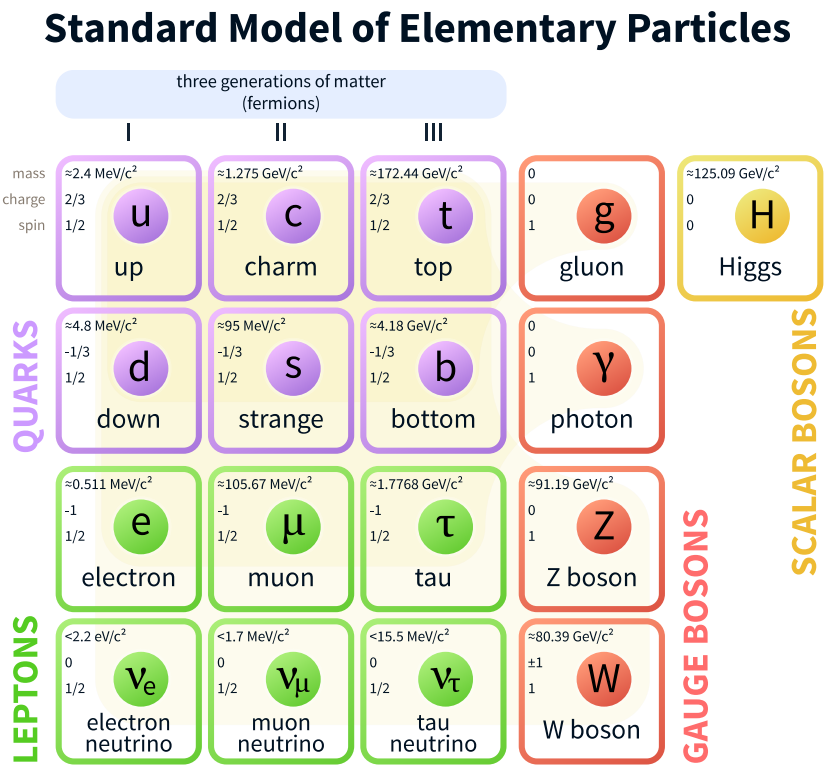

Figure 1.1: Fundamental particles included in the Standard Model [5].

known as electron-like leptons (e, μ and τ). The type of the fermions is also known as flavor, therefore, there are six flavors of quarks (u, d, c, s, t and b) and six flavor of leptons (e, ν_e, μ, ν_μ, τ and ν_τ). Furthermore, fermions can be divided into three generations or families of increasing mass. Each family includes an up- and a down-quark, a negatively charged lepton and a neutrino. The first generation is the lightest one and, in consequence, the most abundant in the universe. Since the second and third generations are heavier, they are implicitly unstable and, thus, they only exist for a short time before decaying into the first family. Consequently, they can only be observed in a highly energetic environment such as the core of a star, cosmic rays or a particle collider.

In turn, fundamental bosons have integer spin and are the interaction mediators. Photons (γ) are responsible for the electromagnetic force. This interaction applies to particles with electrical charge and has an unlimited range given that photons are massless. In spite of this, the strength of the electromagnetic force reduces with distance. The QFT which explains this interaction is Quantum Electrodynamics (QED) [6]. The nuclear weak

interaction carriers are the Z and $W^{\pm}$ bosons. The weak force is responsible for the flavor changes of the quarks and for the radiative decays studied in this thesis. This force has a very short range because of the high mass of the mediators. At energies above the so-called electroweak scale ($\Lambda_{EW} = 246\,\text{GeV}$ [7]) the electromagnetic and weak interactions are unified into the electroweak interaction [8–10]. The strong interaction is mediated by gluons (g) and it acts on particles with color charge. Only gluons and quarks have a color charge, thus they are the only fundamental particles sensitive to the strong force. The QFT underlying this force is Quantum Chromodynamics (QCD). Similarly to photons, gluons are massless particles, which provides an infinite range to the strong interaction. However, the strength of this force increases with distance and, thereby, the potential energy of a system composed of two quarks apart enough is sufficient to produce a new quark-antiquark pair. This phenomenum is called color confinement and it forces quarks to form colorless systems called hadrons [11, 12]. Hadrons can be classified into mesons and baryons depending on the number and type of quarks. The former consist of a quark and an antiquark with opposite color charges. The latter are systems containing three quarks with three different color charges. Theoretically, hadrons with a greater number of confined quarks are not forbidden. In fact, the existence of states with two antiquarks and two quarks confined (tetraquark) has been confirmed [13]. Additionally, a state with the properties of a pentaquark has recently been observed [14]. It is worth noting that each particle has its corresponding antiparticle, which has the same mass but opposite quantum numbers. Particles with vanishing quantum numbers, such as Z and γ, are their own antiparticles.

All the SM interactions are described by the Lagrangian

$$\mathcal{L}_{\text{SM}} = \mathcal{L}_{\text{EW}} + \mathcal{L}_{\text{QCD}} + \mathcal{L}_{\text{Higgs}} + \mathcal{L}_{\text{Yukawa}}\,, \tag{1.1}$$

where the first two terms correspond to the aforementioned fundamental forces. The Higgs term applies for the interactions between the Higgs and the other massive gauge bosons, whereas the last term refers to the Yukawa couplings encapsulating the interactions between the Higgs boson and fermions. The interaction with the Higgs boson is responsible for providing mass to the fermions and the Z and $W^{\pm}$ bosons through the spontaneous symmetry breaking mechanism [15, 16]. In fact, the mass terms are not gauge invari-

ant and, thereby, are not allowed in the SM. This makes the spontaneous symmetry breaking the only mechanism at SM for fermions and bosons to have mass. The characteristics of the SM Lagrangian ensure that it is a local gauge theory [17]. That is, there exists a local transformation of the fields that does not change the physical observables. The SM symmetry group providing this invariance is

$$SU(3)_C \otimes SU(2)_L \otimes U(1)_Y \,, \tag{1.2}$$

where $SU(3)_C$ is the color symmetry of QCD defined by the strong force, $SU(2)_L$ refers to the weak interaction, which only acts on left-handed particles, and $U(1)_Y$ applies to the weak hypercharge. The group of the electroweak symmetry is $SU(2)_L \otimes U(1)_Y$.

Despite being complete, the SM is not a final theory of nature because certain questions remain open. Three fundamental forces are described within the SM, however, the graviton, responsible for gravity forces, is excluded. In fact, the mathematical framework of general relativity is not compatible with a QFT. Another phenomenon unexplained by the SM is the accelerating expansion of the universe (dark energy). The SM also fails to provide dark matter candidates. The contribution of dark matter and dark energy is estimated to be about 95% of the total mass-energy of the universe [18]. The neutrino oscillation has been observed by different experiments, which implies that the neutrinos have a non-zero mass. However, the SM does not provide a mass term for them. Finally, the SM has a mechanism to explain matter-antimatter asymmetry, although it is not enough by many orders of magnitude to explain the cosmological observations in our present Universe. There are extensions of the SM, called beyond SM (BSM), which try to account for one or several of these phenomena. Therefore, it is crucial to search for New Physics (NP) signals and to perform precision measurements to hunt experimental deviations from the SM predictions. This will be the key to find the correct BSM theory.

1.2 CKM matrix and CP symmetry

The quantum state of fermions can be expressed in both, the flavor and the mass bases. These two bases are related by unitary transformations that can

be expressed through a 3×3 complex unitary matrix. The change of basis in the case of quarks is

$$D_{\text{flavor}} = S_D \, D_{\text{mass}} \ , \quad U_{\text{flavor}} = S_U \, U_{\text{mass}} \ , \tag{1.3}$$

where

$$D = \begin{pmatrix} d \\ s \\ b \end{pmatrix} \qquad U = \begin{pmatrix} u \\ c \\ t \end{pmatrix} \ , \tag{1.4}$$

refers to down- and up-type quarks respectively, and S is an unitary transformation matrix, which is different for up- and down-type quarks. The interactions mediated by the $W^{\pm}$ boson imply a change in the electrical charge and, therefore, a transition from up- to down-type quark or vice versa. This type of transition is called charged current and can be expressed as

$$\overline{D}_{\text{flavor}} \, U_{\text{flavor}} \, W^{+} = \overline{D}_{\text{mass}} \, S_D^{\dagger} \, S_U \, U_{\text{mass}} W^{+} \, , \tag{1.5}$$

where some factors have been omitted to emphasize the product $S_D^{\dagger} \, S_U = V_{\text{CKM}}^{\dagger}$. The V_{CKM} matrix is the Cabibbo-Kobayashi-Mashkawa (CKM) matrix [19, 20],

$$V_{\text{CKM}} = \begin{pmatrix} V_{ud} & V_{us} & V_{ub} \\ V_{cd} & V_{cs} & V_{cb} \\ V_{td} & V_{ts} & V_{tb} \end{pmatrix} \ . \tag{1.6}$$

The V_{ij} are the complex matrix elements that represent the strength of the transition from an up-type quark (i) to a down-type quark (j) via the weak interaction. The probability of this transition is proportional to $|V_{ij}|^2$. The parameters of the CKM matrix are not predicted by the SM and must be experimentally determined. Since it is a 3×3 complex matrix, there are 18 parameters. However, the unitary condition $V_{\text{CKM}}^{+} V_{\text{CKM}} = \mathbf{1}$ reduces the number of degrees of freedom to only nine. Due to the freedom to select phases of the quarks, five of the remaining parameters can be absorbed into quark field redefinitions. Hence, V_{CKM} depends only on four parameters (three angles and one phase). This phase is the only source of Charge conjugation Parity (CP) violation in the quark sector of the SM, which can be seen from the fact that $V_{CKM} \neq V_{CKM}^{*}$. There are several parametrizations

for the CKM matrix, one of them is due to Wolfenstein [21], defined as

$$V_{\text{CKM}} = \begin{pmatrix} 1-\lambda^2/2 & \lambda & A\lambda^3(\rho - i\eta) \\ -\lambda & 1-\lambda^2/2 & A\lambda^2 \\ A\lambda^3(1-\rho-i\eta) & -A\lambda^2 & 1 \end{pmatrix} + \mathcal{O}(\lambda^4)\,, \tag{1.7}$$

where the A, λ, ρ and η parameters are now reals and their measured values are $\lambda \simeq 0.22$, $A \simeq 0.81$, $\rho \simeq 0.14$ and $\eta \simeq 0.35$ [22]. The CP violation of the SM is encoded in the η parameter, which only appears in the most suppressed terms $\left(\sim \mathcal{O}(\lambda^3)\right)$. The Wolfenstein parametrization highlights that the strongest coupling happens between quarks of the same family. Transitions between the first and the second families are proportional to λ, whereas transitions from the second to the third family are order λ^2. The least probable transition occurs between the first and the third family and it is order λ^3. The unitary condition provides six vanishing equations that can be expressed as triangles in the complex plane. Since the equations for these triangles mix terms of different orders in λ, they correspond to flat triangles. However, the equation for the unitary triangle, defined as

$$V_{ud}V_{ub}^* + V_{cd}V_{cb}^* + V_{td}V_{tb}^* = 0, \tag{1.8}$$

only includes terms proportional to λ^3 and, therefore, their sides are similar. It is then often called "the" unitary triangle. Since the equation is invariant under rotation and can be normalized, it is possible to fix two of the three apexes to the (0, 0) and (1, 0) points. Therefore, the unitary triangle is fully characterized by the determination of its third apex, located in $(\overline{\rho}, \overline{\eta})$, where $\overline{\rho} = \rho(1 - \frac{\lambda^2}{2})$ and $\overline{\eta} = \eta(1 - \frac{\lambda^2}{2})$. The measurement of the sides and angles of this triangle from different observables is crucial to test the consistency of the SM in the quark sector. That is why testing the properties of the unitary triangles is one of the main goals of LHCb experiment [23]. The current constraints imposed by different experiments can be seen in Figure 1.2.

In the lepton sector a similar matrix arises, known as Pontecorvo-Maki-Nagakawa-Sakata (PMNS) [25, 26]. Similarly to the CKM matrix for quarks, the PMNS matrix describes the mixing and oscillation of neutrinos.

In the case of the weak interaction mediated by the Z boson, the charge is conserved and, thereby, the quark type remains the same. This type of

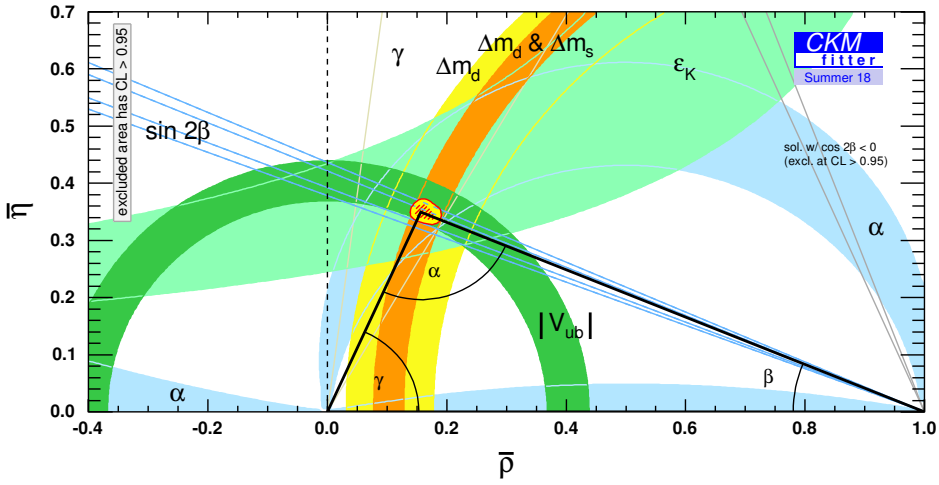

Figure 1.2: Current constraints to the unitary triangle defined by Equation 1.8, as provided by the CKMfitter group [24].

transition is called neutral current and it is described by

$$U_{\text{flavor}}\, U'_{\text{flavor}}\, Z = \overline{U}_{\text{mass}}\, S_U^{\dagger}\, S_U\, U'_{\text{mass}} Z = U_{\text{mass}}\, U'_{\text{mass}} Z \tag{1.9}$$

where again, some factors have been omitted to emphasize that $S_U^{\dagger}\, S_U = \mathbf{1}$ and, in this case, the transition is between two quarks of the same type. This implies that there is no flavor mixing in the neutral current weak interaction, as is the case with the photon and gluon neutral currents. In the later case, g and γ couple to all the quarks with the same strength. The Higgs current has the bases aligned and thus, the mixing matrix is the identity. In conclusion, in the SM framework, any flavor change implies a charge change, that is, the flavor Changing Charged Currents (FCCC) are allowed, and the flavor Changing Neutral Currents (FCNC) are forbidden at tree level.

1.3 Heavy hadron rare decays

Precision tests of the SM aim to find deviations from its predictions. The contribution from NP are expected to appear at loop level, whereas the SM processes normally contribute at tree level. This is not true in all the cases as some processes are forbidden at tree level. These processes could still occurs in the SM at loop order, as the example shown in Figure 1.3, but

their contribution would be suppressed. As a consequence, the contributions from the SM could be comparable to those from NP, or even smaller, because the former are forbidden at tree level.

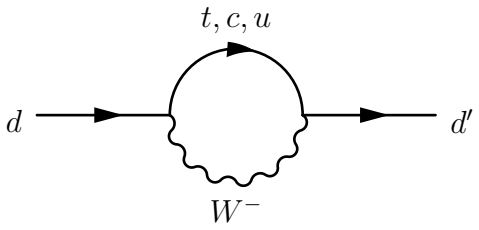

Figure 1.3: Feynman diagram of a FCNC at one loop level of the transition from a down-type quark (d) to another down-type quark (d') .

Glashow-Iliopolus-Maiani (GIM) mechanism [27] predicts vanishing contributions if the mass of the u, s and t quarks in the loop were equal. The suppressed contribution occurs only due to the mass differences between the virtual quarks that contribute to the loop. These contributions are proportional to the squared masses of the quarks at the W-mass scale. The decay processes suppressed by the GIM, CKM or any other mechanism have a low probability to occur and thus, they are generally referred as Rare Decays (RD). They are excellent probes of BSM physics searches because contributions from NP can produce sizable effects, similar or even larger to those from the SM, in sensitive observables. In the SM, the FCNC processes suffer from a double suppression from the CKM hierarchy and the GIM mechanism, which provides a perfect framework to test the SM. However, theoretical calculations of observables involving FCNC are difficult to perform because they include two different contributions, long- and short-distance. The first one is related to the quark hadronization process mediated by the strong interaction, whereas the latter refers to the electroweak interaction responsible for the quark transitions. In this case, the solution is to use an Effective Field Theory (EFT), using the Operator Product Expansion (OPE) formalism [28] within a model-independent approach:

$$\langle f|\mathcal{H}_{eff}|i\rangle = -\frac{G_F}{\sqrt{2}} V_{\rm CKM} \sum_{k=1}^{10} \mathcal{C}_k(\mu)\, \langle f|\mathcal{O}_k(\mu)|i\rangle \ , \tag{1.10}$$

where $|i\rangle$ and $\langle f|$ are the initial and final states in a transition, respectively,

G_F is the Fermi constant, which is proportional to the strength of the electroweak interaction, and V_i are the corresponding CKM matrix elements involved in the decay process. The long-distance contributions are encoded in the $O_k(\mu)$ operators, whereas the Wilson coefficients $\mathcal{C}_k(\mu)$ portray the short-distant effects. Each operator represents a different process:

- $\mathcal{O}_1$ and $\mathcal{O}_2$ are current-current operators;
- $\mathcal{O}_3$-$\mathcal{O}_6$ are strong penguin operators;
- $\mathcal{O}_7$ is the electromagnetic penguin operator;
- $\mathcal{O}_8$ is the chromomagnetic operator;
- $\mathcal{O}_9$ and $\mathcal{O}_{10}$ are the semileptonic operators.

The energy scale μ can be arbitrarily chosen, although its choice is usually based on the observable to study. For b-hadron decays, μ is often chosen to be similar to the bottom quark mass. Since the OPE is not a full theory but an EFT, it is not applicable for arbitrary energies. The Wilson coefficients $C_k(\mu)$ are calculated at the matching scale $\mu = m_W$, in a perturbative expansion in powers of $\alpha_s(m_W)$, and are then evolved down to scales $\mu \sim m_b$using the solution of the renormalization group equations. The resultant EFT is then valid at m_b scales where weak processes are evaluated.

1.4 Photon polarization in $b \to s\gamma$ transitions

The $b \to s\gamma$ transition is a FCNC process characterized by the emission of a photon in the final state. Decays involving such feature are also known as radiative decays. The effective Hamiltonian in the OPE formalism describing $b \to s\gamma$ transitions at leading order is given by

$$\mathcal{H}_{eff} = -\frac{G_F}{\sqrt{2}} V_{ts}^* V_{tb} (\mathcal{C}_7 \mathcal{O}_7 + \mathcal{C}_7' \mathcal{O}_7') \,, \tag{1.11}$$

where $\mathcal{O}_7$ ($\mathcal{O}_7'$) represents the left (right) projection of the electromagnetic penguin operator, which corresponds to the emission of a left (right)-handed photon. The strength of each contribution is encoded in the Wilson coefficients $\mathcal{C}_7$ and $\mathcal{C}_7'$. Since the W^- boson only couples to left-handed quarks in the SM, the only source of right-handed photons is chirality flips. The

probability of these flips is proportional to the non-vanishing mass of the quarks. Therefore, the ratio of right- and left-handed contributions encoded by the Wilson coefficients satisfies

$$|r| = \frac{\mathcal{C}_7'}{\mathcal{C}_7} \sim \mathcal{O}\Big(\frac{m_s}{m_b}\Big)\,. \tag{1.12}$$

Thus, the SM predicts a negligible contribution of the right-handed operator $\mathcal{O}_7'$. The $\bar{b} \to \bar{s}\gamma$ transition is mediated by the W^+ boson, which only couples with right-handed quarks, thus the photons emitted are predominantly right-handed.

The experimental measurement of branching ratios involving the $b \to s\gamma$ transition grants access to $|\mathcal{C}_7|^2 + |\mathcal{C}_7'|^2$ and, hence, allows to impose circular constraints in the $(\mathcal{C}_7, \mathcal{C}_7')$ plane. The photon polarization (α_γ) has a different dependence with the Wilson coefficient, following

$$\alpha_\gamma = \frac{\Gamma(b \to s\gamma_L) - \Gamma(b \to s\gamma_R)}{\Gamma(b \to s\gamma_L) + \Gamma(b \to s\gamma_R)} = \frac{1 - |r|^2}{1 + |r|^2}\,, \tag{1.13}$$

which allows to establish complementary constraints. The photon polarization takes values from -1 to 1, where the lower value corresponds to pure right-handed photons while the upper bound refers to pure left-handed ones. The SM predicts $\alpha_\gamma \simeq 1$ [29] since the W^- bosons only couples to left-handed quarks, as discussed above. As a consequence, a significant deviation from this result would imply the existence of BSM contributions to $\mathcal{C}_7'$, as illustrated in Figure 1.4. This hypothesis is supported by many theories such as models based on Left-Right asymmetries [30], minimal supersymmetry [31] or vector-like quarks [32].

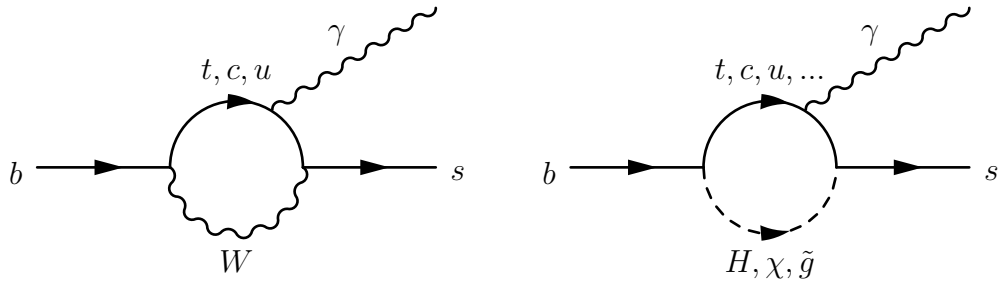

Figure 1.4: The $b \to s\gamma$ penguin diagram, mediated by SM particles (left) and BSM particles (right).

Experimental status

The photon polarization in b-meson radiative decays has been measured using a variety of channels, among which the $B^+ \to K^+\pi^-\pi^+\gamma$ analysis [33] exploits the angular distribution, and the $B_s \to \phi\gamma$ analysis [34, 35] relies on the $B_s - \overline{B_s}$ interference, both performed at LHCb. The former provided the first confirmation of a non-vanishing photon polarization, whereas the latter presented the first measurement of observables sensitive to the photon polarization. Additionally, the angular analysis of decays with virtual photons, such as the $B^0 \to K^{*0}e^+e^-$ decay [36], provides further constraints to the SM. Due to the large B-meson production at B-factories, they offer complementary measurements with low uncertainties, as in the $B^0 \to K_s\pi^0\gamma$ analysis [37]. Figure 1.5 shows the current constraints to the complex C_7' Wilson coefficient with the measurements related to the photon polarization in $b \to s\gamma$ transitions. It can be seen that all these measurements are consistent with the SM predictions. However, the experimental uncertainties are still large and there is plenty of room for NP effects to arise with improved precision.

Radiative b-baryon decays

Radiative decays of b-baryon provide an alternative method to access the photon polarization. Since the angular distributions depend on the spin, the ground state spin ½ in baryonic decays grants a clean access to the helicity structure of the $b \to s\gamma$ process, as opposed to spinless b-mesons. The direct measurement of the photon polarization provided by angular distributions is independent of the form factor and, thus, it is unaffected by those uncertainties, as it happens for the branching ratio measurements. There is no mixing in the baryonic system, which simplifies the measurement of observables without pollution from other sources. Despite the rich phenomenology, the photon polarization asymmetry in radiative b-baryon decays is yet to be explored experimentally. LHCb is an excellent workbench for observing such decays and measuring their properties, thanks to the large amount of b-baryon decays recorded by LHCb during the last years [39]. The branching ratio of the $\Lambda_b^0 \to \Lambda\gamma$ mode has been recently measured for first time and, it constitutes the first radiative b-baryon decay ever observed [40]. This recent

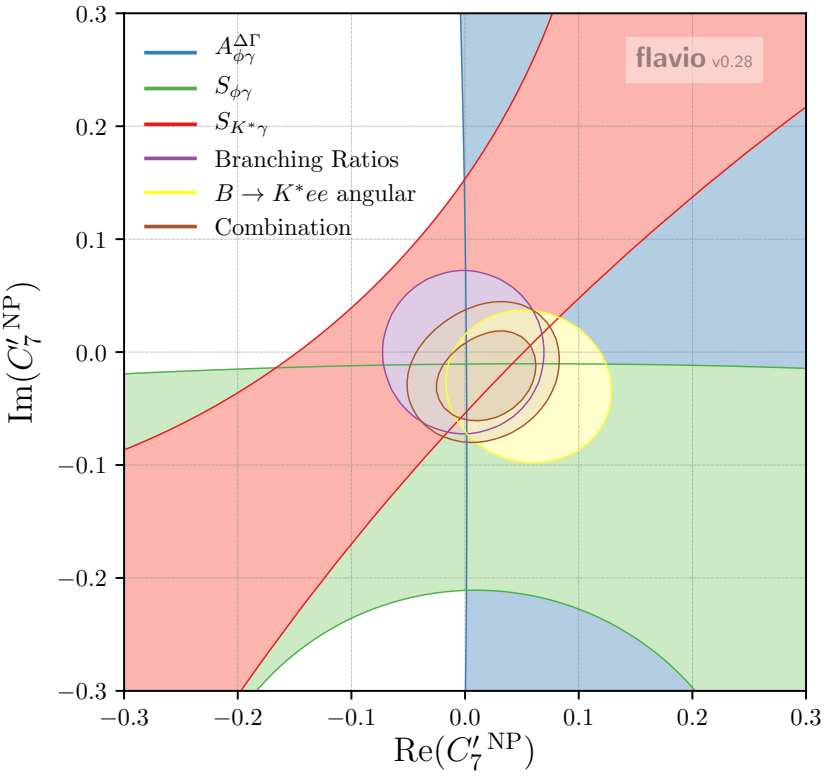

Figure 1.5: Constraints to the C_7' Wilson coefficient in the complex plane from all radiative measurement. Figure taken from [38].

observation enables the measurement of the photon polarization. Moreover, further radiative b-baryon decays can be studied at LHCb, providing complementary tests to the SM.

This thesis focuses on two decay modes: $\Lambda_b^0 \to \Lambda\gamma$ and $\Xi_b^- \to \Xi^-\gamma$, which are mediated by $b \to s\gamma$ transitions, as can be seen in Figure 1.6. Henceforth,

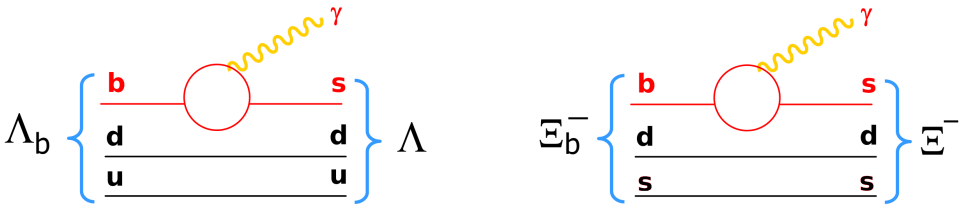

(a) (b)

Figure 1.6: Feynman diagram for the decays (a) $\Lambda_b^0 \to \Lambda\gamma$ and (b) $\Xi_b^- \to \Xi^-\gamma$ showing the $b \to s\gamma$ transition and the spectator quarks.

the conjugate decays are implied unless otherwise specified. A measurement of the photon polarization in these decays would be the first one in b-baryons decays.

The case of $\Lambda_b^0 \to \Lambda\gamma$

The photon polarization is accessible through the angular distribution using the helicity formalism [41]. The particular case of the $\Lambda_b^0 \to \Lambda\gamma$ decay, assuming Λ_b^0 initially polarized and Λ decaying in $p\pi^-$, is studied here. In the helicity formalism, the primary decay ($\Lambda_b^0 \to \Lambda\gamma$) is described by two $H_{\lambda_\Lambda,\lambda_\gamma}$ complex helicity amplitudes ($H_{+\frac{1}{2},+1}$, $H_{-\frac{1}{2},-1}$), with λ_Λ and λ_γ referring to the helicity values of the respective particles. The angular distribution in this case is [42]

$$W(\theta_\Lambda, \theta_p; P_{\Lambda_b}, \alpha_\Lambda, \alpha_\gamma) \propto 1 - \alpha_\Lambda P_{\Lambda_b} \cos\theta_p \cos\theta_\Lambda - \alpha_\gamma(\alpha_\Lambda \cos\theta_p - P_{\Lambda_b} \cos\theta_\Lambda)\,, \tag{1.14}$$

where:

- P_{Λ_b} is the Λ_b^0 initial polarization;
- $\alpha_\Lambda = 0.750 \pm 0.010$ [43] is the $\Lambda \to p\pi$ weak decay parameter;
- α_γ is the photon polarization;

- θ_Λ is the Λ polar helicity angle, defined as the angle between the Λ momentum in the Λ_b^0 rest frame and $\hat{n} = (\overrightarrow{p}_{beam} \times \overrightarrow{p}_{\Lambda_b})/|\overrightarrow{p}_{beam} \times \overrightarrow{p}_{\Lambda_b}|$, a unit vector normal to the Λ_b^0 production plane;

- θ_p is the polar helicity angle of the proton momentum in the Λ rest frame, defined with respect to the axis $z_2 = \overrightarrow{p}_\Lambda/|\overrightarrow{p}_\Lambda|$.

Figure 1.7 shows the decay chain and the definitions of the helicity angles. Equation 1.14 proves that the angular distribution is sensitive not only to the photon polarization but also to the Λ_b^0 initial polarization. However, several LHC experiments have measured the latter to be compatible with zero [44, 45]. Therefore, taking $P_{\Lambda_b} = 0$ the angular distribution simplifies to

$$W(\theta_p; \alpha_\Lambda, \alpha_\gamma) \propto 1 - \alpha_\gamma \alpha_\Lambda \cos\theta_p \,, \tag{1.15}$$

which depends only on θ_p.

The case of $\Xi_b^- \to \Xi^-\gamma$

Although the radiative b-baryon decay $\Xi_b^- \to \Xi^-\gamma$ has not been previously observed, its branching ratio is expected to be sizable for this channel to be observed at LHCb. In this thesis, the subsequent decays $\Xi_b^- \to \Xi^-\gamma$, $\Xi^- \to \Lambda\pi^-$ and $\Lambda \to p\pi$ are considered. A sketch of the decay chain and the helicity angles definition can be seen in Figure 1.8. In this case, the primary decay ($\Xi_b^- \to \Xi^-\gamma$) is described by the complex helicity amplitudes $H_{+\frac{1}{2},+1}$ and $H_{-\frac{1}{2},-1}$, where the first (second) subscript refers to the helicity of the Ξ^- (γ) particle. The expression for the complete angular distribution is [42]:

$$\begin{aligned} W(\eta, \theta_\Lambda, \theta_p, \theta_\Xi; z_\Xi, P_{\Xi_b}, \alpha_\Xi, \alpha_\Lambda, \alpha_\gamma) \propto\; & 1 + \alpha_\Lambda\alpha_\Xi \cos\theta_p + \alpha_\gamma\alpha_\Xi \cos\theta_\Lambda \\ & + \alpha_\Lambda\alpha_\gamma \cos\theta_p \cos\theta_\Lambda - 2\alpha_\Lambda\alpha_\gamma \mathrm{Re}(e^{i\eta} z_\Xi) \sin\theta_p \sin\theta_\Lambda \\ & - P_{\Xi_b}\alpha_\Xi \cos\theta_\Xi \cos\theta_\Lambda - P_{\Xi_b}\alpha_\Xi\alpha_\Lambda\alpha_\gamma \cos\theta_\Xi \cos\theta_p \\ & - P_{\Xi_b}\alpha_\Lambda \cos\theta_\Xi \cos\theta_\Lambda \cos\theta_p - P_{\Xi_b}\alpha_\gamma \cos\theta_\Xi \\ & + 2\alpha_\Lambda P_{\Xi_b} \mathrm{Re}(e^{i\eta} z_\Xi) \cos\theta_\Xi \sin\theta_p \sin\theta_\Lambda \,, \end{aligned} \tag{1.16}$$

where:

- P_{Ξ_b} is the initial polarization of Ξ_b^-;

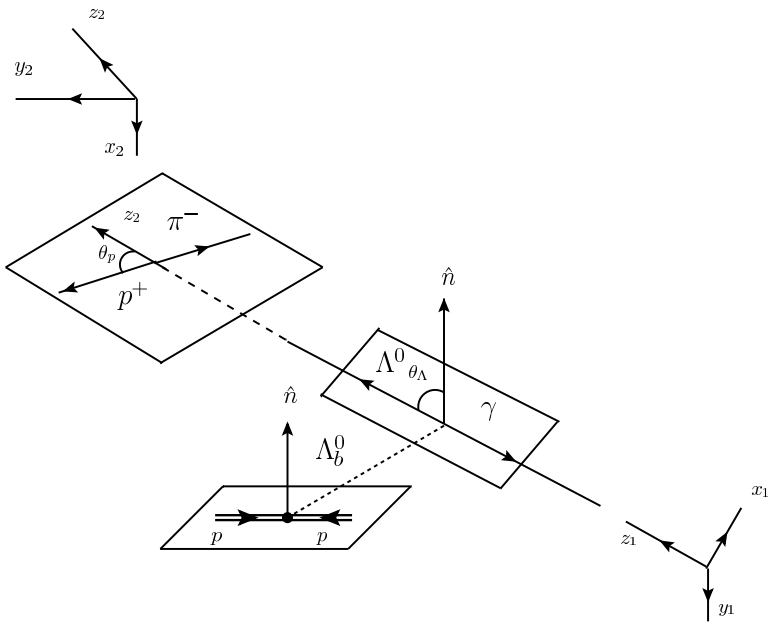

Figure 1.7: Sketch of the $\Lambda_b^0 \to \Lambda\gamma$ decay with the definition of the needed two Cartesian coordinate systems and the two polar helicity angles

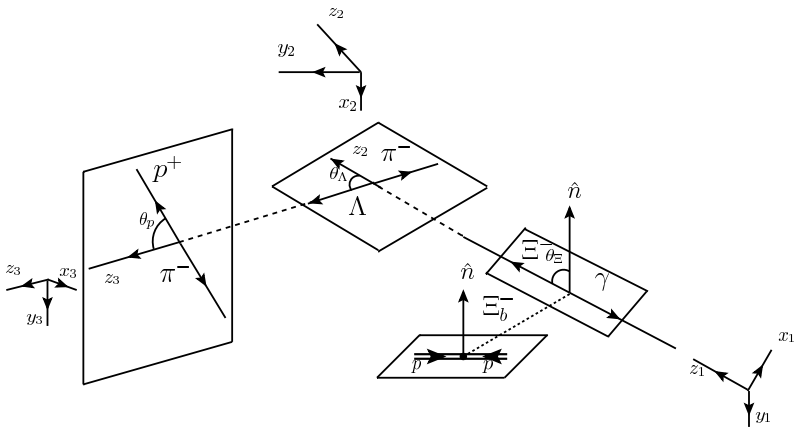

Figure 1.8: Sketch of the $\Xi_b^- \to \Xi^-\gamma$ decay with the definition of the needed three Cartesian coordinate systems and the three polar helicity angles.

- $\alpha_\Xi = -0.392 \pm 0.008$ [43] is the $\Xi^- \to \Lambda\pi^-$ weak decay parameter;
- $\alpha_\Lambda = 0.750 \pm 0.010$ [43] is the $\Lambda \to p\pi$ weak decay parameter;
- α_γ is the photon polarization;
- z_Ξ is a term sensitive to the two possible complex amplitudes of the $\Xi^- \to \Lambda\pi^-$ decay.
- θ_Ξ is the Ξ^- polar angle, defined as the angle between the Ξ^- momentum in the Ξ_b^- rest frame and $\hat{n} = (\overrightarrow{p}_{beam} \times \overrightarrow{p}_{\Xi_b})/|\overrightarrow{p}_{beam} \times \overrightarrow{p}_{\Xi_b}|$, a unit vector normal to the production plane;
- θ_Λ, ϕ_Λ are the polar and azimuthal helicity angles of the Λ momentum in the Ξ rest frame defined with respect to the axes $z_2 = \overrightarrow{p}_\Xi/|\overrightarrow{p}_\Xi|$ and $y_2 = \hat{n} \times \overrightarrow{p}_\Xi/|\hat{n} \times \overrightarrow{p}_\Xi|$, respectively;
- θ_p, ϕ_p are the polar and azimuthal helicity angles of the proton momentum in the Λ rest frame defined with respect to the axes $z_3 = \overrightarrow{p}_\Lambda/|\overrightarrow{p}_\Lambda|$ and $y_3 = \hat{n} \times \overrightarrow{p}_\Lambda/|\hat{n} \times \overrightarrow{p}_\Lambda|$, respectively;
- $\eta = \phi_\Lambda - \phi_p$.

The dependence with respect to the unknown z_Ξ parameter can be removed by integrating out the azimuthal angle η, leading to the simplified angular distribution

$$\begin{aligned} W(\theta_\Lambda, \theta_p, \theta_\Xi; \alpha_\Xi, \alpha_\Lambda, \alpha_\gamma) \propto 1 &+ \alpha_\Lambda\alpha_\Xi \cos\theta_p + \alpha_\gamma\alpha_\Xi \cos\theta_\Lambda \\ &+ \alpha_\Lambda\alpha_\gamma \cos\theta_p \cos\theta_\Lambda - P_{\Xi_b}\alpha_\Xi \cos\theta_\Xi \cos\theta_\Lambda \\ &- P_{\Xi_b}\alpha_\gamma \cos\theta_\Xi - P_{\Xi_b}\alpha_\Xi\alpha_\Lambda\alpha_\gamma \cos\theta_\Xi \cos\theta_p \\ &- P_{\Xi_b}\alpha_\Lambda \cos\theta_\Xi \cos\theta_\Lambda \cos\theta_p \,. \end{aligned} \quad (1.17)$$

Equation 1.17 enables a simultaneous measurement of the photon and Ξ_b^- polarizations. Although the Ξ_b^- polarization has not been measured to date, it is expected to be similar to the Λ_b polarization, that is, close to zero. A further simplification of the angular distribution is possible integrating out

the helicity angle θ_Ξ related with the aforementioned b-baryon polarization. This leads to the following distribution:

$$W(\theta_\Lambda, \theta_p; \alpha_\Xi, \alpha_\Lambda, \alpha_\gamma) \propto 1 + \alpha_\Lambda \alpha_\Xi \cos\theta_p + \alpha_\gamma \alpha_\Xi \cos\theta_\Lambda + \alpha_\Lambda \alpha_\gamma \cos\theta_p \cos\theta_\Lambda \,. \tag{1.18}$$

2 The LHCb detector at the LHC

2.1 The LHC machine at CERN

The Large Hadron Collider (LHC) is, at present, the largest and most powerful particle accelerator in the world [46]. It is a circular proton-proton collider consisting of a 27 km ring located 100 m underground on the Franco-Swiss border near Geneva (Switzerland). It is hosted by the European Organization for Nuclear Energy (CERN), a world wide institution formed by thousands of scientists and technicians.

The LHC accelerates two particles beams close to the speed of light, each one inside a different pipe and circulating in opposite directions. A total of 16 radio-frequency (RF) cavities and 12300 superconducting Niobium-Titanium dipole magnets cooled at 1.9 K [47] are used to boost and guide the particles along the ring. The LHC is the final step of the chain of accelerators at the CERN accelerator complex, as illustrated in Figure 2.1. The program of the LHC is divided in periods called "Runs" separated by "Long Shutdowns" (LS). The LHC operational conditions are rather stable during a Run. Besides, the LS can be used for maintenance and/or upgrade labors. In Run I (2011 - 2012), the proton bunches collided every 50 ns at a center-of-mass energy ($\sqrt{s}$) of 7 TeV in 2011 and 8 TeV in 2012. For Run II (2015-2018), the operational conditions were modified to $\sqrt{s} = 13$ TeV and a bunch-crossing every 25 ns (collision rate of 40 MHz). During the forthcoming Run III (2021 - 2024), the center of mass energy will further increase up to 14 TeV while the bunch crossing rate will be the same as in Run II.

The LHC is mainly designed for proton-proton (pp) collisions. However, there are dedicated runs for lead-proton (Pb-p), proton-lead (p-Pb) and lead-

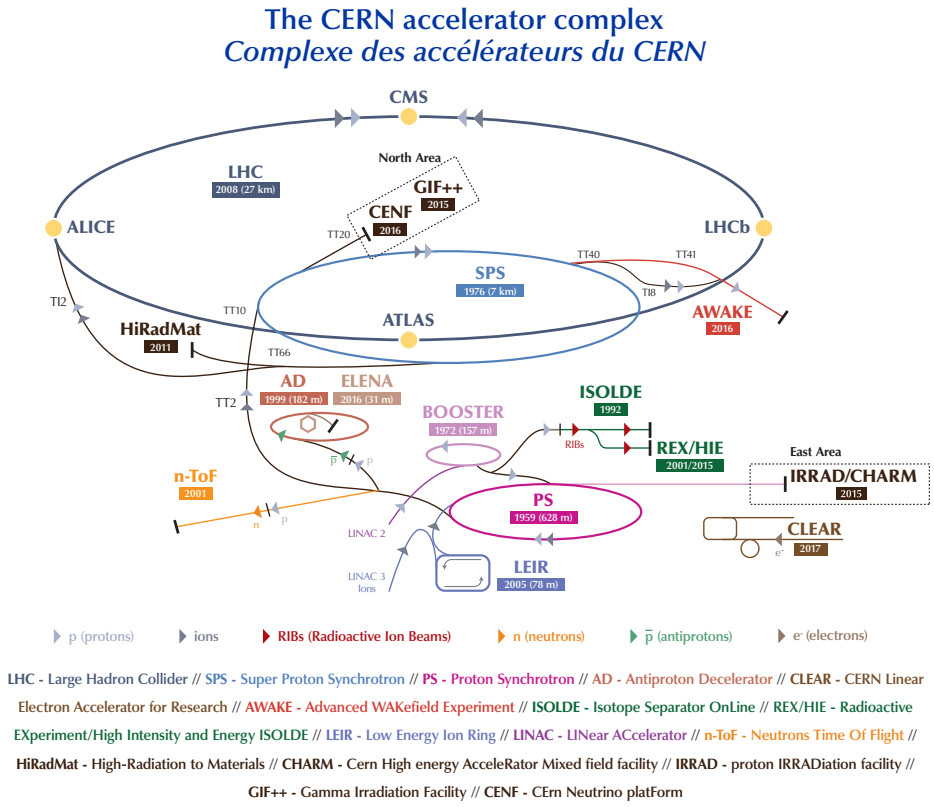

Figure 2.1: Scheme of the CERN accelerator complex [48].

lead (*Pb-Pb*) collisions. During the *pp* collision runs, each beam carries 2808 bunches with $\mathcal{O}(10^{11})$ protons per bunch (the precise number has been slightly changed in the different Runs). These conditions, amongst other not mentioned here, provide a nominal luminosity ($\mathcal{L}_{inst}$) for LHC of order $10^{34}\,\mathrm{cm}^{-2}\,\mathrm{s}^{-1}$.

The collision takes place in four different points at the LHC, called Interaction Points, where four main experiments are located:

- **ATLAS** (A Toridal LHC ApparatuS) and **CMS** (Compact Muon Solenoid): they are General Purpose Detectors (GPD) with a barrel-like shape around the interaction point. These experiments are designed to cover a wide range of SM measurements and direct searches for NP. Moreover, their physics programs focus on the search of the Higgs boson and the study of its properties.

- **LHCb** (Large Hadron Collider beauty): its main interest is the flavour physics, looking for decays involving heavy hadrons containing *b*- or *c*-quarks. It will be covered in depth in Section 2.2.

- **ALICE** (A Large Ion Collider Experiment): it studies the phenomenology of heavy ion collisions and the QCD mechanism through the quark-gluon plasma. Its physics program focus on the Pb ion runs of LHC. However, the data collected during the pp collisions runs is used as well.

There are three other smaller experiments located at the interaction points:

- **TOTEM** (TOTal Elastic and diffractive cross-section Measurement): it is used to measure the pp total cross-section, study elastic scattering and diffractive processes. Besides, it is used to monitor the LHC luminosity. It is located next to CMS.

- **LHCf** (Large Hadron Collider forward): it uses the particle shower from the LHC to study cosmic rays in laboratory conditions. It is located next to ATLAS.

- **MoEDAL** (Monopole and Exotics Detector At the LHC): it looks for exotic phenomena, like massive charged particles and magnetic monopoles. It is located next to LHCb.

2.2 The LHCb experiment

The NP contributions can be accessed using heavy flavour hadrons decays at tree and loop level. Whereas GPDs aim to make direct searches of NP particles, LHCb looks for their indirect effects, which grant access to higher energy scales.

The LHCb detector was designed to perform precision flavor physics studies, in particular of CP symmetry violation and rare decays of beauty and charm hadrons. The LHCb detector was conceived for an instantaneous luminosity of $2 \times 10^{32}\,\mathrm{cm}^{-2}\,\mathrm{s}^{-1}$, two orders of magnitude below the current LHC luminosity. To account of this difference, the beams are defocused just before the collision [49]. This lower luminosity produces fewer pp collisions per bunch crossing (pile-up), meaning less detector occupancy, which enables more precise particle reconstruction and significantly less background. The LHCb integrated luminosity recorded since the start of data-taking can be seen in Figure 2.2. A further benefit of lowering the luminosity is that it is

kept constant throughout the LHC fills. Hence, the detector conditions are kept approximately constant, including the trigger configurations.

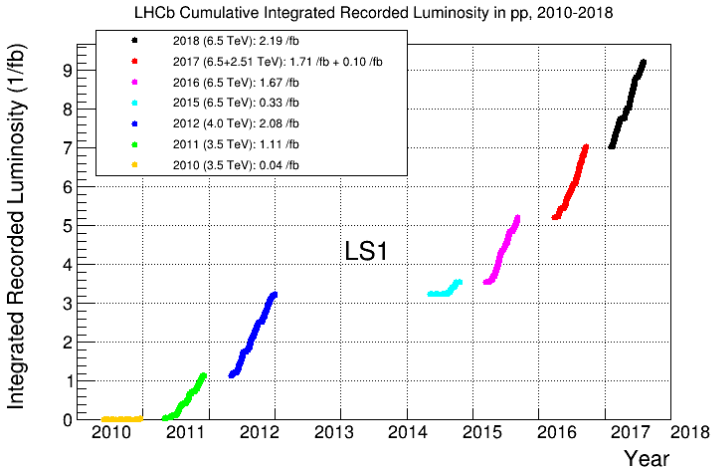

Figure 2.2: LHCb integrated recorded luminosity in pp collisions of data-taking in the period 2010 - 2018 [50].

Due to the production mechanism of the $b\bar{b}$ pair in pp collisions at LHC energies, the $b\bar{b}$ angular distribution peaks mainly in the forward and backward directions, as depicted in Figure 2.3. For this reason, the LHCb was designed as single-arm forward spectrometer (see Figure 2.4) covering the pseudorapidity[1] range from 2 to 5 in the forward direction. This corresponds to an angular acceptance of $[10, 300]$ mrad in the vertical (non-bending) plane and $[10, 250]$ mrad in the horizontal (bending) plane. Thereby, 27% of the b or $\bar{b}$ quarks produced at LHC falls inside the acceptance of LHCb.

The coordinate system of LHCb is defined with the origin at the interaction point. The z axis is parallel to the beam, going from the interaction point to the LHCb detector, *i.e.* along the clockwise LHC beam. The y axis is the vertical one and points upwards. Finally, the x axis is horizontal and points towards the center of the LHC ring.

The LHCb experiment consists of several subdetectors that can be arranged in categories depending on their purpose. In the following sections, the tracking system and the particle identification system are described.

[1]The pseudorapidity describes the angle of a particle relative to the beam axis. It is defined as $\eta = -\ln\tan(\theta/2)$.

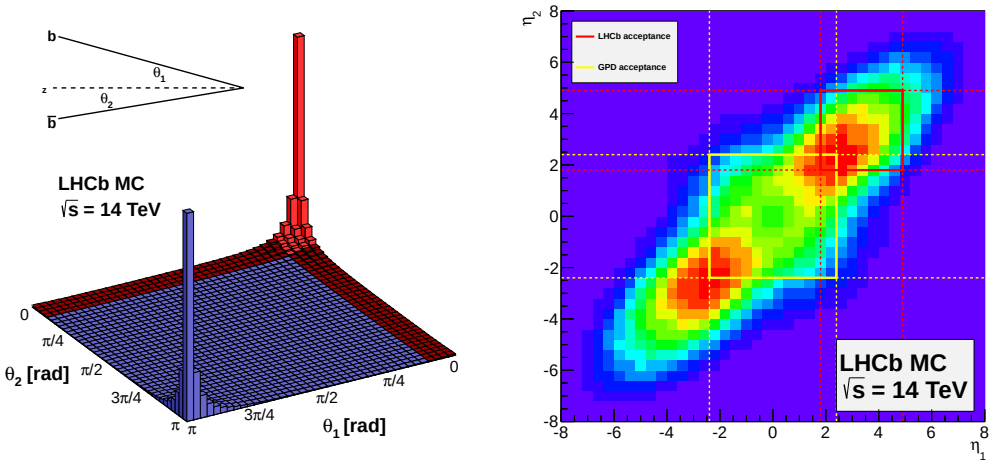

(a) (b)

Figure 2.3: (a) Angular distribution of the $b\bar{b}$ production of $\sqrt{s} = 14\,\text{TeV}$. The forward part is marked in red. (b) Pseudorapidity distribution in $b\bar{b}$ production of $\sqrt{s} = 14\,\text{TeV}$ and its acceptance for GPD (in dashed yellow) and LHCb (in full red) [51].

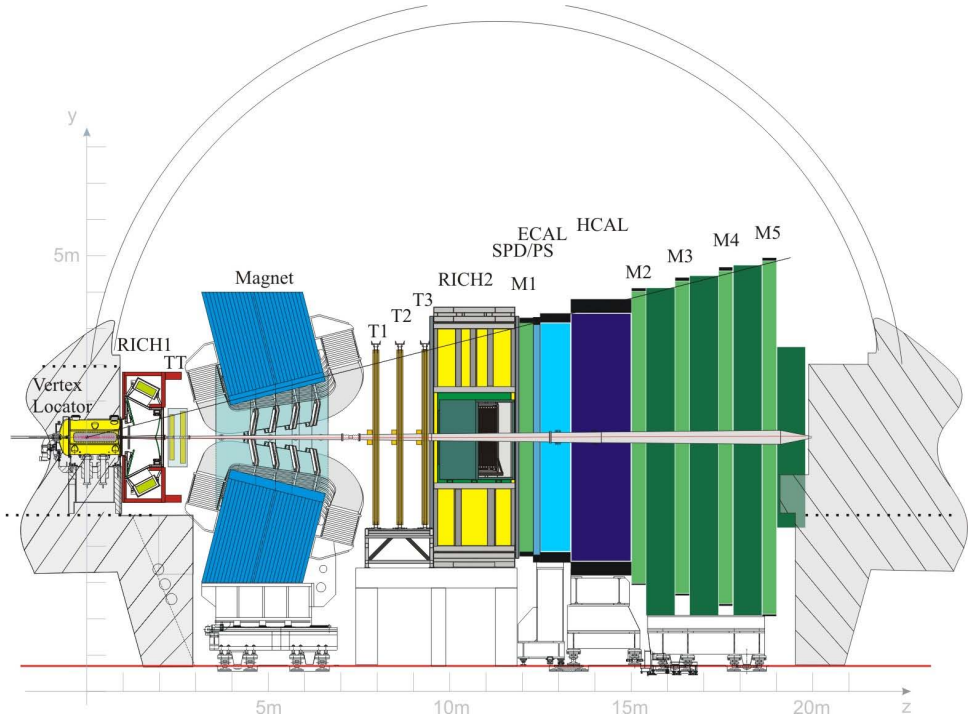

Figure 2.4: Side-view sketch of the LHCb detector [52].

2.2.1 The LHCb tracking system

The purpose of the LHCb tracking system is to reconstruct the trajectories of charged particles, measuring their momenta and estimating their origin vertices. Ideally, this is achieved with minimal perturbation on the trajectory and energy of the measured particles. At LHCb, a mass hypothesis is given to each track during the reconstruction process. The available mass hypotheses are p, $\overline{p}$, $\pi^{\pm}$, $K^{\pm}$, $\mu^{\pm}$ and $e^{\pm}$, considered as stable particles at LHCb. Other composite charged particles, such as Ξ^{-} or Σ^{-}, are reconstructed by the combination of their decay products, instead of using their own track. Only considering the aforementioned mass hypothesis ensures a fast and efficient reconstruction.

The LHCb tracking system is composed by the VErtex LOcator (VELO) detector, surrounding the interaction point, a dipole magnet to bend the charged particles, the Tracker Turicensis (TT) upstream from the magnet and the Tracking (T) station downstream from the magnet. The position of a particle before and after a known magnetic field is enough to determine its charge-momentum ratio. The LHCb tracking system allows to measure the momentum of particles traversing the whole detector with a precision of 0.5% for particles with $p = 5\,\text{GeV}/c$. The reconstruction efficiency for particles with these characteristics is above 96% [53].

VErtex LOcator

The VELO is the subdetector closest to the interaction point and the most densely instrumented, providing high-precision tracking. This precise tracking allows identification and differentiation of primary vertices (PVs) from the displaced secondary vertices (SVs), and the assignement of tracks to the correct PV based on the smallest impact parameter (IP). A PV is a vertex from a pp interaction, conversely, a SV is a decay vertex from a single particle. The IP is the minimum distance from a track to a vertex and it is expected to be zero for particles actually coming from the evaluated vertex.

The VELO is composed of 21 disk modules perpendicular to the beam direction, as shown in Figure 2.5. Each module consists in 2048 silicon strips divided in two sensors, one with strips oriented in the radial direction and the other with concentric strips, enabling to measure the azimuthal (ϕ) and

radial (R) coordinates respectively. The disk modules are divided in halves allowing the VELO to be closed and opened. In the closed position, the VELO is at a distance of 8 mm from the beam, covering the full azimuthal acceptance. Alternatively, during the filling and unstable runs, the VELO can be opened, which prevents damage from the highly energetic protons from the beam and limits the module aging. Two VETO stations are placed upstream from the interaction point. Their purpose is to measure the backward tracks (VELO Pile-Up). This information is crucial for the hardware trigger (described in Section 2.2.3) and helps to improve the resolution of the reconstructed vertices.

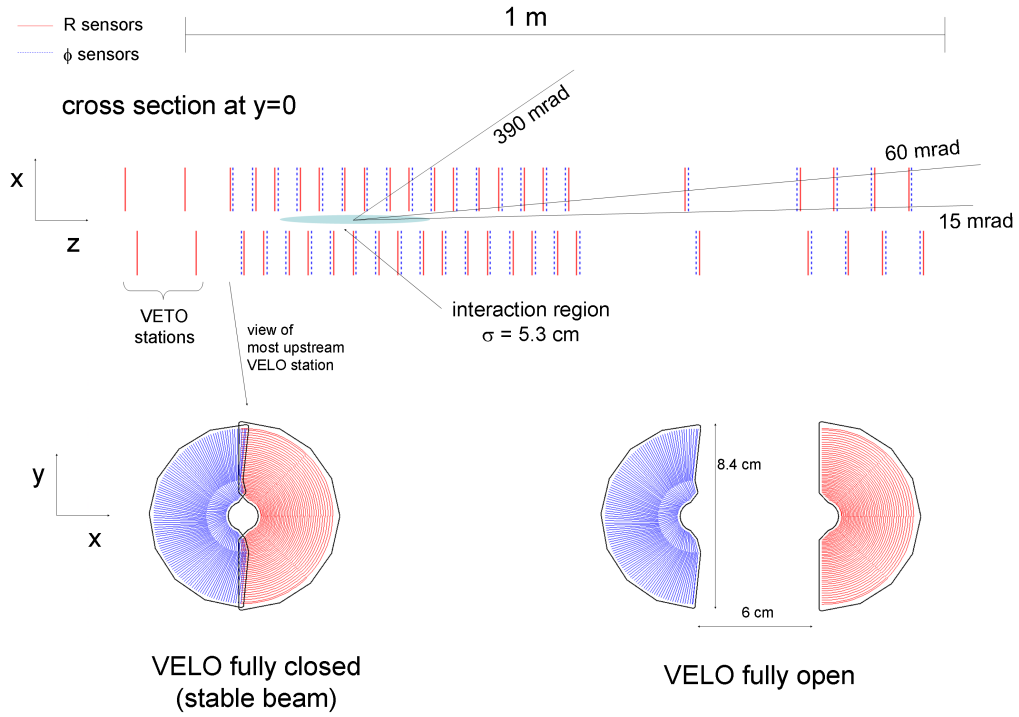

Figure 2.5: Sketch of the VELO detector and a module in close and open positions [54].

Tracker Turicensis

The Tracker Turicensis (TT) or Trigger Tracker provides a measurement of the particle trajectories before they enter the magnet region. The TT consists of 4 layers with silicon strip sensors, providing a spatial resolution of 50 μm in the bending (horizontal) plane and covering a total active area of

$8.4\,\mathrm{m}^2$. The four layers are arranged in two stations (TTa, TTb), separated by 27 cm. The layers have a x-u-v-x configuration. This means that the first and last layers (x) have vertical strips, while in the second (u) and third (v) layers the strips are tilted -5^{o} and $+5^{\mathrm{o}}$ with respect to the beam axis, respectively. This configuration is used to determine the y coordinate by the combination of any two different layers (x-u, u-v or v-x). Considering the higher occupancy in the region closer to the beam pipe, the six sensors surrounding it have a higher channel density. Figure 2.6 shows the layout of the TT.

Dipole magnet

The purpose of the magnet is to bend the trajectory of charged particles in the horizontal plane. This allows to determine the momentum of the particles. The LHCb magnet is a warm dipole magnet that can operate at room temperature. It is composed by two saddle-shaped aluminum coils placed mirror-symmetrically, as shown Figure 2.7. This arrangement is able to generate a vertical integrated magnetic field of 4 Tm along 10 m. It is worth mentioning that the polarity of the magnetic field can be set in the "Up" (positive direction) or "Down" (negative direction) configuration. This change in polarity allows to cancel out some of the charge detection asymmetries and reduce systematic uncertainties from these sources. Approximately half of the data is taken with each magnet polarity.

Tracking Stations

The Tracking (T) Stations provide a measurement of the particle trajectory after traversing the magnet. They consist of three stations (T1, T2, T3) and each one, in turn, is composed of 4 layers (substations) with a x-u-v-x configuration, as the one seen in the TT (Section 2.2.1). The dimensions of each substation are 5971 mm width and 4850 mm height. Each of these layers is divided into the Inner Tracker (IT) and the Outer Tracker (OT), as it can be seen in Figure 2.8. The IT is located in the center region near the beam pipe, where the occupancy is higher and, thereby, a finer granularity is needed. In fact, the IT covers 2% of the LHCb acceptance but the 20% of tracks pass through it. In order to cope with this occupancy, the IT has

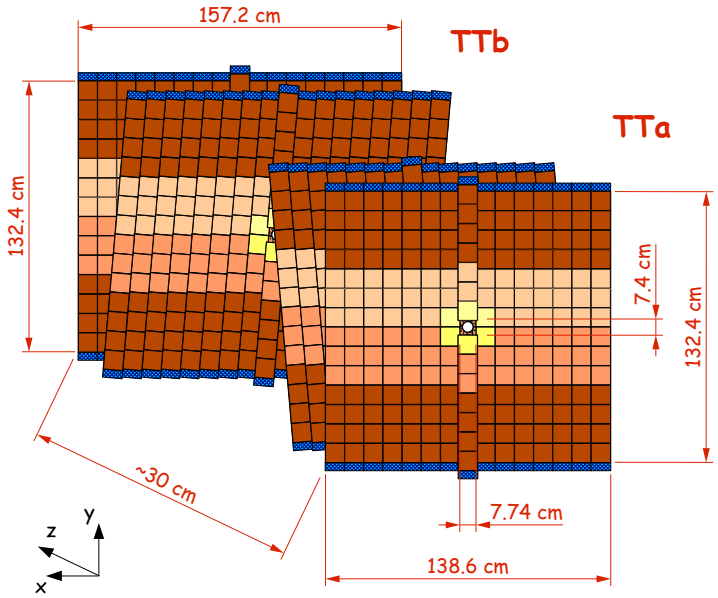

Figure 2.6: Sketch of the TT subdetector [55].

the same technology as the TT (silicon strip sensors), providing a spatial resolution of 50 μm. The strips are mounted on 4 modules surrounding the beam pipe. The particle flux in the remaining area is reduced by a factor 10 as compared to the inner region. Consequently, the OT is made out of straw gas drift tubes filled with argon (70%) and CO_2 (30%). The tubes are 5 m long but are electrically divided into a top and a bottom half. The OT can achieve a spatial resolution of 200 μm in the drift coordinate with a maximum drifting time of 50 ns.

Track types

The particles have a different track type depending on the subsystem used to reconstruct it, as it is shown in Figure 2.9. The track types are defined as:

- **Long tracks**, reconstructed with hits from at least the VELO and T stations. They have the best spatial and momentum resolution among all track types, corresponding to a precision of 0.05%. Therefore, they are used in most of the analyses at LHCb.

- **Downstream tracks**, reconstructed with hits from the TT and T stations. They are mainly the decay products of long-lived particles

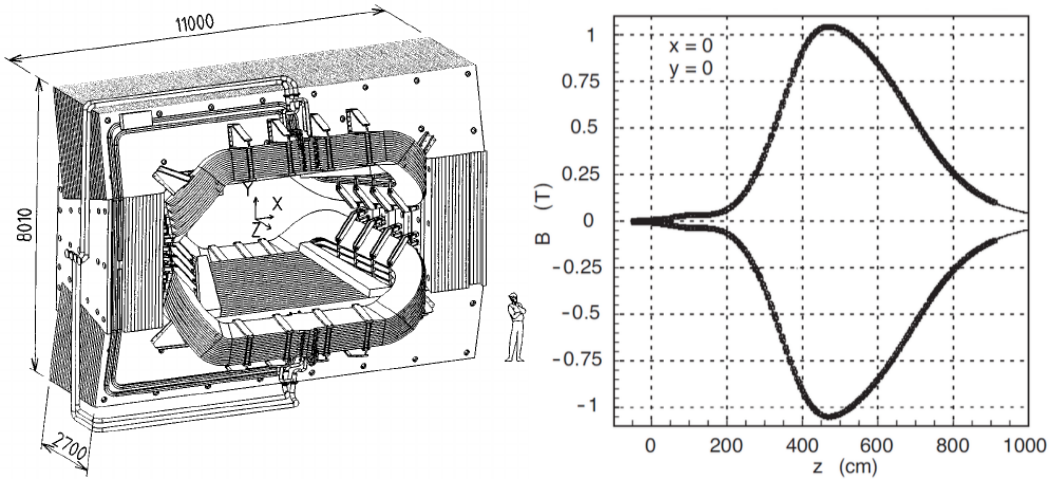

(a) (b)

Figure 2.7: (a) Sketch of the LHCb dipole magnet with its dimensions expressed in mm. (b) Intensity of the magnetic field along the z axis at (x, y) = (0, 0), for the Up and the Down polarities [56].

and have lower resolution and efficiency, since the information from the VELO subdetector is not available.

- **Upstream tracks**, reconstructed with hits from the VELO and the TT. They are produced by low-momentum particles that fall out of the acceptance of the LHCb due to the magnetic bending. Upstream tracks are typically used for background studies by the RICH1 detector.

- **T tracks**, reconstructed with hits from the T station solely. They are mainly the decay products of long-lived particles decaying after the TT. At present, they are mainly used by the RICH2 for pattern recognition and for neutral/charged cluster classification in the calorimeter system.

- **VELO tracks**, reconstructed only with hits from the VELO. They are originated by particles spreading outside the acceptance of LHCb. Their main use is the PV reconstruction.

2.2.2 LHCb Particle Identification System

The precise identification and discrimination of the different particle species produced at LHCb is done by the particle identification (PID) system. This is achieved by combining the information from the RICH detectors, muon

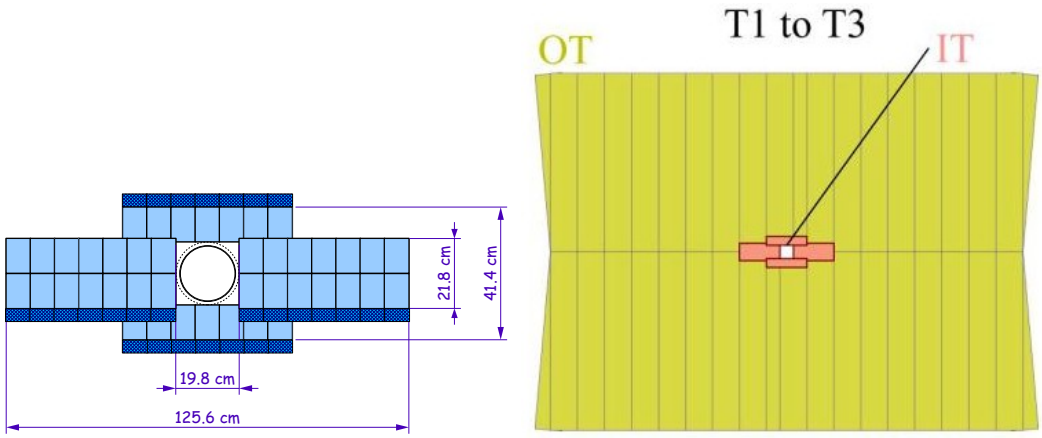

(a) (b)

Figure 2.8: (a) Frontal view of the IT [57]. (b) Sketch of a tracking module with the OT and the IT in different colors [58].

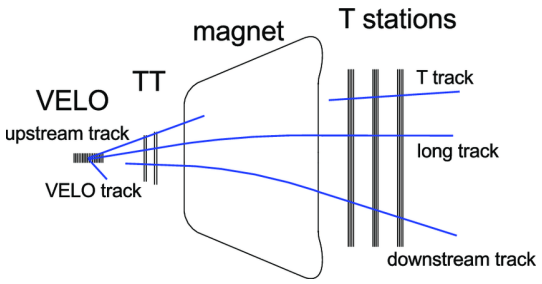

Figure 2.9: Track types at LHCb

chambers and calorimeters. Two particle identification methods are available at LHCb with this setup. The first one, named DLL, computes the likelihood probability of a certain mass hypothesis with respect to the one for π (the most abundant particles in pp collisions). The second method, called ProbNN, is neural network based. It uses the information not only from each subsystem but also their correlations and several DLL to express a probability for each mass hypothesis. The multivariate classifier is trained using simulated samples and, thus, it is sensitive to discrepancies between data and simulation. This is avoided by correcting the PID with pure signal data samples, as described in Section 4.9. As the ProbNN method is based on a multivariate analysis (MVA) technique, its performance depends on the training samples, input variables and MVA hyper-parameters. Regarding these factors, several tunings (V1, V2, V3,...) [59] are available for the ProbNN method. The tunning version selected depends on the use case.

RICH detectors

The LHCb detector has two Ring Imaging Cherenkov (RICH) stations located upstream (RICH1) and downstream (RICH2) of the magnet. The main goal of the RICH detectors is to identify charged particles, particularly, charged hadrons (p, π and K). The RICH detectors exploit the Cherenkov effect, which consists in the emission of photons (Cherenkov light) by charged particles traveling through a medium at speed higher that the speed of light in that medium. The aperture angle of the light cone, θ_C, gives access to the rapidity ($\beta = v/c$) of the particle, following

$$\theta_C = \frac{1}{n\beta}\,. \tag{2.1}$$

Combining this information with the measurement of the momentum by the tracking system allows to determine the mass of the particle and, therefore, to identify it.

Charged particles that do not reach the speed of light in the medium do not trigger the Cherenkov effect. Thus, the sensitive momentum range can be tuned through the choice of the radiator material (medium).

RICH1 is focused on low-momentum particles, between 1 and 60 GeV/c and uses silica aerogel[2] and C_4F_{10} as radiators, as they are sensitive to this momentum range. Alternatively, RICH2, filled with CF_4, is optimized for particles with high momentum, between 15 and 100 GeV/c. The Cherenkov angle as a function of the particle momentum in the RICH2 radiator can be seen in Figure 2.10. To have a precise measurement of the Cherenkov light and avoid interference with other subsystems, the Cherenkov light is guided outside of the LHCb acceptance using spherical and flat mirrors, where photons are detected by Hybrid Photon Detectors (HPD). The layout of the RICH detectors can be seen in Figure 2.11. This setup enables the RICH detectors to identify kaons with an efficiency around 95% and a pion misidentification of 10% for particles with a momentum ranging between 2 GeV/c and 100 GeV/c [61].

[2]Only for Run I.

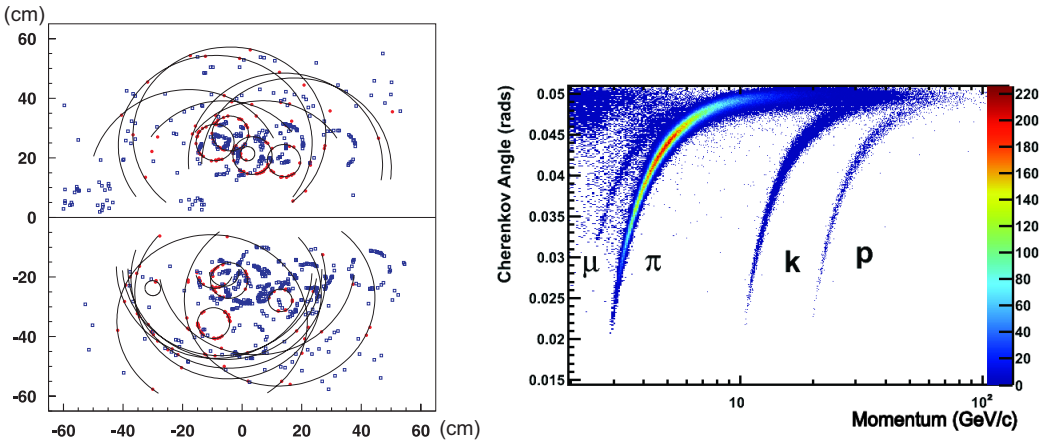

(a) (b)

Figure 2.10: (a) Detected photons in a typical RICH1 event. (b) Reconstructed Cherenkov angle as a function of track momentum in the C_4F_{10} radiator [60].

Calorimeter system

The calorimeter system is intended to measure the energy and the position of hadrons, electrons and photons. This system is composed by the Scintillating Pad Detector (SPD), the Pre-Shower (PS) device, the Electromagnetic Calorimeter (ECAL) and the Hadronic Calorimeter (HCAL). In particular, the ECAL and the HCAL perform a destructive measurement of the energy by converting the particle energy into an electromagnetic or hadronic shower which excites a scintillating medium. The granularity of the calorimeter subsystems decreases with the radial distance to the beam pipe to account for the reduction in particle flux. The SPD, PS and ECAL are divided in three regions (inner, middle and outer) with different cell-size. Due to the ECAL absorption, the hit density in the HCAL is not so high, requiring only two subdivisions instead of three for this subsystem, as shown in Figure 2.12.

The SPD and PS consist each of a single plane of scintillator pads able to detect charged particles. A 15 mm-thick lead layer is installed between the SPD and PS, corresponding to a 2.5 electromagnetic interaction lengths (X_0). The purpose of the lead layer is to initiate an electromagnetic shower that will be measured by the PS. Hadrons can traverse the lead layer without being affected since it corresponds only to 0.06 hadronic interaction lengths (λ_I). The SPD separate electrons from photons, since it detects charged

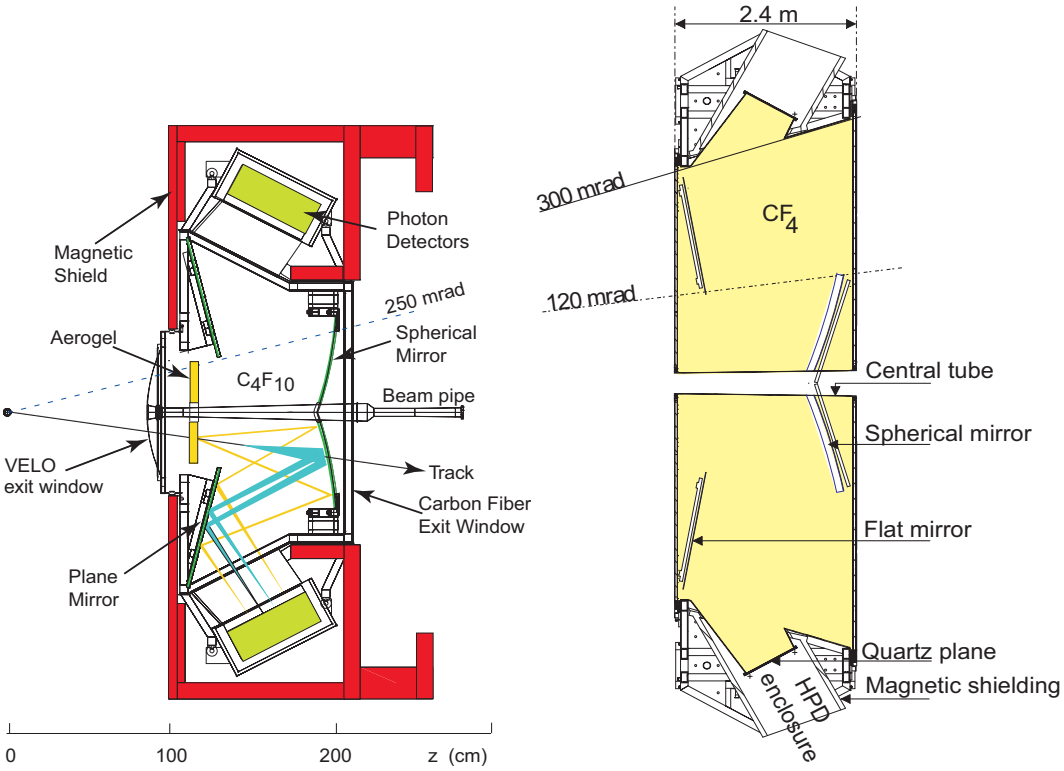

Figure 2.11: Side view of the (a) RICH1 and (b) RICH2 detectors [62].

particles. The PS detector is able to distinguish charged pions from electrons based on the different cluster size and energy deposited produced by the single hadron and the electromagnetic shower. The identification logic can be seen in Figure 2.13. Additionally, the SPD information is used in the hardware trigger as it provides a fast measurement of the event multiplicity. Highly energetic neutral hadrons can leave a print similar to that of an electron in the SPD. This is responsible for about 1% of misidentification.

The ECAL is optimized to measure energy from electromagnetic sources such as photons and electrons. Thus, it is composed by alternative layers of scintillator and lead with a total interaction length equivalent to 25 X_0. This ensures that the full shower produced by the particles will be contained inside the ECAL. The ECAL resolution is

$$\sigma(E)/E = 1\% + 10\%/\sqrt{E[\text{GeV}]} \ [53]\,, \tag{2.2}$$

where the first term is produced by systematic sources and the second one corresponds to the statistical uncertainty. The efficiency of the ECAL cells may vary with time. To cope with this issue, the ECAL is periodically

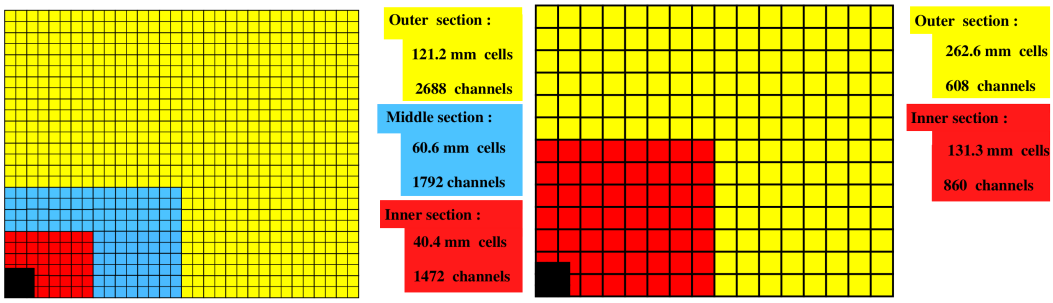

(a) (b)

Figure 2.12: Transverse segmentation of (a) the SPD, the PS and the ECAL, and (b) the HCAL. Only a quarter of the subsystem is shown [63].

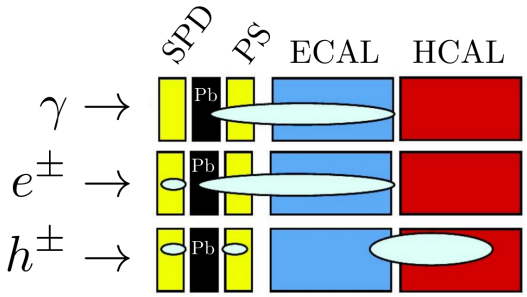

Figure 2.13: Sketch of the calorimeter system of the LHCb. The light blue zones represent the typical response of the system to different species of particles.

calibrated using π^0 produced in the pp collision. On the other hand, the HCAL is optimized to measure the energy of neutral and charged hadrons. The HCAL consists of alternative layers of scintillating material and iron. However, due to space limitation and trigger requirements, the total length of HCAL correspond to 5.6 λ_I. This length provides a fast response for the trigger, but it does not ensure containment of the full shower from the hadron within the HCAL. As a result, the energy resolution from this subsystem is poorer,

$$\sigma(E)/E = 9\% + 65\%/\sqrt{(E[\text{GeV}]}\ [52]\,, \tag{2.3}$$

where, again, the first term is due to systematic sources, such as calibration, and the second is statistical. The HCAL performs self calibrations using a sample of ^{137}Cs embedded in the system.

Muon chambers

At the LHCb detector, the muon chambers are the farthest subsytem from the interaction point. The detection of muons behind the calorimeter system is possible due to their low interaction probability, allowing them to traverse the calorimeter systems without being affected. This property grants the muon chamber the possibility to identify muons and, additionally, to measure their momentum. Furthermore, muon chambers are able to give a fast response in the detection of muons with high transverse momentum (p_T) for trigger purposes. The muon chambers are composed by 5 stations (M1-M5). The stations M2-M4 are made of Multi-Wire Proportional Chambers (MWPC) and are alternated with 80 cm-thick layers of iron (muon filters). The purpose of this muon filters is twofold: on the one hand, they allow to reduce background noise; on the other hand, high p_T muons can be quickly identified since only highly penetrating muons ($p > 6\,\text{GeV}$) can reach the last stations. Conversely, M1 was designed to provide a measurement with a better momentum resolution. Consequently, it had to be located upstream from the calorimeter system to avoid their multiple scattering effect. However, this location is affected by a far higher radiation. To cope with this, M1 is based on triple gas electron multiplier (GEM) technology, which has a higher radiation hardness than the MWPC. The layout of the muon chambers can be seen in Figure 2.14. The transverse section of the muon chambers is divided in four concentric regions, each with double cell size as the previous. This feature helps to cope with the higher particle flux near the beam pipe. This system is able to identify 97% of the muons while having a misidentification rate of 1-3%, coming mainly from pions.

2.2.3 Trigger system

The pp collision rate at the LHC accelerator is 40 MHz. The processing and storage of the huge amount of data produced would be a colossal task that would require several times the whole CERN budget. However, at LHCb, due to the $pp \to b\bar{b}$ production cross-section and its reduced luminosity, the production rate of events with $b\bar{b}$ pairs is 100 kHz. Therefore, every 230 pp collisions, an event containing a b-hadron (formed by the b-quark) is expected on average. Moreover, the detector acceptance covers the decay

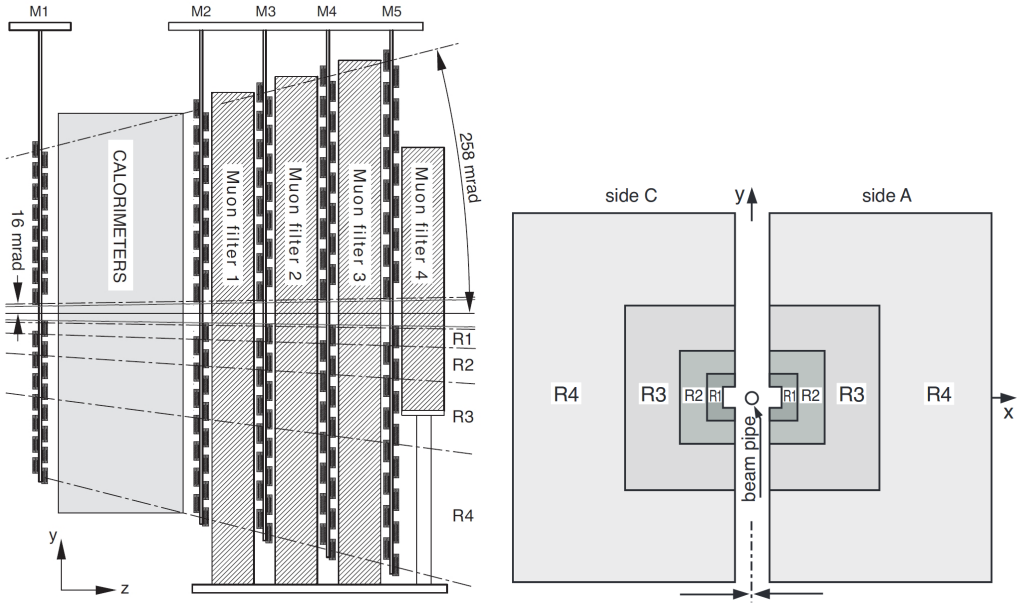

(a) (b)

Figure 2.14: (a) Cross section view of the muon chambers and the relative location of the muon station with respect to the calorimeter system. The muon filters can also be seen. (b) Frontal view of one of the muon stations where the four regions with different granularity are shown [64].

products of the b-hadron only in about 15% of these events. The goal of the trigger system is to reduce the data acquisition rate, discarding events with no physical interest for LHCb while avoiding large biases on relevant observables. This reduction takes place even before storing the data. To achieve this task, the trigger system is divided in three sequential steps: the Level-0 trigger (L0), which is implemented at hardware level, and two High-Level *triggers* (HLT1 and HLT2) based on software. The scheme of the *triggers* for the different Runs at LHCb can be seen in Figure 2.15.

Depending on the role played by the candidate (signal under study), the events selected by the trigger will fall in one of the following categories:

- Triggered on signal (TOS). The signal candidate is the responsible of the trigger decision.
- Triggered independent of signal (TIS). The trigger was fired due the underlying event, and not due to the signal candidate.
- Triggered on Both (TOB). The event does not belong to any of the

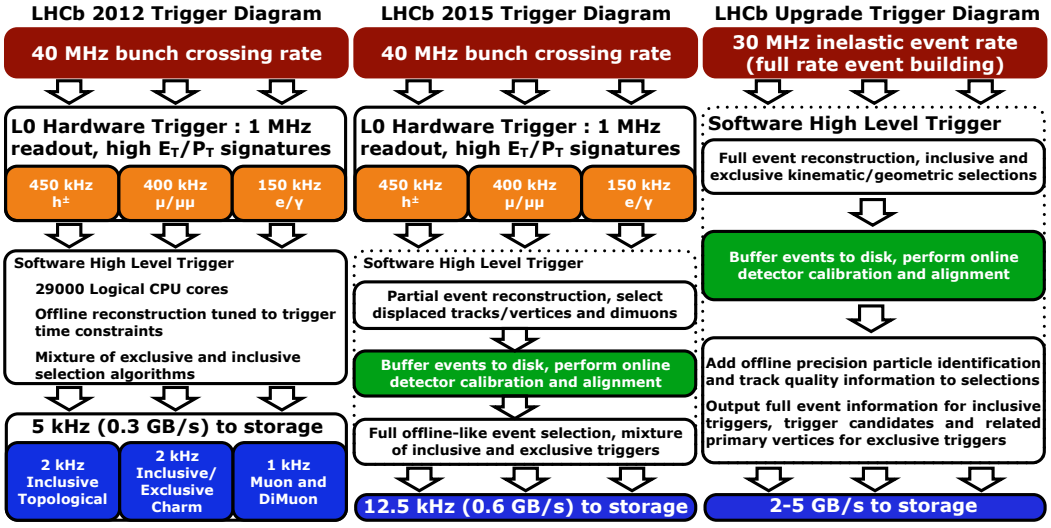

(a) (b) (c)

Figure 2.15: LHCb trigger diagram for (a) Run I, (b) Run II and foreseen for Run III (c) [65].

previous categories. The underlying event or the signal candidates were not able, by themselves, to fire the trigger. The positive trigger decision has been produced only due to a combination of the signal candidate and the underlying event.

It is worth noting that an event can be TIS and TOS simultaneously as long as both, the candidate and the underlying event, are able to fire the trigger independently.

Level-0 trigger

The L0 is the first step in the trigger system and it is based on the hardware fast-response of some of the LHCb systems. It exploits the fact that b-hadrons studied within the LHCb have masses higher than 5 GeV/c^2 and, thus, their decay products can be easily characterized by their high p_T or transverse energy[3] (E_T). Thereby, L0 uses information from the calorimeter system and the muon chambers to detect particles with a p_T higher than a certain value and, additionally, identifying them based on the subsystem where the particle was observed (SPD, PS, ECAL, HCAL and muon

[3]The E_T is related with the distance of a cluster in the ECAL or HCAL to the beam pipe.

stations). This identification provides a set of different L0 categories depending on the species of particle that passes the high p_T cut (L0Hadron, L0Electron, L0Photon, L0Muon and L0DiMuon). Furthermore, the L0 trigger uses information from the SPD and the VELO Pile-Up to compute the event multiplicity and the number of interactions, respectively. This allows the L0 trigger to discard exceedingly complex events that would consume high bandwidth and processing power. The requirements for p_T and multiplicity that an event has to meet in order to pass the L0 trigger have changed along the years of data-taking, allowing L0 to reduce the total rate to 1 MHz.

High Level trigger

The HLT processes only those events that have passed the L0 trigger, the rest of the events have already been discarded at this point. The HLT is a software trigger that runs on a dedicated multicore infrastructure called Event Filter Farm (EFF). The first stage of the High Level Trigger (HLT1) is based on a partial reconstruction of the events. It selects events including high-p_T particles not coming from the PV (large IP). The second stage (HLT2) performs a full reconstruction of the event, granting access to further information about the candidate that is used to make the decision. The full processing of the event within the time budget is possible due to the rate reduction performed by the previous trigger selections.

2.2.4 LHCb software framework

The LHCb framework [66] consists of several projects, each one designed to perform a specific step in the data processing chain. All these projects are based on an object-oriented software architecture called Gaudi [67], which is written in C++ and configured through Python scripts. The main LHCb projects are listed in the following:

- **Gauss** [68, 69] takes care of the generation of simulated data, also called Monte Carlo (MC) simulation. This is achieved in two steps that can be run sequentially or independently. The first phase involves a generator, such as Pythia [70], which simulates the pp collision and the hadronization of all the products from the interaction, and EvtGen [71],

a package designed to produce the decay of the generated particles. The second phase interfaces Geant4 [72], which simulates the behaviour of the particles travelling through matter, e.g. the LHCb detector, and its magnetic field.

The simulation conditions can be customized to emulate different center-of-mass energies, changes in luminosity, detector geometries, *etc.* It is possible to set some requirements to the generation in order to discard events without any interest for the analysis. These requirements, called generator-level cuts, often include vetoes to events where the signal can not be reconstructed by LHCb as well as p_T thresholds.

- **Boole** [73] is used to simulate the detector response to the traversing particles. This process is called digitization and takes into account the energy read by the detector as well as electronic noise, read-out delays, detector inefficiencies, *etc.* Test-beam and data are frequently analyzed to refine the tuning of these effects and minimize discrepancies with reality.

- **Brunel** [74] uses the read-out of the detector to reconstruct the event (tracks and vertices). The information from the particle identification system is merged with the reconstructed tracks.

- **Moore** [75] runs the trigger using an instance of the Brunel project for HLT reconstruction. It is used to emulated the L0 trigger on simulated events.

- **DaVinci** [76] is the software dedicated to physics analysis. Its main purpose is to combine the final state particles (reconstructed by Brunel) following a given criteria to extract an interesting decay chain. Additionally, DaVinci is used to run the Stripping, which sorts the data based on a set of inclusive and exclusive selections (streams) to optimize the resources.

The LHCb framework is oriented in a way that the discrepancies between data and MC simulation from processing sources get reduced as much as possible. This is achieved by processing in the same way these two kinds of data in Moore (HLT), Brunel and DaVinci. The only differences could arise

from the steps exclusively used for simulation, which are Gauss, Boole and Moore (L0). Nevertheless, an extensive work is been performed to precisely describe the real conditions, which ensures an improved agreement between MC and data.

2.3 LHCb Upgrade

The performance of the LHCb detector during the Run I and Run II data-taking periods has been remarkable, providing a plethora of results on rare phenomena and precision measurements [77]. In order to continue pushing the boundaries of the knowledge, the LHCb detector is performing at present an extensive upgrade [78] that is being installed during the LS2 (2018 - 2020). The main goal of this upgrade is to profit from the full capabilities of the LHC accelerator. The LHCb detector will run at a higher instantaneous luminosity ($\mathcal{L}_{inst} = 10^{33}$ cm^{-2} s^{-1}) during the Run III (2021 - 2024), which will exploit a higher c- and b-quark production. This will provide an integrated luminosity of 25 fb^{-1} by the end of Run III, a remarkable improvement taking into account that the combined integrated luminosity of Run I and Run II is 9 fb^{-1}. An improvement of the detector characteristics will also provide more precise measurements, which will allow harder selection criteria and will grant higher efficiencies, specially for multihadronic final states. As a consequence, the systematic and statistical uncertainties will be reduced. Another consequence is that the experiment will open the possibility to explore new signatures. Most of the detector channels will be replaced with systems with higher granularity as shown in Figure 2.16. This will mitigate the larger occupancy level. Figure 2.16 shows the upgrade plans for the LHCb detector.

The LHCb layout for the Run III can be seen in Figure 2.17. As a general upgrade, the radiation hardness of the systems has been improved to cope with the increased particle flux.

The main changes are:

- **VELO** [79]: the new VELO detector will use silicon pixel technology. Thus, it will be able to withstand a higher track multiplicity and will provide information on (x, y, z) position, instead of (R, ϕ, z) coor-

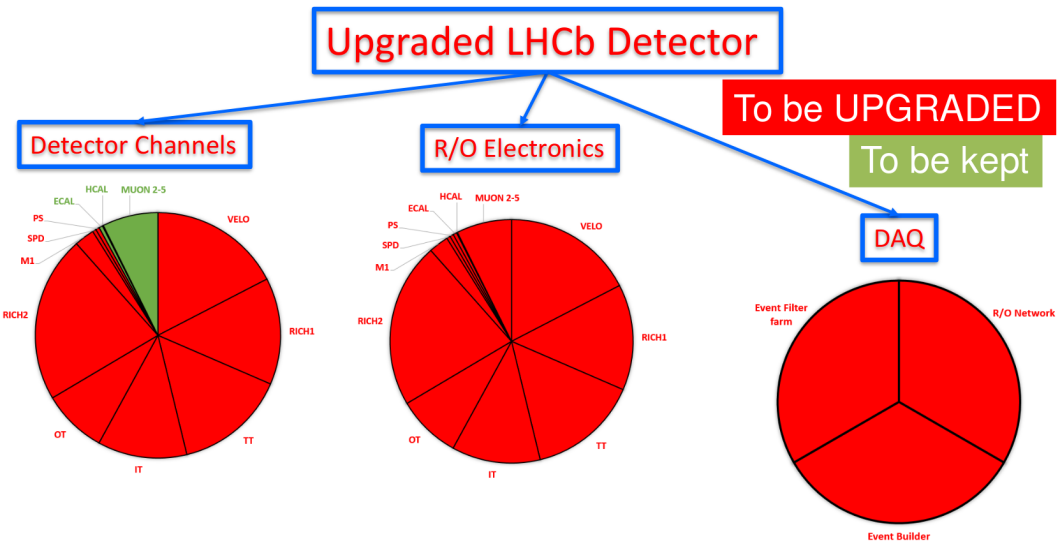

Figure 2.16: Pie charts with the proportion of the LHCb systems that will be replaced (red) or kept (green) during the Upgrade.

dinates, which required a more complex reconstruction. Additionally, the upgraded VELO will cover a region closer to the beam pipe (only 5.1 mm as compared with the 8.2 mm for the current VELO). The future VELO will still be divided into two halves that can be opened and closed. Each of these halves will include 26 modules instead of 21 as the original VELO.

- **Upstream Tracker (UT)** [80]: The current TT will be replaced by the UT. It will use the same technology as its predecessor (silicon strips) and the same layout (four layers in x-u-v-x configuration). The main improvements are a finer granularity, a larger acceptance near the beam pipe and a reduced material thickness, reducing the probability of producing multiple scattering.

- **Scintillating Fiber (SciFi) tracker** [80]: The Tracking Stations (OT + IT) will be replaced by an homogeneous detector made of scintillating fibers. This technology provides a finer granularity, a detection efficiency above 99% and a uniform spatial resolution (100 μm in the bending plane). The configuration of the SciFi will be the same as for the T stations: three stations with four layers each in a stereo configuration (x-u-v-x).

- **RICH** [81]: The modifications in the RICH detectors are focused in

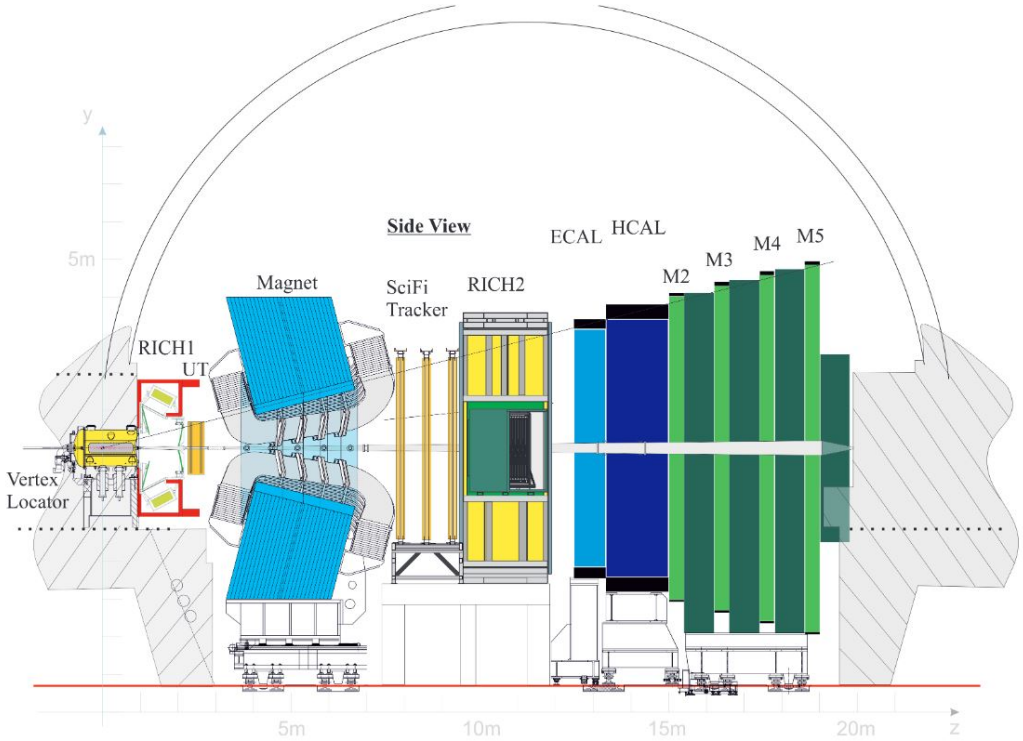

Figure 2.17: Side view sketch of the LHCb upgraded detector.

their mirror system, which will be modified to face the higher occupancy. The spherical mirrors will be replaced by mirrors with higher radius, leading to an increased focal length. New flat mirrors will be installed in the RICH1, which will provide a higher reflectivity. Besides, the HPD will be replaced by Multi Anode Photon Multiplier tubes (MaPMT) to provide improved read-out.

- **Calorimeter:** [81] The SPD, the PS and the lead layer between them will be removed, since e and γ identification (their main purpose at L0) will be done in the HLT. Conversely, ECAL and HCAL will be kept as they are since they will maintain acceptable performances despite the higher luminosity.

- **Muon system** [81]: The muon system will undergo few modifications since the current performance fulfills the requirements for Run III. The M1 station will be removed and an additional shielding will be placed in front of M2 to reduce background.

- **Trigger system** [82]: The hardware trigger (L0) imposes a bottleneck for the efficiency of the trigger system with the increased luminosity,

as shown in Figure 2.18. In fact, it is expected that L0 would discard

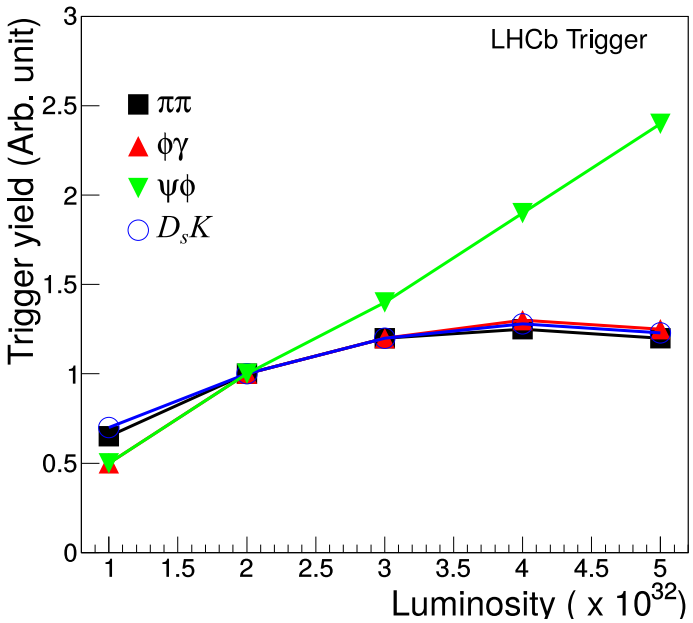

Figure 2.18: L0 trigger efficiency normalized to that of Run I as a function of the instantaneous luminosity at LHCb for selected decays [83]. The green triangles represents the trigger yield of the muon L0 trigger selecting $B_s \to J/\psi\phi$ candidates. The other decay channels are selected using the hadronic L0 trigger. The selection efficiency for these decay modes saturate before the nominal Run III luminosity ($\mathcal{L}_{inst} = 10^{33}$ cm^{-2} s^{-1}).

almost half of the events with signal candidates in Run III conditions. Therefore, the hardware trigger will be fully removed. This implies that the detector will be read out at 40 MHz and, thus, the front-end electronics of all the subsystems must be replaced to operate at collision rate. Along with L0, the subsystems dedicated to provide information for the hardware trigger decision (VELO Pile-Up, SPD and M1) will also be removed since they are no longer needed.

3 Performance of Downstream tracking algorithms

3.1 Introduction

As described in the previous chapter, the track reconstruction plays a crucial role in LHCb. During the PhD period, the author devoted a significant part of his thesis work to understand and improve the tracking reconstruction algorithms for long-lived particles (LLP), specially those involved in b-baryon decays. This interest granted the author a position as Tracking Liaison[1] of the Rare Decays Working Group. One of the outcomes of this task has been the development of a new method to determine the efficiency of a specific algorithm for LLP [84], as explained in the following.

3.2 Tracking algorithms

Particles traversing the LHCb detector leave energy deposits in the active volumes of the detector. These deposits are converted to hits if they are above a certain threshold. The track reconstruction consists in the processing of these hits in order to obtain the final tracks. The tracking reconstruction sequence is divided in three stages. The first one, the pattern recognition, aims at finding the pattern of the track by connecting the hits. This is

[1]Responsible of the tracking activities in a Physics Analysis Working Group. Among other tasks, a tracking liaison should attend the *Tracking&Alignment* Working Group meetings, report issues to the tracking coordinators and provide technical assistance to the analysts. Furthermore, a tracking liaison can develop and maintain tracking tools and provide tracking efficiency tables.

performed by several pattern finding algorithms, each intended to reconstruct one of the track types described in Section 2.2.1. The pattern recognition algorithms, in running sequence order, are the following:

- **`FastVelo`** [85] processes hits in the VELO detector and produces VELO seeds. Due to the negligible magnetic field inside the VELO volume and the module density, the VELO seeds are searched for and built as a straight line. If a VELO seed has not been used to built a larger track, it is then called a VELO track. For the Upgrade, the equivalent algorithm is called `PrPixelTracking`.

- **`PatForward`** [86] takes the VELO seeds an extrapolates them to the T stations taking a general assumption about their momentum. Once the first hit of the T stations is added, the track momentum is computed and the track trajectory is re-evaluated. Then, other compatible hits are added to the track, creating a Long track. Lastly, hits from the TT can be added to the track to improve its resolution [87]. `PrForwardTracking` is the analogous algorithm for the Upgrade.

- **`PatSeeding`** [88] searches and builds T tracks from the hits in the T stations. This is performed by taking a hit in T1 and assuming that its track comes from the PV, which provides a momentum and trajectory hypothesis. Based on this hypothesis, compatible hits from other stations are added, thus improving the momentum and trajectory estimation. Due to the weak magnetic field inside the T stations, the estimation of the momentum has a limited resolution. This algorithm is improved for the Upgrade taking several ranges of momentum estimation and starting first to reconstruct high momentum tracks, which trajectories are less affected by the magnetic field. The new algorithm is named `HybridSeeding` [89].

- **`PatMatch`** [90] tries to match VELO seeds with T tracks to create Long tracks. Compatible hits in the TT are added afterwards. The analogous algorithm for the Upgrade is `PrMatchNN`.

- **`PatLongLivedTracking`** [91] starts from T tracks and extrapolate them to the TT. The compatible hits in the TT are added to the

track to build a Downstream track. The equivalent algorithm that will be used during the Upgrade is called `PrLongLivedTracking`.

- **`PatVeloTT`** [92] takes the VELO seeds and adds compatible TT hits to build an Upstream track. The equivalent algorithm for the Upgrade is `PrVeloUT`.

The second stage of the tracking reconstruction is the Track fit. Once the pattern recognition has been connected and associated to a track, a Kalman Fit [93–95] is performed, which provides the best possible estimation of the real trajectory. The Kalman Filter takes into account effects from the magnetic field, the multiple scattering and the material interaction. The last stage is the track removal and clone (duplicates) killer, which aims at removing two types of problematic tracks. On the one hand, tracks failing the Kalman Filter stage. On the other hand, since different algorithms can produce the same or a shorter version of the track, two or more tracks can share a significant amount of hits. For each set of clone tracks, the clone killer algorithm keeps the better[2] track, while removing the rest.

3.3 Tracking efficiency at LHCb

The correct estimation of the tracking efficiency is crucial for many analyses focused on determining branching ratios (such as the measurements presented in this thesis) or production cross sections. Additionally, the tracking efficiency contributes to the systematic uncertainty in many analyses. Moreover, the tracking efficiency is also a key feature in order to qualify tracking algorithms and to find possible implicit sources of inefficiency.

An accessible technique to extract the tracking efficiency consists in using the simulated information as

$$\epsilon = \frac{N_{\text{reconstructed}}}{N_{\text{reconstructible}}}\,, \tag{3.1}$$

where $N_{\text{reconstructed}}$ is the number of tracks reconstructed by a tracking algorithms and $N_{\text{reconstructible}}$ is the number of tracks that fulfills the minimum requirements defined for each subsystem to allow reconstruction. However,

[2]The evaluation of the goodness of a track is based on the χ^2 provided by the Kalman Filter. Also, longer tracks are preferred.

a method relying solely on simulated information is sensitive to discrepancies between data and simulation. For this reason, having a method to compute the efficiency using data is important. At LHCb, a tag-and-probe method [96] is used exploiting $J/\Psi \to \mu^+\mu^-$ decays to determine the efficiency from data and to accordingly apply corrections to simulation. A new alternative method devoted to determine the Downstream algorithm performance, which uses long-lived strange baryons, have been developed and it is presented here.

Data Simulation discrepancies

At LHC experiments, the strong interactions and hadronic physics dominating the pp collisions are simulated using event generators such as Pythia [70], Herwig [97] and Sherpa [98]. Although these generators are widely used, it is still important to test the modelling of the underlying physics and, if needed, apply corrections to achieve a better agreement between simulation and data. In particular, the number of particles produced in the collision and their kinematic spectrum are two variables known to mismatch. The former can be seen in Figure 3.1 for events containing at least one b-hadron and Run II conditions. On the one hand, the number of particles has a strong correlation with the detector occupancy which in turn affects the detection efficiency. On the other hand, the tracking algorithms at LHCb have a better performance on high momentum tracks. Additionally, environment and aging effects of the detector are difficult to reproduce during the whole run period. All these effects combined induce discrepancies between the simulation and the data that need to be properly calibrated.

3.4 Performance of Downstream tracking

The selection and reconstruction of LLPs at the LHCb experiment is a challenge. These particles can decay far from the primary interaction vertex and are hard to identify. Monitoring the performance of the present tracking algorithms for LLPs is key for the understanding of many physics analyses, and for being be able to develop new techniques to improve the algorithms.

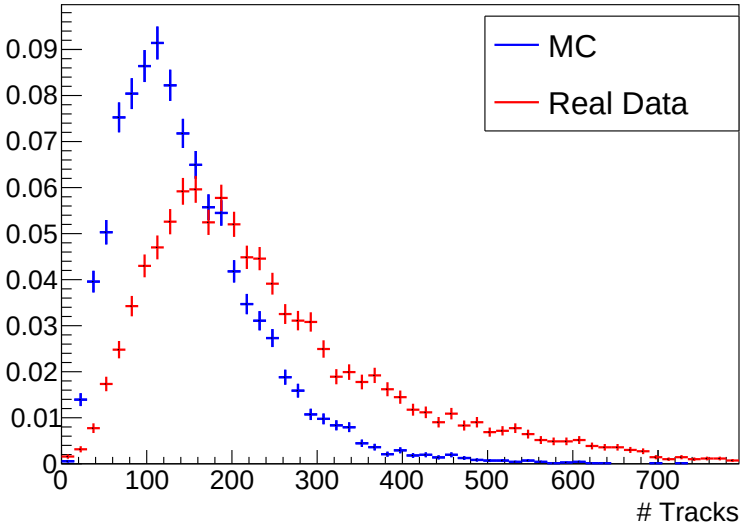

Figure 3.1: Distribution of the number of reconstructed tracks per event in MC (blue) and Run II data (red).

3.4.1 Principle of the method

This method uses Long tracks reconstructed as Downstream tracks from $\Lambda \to p\pi$ decays to evaluate the performance of the Downstream algorithm. The algorithms used to reconstruct Long and Downstream track types, described in Section 3.2, are different: Long tracks derive from VELO seeds (`FastVelo`) which are extended with hits in the T stations (`PatForward`), and the Downstream tracks proceed from seeds in the T stations (`PatSeeding`) which are matched to hits in the TT (`PatLongLivedTracking`). Therefore, while Long tracks are reconstructed in the forward direction, the Downstream tracks are reconstructed backward. Technically, this method applies the Downstream algorithm to all the hits, even those previously used to produce Long tracks, thus creating two different Downstream track categories: "real" and "false". The "real" Downstream tracks are those that would appear in standard conditions, *i.e.* those composed of hits that were not used to reconstruct a Long track. The "false" Downstream tracks correspond to actual Long tracks, reconstructed by the Downstream tracking algorithm without considering the VELO information. The three track categories considered in this method can be seen in Figure 3.2. The "false" Downstream tracks are selected as those which share a high number of hits with a Long track in the downstream region (TT and T stations). Only the "false" Downstream tracks will be

considered here to estimate the efficiency. The efficiency is computed as

$$\epsilon = \frac{N(\Lambda)_{\mathrm{FD}}}{N(\Lambda)_{\mathrm{L}}}\,, \tag{3.2}$$

where $N(\Lambda)_{\mathrm{FD}}$ is the number of "false" Downstream tracks (matched to a Long track) and $N(\Lambda)_{\mathrm{L}}$ is the number of Long tracks. In both cases the tracks come from the decay of a long-lived particle.

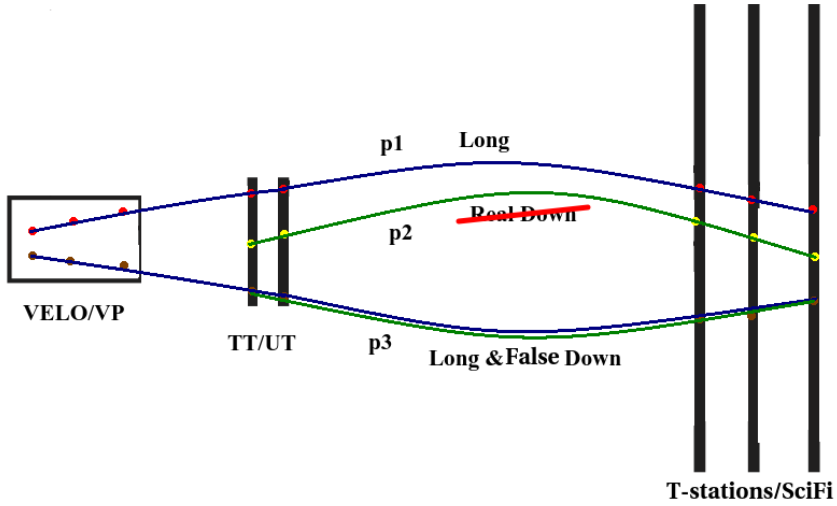

Figure 3.2: Sketch of the method showing a Long track, a "real" Downstream track and a "false" Downstream track associated with a Long track.

The sketch of the method is shown in Figure 3.2. First, the Long tracking algorithm reconstruct the tracks for particles $p1$ and $p3$ but not $p2$ because it does not have any hits in the VELO. Second, the Downstream algorithm reconstructs $p2$ and $p3$, since both have hits in the TT and T stations, but not $p1$ due to inefficiencies in the algorithm. Then, the Downstream and Long tracks for $p3$ are matched. Finally, the efficiency is computed as the number of reconstructed and matched Downstream tracks ($p3$) over the number of reconstructed Long tracks ($p1$ and $p3$).

3.4.2 Data samples

The testing and application of the method relies on MC simulation and data samples for several running periods, which ensures the validity of the method under different conditions. As MC proxy for Run II, a simulated sample of events containing at least one b-hadron (inclusive b) with 2016 conditions is used. The data proxy for Run II consists in a sample of data collected

during 2018. To date, no inclusive b MC samples simulated with Upgraded conditions are available. Instead, $\Lambda \to p\pi$ decays in a $B_s \to \phi\phi$ sample simulated with Upgrade conditions are used to evaluate the efficiency for Run III.

The selection strategy followed to achieve a pure sample of $\Lambda \to p\pi$ candidates, detailed in Table 3.1, is similar to that used by the PID group at LHCb [99].

Variable	Requirement	Units
L0	`L0All`	
HLT1	`Hlt1TrackAllL0`	
HLT2	`Hlt2PIDLambda2PPi(LL/DD)`	
p p	> 2000	MeV/c
p χ^2_{IP}	> 4	
π^- p	> 2000	MeV/c
p χ^2_{IP}	> 4	
Λ ΔM	< 15	MeV/c^2
Λ χ^2_{Vtx}	< 9	

Table 3.1: Selection requirements imposed on the $\Lambda \to p\pi$ candidates for evaluating the performance of the Downstream algorithm. The used variables will be described in Section 4.1.3.

3.4.3 Proof of principle

This method relies on the hypothesis that the Downstream algorithm performance in the VELO region is the same as in the region between the VELO and the TT. For this:

- The Downstream tracking efficiency should not depend on the origin position of the track, as it can be observed in Figure 3.3a.
- Results on simulation should be compatible with other methods based on truth information from simulation (MC method). This can be seen in Figure 3.3a.

- The momentum and spatial resolution from "false" Downstream tracks should be compatible with those from "real" Downstream tracks, as shown in Figure 3.3b. No discontinuity or bias are observed.

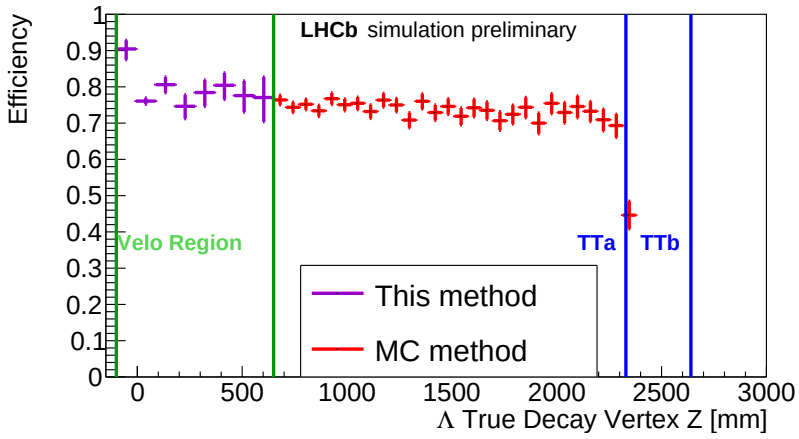

(a)

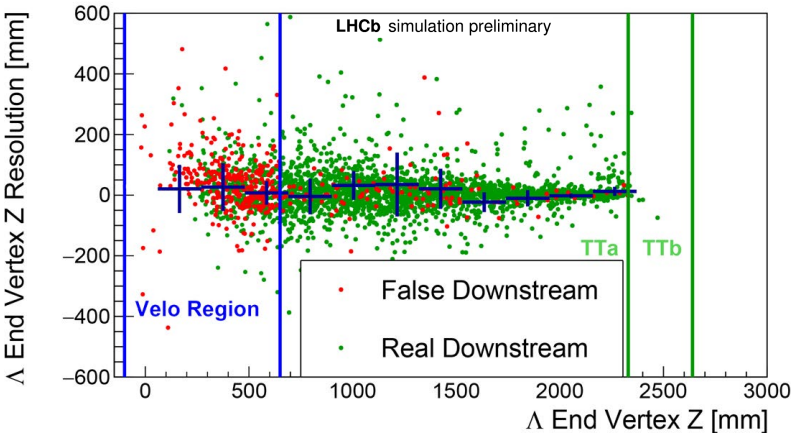

(b)

Figure 3.3: (a) Downstream tracking efficiency as function of the z coordinate of the Λ decay vertex for this method (violet) as compared to the MC method (red). (b) Resolution of the reconstructed z coordinate of the Λ decay vertex as function of that z position for "false" Downstream tracks (red) and "real" Downstream tracks (green).

3.4.4 Results

The method can be used to extract the average value of the Downstream tracking efficiency and its dependence on different variables. In Figure 3.4,

the efficiency as a function of the z coordinate of the Λ decay vertex inside the VELO region is shown. The Λ decay vertex corresponds to the track origin position. No dependence of the efficiency with the starting point of the track is observed, both for the simulation and the data sample. In addition, the efficiency is compatible in the whole range for both cases. The

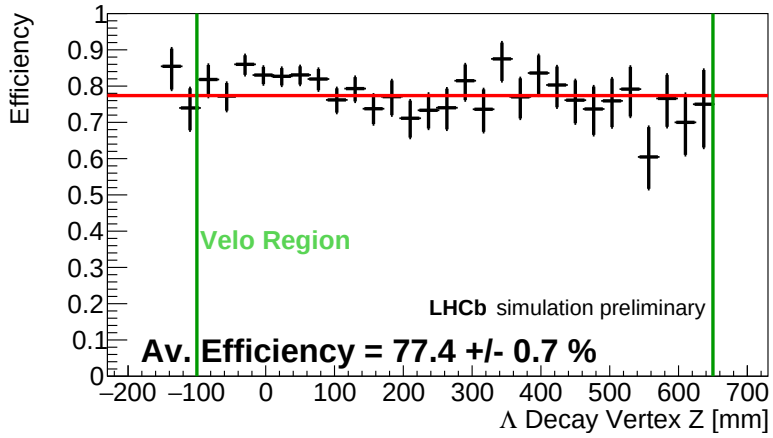

(a)

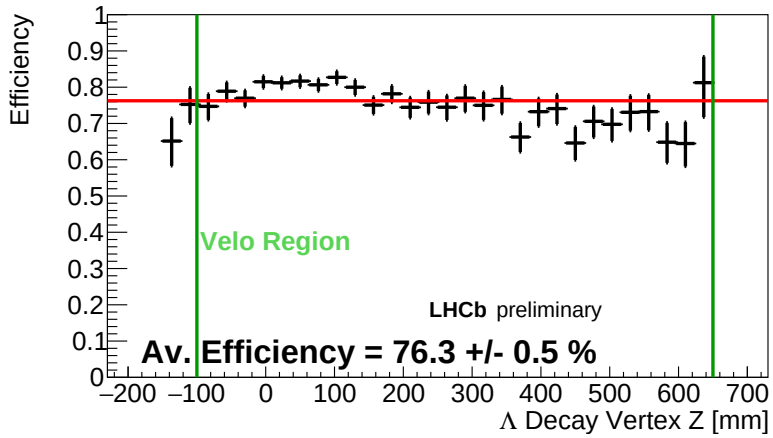

(b)

Figure 3.4: Downstream tracking efficiency as function of the z coordinate of the Λ decay vertex for Run II (a) simulated and (b) data.

Downstream tracking efficiency as a function of the transverse momentum of the track is shown in Figure 3.5 for simulation and data samples. The efficiency is also compatible and shows a similar behavior. This method can also be applied to samples with the Upgraded LHCb conditions to test the performance of the tracking algorithms with the new detector. Figure 3.6 shows the efficiency of the Downstream tracking algorithm as a function of

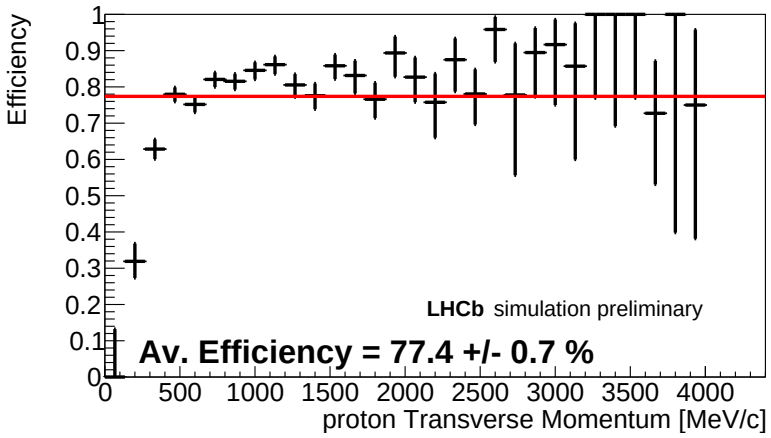

(a)

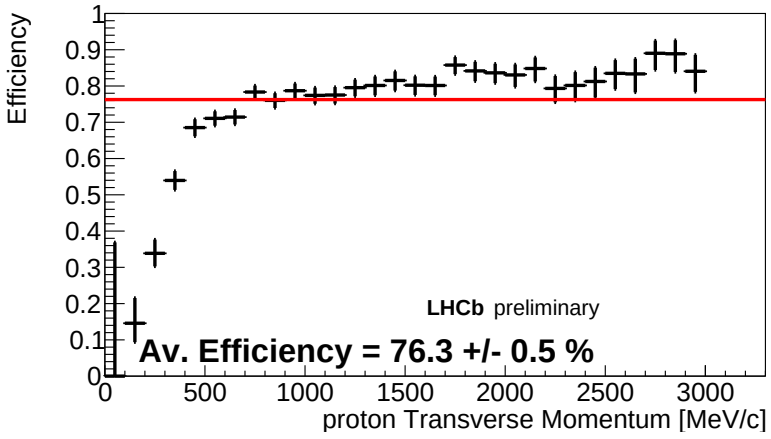

(b)

Figure 3.5: (Downstream tracking efficiency as function of the transverse momentum of the track for Run II (a) simulated and (b) data.

z coordinate of the Λ decay vertex and of the transverse momentum of the track for simulated upgraded conditions. Two conclusions can be drawn from these results. On the one hand, the efficiency continues to be independent of the starting point of the track. On the other hand, the average efficiency is expected to be largely improved thanks to the optimization of the algorithms and the Upgraded detector. In addition, an improvement of the efficiency in the low p_T region will be achieved. Finally, Figure 3.7 shows that the

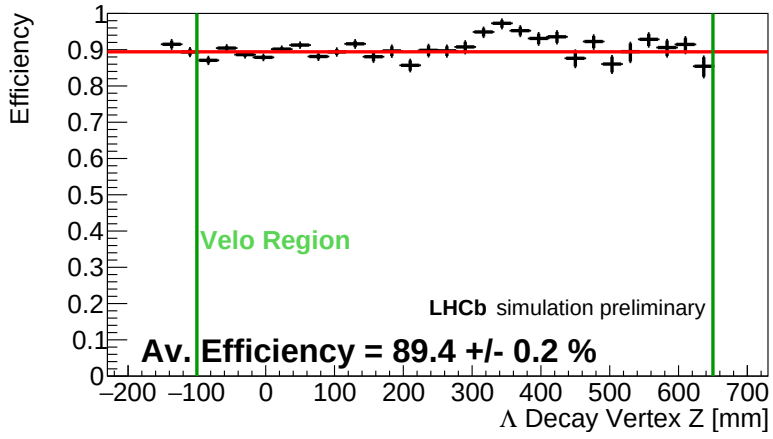

(a)

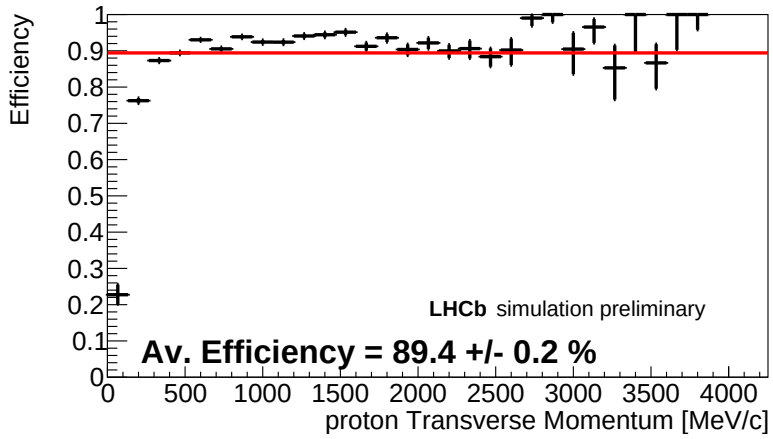

(b)

Figure 3.6: (a) Downstream tracking efficiency as function of the z coordinate of the Λ decay vertex, and (b) the transverse momentum of the track for simulated Upgraded conditions.

momentum resolution for the "false" Downstream tracks does not have any bias or unexpected behavior, and it is improved in the Upgrade.

This method assumes that there is no correlation in the reconstruction of

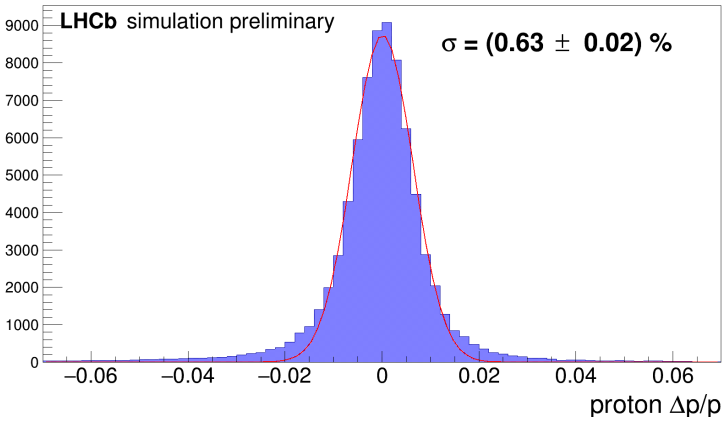

(a)

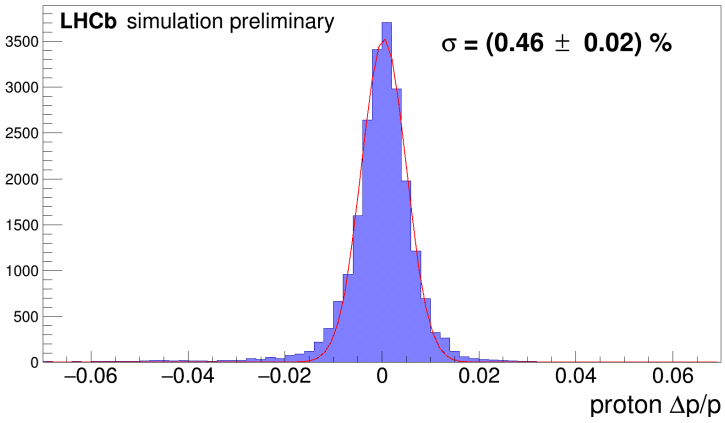

(b)

Figure 3.7: Momentum resolution of "false" Downstream tracks for simulated data with 2016 conditions (a) and the Upgrade (b).

Long and Downstream tracks. This correlation is expected to be low since the reconstruction algorithms and the track seeds are different. However, any inefficiency related to detector effects is shared among the reconstruction algorithms. Therefore, further studies could be performed to evaluate potential systematic uncertainties related to this correlation.

3.5 Summary and conclusions

A new method has been developed to evaluate the performance of the Downstream tracking algorithm at LHCb using real and simulated data. The results obtained on simulation are in reasonable agreement with other methods. A summary of the results is shown in Table 3.2. For results based on

	Efficiency (%)	
	This method	MC Info
Simulation Run II	$\mathbf{77.4 \pm 0.8}$	74.5 ± 0.3
Data Run II	$\mathbf{76.3 \pm 0.5}$	-
Simulation Run III	$\mathbf{89.4 \pm 0.2}$	89.7 ± 0.1 [89]

Table 3.2: Downstream tracking efficiencies for data and simulation in both, Run II and Upgrade conditions, extracted with the method presented in this document. The comparison with the MC method is also shown. The efficiencies are averaged over the phase space of the tracks of the from $\Lambda \to p\pi$ decays.

Run II simulation further studies will be required to account for systematic uncertainties. The performance obtained with this method using simulation is compatible with the one obtained using data. This validates the tracking efficiency obtained from LHCb simulations. The method can be used to calibrate the Downstream tracking algorithm with data during Run III. We have tested that the efficiency will largely increase with the Upgraded LHCb detector. As a final remark, the method presented here can be extrapolated to other track types (Upstream and T tracks) or to any other experiment with a similar track topology.

4

Reconstruction and selection of $\Lambda_b^0 \to \Lambda\gamma$ and $\Xi_b^- \to \Xi^-\gamma$ decays

4.1 Event reconstruction

This chapter discusses the reconstruction and selection of the $\Lambda_b^0 \to \Lambda\gamma$ and $\Xi_b^- \to \Xi^-\gamma$ decay channels. As explained in Section 1.3, rare decays are suppressed in the SM and, thus, their observation is difficult. Moreover, the reconstruction of these decays is challenging at LHCb due to the absence of information about the b-baryon decay vertex (hereafter referred to as secondary vertex, SV), since it implies the reconstruction of a LLP and a photon. The latter is detected solely using calorimeter system information, which measures the photon energy but not its direction, thus the photon is assumed to come from the proton-proton interaction point, *i.e.* primary vertex (PV). For decays involving short-lived particles this is a good approximation, since the radiative and the following decays occur close enough to infer the SV. Conversely, long-lived particles decaying weakly fly from several centimeters to meters, too much to make this assumption. Furthermore, they mostly decay outside the VELO and, thus, the information of this detector is not available for the reconstruction of their decay products. This reduces the resolution for long-lived particles. Despite the lack of a reconstructed SV vertex, the b-baryon momentum can still be obtained by the direct sum of the long-lived particle and photon momenta.

A $\Lambda_b^0 \to \Lambda\gamma$ candidate requires the reconstruction of a Λ baryon from two Long tracks, compatible with a proton (p) and a pion (π^-) hypotheses, pointing to a common displaced vertex. The Λ is later combined with

an energetic photon to produce the initial $\Lambda_b^0 \to \Lambda\gamma$ candidate. This event topology can be seen in Figure 4.1. For this channel, the selection strategy followed in this thesis is the same as in [40]. The main background con-

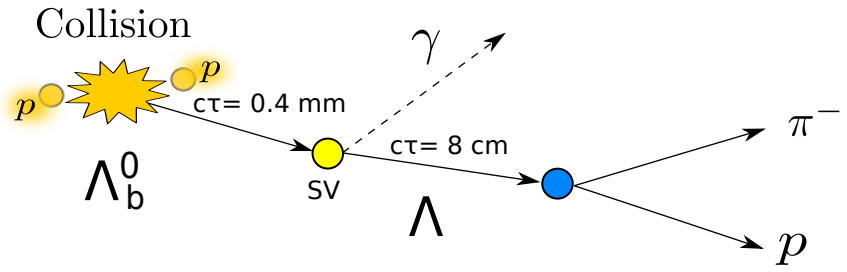

Figure 4.1: Topology of the $\Lambda_b^0 \to \Lambda\gamma$ decay.

tribution is the combination of a random photon with a real Λ produced at the interaction point. Additionally, the huge production rate of prompt Λ baryons from pp collisions hampers to distinguish the Λ from the Λ_b^0 decay. At present, Downstream tracks are not included in the HLT1 selection criteria at LHCb. Due to the limited spatial and momentum resolution for Downstream tracks, the separation between signal and background events is poor. As a consequence, the number of selected Downstream candidates overflows the trigger rate. Therefore, only Long tracks can fire the HLT1 trigger.

The reconstruction of $\Xi_b^- \to \Xi^-\gamma$ decay involves the combination of two tracks compatible with the p and π^- hypotheses, and originating from a common displaced vertex. This is identified as a Λ, which is combined with a track from a π^- to form the Ξ^-. The Ξ_b^- candidate is reconstructed as the later combination of an energetic photon and the Ξ^-. Henceforth, the pion produced in the Λ decay will named π_Λ, whereas the tag π_Ξ will refer to the pion produced in the Ξ^- decay. A sketch of the full decay chain is shown in Figure 4.2. Since this is the first experimental attempt to search for the $\Xi_b^- \to \Xi^-\gamma$ decay, the selection criteria have been designed from scratch. In particular, the HLT2 and stripping algorithms to specifically reconstruct $\Xi_b^- \to \Xi^-\gamma$ candidates have been developed as part of the work for this thesis. Similarly to the $\Lambda_b^0 \to \Lambda\gamma$ case, the main source of background is due to combinations of Ξ^- candidates and random photons, consequence of the lack of information on the photon direction. Conversely, the Λ origin vertex is reconstructed thanks to the combination of the track of the π_Ξ^- and the

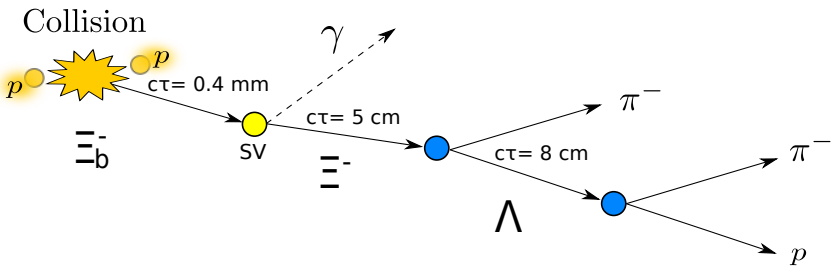

Figure 4.2: Topology of the $\Xi_b^- \to \Xi^-\gamma$ decay.

Λ baryon. The ability to reconstruct the Ξ^- decay vertex, combined with the lower production of prompt Ξ^- baryons, allows to trigger on events reconstructed not only with Long tracks but also Downstream tracks. Lastly, especially for Downstream tracks, the π^- mesons from the Ξ^- and Λ decays can be swapped. Since all the particles in the chain ($\gamma\pi_\Xi\pi_\Lambda p$) belong to the correct decay, the masses of the Ξ^- and Ξ_b^- are correctly reconstructed. However, the Λ will have an unusually high mass, as illustrated in Figure 4.3. These wrongly reconstructed Λ can easily be mitigated through a requirement on the Λ mass.

Three different reconstruction modes, based on the track types of the final state particles, are considered for $\Xi_b^- \to \Xi^-\gamma$ decay: Long-Long-Long (LLL), Down-Down-Long (DDL) and Down-Down-Down (DDD). The first two indices refer to the Λ decay products, while the third one refers to the π^- originated in the Ξ^- decay (π_Ξ).

4.1.1 Momentum post-calibration

The ECAL detector channels are calibrated using large samples of photons and neutral pions ($\pi^0 \to \gamma\gamma$) [100]. This calibration takes into account the geometrical acceptance and the energy loss due to material interaction, specially in PS subdetector system. These effects are parametrized using mainly low energy photons. The extrapolation of this parametrization to high energy photons from b-hadron decays induces a bias in the energy measurement at percent level. For γ's from b-hadron decays, a post-calibration is then applied on the photon energy to both, simulation and data, and then are propagated to the related variables. The parameters of the post-calibration are extracted by aligning the reconstructed mass of $B \to K^*\gamma$ events with its known mass. Figure 4.4 shows the existing bias in the b-baryon mass and how it is solved

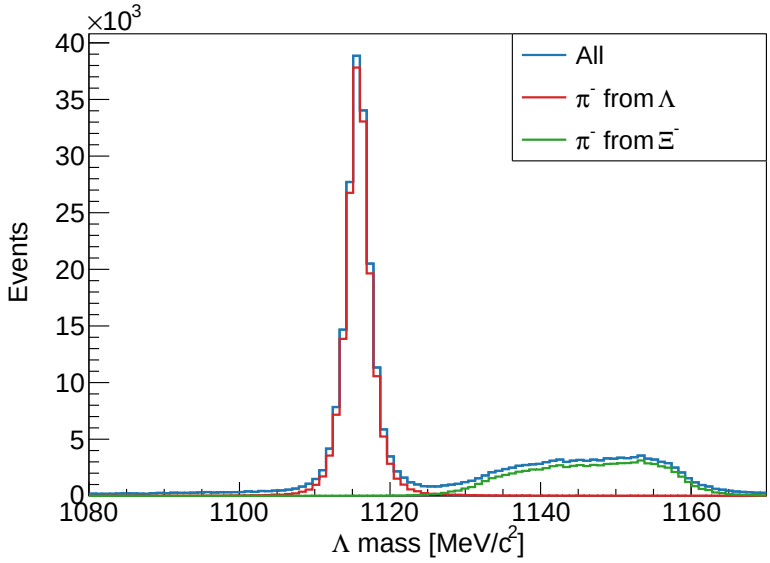

Figure 4.3: Invariant mass distribution of Λ candidates after the stripping selection in simulation. The Λ candidates reconstructed with its π^- appear in blue, whereas those wrongly reconstructed are shown in red.

with the post-calibration.

4.1.2 Normalization and control channels

Additional decay modes are used in this analysis for normalization and control. These channels have been previously studied and are relatively well known. The use of control samples allows to verify the agreement between data and simulation for key kinematic variables, and to apply corrections if needed. The normalization samples are used to translate the observed yield of the radiative channel into an absolute branching ratio. This is particularly important in pp collision machines where absolute precise measurements are difficult to perform and they are affected by high systematic uncertainties. The branching ratio is computed using the relation between the extracted yields of the radiative and normalization channels, and the known branching ratio of the normalization channel. Since this is computed as a ratio, the more similar to the radiative the reconstruction of the normalization channel is, the more sources of uncertainty are canceled. The normalization and control channels considered in this analysis are:

- $\Lambda_b^0 \to \Lambda J/\psi$ for control and normalization of the $\Lambda_b^0 \to \Lambda\gamma$ decay. This

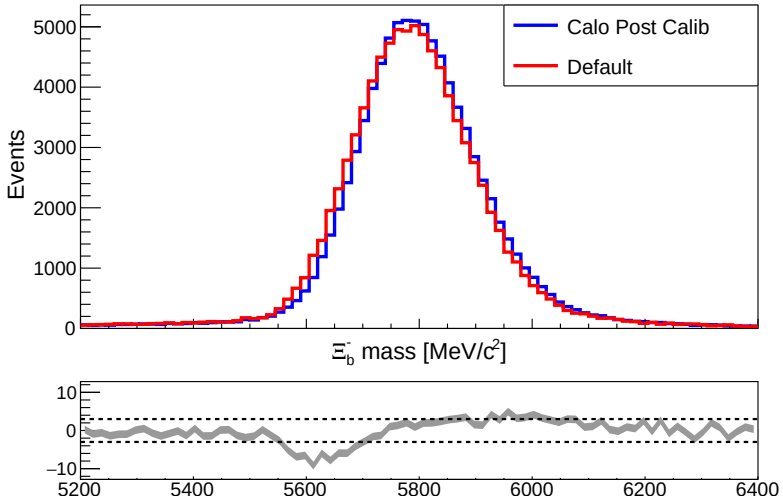

Figure 4.4: Reconstructed mass of the Ξ_b^- baryon in the radiative decay $\Xi_b^- \to \Xi^-\gamma$ from simulation before (blue) and after (red) the momentum (calorimeter) post-calibration.

channel shares the hadronic part in the final state with the $\Lambda_b^0 \to \Lambda\gamma$ decay, which allows to perform the study of the MC-data agreement. Furthermore, it is used as normalization channel to reduce systematic uncertainties by canceling the $\mathcal{L}$, $\sigma_{b\bar{b}}$, f_{Λ_b}, and $\mathcal{B}(\Lambda \to p\pi)$ terms in the ratio of branching ratios, as discussed in Section 6.2.3. The $\Lambda_b^0 \to \Lambda J/\psi$ decay channel is also used to control the both, the $\Lambda_b^0 \to \Lambda J/\psi$ and $\Xi_b^- \to \Xi^- J/\psi$ helicity angular distributions.

- $\Lambda_b^0 \to pK^- J/\psi$ to control the Λ_b^0 part of the $\Lambda_b^0 \to \Lambda\gamma$ decay. For this, the use of the much more statistically abundant and cleaner $\Lambda_b^0 \to pK^- J/\psi$ decay, as compared to $\Lambda_b^0 \to \Lambda J/\psi$, is preferred. The study of MC-data agreement for the kinematic distribution of the Λ_b^0 is performed with this channel, as explained in Section 4.6.

- $\Xi_b^- \to \Xi^- J/\psi$ for control and normalization of the $\Xi_b^- \to \Xi^-\gamma$ mode. This channel provides the largest number of events[1] due to its branching ratio, and shares its hadronic part with $\Xi_b^- \to \Xi^-\gamma$, which allows to check the MC-data agreement. Furthermore, it is used as normalization channel to reduce systematic uncertainties by canceling the $\mathcal{L}$, $\sigma_{b\bar{b}}$, f_{Ξ_b},

[1]The decay mode for Ξ_b^- with highest the branching ratio is $\Xi_b^- \to \Xi^- l^- \nu_l X$. However, the presence of the neutrino makes its reconstruction significantly more challenging.

$\mathcal{B}(\Xi^- \to \Lambda\pi^-)$ and $\mathcal{B}(\Lambda \to p\pi)$ terms in the ratio of branching ratios. Due to the complexity of the theoretical helicity angular distribution of the $\Xi_b^- \to \Xi^- J/\psi$ decay channel, this channel is not used as control channel for the photon polarization measurement.

The reconstruction of the $\Lambda_b^0 \to \Lambda J/\psi$ and $\Xi_b^- \to \Xi^- J/\psi$ dimuonic decays is quite similar to the case of $\Lambda_b^0 \to \Lambda\gamma$ and $\Xi_b^- \to \Xi^-\gamma$ radiative decays, respectively. Differences arise from the J/ψ meson decaying into two muons. Since the J/ψ meson is a resonance, it does not fly before decaying and, thus, its decay shares vertex position with the b-baryon. This feature facilitates the determination of the SV since it makes use of three particles. However, it is still possible to skip the SV reconstruction and use instead a combination of the hadron and the J/ψ momenta to reconstruct the b-baryon. Following this procedure, the reconstruction of the origin vertex of the photon is emulated, providing an excellent control tool for radiative decays, specially regarding the angular distributions. This strategy is used in the $\Lambda_b^0 \to \Lambda J/\psi$ reconstruction. Using the same strategy for the $\Xi_b^- \to \Xi^- J/\psi$ reconstruction would lead to a low expected yield. The information from the SV in the $\Xi_b^- \to \Xi^- J/\psi$ allow to develop a selection strategy efficient enough to cope with the lower resolution of Downstream tracks. Therefore, the track topologies LLL, DDL and DDD for the $\Xi_b^- \to \Xi^- J/\psi$ decay channel are selected following the same criteria. The topology of the $\Lambda_b^0 \to \Lambda J/\psi$ and $\Xi_b^- \to \Xi^- J/\psi$ dimuonic decays can be seen in Figures 4.5 and 4.6, respectively.

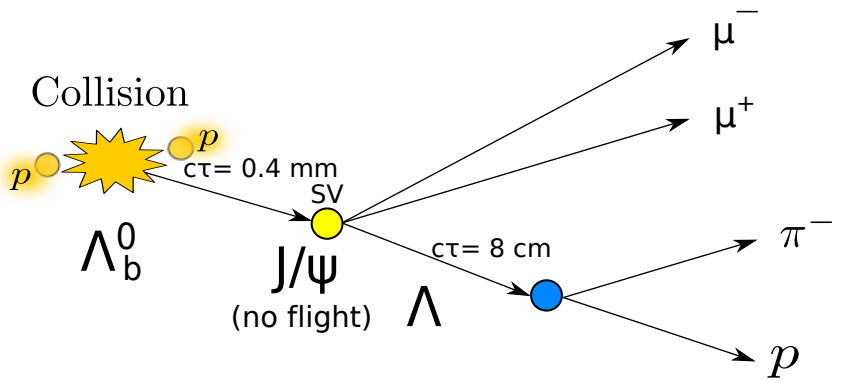

Figure 4.5: Topology of the $\Lambda_b^0 \to \Lambda J/\psi$ decay.

The $\Lambda_b^0 \to pK^- J/\psi$ requires the combination of four tracks in the same vertex to form the Λ_b^0. Two of the tracks must be compatible with a p and

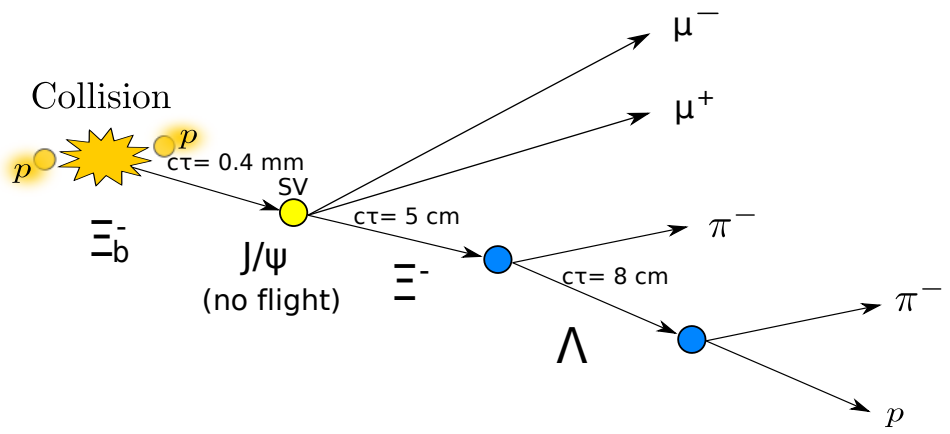

Figure 4.6: Topology of the $\Xi_b^- \to \Xi^- J/\psi$ decay.

a K^- hypotheses. The other two tracks have to be compatible with muon tracks and their invariant mass must be compatible with the J/ψ mass. This decay is depicted in Figure 4.7.

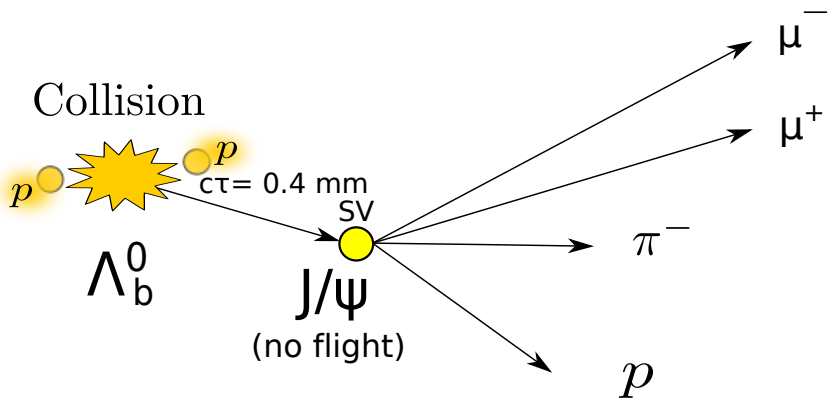

Figure 4.7: Topology of the $\Lambda_b^0 \to pK^- J/\psi$ decay.

4.1.3 Variables of interest

The tools and techniques at LHCb to select the aforementioned channels exploit the fact that particles produced in a heavy hadron decay have a higher transverse momentum and are significantly displaced from the PV. The variables included in the selection criteria are described in the following:

- $\boldsymbol{p_T}$: The transverse momentum is the momentum of a particle in the plane perpendicular to the beam axis, and is defined as $p_T = \sqrt{p_x^2 + p_y^2}$.
- **DOCA**: The Distance Of Closest Approach is defined as the smallest distance between two tracks, as illustrated in Figure 4.8a. This defini-

tion can be extended to intermediate particles that do not produce a track but, whose direction can be computed from their decay products. A small DOCA implies that the two tracks have been originated at the same vertex.

- **MT-DOCA**: The MoTher DOCA is the DOCA of a particle with respect to its mother. A small MT-DOCA ensures the correct reconstruction of the mother particle.

- **IP**: The Impact Parameter is the equivalent of the DOCA for a track and a vertex. It is defined as the smallest distance between a vertex and the extrapolation of the track, as pictured in Figure 4.8b. A small IP implies that the evaluated track has been originated in the vertex. The IP is commonly used to select those tracks that do not come from the PV and, thus, have a high IP with respect to the PV.

- $\boldsymbol{\chi^2}$: The quality of the track or vertex reconstruction from the track or vertex fit allows to select real tracks and vertices which position have been correctly computed. This quantity is usually normalized by the number of degrees of freedom (ndf), and expressed as χ^2/ndf.

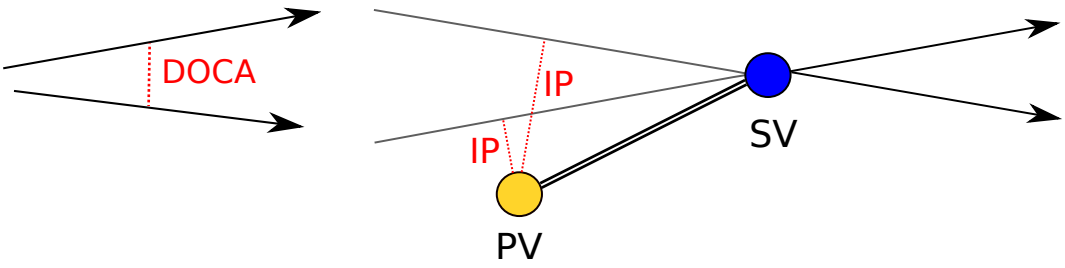

(a) (b)

Figure 4.8: (a) Definition of the DOCA variable (red dashed line). It is worth mentioning that DOCA is evaluated using the three spatial dimensions. (b) Sketch of a particle (double line) originated at the PV and decaying in two tracks at the SV. The IP of these decay products (extrapolated backward) with respect to the PV is shown (red dashed lines).

- **DIRA**: The DIRection Angle is the angle between the path defined by the position of the origin and decay vertices of the particle, and

its momentum direction reconstructed from its decay products. The DIRA is zero if the decay is properly reconstructed. The DIRA can also be defined using the PV instead of the origin vertex. A large DIRA_{PV} implies that the particle is not originated at the PV. The DIRA definition is illustrated in Figure 4.9.

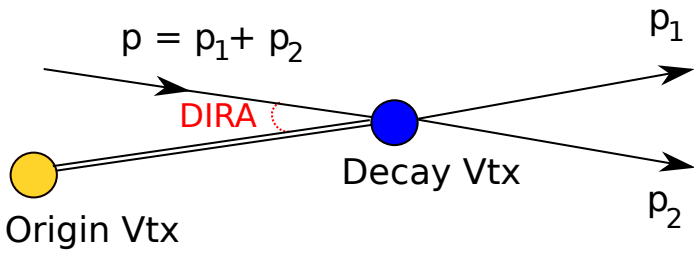

Figure 4.9: Topology of a particle (double line) originated at "Origin Vtx" and decaying in two tracks at "Decay Vtx". The combination of these decay products gives the momentum direction. The DIRA angle is shown (red dashed line).

- **Ghost Prob**: The Ghost probability is the output of a multivariate classifier that combines information from the track fit quality using different tracking devices. It grants rejection against ghost tracks, for which a significant fraction of hits associated to the track does not belong to it.

- **FD**: The Flight Distance is the length traveled by a decaying particle. It is computed as the distance between the production and the decay vertex. The FD is specially useful taking the assumption that the particle is originated at the PV. Hereby, a FD larger than expected implies that the hypothesis of PV as origin point for the particle is false and, thus, that the particle has been produced in a secondary vertex.

- $\mathcal{A}_p$: The momentum asymmetry is defined as the normalized difference between the momentum of a given particle (p) and the total momentum of the tracks in a cone around the particle (p_{Cone}):

$$\mathcal{A}_p = \frac{p - p_{\text{Cone}}}{p + p_{\text{Cone}}}\,. \tag{4.1}$$

  The transverse momentum asymmetry is defined with an equivalent expression, replacing p with p_T.

- **γ CL**: The Confidence Level of the photon helps to the discriminate photons from hadrons using PS, ECAL, HCAL and cluster-track matching information.

- **DLS**: The Decay Length Significance of a decaying particle express the level of certainty on the FD measured from the PV.

- **PID**: The Particle IDentificacion requirements for a particle combine the information from the PID system to compute the likelihood of a certain mass hypothesis. The methods used for this work are DLL, ProbNN and PID, and they are described in Section 2.2.2.

4.2 Data samples

This analysis uses *pp* collision data acquired by the LHCb experiment during the Run II of the LHC at a center of mass energy of $\sqrt{s} = 13$ TeV. In particular, for the $\Lambda_b^0 \to \Lambda\gamma$ channel, data from 2016 has been used (as in [40]), whereas for the $\Xi_b^- \to \Xi^-\gamma$ decay data from 2018 is exploited. The reason for this choice was the inclusion in 2018 of selection variables crucial for the analysis, which, to date, are only available in the 2018 data sample. Table 4.1 lists the data samples used in the analysis.

Year	**Energy** (TeV)	**Decay**	**Luminosity** (fb^{-1})
2016	13	$\Lambda_b^0 \to \Lambda\gamma$ $\Lambda_b^0 \to \Lambda J/\psi$ $\Lambda_b^0 \to pK^- J/\psi$	1.67
2018	13	$\Xi_b^- \to \Xi^-\gamma$ $\Xi_b^- \to \Xi^- J/\psi$	2.19

Table 4.1: Data taking periods used in this analysis. Details about the recorded luminosity and the center of mass energy are given for each year.

These chosen samples allow to develop a precise experimental strategy and serve as proof of concept for these novel analyses. As a next step, the analysis will be extended including the whole Run II data. Simulated samples generated by the centralized production of the LHCb experiment are used to optimize the selection criteria, to obtain efficiencies, to study

background sources and to model invariant mass shapes. General purpose simulated samples only requires that the generated decay chain is contained inside the LHCb detector. The generation can be optimized by requesting that the generated event fulfills a selection criteria, such as the stripping line used for data. The samples reproduce the running conditions for 2016 and 2018 data taking periods. A comprehensive list of the simulated samples included in this analysis can be seen in Table 4.2.

Year	**Energy** (TeV)	**Decay**	**# events**	**Filtered**
2016	13	$\Lambda_b^0 \to \Lambda\gamma$	513448	✓
		$\Lambda_b^0 \to \Lambda J/\psi$	4016916	
		$\Lambda_b^0 \to pK^- J/\psi$	1046532	
2018	13	$\Xi_b^- \to \Xi^-\gamma$	805172	✓
		$\Xi_b^- \to \Xi^- J/\psi$	823513	✓

Table 4.2: Summary of the MC samples used for this analysis and their generated statistics.

4.3 Trigger and stripping

4.3.1 Trigger and stripping for radiative channels

The first steps in the selection chain for the signal candidates are performed by the Trigger system, as described in Section 2.2.3. In this analysis, all the trigger requirements are Trigger On Signal (TOS), implying that the signal candidate is sufficient to fire the trigger.

The L0 stage for radiative decays selects those events with a highly energetic photon (`L0Photon`) or electron (`L0Electron`). The latter is responsible for selecting those events wherein the photon is converted in the material into an e^-e^+ pair after the magnet. These trigger lines are fired by the presence of a cluster in the ECAL with an E_T above a threshold and a low SPD multiplicity. The E_T threshold is different for 2016 and 2018 data-taking periods. Due to configuration issues, this threshold varied during 2016. The effect of the different thresholds will be detailed and evaluated in Section 6.2.9. Table 4.3 lists the requirements imposed by `L0Photon` and

L0Electron.

Variable	L0Photon	L0Electron	Units
E_T (2016)	$> (2304 - 2976)$	$> (2122 - 2616)$	MeV
E_T (2018)	> 2952	> 2376	MeV
SPD multiplicity	< 450	< 450	

Table 4.3: Selection requirements applied on the L0 stage for the radiative channels. Candidates must fire any of the two lines.

At the HLT1 stage, the candidate should fire the Hlt1TrackMVA or Hlt1TwoTrackMVA lines. The former searches for events with at least one good quality track with a high p_T and displaced from the PV. These requirements ensure that the decision is taken on tracks originated from heavy hadron decays, while rejecting fake tracks and particles produced directly from the hadronization process. Hlt1TwoTrackMVA imposes equivalent requisites for two tracks, which should point to the same vertex. Besides, the combination of the two tracks has to fulfill extra conditions, ensuring the quality of the combination and an origin different from the hadronization vertex. The efficiency of these HLT1 lines is further optimized by using a multivariate analysis (MVA) technique. The full list of requirements imposed by Hlt1TrackMVA or Hlt1TwoTrackMVA can be found in Table 4.4.

During Run I, no HLT2 line reconstructing exclusively radiative b-baryon decays was available. At the begining of Run II, dedicated trigger lines were included to select the $\Lambda_b^0 \to \Lambda\gamma$ and $\Xi_b^- \to \Xi^-\gamma$ decays. The former uses a selection named HLT2RadiativeLb2L0GammaLL. The trigger algorithm selecting the latter is the Hlt2RadiativeHypb2L0HGammaXi line. A summary of the selection requirements of these two lines is given in Table 4.5 and Table 4.6.

Finally, the candidates are reconstructed and further filtered by the stripping procedure, which follows a strategy similar to the trigger. The selection criteria applied to the $\Lambda_b^0 \to \Lambda\gamma$ channel by the dedicated stripping algorithm, called StrippingLb2L0Gamma, are shown at Table 4.7. Similarly, the requirements applied by StrippingXib2XiGamma_(LLL/DDL/DDD) are listed in Table 4.8. This stripping algorithm is responsible for reconstructing the $\Xi_b^- \to \Xi^-\gamma$ decay mode, for the different track type combinations. In or-

Variable	`Hlt1TrackMVA`	`Hlt1TwoTracksMVA`	Units
Track p_T	$[1000, 25\,000]$	> 500	MeV/c
Track p	–	> 5000	MeV/c
Track χ^2	< 2.5	< 2.5	
Track χ^2_{IP}	> 7.4	> 4	
Track Ghost Prob	< 0.2	–	
Intermediate hadron mass	–	> 1000	MeV/c^2
Intermediate hadron η	–	$(2, 5)$	
Intermediate hadron p_T	–	> 2000	MeV/c
Intermediate hadron $DIRA_{\text{PV}}$	–	> 0	mrad
Intermediate hadron χ^2_{Vtx}	–	< 10	
χ^2			
χ^2_{FD}		MVA	
Sum p_T			MeV/c
Number of tracks with $\chi^2_{\text{IP}} < 16$			

Table 4.4: Selection requirements applied on the HLT1 lines relevant for this analysis. The last four variables are used as input for a MVA method. Candidates must fire any of the two lines.

Variable	Requirement	Units
Track p	> 2000	MeV/c
Track p_T	> 250	MeV/c
Track χ^2_{IP}	> 36	
Track χ^2	< 3	
Tracks DOCA	< 0.2	mm
Tracks and γ $\sum p_T$	> 5000	MeV/c
p DLLp	> 0	
Λ p_T	> 1500	MeV/c
Λ IP	> 0.1	mm
Λ χ^2_{Vtx}	< 15	
Λ χ^2_{FD}	> 0	
Λ ΔM	< 20	MeV/c^2
Λ τ	> 2	ps
γ p	> 5000	MeV/c
γ p_T	> 2000	MeV/c
Λ_b^0 p_T	> 1000	MeV/c
Λ_b^0 $\chi^2_{\text{MT-DOCA}}$	< 9	
Λ_b^0 ΔM	< 1000	MeV/c^2

Table 4.5: Selection of `HLT2RadiativeLb2L0GammaLL` the HLT2 exclusive line for the $\Lambda_b^0 \to \Lambda\gamma$ decay channel.

Variable	Requirement	Units
Track p	> 2000	MeV/c
Track p_T	> 200	MeV/c
Track χ^2_{IP}	> 20	
Track χ^2	< 4	
Tracks $\sum p_T$	> 500	MeV/c
Tracks and γ $\sum p_T$	> 5000	MeV/c
Λ ΔM	< 20	MeV/c^2
Λ τ	> 4.5	ps
Ξ_{LLL} mass	$\in (1290, 1355)$	MeV/c^2
Ξ_{DDL} mass	$\in (1270, 1370)$	MeV/c^2
Ξ_{DDD} mass	$\in (1270, 1375)$	MeV/c^2
Ξ τ	> 2	ps
Ξ DIRA$_{\text{PV}}$	> 0.95	mrad
Ξ χ^2_{PV}	> 10	
Ξ p	> 10000	MeV/c
Ξ p_T	> 1000	MeV/c
γ p	> 5000	MeV/c
γ p_T	> 2000	MeV/c
Ξ_b p_T	> 1000	MeV/c
Ξ_b p	> 20000	MeV/c
Ξ_b $\chi^2_{\text{MT-DOCA}}$	< 9	
Ξ_b ΔM	< 1000	MeV/c^2

Table 4.6: Selection of the `Hlt2RadiativeHypb2L0HGammaXi` HLT2 exclusive line for the $\Xi_b^- \to \Xi^-\gamma$ decay channel.

Variable	Requirement	Units
Track MAX χ^2/ndf	< 3	
Track MIN χ^2/ndf	< 2	
Track MIN χ^2_{IP}	> 16	
Track Ghost Prob	< 0.4	
π p	> 2000	MeV/c
π p_T	> 300	MeV/c
p p	> 7000	MeV/c
p p_T	> 800	MeV/c
Tracks and γ $\sum p_T$	> 5000	MeV/c
Λ χ^2_{Vtx}	< 9	
Λ_{LL} IP	> 0.05	
Λ_{LL} ΔM	< 20	MeV/c^2
Λ_{DD} ΔM	< 30	MeV/c^2
Λ p_T	> 1000	MeV/c
γ p_T	> 2500	MeV/c
γ CL	> 0.2	
Λ_b^0 p_T	> 1000	MeV/c
Λ_b^0 $\chi^2_{\text{MT-DOCA}}$	< 7	
Λ_b^0 ΔM	< 1100	MeV/c^2

Table 4.7: Stripping requirements applied to reconstruct $\Lambda_b^0 \to \Lambda\gamma$ candidates by the `StrippingLb2L0Gamma` line.

der to reduce the stripping rate, the candidates are required to be triggered by the `L0Photon` or `L0Electron` lines. The selection was optimized using the $\Xi_b^- \to \Xi^-\gamma$ MC sample with 2015 conditions. A further tuning of this stripping line was performed latter at the end of 2018.

Variable	Requirement	Units
Track χ^2/ndf	< 4	
Track χ^2_{IP}	> 16	
Track Ghost Prob	< 0.4	
p p_T	> 630	MeV/c
π_Λ p_T	> 120	MeV/c
π_Ξ p_T	> 130	MeV/c
Λ p_T	> 850	MeV/c
Λ χ^2_{Vtx}	< 9	
Ξ^- p_T	> 500	MeV/c
Ξ^- p	> 10000	MeV/c
Ξ^- χ^2_{Vtx}	< 8	
$\Xi^-\Delta$M	< 30	MeV/c^2
γ p_T	> 2500	MeV/c
γ CL	> 0.15	
Ξ_b^- p_T	> 500	MeV/c
Ξ_b^- p	> 15000	MeV/c
$\Xi_b^-\Delta$M	< 800	MeV/c^2
Ξ_b^- $\chi^2_{\text{MT-DOCA}}$	< 15	
Trigger lines	`L0Electron` or `L0Photon`	

Table 4.8: Stripping requirements applied to reconstruct $\Xi_b^- \to \Xi^-\gamma$ candidates by the `StrippingXib2XiGamma_(LLL/DDL/DDD)` line.

4.3.2 Trigger and stripping for normalization and control channels

The selection criteria followed to achieve clean normalization and control samples exploits the fact that a dimuonic decay of a b-hadron is characterized by the emission of high-p_T muons. At L0 stage, these events are selected

by the `L0Muon` and `L0DiMuon` lines. The latter has a softer p_T selection and requests two muons. Table 4.9 lists the selection requirements. For

Variable	`L0Muon`	`L0DiMuon`	Units
SPD multiplicity	< 450	< 900	
$\mu\ p_T$	> 1480	–	MeV/c
$\mu^+\ p_T \times \mu^-\ p_T$	–	> 1680000	MeV^2/c^2

Table 4.9: Selection requirements applied on the L0 stage for the normalization and control channels. Candidates must fire any of the two lines.

HLT1, the candidate fires the `Hlt1TrackMuon` or the `Hlt1DiMuonHighMass` lines. The former applies requirements over one of the muon candidates, whereas the latter imposes requirements over the tracks of the two muons and their combination. The selection criteria at HLT1 level is summarized in Table 4.10. At HLT2 level, the line `Hlt2DiMuonDetachedJPsi` selects

Variable	`Hlt1DiMuonHighMass`	`Hlt1TrackMuon`	Units
Track χ^2/ndf	< 4	< 2	
$\mu\ p_T$	> 500	> 1000	MeV/c
$\mu\ p$	> 6000	> 8000	MeV/c
μ IP	–	> 0.1	mm
$\mu\ \chi^2_{\text{IP}}$	–	> 16	
J/ψ mass	> 2700	–	MeV/c^2
Trigger lines	`L0Muon` or `L0DiMuon`		

Table 4.10: Selection requirements applied on the HLT1 stage for the normalization and control channels. Candidates must fire any of the two lines.

the candidates for the $\Lambda_b^0 \to \Lambda J/\psi$, $\Xi_b^- \to \Xi^- J/\psi$ and $\Lambda_b^0 \to pK^- J/\psi$ channels. This line is triggered by two muon tracks whose combination is compatible with a J/ψ meson not originated at the PV. Table 4.11 reports the requirements of the line triggered by a J/ψ produced in a heavy hadron decay.

The stripping step reconstructs and uses the full decay chain to select the candidate, and, thus, a different stripping algorithm is used for each decay channel:

Variable	`Hlt2DiMuonDetachedJpsi`	Units
Track Ghost Prob	< 0.4	
Track χ^2/ndf	< 5	
J/ψ ΔM	< 120	MeV/c^2
J/ψ χ^2_{Vtx}	< 25	
DLS	> 3	

Table 4.11: Selection requirements applied on the HLT2 stage triggering on the J/ψ meson of the normalization and control channels.

- The `Lb2L0Gamma_Lb2L0Jpsi` stripping algorithm reconstructs the $\Lambda_b^0 \to \Lambda J/\psi$ channel, aligned with the $\Lambda_b^0 \to \Lambda\gamma$ stripping line. This stripping line does not reconstruct the Λ_b^0 decay vertex, following the same procedure as for the radiative decay.

- The `B2XMuMu` stripping line selects $\Lambda_b^0 \to pK^- J/\psi$ candidates. This is an inclusive line which selects the topology of the event without applying particle identification (PID) cuts. After the stripping, the proper mass hypothesis is assigned to each particle.

- The stripping algorithm selecting $\Xi_b^- \to \Xi^- J/\psi$ candidates is called `HeavyBaryon_Xib2JpsiXi`.

The full list of requirements imposed by the stripping algorithms to the $\Lambda_b^0 \to \Lambda J/\psi$ and $\Xi_b^- \to \Xi^- J/\psi$ candidates appears in Table 4.12. The requirements for the line `B2XMuMu` are more complex in order to include all the possibilities of the inclusive stripping lines. The `B2XMuMu` requirement can be consulted in the $\Lambda_b^0 \to pK^- J/\psi$ analysis [101].

4.4 Preselection

4.4.1 Preselection for the radiative channels

The preselection is a filtering step based on linear cuts applied on top of the stripping, whose purpose is to reduce the data sample size while keeping as much signal as possible. The selection criteria are optimized using signal and background samples filtered by the corresponding trigger and stripping

Variable	`HeavyBaryon_Xib2JpsiXi`	`Lb2L0Gamma_Lb2L0Jpsi`	Units
$\sum p_T$	–	> 5000	MeV/c
Track χ^2/ndf	< 4	< 3	
Track $\chi^2_{\rm IP}$	–	> 16	
π p_T	> 100	> 300	MeV/c
π p	–	> 2000	MeV/c
p p_T	> 500	> 800	MeV/c
p p	–	> 7000	MeV/c
π PIDK	< 5	–	
π_Ξ $\chi^2_{\rm IP}$	> 9	–	
Λ p_T	–	> 1000	MeV/c
Λ IP	–	> 0.05	mm
Λ LL (DD) ΔM	< 15	< 20 (30)	MeV/c^2
Λ $\chi^2_{\rm Vtx}$	< 20	< 9	
Ξ^- ΔM	< 30	–	MeV/c^2
Ξ^- $\chi^2_{\rm Vtx}$	< 25	–	
DLS	> 5	–	
J/ψ ΔM	< 80	< 100	MeV/c^2
b-baryon ΔM	< 300	< 1100	MeV/c^2
b-baryon $\chi^2_{\rm Vtx}$	< 25		
b-baryon χ^2_{DOCA}	–	< 7	
b-baryon p_T	–	> 1000	MeV/c

Table 4.12: Stripping selection for the $\Lambda_b^0 \to \Lambda J/\psi$ and $\Xi_b^- \to \Xi^- J/\psi$ decay channels.

lines. The simulated samples are used as a proxy for the signal. The matching between the reconstructed and the simulated candidates (MC matching) ensures that only signal candidates are considered in the optimization procedure. On the other hand, the background sample is obtained taking the sidebands of the mass distribution in the data sample. The low mass sideband (LSB) corresponds to data candidates (Ξ_b^- or Λ_b^0) whose reconstructed invariant mass falls 300 MeV/c^2 or below the known value, whereas those candidates with a reconstructed invariant mass higher than 300 MeV/c^2 over the known value belongs to the high mass sideband (HSB). Complementary, the signal region corresponds to those candidates with a mass within the central interval, e.g. PDG mass $\pm$ 300 MeV/c^2. The invariant mass of the intermediate states (Ξ^- and Λ) shows a clean peak. The main background is expected to come from random combinations of photons and real Ξ^- or Λ baryons. As a consequence, the preselection focuses on high-p_T tracks with a vertex displaced from the PV, while only requiring soft particle identification. The preselection applied on $\Lambda_b^0 \to \Lambda\gamma$ candidates is listed in Table 4.13. The $\Xi_b^- \to \Xi^-\gamma$ decay mode has to follow the preselection described in Table 4.14.

Variable	Requirement	Units
Track p	$\in (3, 100)$	GeV/c
Track Ghost Prob	< 0.2	
π ProbNNpi	> 0.2	
p ProbNNp	> 0.2	
Λ IP	> 0.15	mm
Λ χ^2_{IP}	> 16	
Λ χ^2_{FD}	> 225	
Λ M	$\in (1110, 1122)$	MeV/c^2
γ p_T	> 3000	MeV/c
Λ_b^0 p_T	> 4000	MeV/c
Λ_b^0 MT-DOCA	< 0.05	mm
Λ_b^0 $\chi^2_{\text{MT-DOCA}}$	< 5	
Λ_b^0 ΔM	< 1000	MeV/c^2

Table 4.13: Preselection requirements applied on $\Lambda_b^0 \to \Lambda\gamma$ candidates

Variable	LLL	DDL	DDD	Units
Ξ_b^- p_T	> 4000	> 4000	> 4000	MeV/c
Ξ_b^- MT-DOCA	< 0.05	–	–	mm
Ξ^- ΔM	< 12	< 12	< 12	MeV/c^2
Ξ^- p_T	> 2000	> 2000	> 2000	MeV/c
Ξ^- IP	> 0.15	–	–	mm
Ξ^- FD	–	> 50	> 300	mm
Λ^0 ΔM	< 12	< 12	< 12	MeV/c^2
Λ^0 p_T	> 1500	> 1500	> 1500	MeV/c
Λ^0 IP	> 0.15	–	> 1.5	mm
Λ^0 χ^2_{IP}	–	–	> 10	
Λ^0 FD	> 50	> 400	> 400	mm
p ProbNNp	> 0.2	> 0.2	> 0.2	
Track Ghost Prob	< 0.2	> 0.2	> 0.2	
π_Ξ ProbNNpi	> 0.2	> 0.2	> 0.2	
π_Ξ First hit Z	< 400	–	–	mm
π_Ξ χ^2_{IP}	–	> 150	–	
π_Ξ IP	–	> 0.5	> 6	mm
π_Ξ p_T	–	> 300	> 250	MeV/c
π_Λ ProbNNpi	> 0.2	> 0.2	> 0.2	
π_Λ χ^2_{IP}	> 150	–	–	
π_Λ p_T	> 250	> 300	> 300	MeV/c
π_Λ p	–	> 3000	> 3000	MeV/c

Table 4.14: Preselection requirements applied on $\Xi_b^- \to \Xi^-\gamma$ candidates for the three track topologies (LLL, DDL and DDD).

4.4.2 Preselection for the normalization and control channels

Since the normalization and control channels have been previously studied, their preselections are already defined. Here, the requirements are listed in Table 4.15 for $\Lambda_b^0 \to \Lambda J/\psi$ [45] and $\Xi_b^- \to \Xi^- J/\psi$ [102], and in Table 4.16 for $\Lambda_b^0 \to pK^- J/\psi$ [101]. For a comprehensive description of the selection the corresponding analyses documentation should be consulted.

Variable	$\Lambda_b^0 \to \Lambda J/\psi$	$\Xi_b^- \to \Xi^- J/\psi$	Units
Track χ^2_{IP}	< 4	< 4	
p p_T	–	> 500	MeV/c
π p_T	–	> 100	MeV/c
π ProbNNpi	> 0.2	> 0.2	
p ProbNNp	> 0.2	> 0.2	
μ ProbNNmu	> 0.2	> 0.2	
Λ ΔM	< 6	< 6	MeV/c^2
Λ IP	> 0.15	–	mm
Λ χ^2_{IP}	> 16	–	
Λ χ^2_{FD}	> 225	–	
Ξ^- ΔM	–	< 11	MeV/c^2
Ξ^- χ^2_{Vtx}	–	< 16	
J/ψ ΔM	< 60	< 60	MeV/c^2
J/ψ χ^2_{Vtx}	< 16	< 16	
b-baryon p_T	> 4000	–	MeV/c
b-baryon τ	–	(0.3, 14)	ps
PV_z	–	< 100	mm
PV χ^2_{IP}	–	< 25	

Table 4.15: Preselection for the $\Lambda_b^0 \to \Lambda J/\psi$ and $\Xi_b^- \to \Xi^- J/\psi$ decay channels.

Variable	$\Lambda_b^0 \to pK^-J/\psi$	Units
p p_T	> 400	MeV/c
K p_T	>400	MeV/c
p p	> 7500	MeV/c
K p	> 2000	MeV/c
p PIDp	> 0	
p (PIDp - PIDK)	> 8	
K PIDK	> 0	
p IsMuon	$= 0$	
p IsMuon	$= 0$	
J/ψ ΔM	< 100	MeV/c^2
Λ_b^0 $\chi^2_{\rm Vtx}$	< 4	
Λ_b^0 DIRA	> 0.9999	

Table 4.16: Preselection requirements for the $\Lambda_b^0 \to pK^-J/\psi$ candidates.

4.5 Mass fit for the normalization and control channels

The remaining background contamination after trigger, stripping and preselection can be subtracted using the sPlot technique [103], as shown in Figure 4.10. This statistical tool is able to unfold different distributions when several components are merged into a single sample. This is achieved through the maximum likelihood fit in the variable of interest, in this case, the b-baryon invariant mass. The distributions used in the fit include a a double-sided crystal-ball [104] to model the signal, and an exponential to model the background. The mass fit model will be further described in Section 6.2.

4.6 Re-weighting of the simulated samples

Simulated samples are used to compute the selection criteria efficiencies and to identify the variables to discriminate between signal and background. As outlined in Section 3.3, the simulation could differ from the data. To ensure

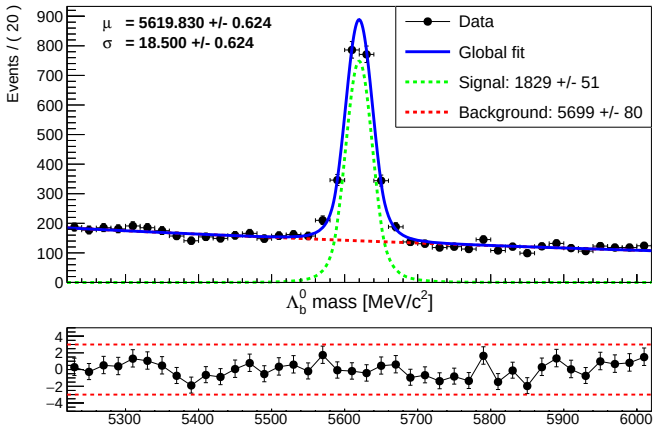

(a)

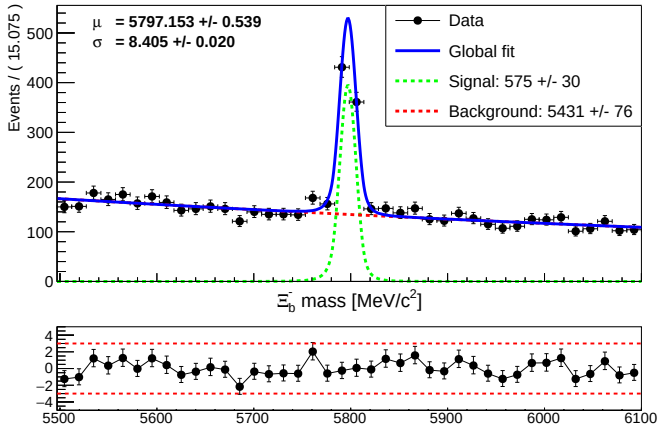

(b)

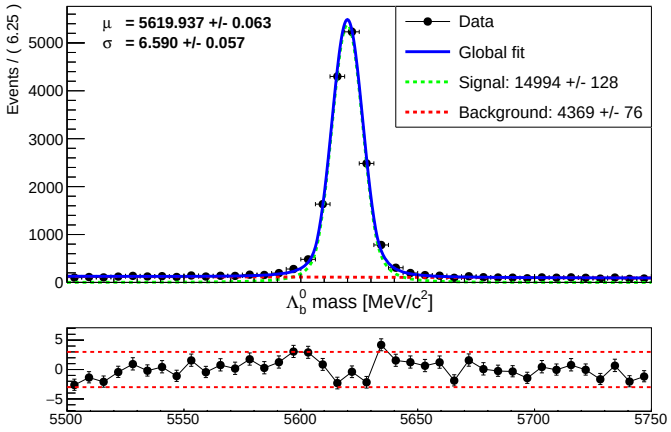

(c)

Figure 4.10: Invariant mass fit and signal yields for the (a) $\Lambda_b^0 \to \Lambda J/\psi$, (b) $\Xi_b^- \to \Xi^- J/\psi$ and (c) $\Lambda_b^0 \to pK^- J/\psi$ normalization and control channels.

accurate results, the distributions of the selected MC and data candidates are compared using the control channels. Discrepancies in the p_T of the b-hadron are found (see Figure 4.11). These discrepancies are corrected by applying weights on the simulated samples. In this procedure, called

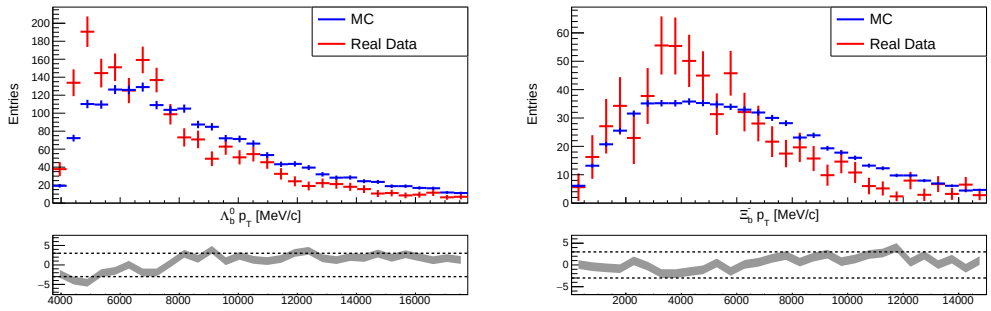

(a) (b)

Figure 4.11: Discrepancies between s-weighted data (red) and MC (blue) in the p_T distribution of the b-baryon for the (a) $\Lambda_b^0 \to \Lambda J/\psi$ and (b) $\Xi_b^- \to \Xi^- J/\psi$ decays.

"re-weighting", the weights are extracted from bin-by-bin ratios of unfolded signal data (using the sPlot technique) and MC distributions, for control samples. In this analysis, these weights are obtained from the ratio of the 2-dimensional distribution (p, p_T) of the b-hadron, which preserves the correlation between the two kinematic variables. Figure 4.12 compares the weights extracted from $\Lambda_b^0 \to pK^- J/\psi$ and $\Xi_b^- \to \Xi^- J/\psi$ control samples. Since the two decays show a similar behavior, along with the larger statistics of the former, the $\Lambda_b^0 \to pK^- J/\psi$ weights are chosen to correct both, the $\Lambda_b^0 \to \Lambda\gamma$ and $\Xi_b^- \to \Xi^-\gamma$ radiative decays. A satisfactory agreement between data and MC is obtained in the $\Lambda_b^0 \to \Lambda J/\psi$ and $\Xi_b^- \to \Xi^- J/\psi$ modes after correction, as shown in Figure 4.13.

The effect of the re-weighting on other relevant variables is given in Section A.2. Additionally, the good modeling of the simulation for the photon kinematic and geometric distributions is checked using the $B^0 \to K^*\gamma$ decay channel, as discussed in Section A.2.2.

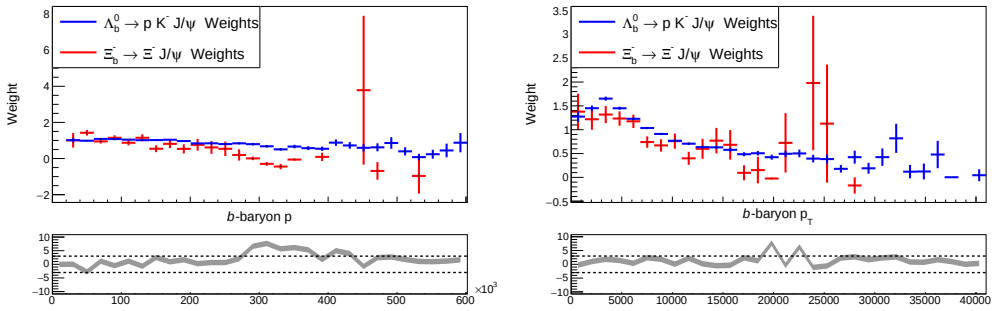

(a) (b)

Figure 4.12: Weights computed from $\Lambda_b^0 \to pK^-J/\psi$ (blue) and $\Xi_b^- \to \Xi^-J/\psi$ (red) for the (a) momentum and (b) transverse momentum distributions.

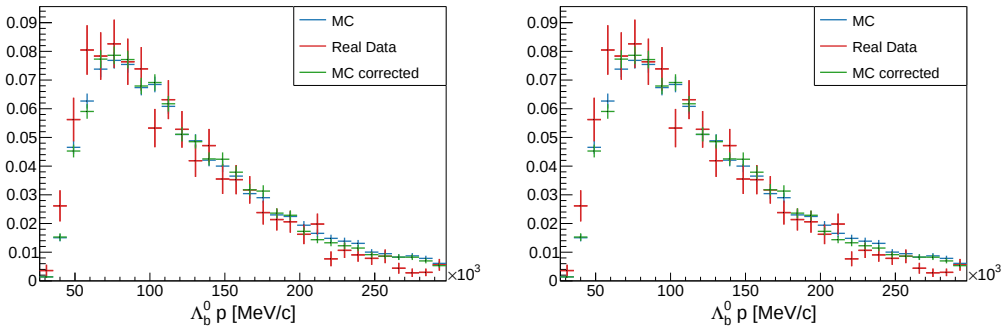

(a)

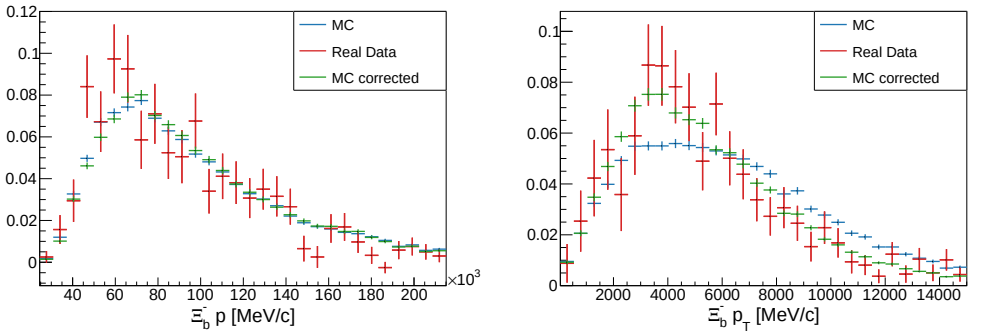

(b)

Figure 4.13: Distributions of the p (left) and p_T (right) for background subtracted data (red), MC (blue) and corrected MC (green) for the (a) $\Lambda_b^0 \to \Lambda J/\psi$ and (b) $\Xi_b^- \to \Xi^-J/\psi$ decays.

4.7 Boosted Decision Tree

A multivariate analysis (MVA) technique [105] is exploited for the radiative channels to further suppress the remaining combinatorial background. This method provides significantly enhanced discriminant power than linear selection criteria when the variables are correlated. The MVA optimizes the selection process by combining a bunch of variables in to a single one, whose requirement must be optimized. The MVA classifier is trained using reweighted MC-matched candidates from the simulation samples as signal, and candidates from the high mass sideband from data samples as background proxy[2]. In both cases, candidates are required to have passed the trigger, stripping and preselection conditions. The input variables, listed in Table 4.17, are chosen by its discriminant power.

The distributions of the background and the signal samples of these variables can be seen in Figure 4.14 and Figure 4.15, for the $\Lambda_b^0 \to \Lambda\gamma$ and the $\Xi_b^- \to \Xi^-\gamma$ decay channels, respectively. Several MVA approaches were explored in this analysis, and the optimal one was proved to be a Boosted Decision Tree (BDT) using the XGBoost algorithm [106] for the two decay channels.

A BDT is a classifier based on machine learning techniques, and its response is the weighted combination of several Decision Trees (DT). The DT is a classifier applying sequential rectangular cuts to a initial sample (root node). The samples resulting from the sequential set of binary decisions are known as leaves. The signal purity of the leaves is used to determine the optimal set of cuts. The sketch of a general decision tree is depicted in Figure 4.16. During the training phase of a BDT, the DTs are built sequentially, and each one uses a modified subset of the initial data set[3]. In a Gradient BDT, as that implemented by XGBoost, each DT adds gradients to the *loss function*[4] based on the classification complexity of the events. The next DT uses those gradients to improve the classification for the complex

[2]Real signal candidates suffering energy losses, such as bremsstrahlung, could be reconstructed with an invariant mass belonging to the low mass sideband range. This possible signal contribution is avoided by considering only the high mass sideband as background proxy.

[3]The subsets used for different DT can share events.

[4]Function used to optimize each rectangular cut in a DT.

Variable	$\Lambda_b^0 \to \Lambda\gamma$	$\Xi_b^- \to \Xi^-\gamma$		
		LLL	DDL	DDD
H_b p_T	✓	✓	✓	✓
H_b p			✓	✓
H_b MT-DOCA	✓	✓	✓	✓
Ξ^- IP		✓	✓	✓
Ξ^- FD		✓		✓
Ξ^- Cone(1.0) $\mathcal{A}_{p_T}$		✓	✓	✓
Ξ^- Neutral Cone(1.0) $\mathcal{A}_p$				✓
$\Lambda\pi_\Xi$ DOCA		✓	✓	
γ p_T	✓	✓	✓	✓
γ η	✓	✓	✓	✓
γ Cone(1.0) $\mathcal{A}_{p_T}$	✓	✓	✓	✓
γ Neutral Cone(1.0) $\mathcal{A}_{p_T}$		✓	✓	✓
γ Neutral Cone(1.0) $\mathcal{A}_p$		✓	✓	
Λ p_T	✓	✓	✓	✓
Λ IP	✓			✓
Λ χ^2_{IP}	✓	✓		
Λ FD	✓	✓	✓	✓
Λ Cone(1.0) $\mathcal{A}_{p_T}$	✓			
Λ Cone(1.0) $\mathcal{A}_p$	✓			
$p\pi_\Lambda$ DOCA	✓			
Tracks and γ $\sum p_T$	✓	✓	✓	✓
π_Ξ p_T			✓	✓
π_Ξ χ^2_{IP}		✓		
π_Λ p_T	✓		✓	✓
π_Λ IP	✓	✓	✓	
p p			✓	
p χ^2_{IP}	✓			

Table 4.17: List of variables used as input for the BDT for the $\Lambda_b^0 \to \Lambda\gamma$ and the $\Xi_b^- \to \Xi^-\gamma$ decay channels.

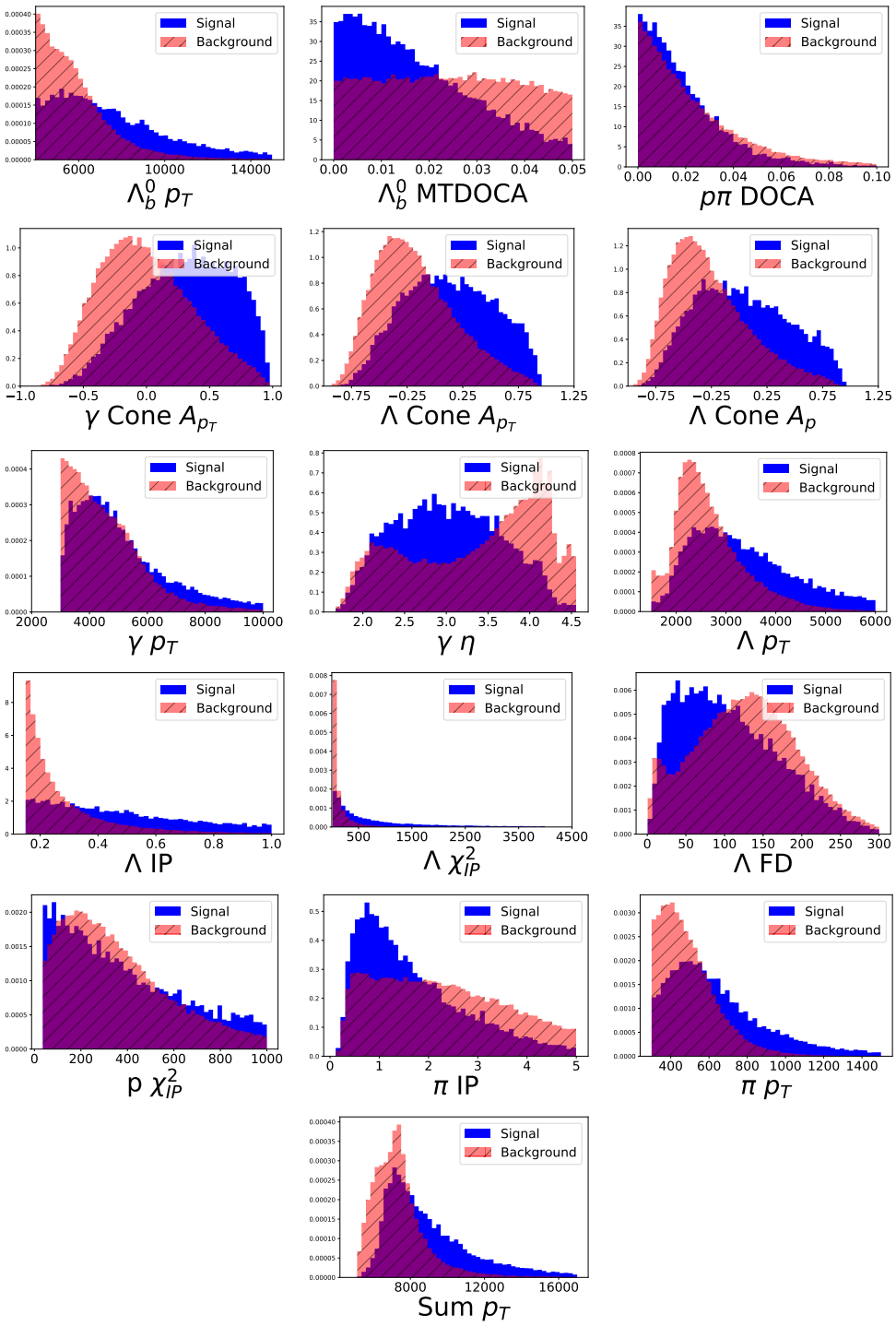

Figure 4.14: Distributions of the input variables used in the BDT training, for MC signal (blue) and background from high mass data sideband (red), for the $\Lambda_b^0 \to \Lambda\gamma$ decay channel.

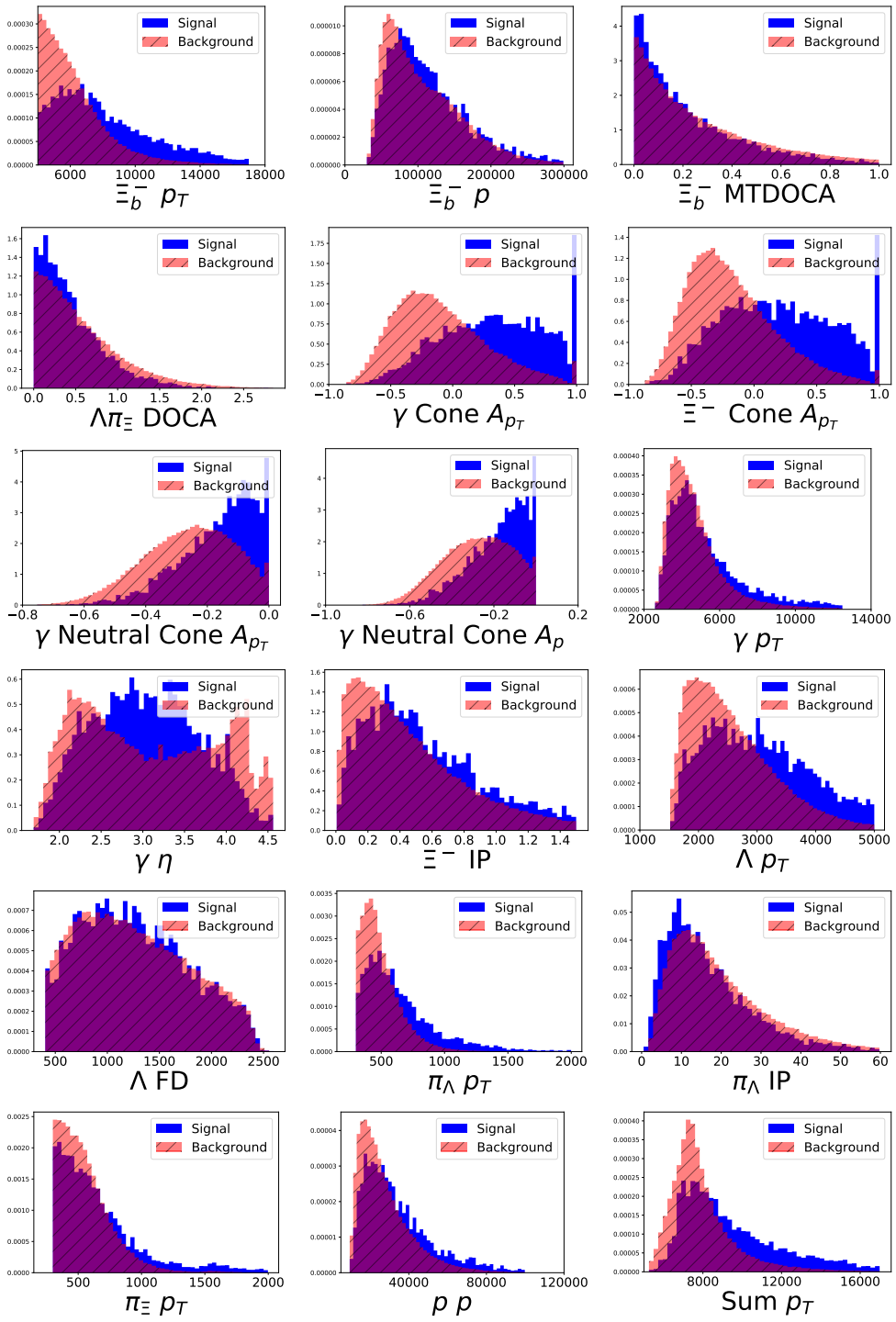

Figure 4.15: Distributions of the input variables used in the BDT training, for MC signal (blue) and background from high mass data sideband (red), for the $\Xi_b^- \to \Xi^-\gamma$ decay channel for DDL topology. The other topologies present similar behavior.

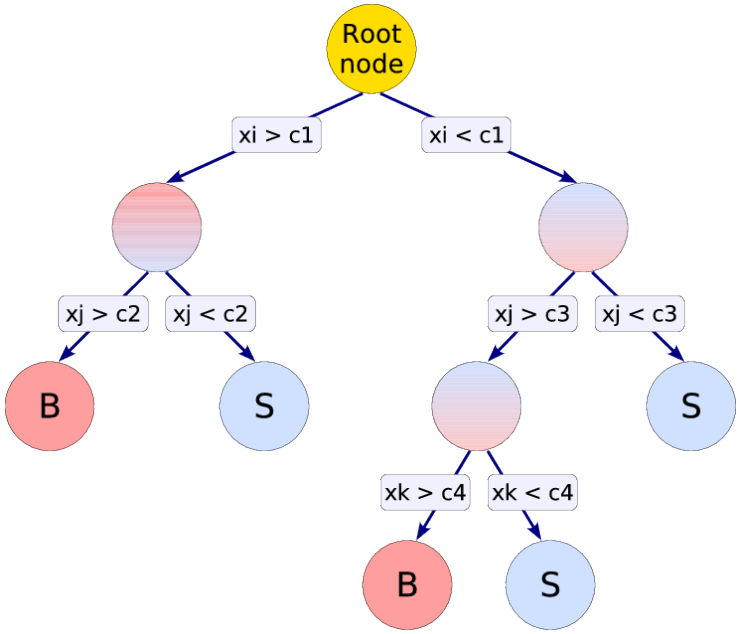

Figure 4.16: Structure of a general Decision Tree [107].

events.

The BDT algorithm is optimized throughout the hyper-parameters space. The most important ones for this analysis:

- **Number of trees**: number of DT used to take the weighted (boosted) decision.
- **Learning rate (η)**: proportion of information acquired in the building step of a DT and provided to the following DT.
- **Maximum Depth**: the maximum number of binary decisions allowed between the root node and a leaf.
- **Gamma**: the minimum reduction in the loss function required to make a further partition on a intermediate node of the DT.

The BDT configuration is optimized using an hyper-parameter search. This search executes the training and testing procedures for the possible hyper-parameter combinations. Table 4.18 reports the BDT configuration for each decay channel.

The small available statistics of the samples used in the training and the possibility of suffering performance estimation biases are intrinsic limitations of the MVA technique. This is avoided using the k-folding cross-validation

	# trees	Learning rate	Max Depth	Gamma
$\Lambda_b^0 \to \Lambda\gamma$	800	0.2	2	0.0
$\Xi_b^- \to \Xi^-\gamma$ (LLL)	300	0.3	2	0.3
$\Xi_b^- \to \Xi^-\gamma$ (DDL)	600	0.1	2	0.6
$\Xi_b^- \to \Xi^-\gamma$ (DDD)	400	0.1	3	0.3

Table 4.18: Hyper-parameter values for the optimal $\Lambda_b^0 \to \Lambda\gamma$ and $\Xi_b^- \to \Xi^-\gamma$ BDT configurations.

technique [108] with $k = 5$. In the k-folding method, the data set is split in k subsets and k classifiers are trained. Each classifier is trained using $k-1$ subsets and tested in the remaining one. This provides k independent classifiers, which reduces the sources of biases and provides further checks of overtraining. The absence of overtraining is verified by comparing the BDT response in the training and testing samples. Figure 4.17 shows the agreement between these two distributions, as expected in the case of no overtraining.

The signal and background samples provided to the BDT for training have significantly different invariant mass distributions. Since this variable is used to characterize the samples, it must be ensured that the classifier has no access to this variable through correlations with the input variables. Otherwise, the classifier would be inefficient against the combinatorial background while only removing the HSB. Figure 4.18 shows the response of the BDT in bins of the mass. The observed flat distributions imply that the BDT can not cause artificial peaks in the signal region.

The optimal condition on the classifier output is optimized maximizing the Punzi Figure of Merit (FoM) [109], defined as:

$$\text{FoM} = \frac{\epsilon(t)}{a/2 + \sqrt{B(t)}}, \tag{4.2}$$

where t is the cut value, ϵ is the signal efficiency, B is the expected number of background candidates in the signal region and a is the target statistical significance to observe the signal. The a parameter is fixed to 5 in this analysis. The value of ϵ is extracted from simulation, whereas B is obtained by fitting the mass distribution in the HSB in data and extrapolating the number of background events to the signal region. The distribution of the

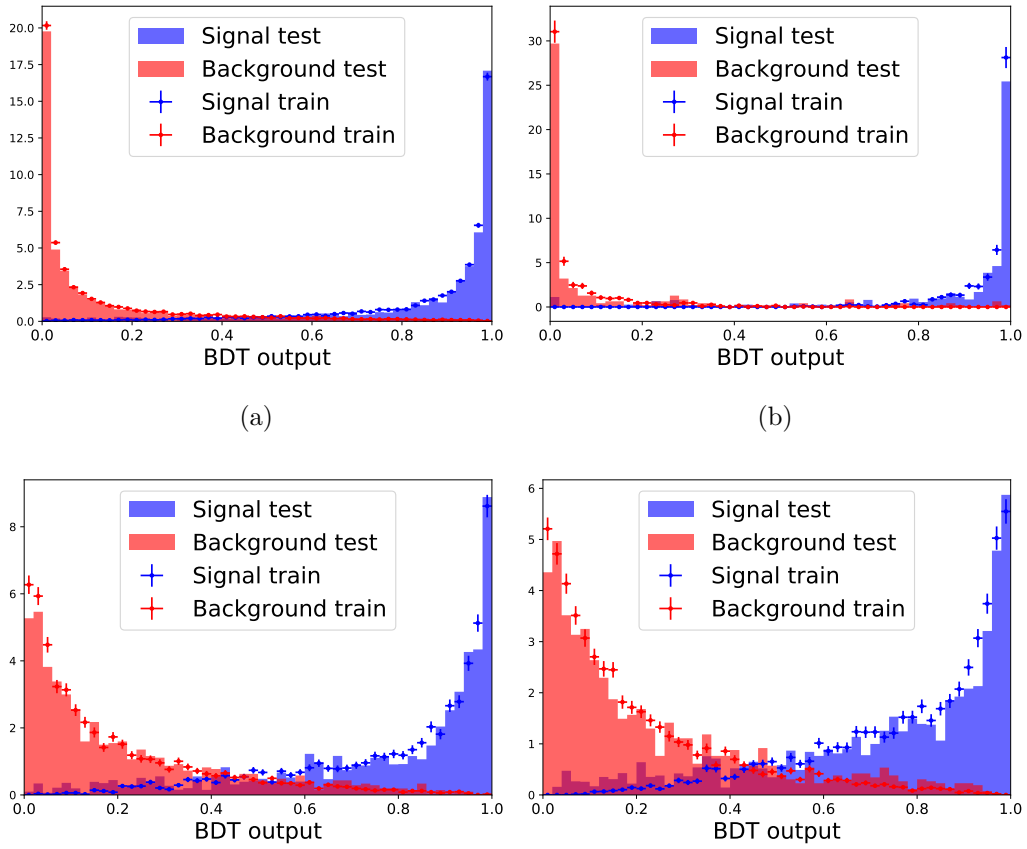

Figure 4.17: Response of the BDT used in the (a) $\Lambda_b^0 \to \Lambda\gamma$ decay channel and $\Xi_b^- \to \Xi^-\gamma$ for topologies (b) LLL, (c) DDL and (d) DDD for the signal (blue) and background (red) samples used for training (points) and testing (filled histogram).

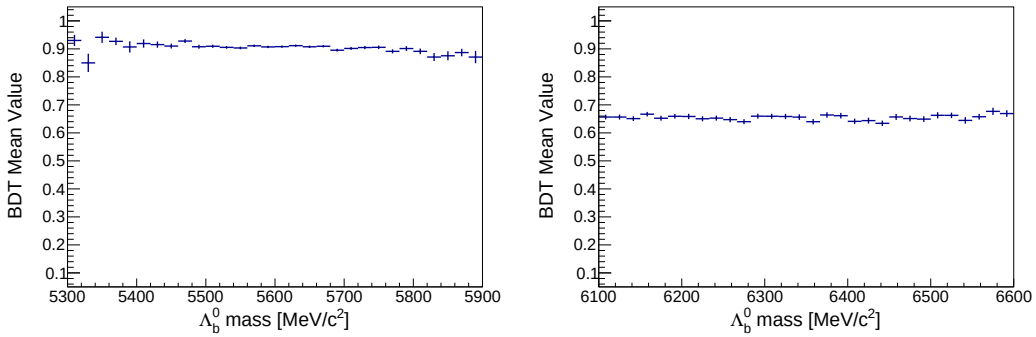

(a)

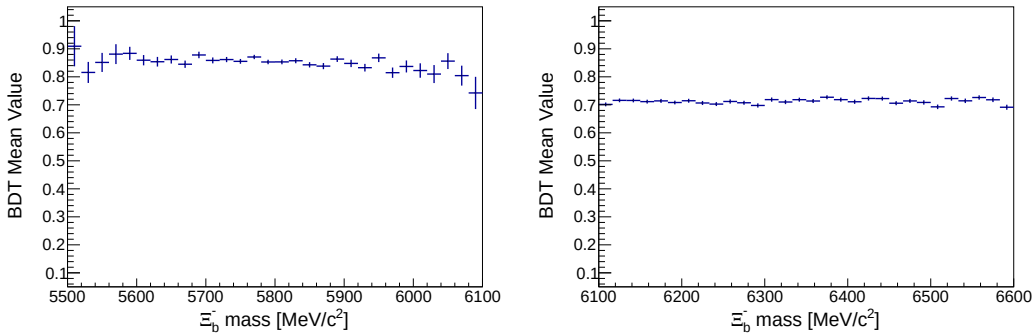

(b)

Figure 4.18: Average BDT response as a function of the invariant mass of the b-baryon for MC signal (left) and background from high mass data sideband (right) in the (a) $\Lambda_b^0 \to \Lambda\gamma$ and (b) $\Xi_b^- \to \Xi^-\gamma$ decays. For simplicity, only DDL topology is shown for $\Xi_b^- \to \Xi^-\gamma$ decay channel, the other topologies present similar behaviors.

Punzi FoM for the signal samples can be seen in Figure 4.19.

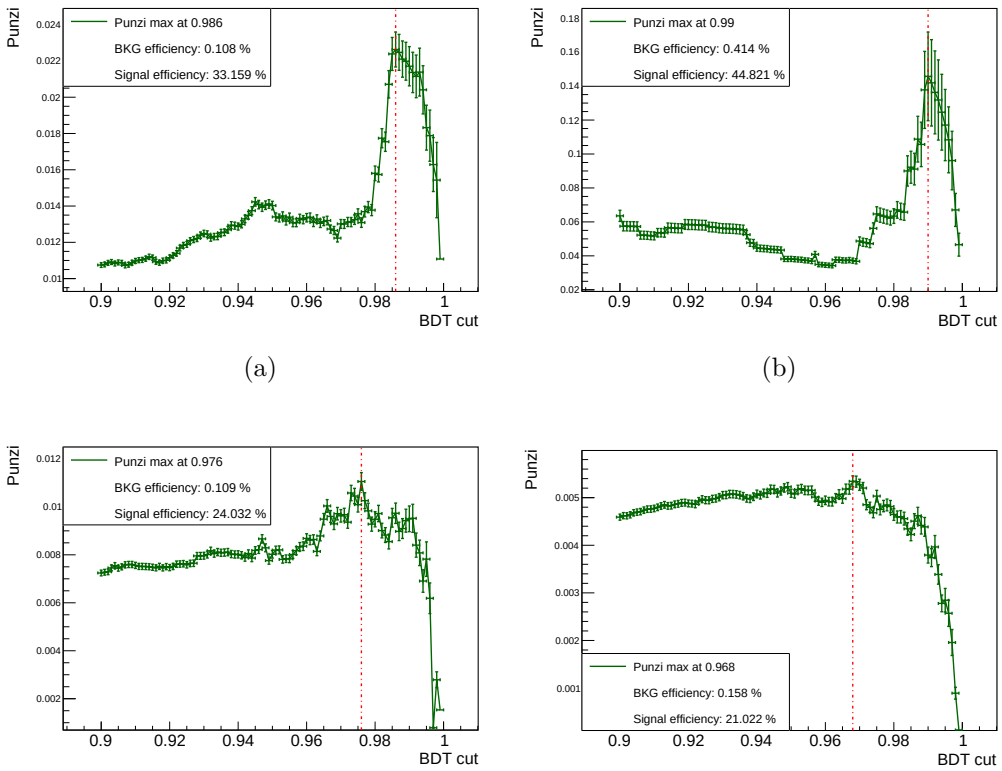

Figure 4.19: Punzi Figure of Merit as a function of the requirement (cut value) on the BDT response for (a)$\Lambda_b^0 \to \Lambda\gamma$ and $\Xi_b^- \to \Xi^-\gamma$ for topologies (b) LLL, (c) DDL and (d) DDD. The optimal cut along with the background rejection and signal efficiency are also shown.

4.8 γ/π^0 separation

The last stage of the selection criteria is responsible for removing background produced by π^0 misidentified as photons. This is achieved through the use of a MVA technique based on a Multi Layer Perceptron based on the information from the calorimeter energy and the cluster shape. The MVA provides a variable named `IsPhoton` [110], which in this analysis is required to be `IsPhoton` > 0.6.

The invariant mass distributions after each selection step for the $\Lambda_b^0 \to \Lambda\gamma$ and $\Xi_b^- \to \Xi^-\gamma$ decay channels for data events in the mass side-bands are shown in Figure 4.20.

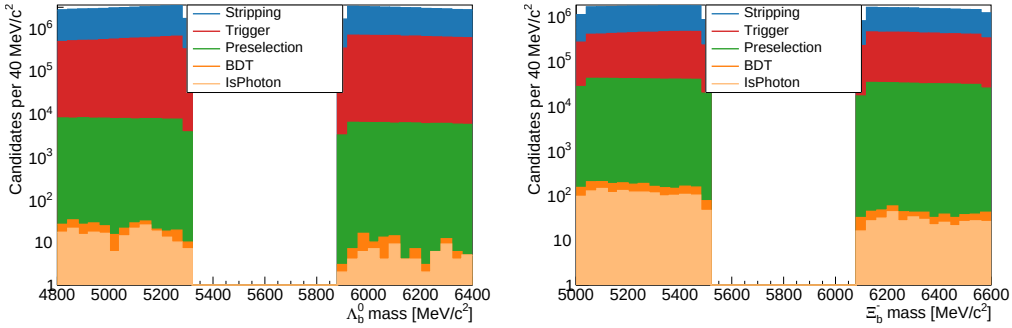

(a) (b)

Figure 4.20: Effect of each selection stage in the side-bands of the b-baryon invariant mass distribution for the (a) $\Lambda_b^0 \to \Lambda\gamma$ and (b) $\Xi_b^- \to \Xi^-\gamma$ decay channels.

4.9 Efficiencies

The efficiency of the reconstruction and selection criteria described in the previous sections is evaluated using MC samples. The only exception to this are the PID and the `IsPhoton` efficiencies, which are known not to be well reproduced by the simulation. Instead, these efficiencies are obtained from clean data samples used for calibration provided by the PID and Calo Objects LHCb groups, respectively. The global efficiency is computed as:

$$\epsilon_{\text{sel}} = \epsilon_{\text{acc}}\, \epsilon_{\text{reco + strip}}\, \epsilon_{\text{trigger}}\, \epsilon_{\text{Presel}}\, \epsilon_{\text{PID}}\, \epsilon_{\text{BDT}}\, \epsilon_{\texttt{IsPhoton}} \tag{4.3}$$

where:

- ϵ_{acc} is the ratio between the number of signal events fully contained inside the detector acceptance and those produced in the whole space (4π);

- $\epsilon_{\text{reco + strip}}$ is the combined efficiency for the event reconstruction (tracking and vertexing) along with the stripping selection;

- $\epsilon_{\text{trigger}}$ is evaluated on top of the stripping stage and takes into account L0, HL1 and HLT2 together. The efficiency for each trigger level is evaluated on top of the previous one;

- ϵ_{Presel} is the efficiency of the preselection described in Section 4.4, excluding the PID and `IsPhoton` conditions;

- ϵ_{PID} is the efficiency of charged PID variables, which is extracted using data-driven methods [111]. The PID efficiency of p, π and μ is extracted from a calibration sample of $\Lambda \to p\pi$, $J/\psi \to \mu^+\mu^-$ and $D^0 \to K^+\pi^-$ decays, respectively. From these samples, efficiency maps as a function of the particle momentum and pseudorapidity are extracted, which are then used to compute the PID selection efficiency. These are shown in Figure 4.21;

- ϵ_{BDT} is the efficiency of the BDT applying the optimal cut, defined by the Punzi FoM;

- $\epsilon_{\texttt{IsPhoton}}$ is the efficiency of the neutral PID, responsible for the γ/π^0 separation. This efficiency is extracted using data-driven techniques from $B^0 \to K^*\gamma$ samples. The data samples used for this purpose are from 2018 data-taking period since no 2016 data samples are available yet. No significant differences are expected between 2016 and 2018 samples for `IsPhoton` distributions.

Table 4.19 shows the efficiencies for the $\Lambda_b^0 \to \Lambda\gamma$ and $\Lambda_b^0 \to \Lambda J/\psi$ decay channels, while Table 4.20 lists the selection efficiencies for $\Xi_b^- \to \Xi^-\gamma$ (split by topologies and all together) and $\Xi_b^- \to \Xi^- J/\psi$ decays.

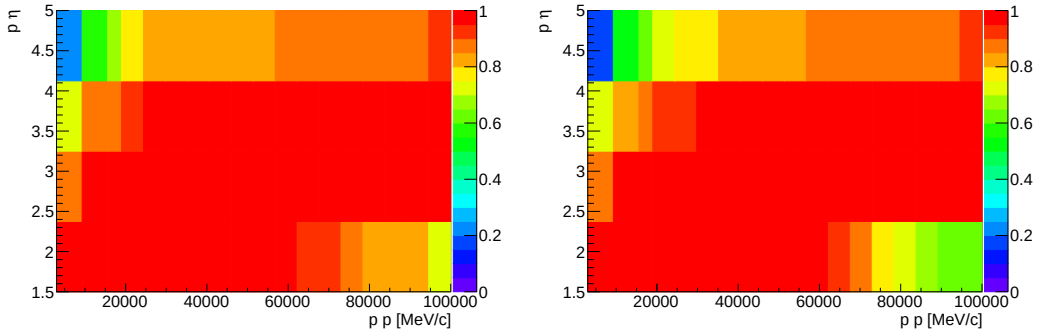

(a)

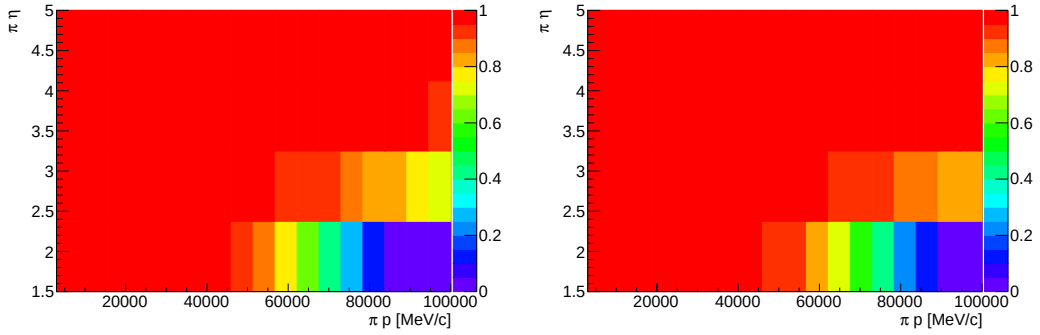

(b)

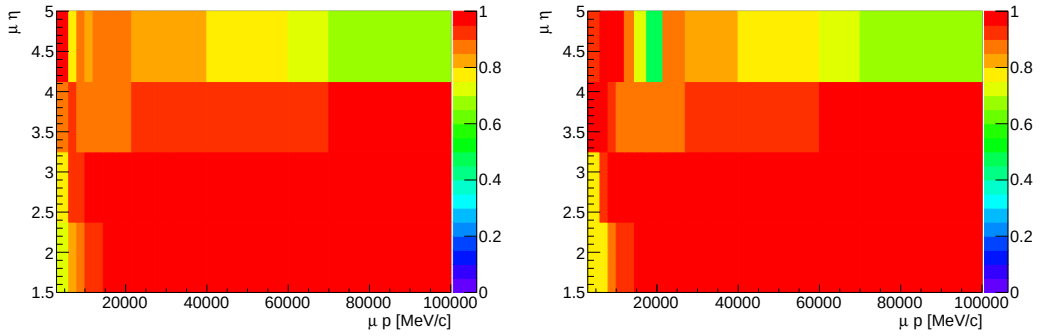

(c)

Figure 4.21: PID efficiency maps as a function of the particle momentum and pseudorapidity on (a) protons, (b) pions and (c) muons, for 2016 (left) and 2018 (right) data conditions.

Efficiency [%]	$\Lambda_b^0 \to \Lambda\gamma$	$\Lambda_b^0 \to \Lambda J/\psi$
ϵ_{acc}	50.19 ± 0.14	19.8 ± 0.1
$\epsilon_{\text{reco+strip}}$	0.9479 ± 0.0007	4.45 ± 0.02
ϵ_{L0}	92.31 ± 0.04	88.7 ± 0.1
ϵ_{HLT1}	33.61 ± 0.09	91.8 ± 0.1
ϵ_{HLT2}	32.0 ± 0.1	92.7 ± 0.1
ϵ_{Presel}	49.5 ± 0.3	13.0 ± 0.1
ϵ_{PID}	97.4 ± 0.1	90.2 ± 0.4
ϵ_{BDT}	33.2 ± 0.4	–
$\epsilon_{\texttt{IsPhoton}}$	91.7 ± 0.4	–
ϵ_{Sel}	0.0070 ± 0.0001	0.0838 ± 0.0009

Table 4.19: Efficiencies for the different reconstruction and selection steps for the $\Lambda_b^0 \to \Lambda\gamma$ and $\Lambda_b^0 \to \Lambda J/\psi$ decay modes.

Efficiency [%]	$\Xi_b^- \to \Xi^-\gamma$				$\Xi_b^- \to \Xi^- J/\psi$
	LLL	DDL	DDD	All	
ϵ_{acc}		33.53 ± 0.11			17.31 ± 0.09
$\epsilon_{\text{reco+strip}}$	0.0156 ± 0.0002	0.1231 ± 0.0004	0.2186 ± 0.0006	0.3572 ± 0.0009	1.320 ± 0.001
ϵ_{L0}		100.0 ± 0.0			82.758 ± 0.05
ϵ_{HLT1}	59.9 ± 0.5	23.9 ± 0.2	22.2 ± 0.1	24.43 ± 0.09	92.56 ± 0.04
ϵ_{HLT2}	67.3 ± 0.6	66.1 ± 0.3	52.7 ± 0.3	58.8 ± 0.2	90.03 ± 0.04
ϵ_{Presel}	38.6 ± 0.8	46.9 ± 0.4	49.4 ± 0.3	47.5 ± 0.3	75.81 ± 0.07
ϵ_{PID}	95.9 ± 0.6	95.5 ± 0.3	96.0 ± 0.3	95.8 ± 0.2	88.37 ± 0.06
ϵ_{BDT}	44.8 ± 1.3	24.0 ± 0.6	21.0 ± 0.5	25.0 ± 0.4	–
$\epsilon_{\texttt{IsPhoton}}$	90.6 ± 1.2	90.5 ± 0.9	91.5 ± 0.8	91.0 ± 0.5	–
ϵ_{Sel}	0.00032 ± 0.00001	0.00064 ± 0.00002	0.00078 ± 0.00002	0.00176 ± 0.00003	0.1055 ± 0.0006

Table 4.20: Efficiencies for the different reconstruction and selection steps for the $\Xi_b^- \to \Xi^-\gamma$ and $\Xi_b^- \to \Xi^- J/\psi$ decay modes.

5 Sensitivity studies for the photon polarization

5.1 Introduction

A main goal of this thesis is the measurement of the photon polarization through an angular analysis, as described in Section 1.4. In this chapter, sensitivities studies are performed to demonstrate the feasibility of such an analysis, along with estimates of the physics reach and the main expected experimental uncertainties.

5.2 Experimental effects

Three main experimental effects drive the determination of the sensitivity to the photon polarization: data sample size, reconstruction ability (resolution and acceptance) and backgrounds. Each of these contributions are further described and studied independently in the following.

The general procedure adopted to asses the feasibility and reach of the analysis relies on the generation of a large number of independent datasets, based on a input probability density function (PDF). A fit with the same PDF is then performed on each of the datasets. The distribution of the parameters extracted in this way is fitted to a Gaussian (normal) distribution. The width of this distribution is the uncertainty associated to the effect under consideration. Furthermore, the stability and performance of the fitting procedure are tested by the pull distributions $\mathcal{P}(x)$, defined as:

$$\mathcal{P}(x) = \frac{x_{\text{Fit}} - x_{\text{Gen}}}{\sigma_x}\,, \tag{5.1}$$

where x_{Fit} and x_{Gen} are the fitted and generated values of a given parameter,

respectively, and σ_x is the estimated statistical uncertainty from the fit. The shape of the pull distributions should be compatible with a standard normal distribution to reflect a behaved fit. Mean values different from zero indicate the presence of a bias introduced by the fit, while width values higher (lower) than one indicate an under (over) estimation of the statistical uncertainties. The process of generating and fitting a single dataset is called pseudo-experiment. The set of pseudo-experiments can also be referred here as MC Toys or MC study.

The computing framework used to perform the pseudo-experiments is RooStat [112]. One thousand pseudo-experiments are generated and fitted with an unbinned maximum likelihood method. This number ensures a large enough sample to extract the sensitivity and pull distributions with low uncertainty, while allowing the MC studies to be performed in an acceptable time.

5.2.1 Statistical uncertainty

The statistical uncertainty is primarily determined by the signal yield. Pseudo-experiments with samples ranging from 50 to 4000 signal events are generated using the theoretical angular distribution, shown in Equations 1.15 and 1.18. The generated value of the photon polarization is the SM prediction ($\alpha_\gamma = 1$). The results of this study are summarized in Figure 5.1. The statistical sensitivity for $\Lambda_b^0 \to \Lambda\gamma$ and $\Xi_b^- \to \Xi^-\gamma$ decays obeys a $1/\sqrt{N}$ function, as expected, where N is the signal yield. Moreover, the sensitivity for the $\Lambda_b^0 \to \Lambda\gamma$ decay channel is sightly better (about 15%) than for the $\Xi_b^- \to \Xi^-\gamma$ mode. The reason behind this is the higher absolute value of the Λ weak decay parameter, α_Λ, as compared with α_Ξ. This larger value is translated into a larger slope in the angular distribution and, thus, the α_γ parameter is easier to fit. The results for the considered range of the signal yield show that it is possible to measure the photon polarization with an statistical sensitivity between 3% and 25%.

Datasets of 1000 events each are considered hereafter, despite the estimation of a lower expected signal yield (given in Section 6.2.5) . This is mainly due to the high uncertainty of these estimations. Furthermore, the goal of this chapter is to provide a qualitative estimation of the sensitivity

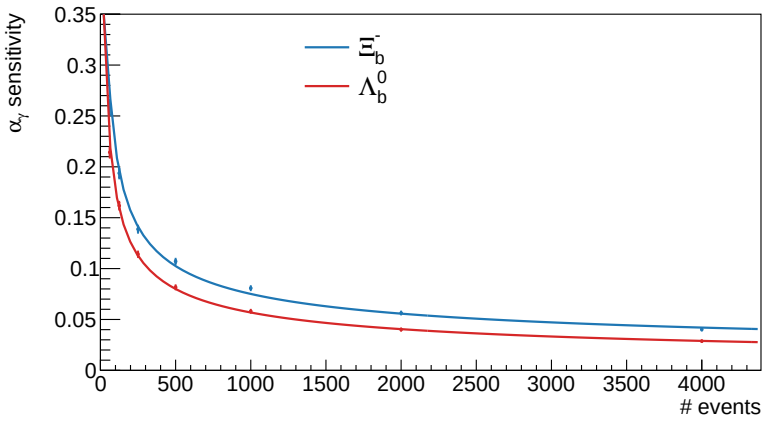

Figure 5.1: Statistical sensitivity to the photon polarization as a function of the number of reconstructed signal events for the $\Lambda_b^0 \to \Lambda\gamma$ (red) and $\Xi_b^- \to \Xi^-\gamma$ (blue) decays . The distribution is fitted to a $1/\sqrt{N}$ function for better visualization.

to the photon polarization induced by different effects. The number of generated events per pseudo-experiment ensures a well-behaved fit, while offers a straightforward extrapolation to other yields.

5.2.2 Values of the parameters α_γ, P_{Λ_b} and P_{Ξ_b}

To asses the correlation between the value of the photon polarization and its uncertainty, an MC study varying the generated value of α_γ is performed. The results are shown in Figure 5.2. A small dependence on the absolute value of α_γ is observed for the two radiative channels, with lower uncertainty at larger slopes ($|\alpha_\gamma| = 1$). The sensitivity is found to be the same for positive and negative values of the photon polarization.

The angular distribution also provides access to the initial polarization of the b-baryon, thus it is possible to extract P_{Λ_b} and P_{Ξ_b} along with α_γ. In order to test the sensitivity to the b-baryon initial polarization, pseudo-experiments are performed using Equation 1.14 to simultaneously fit α_γ and P_{Λ_b} for $\Lambda_b^0 \to \Lambda\gamma$ decays. Similar pseudo-experiments are performed using Equation 1.17 to simultaneously fit α_γ and P_{Ξ_b} for $\Xi_b^- \to \Xi^-\gamma$ decays. The P_{Ξ_b} and P_{Λ_b} parameters are ranged between -0.1 and 0.1, since this is the maximum polarization measured for Λ_b [45]. Figure 5.3 shows the achieved sensitivity to the initial b-baryon polarization, for different α_γ val-

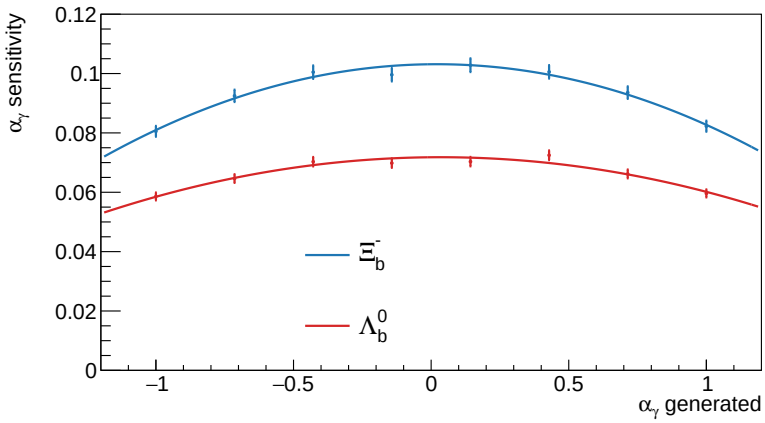

Figure 5.2: Sensitivity to the photon polarization as a function of its value for the $\Lambda_b^0 \to \Lambda\gamma$ (red) and $\Xi_b^- \to \Xi^-\gamma$ (blue) decays. A fit to a second order polynomial distribution is overlaid for better visualization.

ues. The sensitivity to the b-baryon polarization is maximal for $\alpha_\gamma = 1$ (SM value), while it is independent of the b-baryon polarization. The same pseudo-experiments are used to test the effect of the simultaneous fit on the sensitivity to α_γ. The results, depicted in Figure 5.4, show that the photon polarization can be extracted with the same accuracy with a simultaneous fit regardless the value of P_{Λ_b} and P_{Ξ_b}, provided enough statistics.

5.2.3 Reconstruction effects

The shape of the angular distribution is sensitive to reconstruction imperfections, as illustrated in Figure 5.5. To account for these effects, extra terms are included in the modeling of the angular distribution:

$$\Gamma(\boldsymbol{\theta};\boldsymbol{\xi}) = [W(\boldsymbol{\theta};\boldsymbol{\xi}) \circledast \mathcal{R}(\boldsymbol{\theta})]\, \mathcal{A}(\boldsymbol{\theta})\,, \tag{5.2}$$

where $\boldsymbol{\theta}$ denotes the set of angular variables, and $\boldsymbol{\xi}$ the vector of parameters (decay asymmetry parameters, polarization and α_γ). The theoretical angular distribution discussed in Section 1.4, $W(\boldsymbol{\theta};\boldsymbol{\xi})$, is convoluted by the resolution function $\mathcal{R}(\boldsymbol{\theta})$, and $\mathcal{A}(\boldsymbol{\theta})$ is the acceptance function. The effects of the signal event reconstruction also have a direct impact on the photon polarization sensitivity, and require to be accurately modeled to be included in the PDF. The contribution of these effects is evaluated through the pseudo-experiments, as described below.

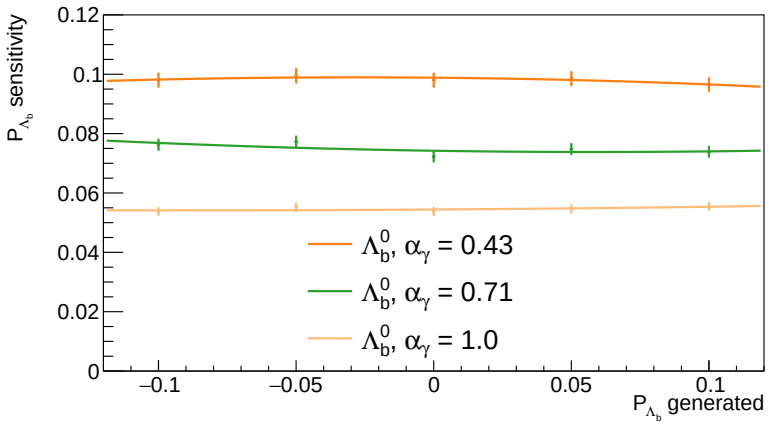

(a)

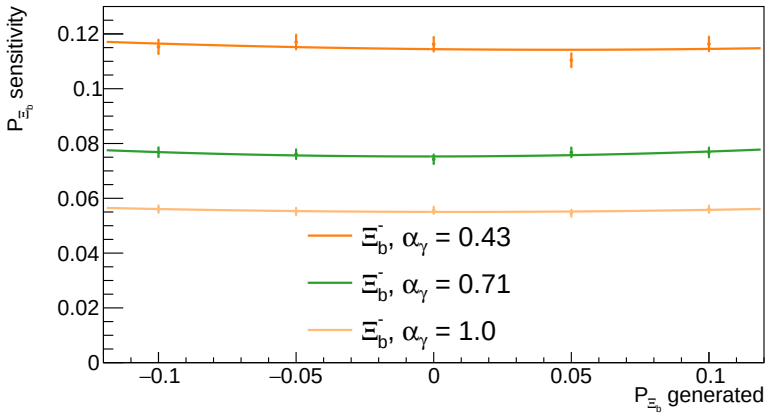

(b)

Figure 5.3: Sensitivity to the (a) Λ_b^0 and (b) Ξ_b^- initial polarization as a function of its value for the $\Lambda_b^0 \to \Lambda\gamma$ and $\Xi_b^- \to \Xi^-\gamma$ decays, respectively. A fit to a second order polynomial distribution is overlaid for better visualization.

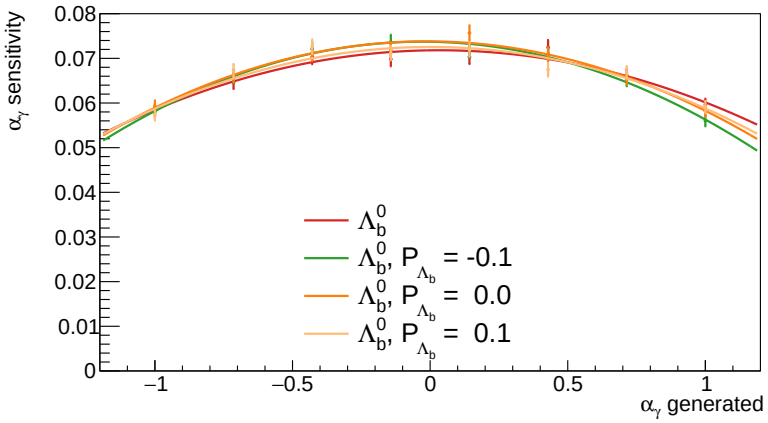

(a)

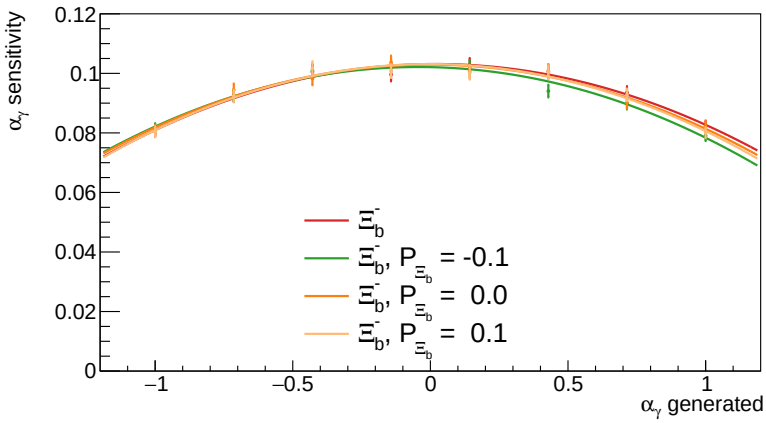

(b)

Figure 5.4: Sensitivity to the photon polarization as a function of its value for different assumptions of the initial b-baryon polarization in the (a) $\Lambda_b^0 \to \Lambda\gamma$ and (b) $\Xi_b^- \to \Xi^-\gamma$ decays. The red lines use Equations 1.15 and 1.18, which have no dependence with the initial polarization of the b-baryon, while the other lines are based upon Equations 1.14 and 1.17.

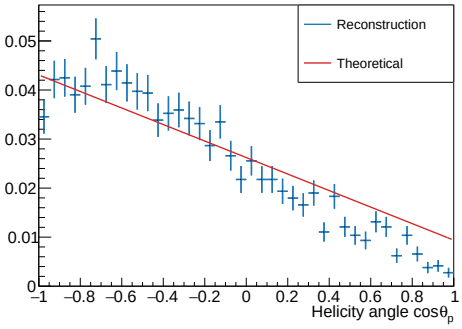

(a)

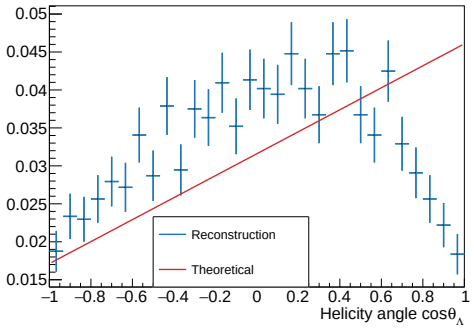

(b)

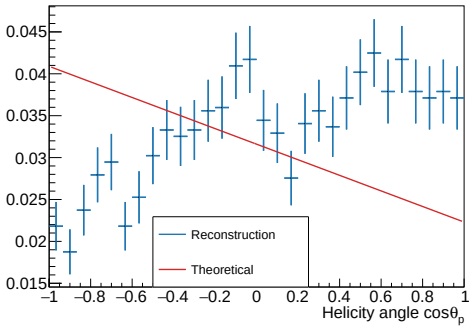

(c)

Figure 5.5: Distributions of the (a) proton helicity angle for $\Lambda_b^0 \to \Lambda\gamma$, and the (b) Λ and (c) proton helicity angles for $\Xi_b^- \to \Xi^-\gamma$, for simulated events after selection. The theoretical angular distribution is superimposed for comparison. Only Long tracks are considered here.

Angular resolution

The resolution is induced by the finite granularity of the detector and the limited accuracy of the reconstruction system. Specifically, the limited track momentum resolution is directly translated to the helicity angles, smearing the angular distribution and diluting the information on the photon polarization. The angular resolution function for a given angular variable, θ, is extracted from signal MC samples and is defined as:

$$\mathcal{R}(\theta) = \theta_{\text{Gen}} - \theta_{\text{Rec}} \tag{5.3}$$

where θ_{Gen} is the helicity angle generated by the simulation and θ_{Rec} is the helicity angle reconstructed by the tracking and reconstruction systems. The angular resolution is modeled by a Gaussian distribution. The results of the fits are shown in Figure 5.6 for the $\Lambda_b^0 \to \Lambda\gamma$ and $\Xi_b^- \to \Xi^-\gamma$ decays, where

no biases are observed. The corresponding resolution values are reported in Table 5.1. The modeling of the angular resolution as a function of $\cos\theta$

Angle	Resolution [mrad]
$\Lambda_b^0 \to \Lambda\gamma$ (θ_p)	19.4 ± 1.1
$\Xi_b^- \to \Xi^-\gamma$ (θ_Λ)	29.9 ± 2.7
$\Xi_b^- \to \Xi^-\gamma$ (θ_p)	48.4 ± 4.9

Table 5.1: Values of the resolution for the proton helicity angle of $\Lambda_b^0 \to \Lambda\gamma$ decay , and for the Λ and proton helicity angles of the $\Xi_b^- \to \Xi^-\gamma$ decay.

would have lead to issues related with the generation of values outside the mathematical range of the cosine function $[-1, 1]$, produced by the smearing. This complication is bypassed by modeling the angular resolution as a function of θ.

The correlation between the resolution functions of the two helicity angle in $\Xi_b^- \to \Xi^-\gamma$ decays has to be investigated. If the correlation is significant, a correlation term has to be included in the 2-dimensional PDF. This study is shown in Figure 5.7, where it can be seen that the correlation is negligible. Therefore, the two helicity angles can be treated independently.

The PDFs used for the generation of the pseudo-experiments are modified then as:

$$\Gamma_{\Lambda_b^0}(\theta_p; \alpha_\Lambda, \alpha_\gamma) = W(\theta_p; \alpha_\Lambda, \alpha_\gamma) \circledast \mathcal{R}(\theta_p)\,, \tag{5.4}$$

$$\Gamma_{\Xi_b^-}(\theta_\Lambda, \theta_p; \alpha_\Lambda, \alpha_\Xi, \alpha_\gamma) = W(\theta_\Lambda, \theta_p; \alpha_\Xi, \alpha_\Lambda, \alpha_\gamma) \circledast \mathcal{R}(\theta_\Lambda, \theta_p)\,, \tag{5.5}$$

where $W(\theta_p; \alpha_\Lambda, \alpha_\gamma)$ and $W(\theta_\Lambda, \theta_p; \alpha_\Xi, \alpha_\Lambda, \alpha_\gamma)$ are the theoretical angular distribution of $\Lambda_b^0 \to \Lambda\gamma$ and $\Xi_b^- \to \Xi^-\gamma$ defined by Equations 1.15 and 1.18, respectively. The W distributions are convoluted with the resolution defined as:

$$\mathcal{R}(\theta_p) = \mathcal{N}(0, \sigma_{\theta_p})\,, \tag{5.6}$$

$$\mathcal{R}(\theta_\Lambda, \theta_p) = \mathcal{N}(0, \sigma_{\theta_\Lambda})\,\mathcal{N}(0, \sigma_{\theta_p})\,, \tag{5.7}$$

where $\mathcal{N}(\mu, \sigma)$ is a normal distribution with mean μ and width σ. As previously argued, the μ parameter is fixed to zero as no biases are found. It should be emphasized that in this study the generation is performed

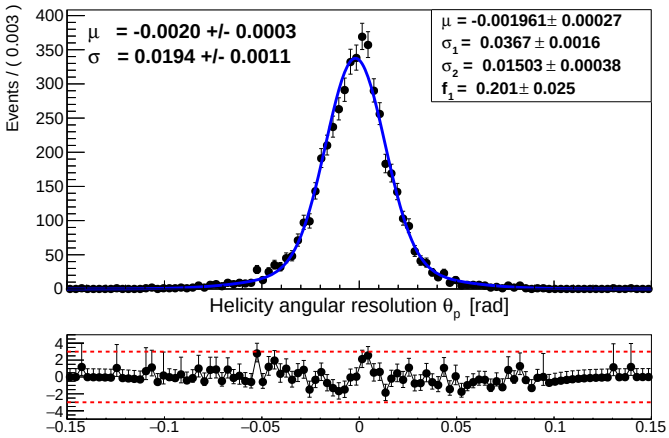

(a)

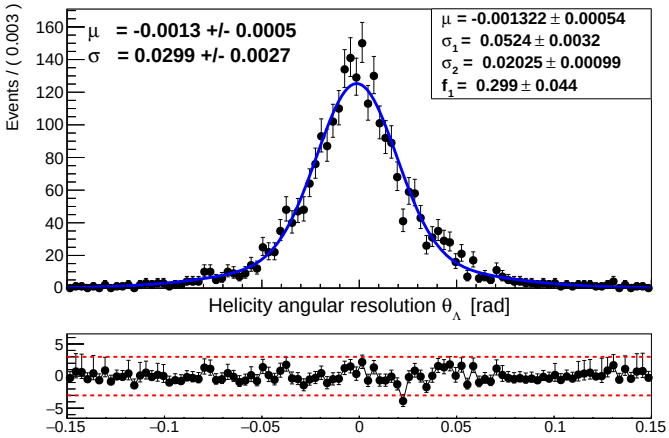

(b)

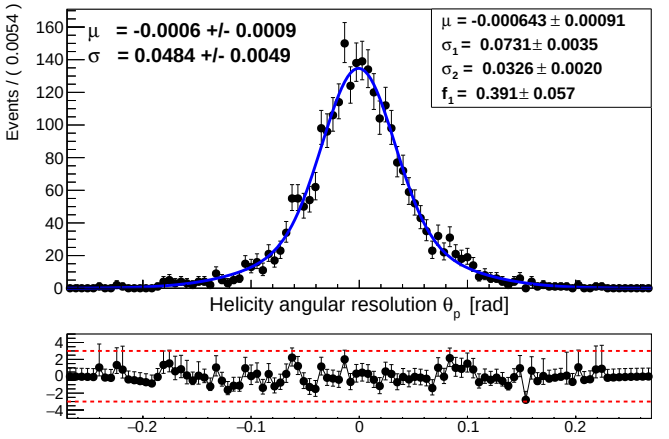

(c)

Figure 5.6: Gaussian fits to the (a) proton helicity angle for $\Lambda_b^0 \to \Lambda\gamma$, and the (b) Λ and (c) proton helicity angles for $\Xi_b^- \to \Xi^-\gamma$.

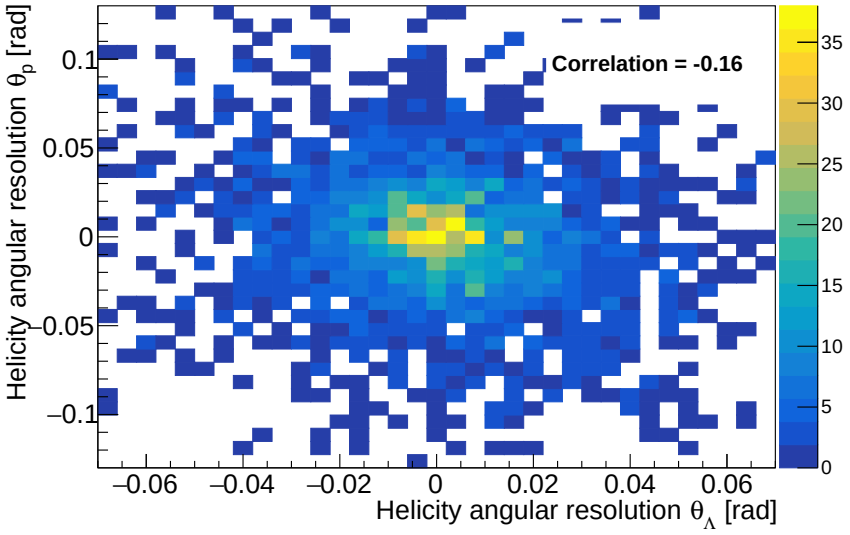

Figure 5.7: Correlation between the proton and Λ helicity resolutions of the $\Xi_b^- \to \Xi^-\gamma$ decay.

including the resolution, but the fit uses the nominal configuration without resolution, *i.e.*, Equations 1.15 and 1.18 directly.

Angular acceptance

The acceptance is a selection efficiency which depends on the helicity angle, thus, it is produced by the selection criteria and induces a change in the angular shape with respect to the theoretical distribution. The angular acceptance is computed as the ratio, bin by bin, of the generated distribution for all simulated events after and before applying the selection criteria. The acceptance is extracted from MC samples, thus MC-data agreement needs to be checked (see Section 6.3.2). The angular acceptance for the $\Lambda_b^0 \to \Lambda\gamma$ and $\Xi_b^- \to \Xi^-\gamma$ decays reconstructed with Long tracks appears in Figure 5.8.

The acceptance is modeled by a polynomial function, whose order is determined by a compromise between the fit χ^2 and its stability. For $\Xi_b^- \to \Xi^-\gamma$ decays, the second order polynomial is chosen as optimal for both helicity angles. A third order polynomial is required for the $\Lambda_b^0 \to \Lambda\gamma$ decay. The reason behind the particular shape of the acceptance is the mass asymmetric decays $\Xi^- \to \Lambda\pi^-$ and $\Lambda \to p\pi$. For decays wherein one of the decay products flies backward in the reference frame of its mother ($\cos\theta = \pm 1$), this particle has a low p_T and, thus, the event is rarely

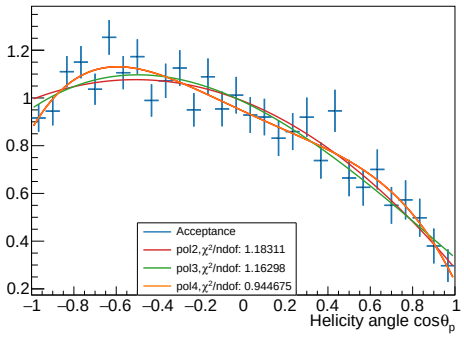

(a)

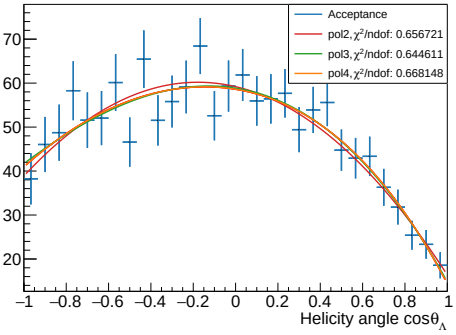

(b)

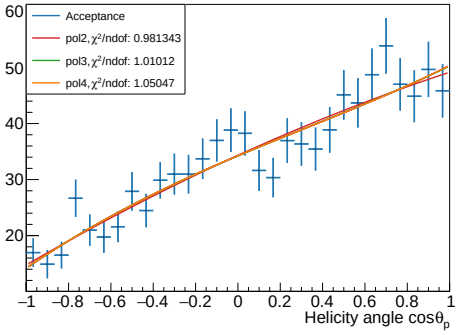

(c)

Figure 5.8: Acceptance for the (a) proton helicity angle of $\Lambda_b^0 \to \Lambda\gamma$ decay, and for the (b) Λ and (c) proton helicity angles of the $\Xi_b^- \to \Xi^-\gamma$ decay after the full selection. Polynomial of different orders are overlaid, along with the χ^2 of the associated fit.

selected. This is specially true in the case of the pion going backward, due to its low mass. Finally, the optimal scenario occurs when the pion inherits most of the p_T from its mother, while the other particle takes a small fraction ($\cos\theta \simeq -0.8$). Due to the mass difference, both particles have enough momentum to be likely selected.

As for the angular resolution function, the correlation between the acceptance of the two helicity angles for $\Xi_b^- \to \Xi^-\gamma$ decays needs to be checked. Figure 5.9 shows the result of this study. Since no correlation is observed, the acceptance of the two helicity angles can be factorized.

Therefore, the PDFs used in the pseudo-experiments for the generation and the fitting, including acceptance effects, is the following:

$$\Gamma_{\Lambda_b^0}(\theta_p;\alpha_\Lambda,\alpha_\gamma) = W(\theta_p;\alpha_\Lambda,\alpha_\gamma)\,\mathcal{A}(\theta_p)\,, \tag{5.8}$$

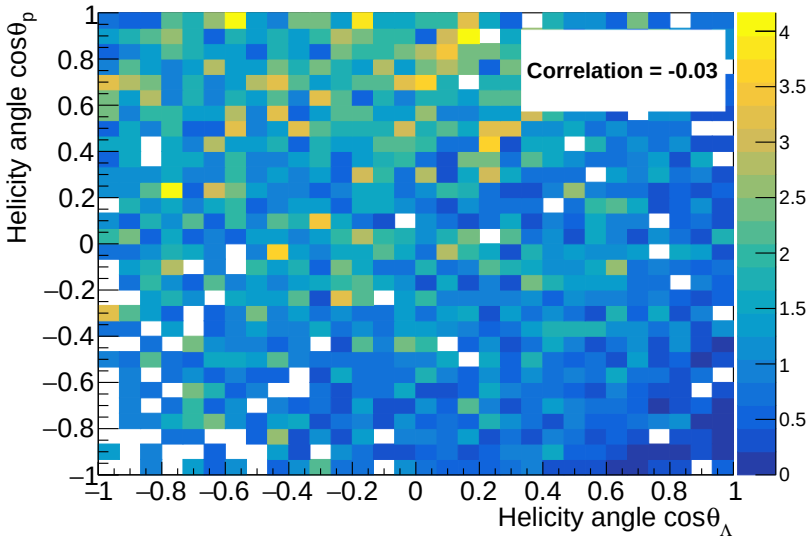

Figure 5.9: Correlation between the angular acceptance of Λ and proton helicity angles of the $\Xi_b^- \to \Xi^-\gamma$ decay.

$$\Gamma_{\Xi_b^-}(\theta_\Lambda, \theta_p; \alpha_\Xi, \alpha_\Lambda, \alpha_\gamma) = W(\theta_\Lambda, \theta_p; \alpha_\Xi, \alpha_\Lambda, \alpha_\gamma)\, \mathcal{A}(\theta_\Lambda, \theta_p)\,, \tag{5.9}$$

where now, the theoretical angular distributions, W, defined by Equations 1.15 and 1.18, are multiplied by the angular acceptance $\mathcal{A}$, which can be parametrized as:

$$\mathcal{A}(\theta_p) = 1 + a\ \cos\theta_p + b\ \cos^2\theta_p + c\ \cos^3\theta_p \tag{5.10}$$

$$\mathcal{A}(\theta_\Lambda, \theta_p) = [1 + a'\ \cos\theta_\Lambda + b'\ \cos^2\theta_\Lambda][1 + a''\ \cos\theta_p + b''\ \cos^2\theta_p] \tag{5.11}$$

The parameters a, b, c, a', b', a'' and b'' are obtained from the fit to the MC acceptance distributions and they are reported in Table 5.2.

Angle	$a^{(','')}$	$b^{(','')}$	$c^{(','')}$
$\Lambda_b^0 \to \Lambda\gamma\ (\cos\theta_p)$	-0.43 ± 0.06	-0.35 ± 0.04	0.11 ± 0.09
$\Xi_b^- \to \Xi^-\gamma\ (\cos\theta_\Lambda)$	-0.19 ± 0.03	-0.53 ± 0.04	-
$\Xi_b^- \to \Xi^-\gamma\ (\cos\theta_p)$	0.50 ± 0.04	-0.07 ± 0.06	-

Table 5.2: Values of the parameters for the acceptance function for the proton helicity angle of $\Lambda_b^0 \to \Lambda\gamma$ decay, and for the Λ and proton helicity angles of the $\Xi_b^- \to \Xi^-\gamma$ decay.

Results

The impact of the resolution and acceptance on the sensitivity to the photon polarization are tested using one thousand pseudo-experiments with 1000 events each. They are generated using Equations 5.4 and 5.5 for the resolution, and Equations 5.8 and 5.9 for the acceptance, in the $\Lambda_b^0 \to \Lambda\gamma$ and $\Xi_b^- \to \Xi^-\gamma$ cases respectively. The only free parameter is the photon polarization, the other paramters are fixed to values obtained from the simulation or measured (*e.g.* α_Ξ and α_Λ). The results of these MC studies are shown in Figure 5.10, where the statistical sensitivity, previously studied, is shown for comparison. It is worth-mentioning that the sensitivity extracted here due to resolution and acceptance effects, is combined with the statistical one.

5.2.4 Background

After the selection criteria, some irreducible background contributions remain in the sample, which has its own angular distribution. In order to avoid biases, it is needed to include in the fit all background contributions. The angular distribution for the background is assessed from the signal region in the data samples after applying an inverse cut of the BDT (BDT response < 0.6). This ensures that only the background is considered, since most of the signal events are removed. The angular distribution for the background obtained by this method is shown in Figure 5.11. Similar plots are obtained for events reconstructed with only Downstream tracks and both, Downstream and Long tracks. Polynomial functions of several orders are fitted to the background distributions. The third order polynomial gives the best compromise for all the cases. The angular distribution of the background is also affected by the acceptance, which is already included in the distribution.

The value of the parameters, extracted from the fit and used for the MC study, can be seen in Table 5.3.

The correlation between the two helicity angles for background in the $\Xi_b^- \to \Xi^-\gamma$ decay is found to be negligible, as it can be seen in Figure 5.12. Therefore, no correlation term is included.

The effect of the background on the sensitivity to α_γ is studied with 1000 pseudo-experiments with 1000 signal events each and varying the yield

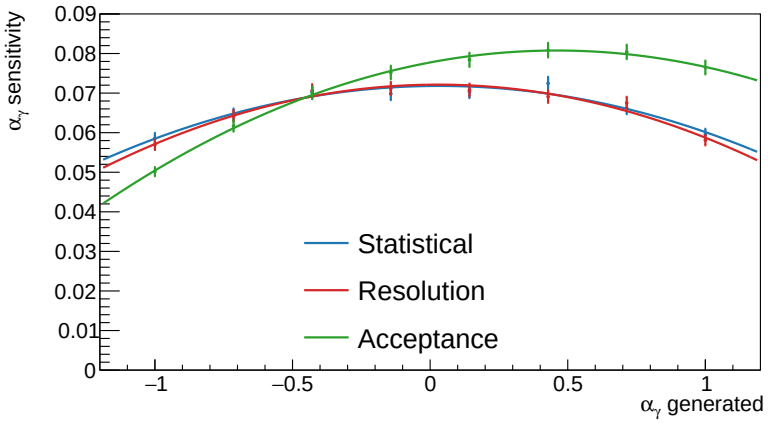

(a)

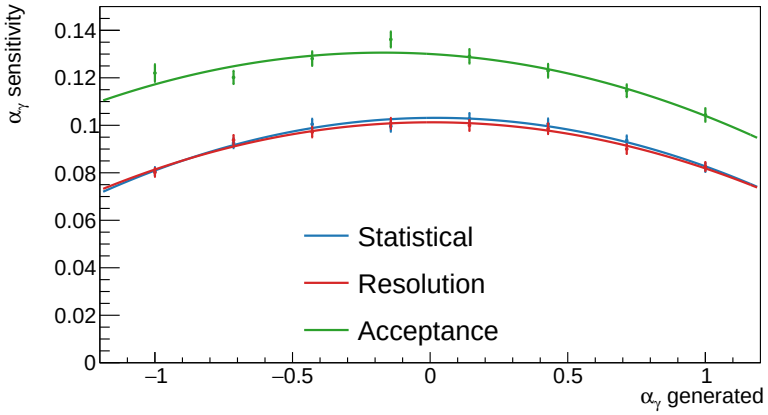

(b)

Figure 5.10: Sensitivity of the photon polarization as a function of its value for the (a) $\Lambda_b^0 \to \Lambda\gamma$ and the (b) $\Xi_b^- \to \Xi^-\gamma$ decays, including statistical (black), angular resolution (red) and acceptance (green) effects. A second order polynomial is superimposed for better visualization.

Angle	$a^{(','')}$	$b^{(','')}$	$c^{(','')}$
$\Lambda_b^0 \to \Lambda\gamma$ $(\cos\theta_p)$	-0.826 ± 0.008	-0.736 ± 0.006	0.563 ± 0.010
$\Xi_b^- \to \Xi^-\gamma$ $(\cos\theta_\Lambda)$	-0.413 ± 0.006	-0.709 ± 0.004	0.103 ± 0.009
$\Xi_b^- \to \Xi^-\gamma$ $(\cos\theta_p)$	0.133 ± 0.009	-0.243 ± 0.006	0.217 ± 0.013

Table 5.3: Values of the parameters for the background function for the proton helicity angle of the $\Lambda_b^0 \to \Lambda\gamma$ decay, and for the Λ and proton helicity angles of the $\Xi_b^- \to \Xi^-\gamma$ decay.

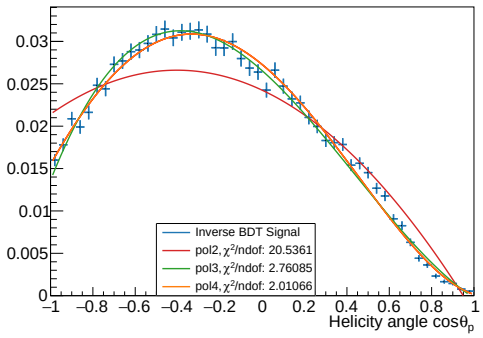

(a)

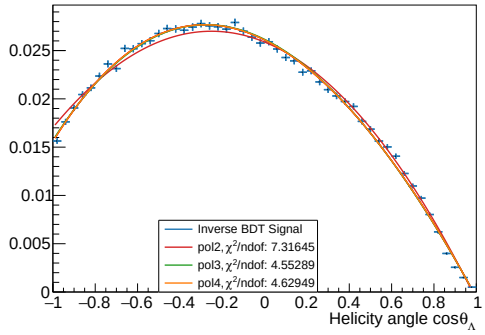

(b)

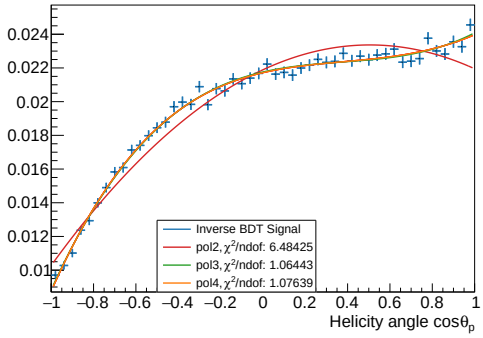

(c)

Figure 5.11: Background shapes for the (a) proton helicity angle of the $\Lambda_b^0 \to \Lambda\gamma$ decay, and for the (b) Λ and (c) proton helicity angles of the $\Xi_b^- \to \Xi^-\gamma$ decay with an inverse BDT cut.Polynomials of different orders are overlaid, along with the χ^2 of the fit.

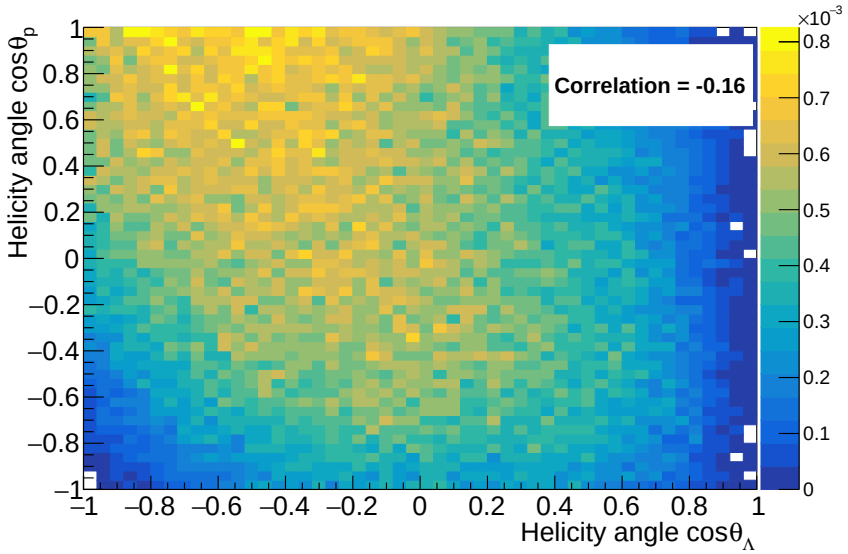

Figure 5.12: Correlation between the Λ and proton helicity angles for background of the $\Xi_b^- \to \Xi^-\gamma$ decay.

of background. The PDF used for this study is the following:

$$\Gamma_{\Lambda_b^0}(\theta_p;\alpha_\Lambda,\alpha_\gamma) = \frac{S}{S+B}W(\theta_p;\alpha_\Lambda,\alpha_\gamma) + \frac{B}{S+B}W_B(\theta_p)\,, \tag{5.12}$$

$$\begin{aligned}\Gamma_{\Xi_b^-}(\theta_\Lambda,\theta_p;\alpha_\Xi,\alpha_\Lambda,\alpha_\gamma) = &\frac{S}{S+B}W(\theta_\Lambda,\theta_p;\alpha_\Xi,\alpha_\Lambda,\alpha_\gamma) \\ &+ \frac{B}{S+B}W_B(\theta_\Lambda,\theta_p)\,,\end{aligned} \tag{5.13}$$

where W_B is the background distribution and $\frac{S}{S+B}$ ($\frac{B}{S+B}$) is the signal (background) fraction (signal yield fixed to 1000). The samples are generated with the SM value for the photon polarization ($\alpha = 1$). For the fit, three different strategies are tested regarding the signal fraction: to fix the value, to let it float and to apply Gaussian constrains with a width of 10% of the mean value. The result of this MC study is shown in Figure 5.13.

5.3 Discussion of the results

The measurement of the photon polarization in b-baryon decays with good accuracy is feasible, providing that the systematic effects are kept under control. The effect of the resolution is diluted by the statistical uncertainty for the yield evaluated (1000) or lower, thus no needed to be considered in the nominal analysis configuration. On the other hand, the acceptance has a different contribution to the sensitivity of α_γ depending on its value. The best scenario for the $\Xi_b^- \to \Xi^-\gamma$ decay is the SM value, while this value is suboptimal for the $\Lambda_b^0 \to \Lambda\gamma$ channel. Finally, the three fit strategies regarding the background yield offer similar results. Fixing the yield reduces the photon polarization uncertainty but it is sensitive to biases due to under- or over-estimation of the yield. Letting the background yield to float solves completely this issue but at the cost of a reduction of sensitivity. The Gaussian constrains provides advantages from the other two strategies, delivering an improved sensitivity while having some level of bias-proof from wrong yield estimation. A low S/B rate would pollute the angular distribution, drastically increasing the uncertainty due to this source.

As a final remark, the studies performed here are intended to be qualitative, thus the signal yield has been fixed to 1000 and each effect has been studied independently. Studies combining all the effects are performed in Section 6.3.

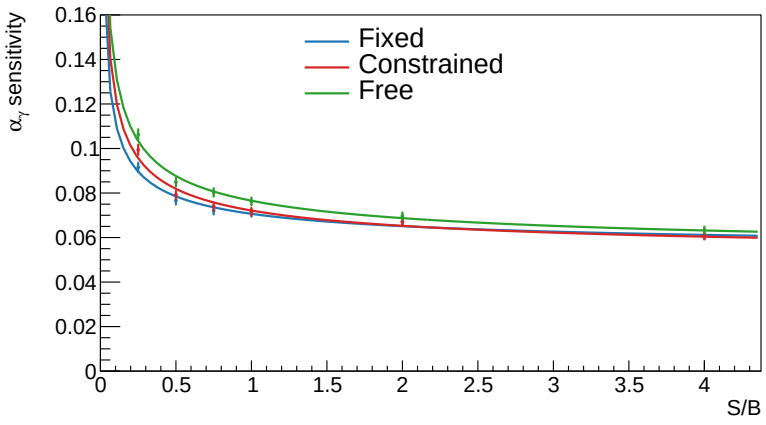

(a)

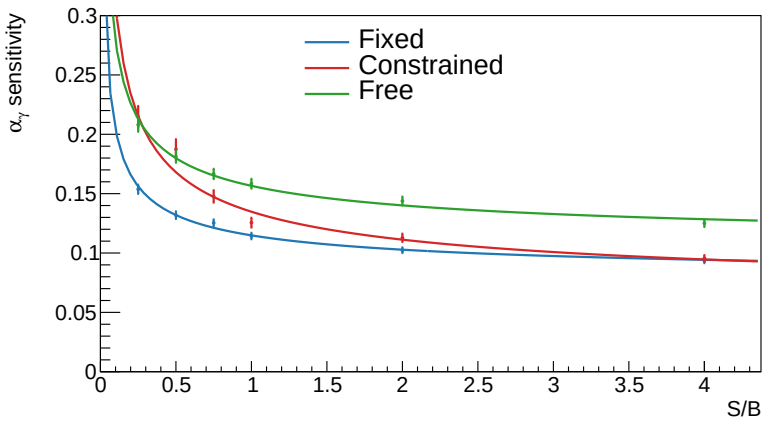

(b)

Figure 5.13: Sensitivity of the photon polarization as a function of the signal over background ratio (S/B) for the (a) $\Lambda_b^0 \to \Lambda\gamma$ and the (b) $\Xi_b^- \to \Xi^-\gamma$ decays for different fit strategies: fixing (black), letting float (red) and applying Gaussian constrains (green) on the background yield. An $a + b/\sqrt{(S/B)}$ function is overlaid for better visualization.

6 Measurement of branching ratios and photon polarization

6.1 Analysis strategy

The objective of the analysis described in this thesis is twofold. On the one hand, the search for the rare radiative b-baryon decays $\Lambda_b^0 \to \Lambda\gamma$ and $\Xi_b^- \to \Xi^-\gamma$. On the other hand, the first measurement of the photon polarization in a b-baryon decay channel, using the observed signal.

The $\Lambda_b^0 \to \Lambda\gamma$ decay has been recently observed using data collected in 2016 [40], and using the $B_d \to K^*\gamma$ decay as normalization channel. In this work, the $\Lambda_b^0 \to \Lambda\gamma$ analysis is performed using $\Lambda_b^0 \to \Lambda J/\psi$ as normalization channel, thus providing a complementary measurement. This channel has the advantage of sharing the same hadronic part with the radiative decay, canceling most of the dependencies with external measurements in the ratio of branching ratios, as it will be explained in Section 6.2.3.

The $\Xi_b^- \to \Xi^-\gamma$ decay has never been measured before, therefore, the analysis aims to provide first observation. The data-taking period analyzed for the $\Xi_b^- \to \Xi^-\gamma$ analysis is 2018. For the selection procedure, the data is split in three different track topologies (LLL, DDL and DDD), as described in Section 4.1, to optimize selection criteria. Following a similar strategy as for the $\Lambda_b^0 \to \Lambda\gamma$ analysis, the chosen normalization channel is the $\Xi_b^- \to \Xi^- J/\psi$ decay. This channel shares the same hadronic part with the radiative decay, providing all the advantages previously mentioned. A simultaneous fit is performed to the mass distribution of the radiative and normalization channels to extract the ratio of signal yields. This is used as an input to the

ratio of branching ratios to obtain the measurement of the radiative b-decay branching ratio. Potential analyzer biases are avoided by blinding the signal mass region in the mass fit until the analysis procedure is fixed and checked. The analysis method and results are described in detail in Section 6.2.

Additionally, this work aims to provide the first measurement of the photon polarization in b-baryon decays. For this purpose, the $\Lambda_b^0 \to \Lambda\gamma$ decay channel is used following the same reconstruction and selection criteria, and data sample as that used for the $\Lambda_b^0 \to \Lambda\gamma$ branching ratio measurement. The impact of reconstruction effects and backgrounds on the measurement of the photon polarization have been studied in Chapter 5. The background contribution is minimized by using candidates belonging to the mass signal region. Finally, the photon polarization is measured performing a fit to the angular distribution of the $\Lambda_b^0 \to \Lambda\gamma$ decay channel considering the background and reconstruction effects. Section 6.3 details the procedure to accomplish this goal.

6.2 Search for b-baryon decays

In order to perform the search for the $\Lambda_b^0 \to \Lambda\gamma$ and $\Xi_b^- \to \Xi^-\gamma$ decay channels and measure their branching ratios, a clean signal sample is needed. However, some irreducible background contributions remain in the datasets after the selection criteria is applied, as described in Chapter 4. The signal is statistically isolated from the background components by a fit to the invariant mass distribution of the selected candidates. The mass fit involves a simultaneous unbinned maximum likelihood fit to the radiative ($\Lambda_b^0 \to \Lambda\gamma$ or $\Xi_b^- \to \Xi^-\gamma$) and the normalization ($\Lambda_b^0 \to \Lambda J/\psi$ or $\Xi_b^- \to \Xi^- J/\psi$) decay modes. With this strategy, the available statistics to extract some of the parameters, such as the mean mass and the resolution, is increased. This is a standard technique in decays with low yield, as for these analyses. Additionally, a simultaneous fit allows to extract from a single fit the radiative and control channel yields, preserving the correlations.

6.2.1 Signal description

The invariant mass distribution for the signal candidates is modeled by a double-sided crystal-ball (DSCB) [104], defined as:

$$\mathrm{CB}(m;\mu,\sigma,\alpha_i,n_i) = \begin{cases} A_L\left(B_L - \frac{m-\mu}{\sigma}\right)^{-n_L}, & \text{for } \frac{m-\mu}{\sigma} \leq -\alpha_L \\ \exp\left(-\frac{(m-\mu)^2}{2\,\sigma^2}\right), & \text{for } -\alpha_L < \frac{m-\mu}{\sigma} < \alpha_R \\ A_R\left(B_R + \frac{m-\mu}{\sigma}\right)^{-n_R}, & \text{for } \frac{m-\mu}{\sigma} \geq \alpha_R \end{cases}, \quad (6.1)$$

where $i = \{L, R\}$, referring to the left- and right-side of the distribution, $\alpha_{L,R} > 0$, and:

$$A_i = \left(\frac{n_i}{\alpha_i}\right)^{n_i} \exp\left(-\frac{\alpha_i^2}{2}\right), \quad B_i = \frac{n_i - 1}{\alpha_i}. \quad (6.2)$$

This function is composed of a Gaussian core, parametrized by two free parameters (μ and σ), and two independent power-law tails, with two free parameters each one ($\alpha_{L,R}$ and $n_{L,R}$). The left-hand side tail accounts for energy losses due to interactions with the detector material, while the right-hand side tail considers ECAL pile-up deposits, which artificially raise the reconstructed momentum of the photon. The parameters for the tails are extracted from a fit to simulated samples satisfying the full selection, and then fixed in the data fit. The peak position and the width of the Gaussian are left to float in the data fit. Since the fit is simultaneous, the Gaussian parameters for the radiative and control channels are related as follows:

$$\mu^{\text{radiative}} = \mu^{\text{norm}}, \qquad \sigma^{\text{radiative}} = \sigma^{\text{norm}}\, f_\sigma\,. \quad (6.3)$$

The f_σ parameter is a scale factor obtained from the MC fit, which takes into account the difference in the invariant mass resolution, produced by the better momentum of the J/ψ with respect to the photon. Figures 6.1 and 6.2 show the result from the MC simultaneous fit to the radiative and normalization channels, and Tables 6.1 and 6.2 list the parameters obtained, for $\Lambda_b^0 \to \Lambda\gamma$ and $\Xi_b^- \to \Xi^-\gamma$ analyses, respectively.

The high number of simulated events for the $\Xi_b^- \to \Xi^- J/\psi$ normalization channel produces that the fit reaches the machine accuracy and the result cannot be further improved for the described signal parametrization. Due to

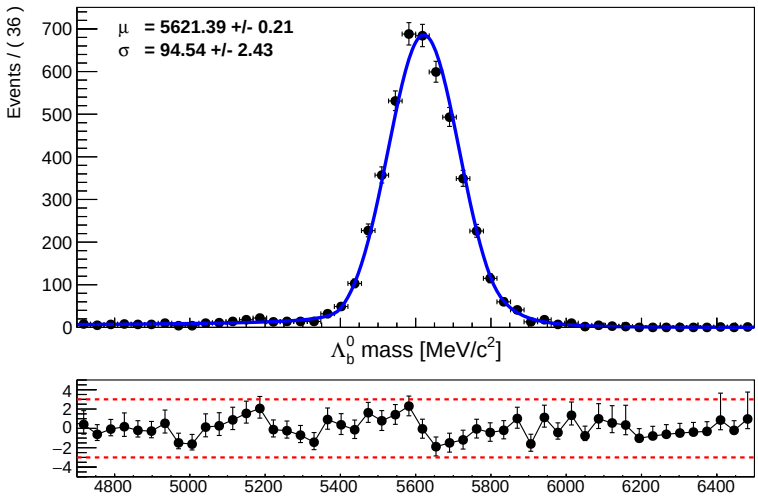

(a)

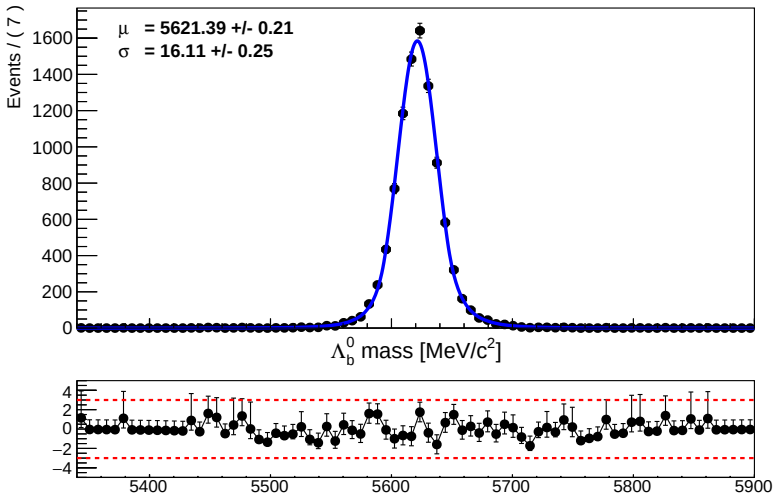

(b)

Figure 6.1: Simultaneous fit to the Λ_b^0 invariant mass distributions of (a) $\Lambda_b^0 \to \Lambda\gamma$ and (b)$\Lambda_b^0 \to \Lambda J/\psi$ in the full mass range for signal MC selected candidates. A DSCB function is used for the mass modeling.

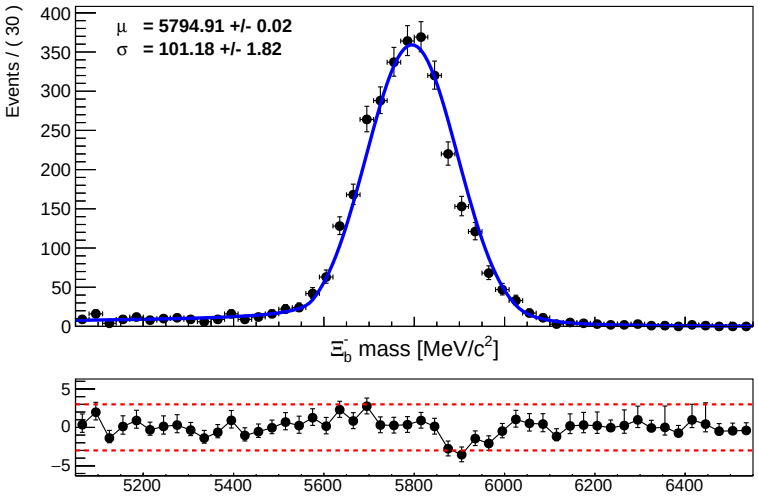

(a)

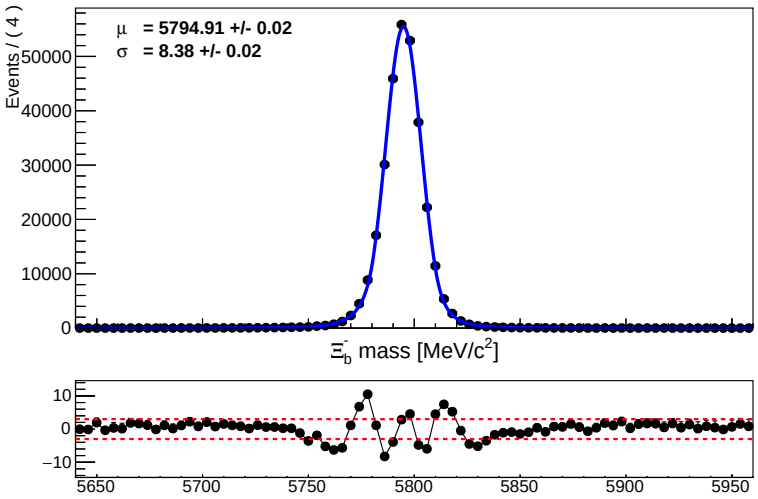

(b)

Figure 6.2: Projections of the simultaneous fit to the Ξ_b^- invariant mass distributions of (a) $\Xi_b^- \to \Xi^-\gamma$ and (b) $\Xi_b^- \to \Xi^- J/\psi$ in the full mass range for signal MC selected candidates. A DSCB function is used for the mass modeling. All track topologies (LLL, DDL and DDD) are combined.

Parameter	$\Lambda_b^0 \to \Lambda\gamma$	$\Lambda_b^0 \to \Lambda J/\psi$	Units
μ	5621.4 ± 0.2		MeV/c^2
σ	94.54 ± 2.43	16.1 ± 0.2	MeV/c^2
f_σ	5.87 ± 0.12	–	
α_L	2.34 ± 0.09	1.71 ± 0.09	
n_L	0.54 ± 0.13	4.8 ± 0.7	
α_R	1.87 ± 0.12	1.57 ± 0.07	
n_R	4.8 ± 1.4	5.2 ± 0.7	

Table 6.1: Fitted parameters obtained from simultaneous mass fit to $\Lambda_b^0 \to \Lambda\gamma$ and $\Lambda_b^0 \to \Lambda J/\psi$ signal candidates in simulation.

Parameter	$\Xi_b^- \to \Xi^-\gamma$	$\Xi_b^- \to \Xi^- J/\psi$	Units
μ	5794.91 ± 0.02		MeV/c^2
σ	101.18 ± 1.82	8.37 ± 0.02	MeV/c^2
f_σ	12.1 ± 0.2	–	
α_L	2.16 ± 0.11	1.70 ± 0.01	
n_L	0.45 ± 0.14	4.33 ± 0.11	
α_R	2.3 ± 0.2	1.86 ± 0.02	
n_R	2.2 ± 0.9	4.31 ± 0.12	

Table 6.2: Fitted parameters obtained from simultaneous mass fit to $\Xi_b^- \to \Xi^-\gamma$ and $\Xi_b^- \to \Xi^- J/\psi$ signal candidates in simulation.

this, discrepancies higher than 5σ appears between the data and the fitted distribution in Figure 6.2.

The mass resolution of the b-baryon in the $\Xi_b^- \to \Xi^- J/\psi$ channel is found to be better than in the $\Lambda_b^0 \to \Lambda J/\psi$. This is caused by the different algorithms used to combine the J/ψ and the strange baryon. For the $\Lambda_b^0 \to \Lambda J/\psi$ decay, the algorithm solely sums the momentum of the Λ and the J/ψ and does not compute the spacial decay point. This aligns the $\Lambda_b^0 \to \Lambda J/\psi$ reconstruction with that of the $\Lambda_b^0 \to \Lambda\gamma$. For the $\Xi_b^- \to \Xi^- J/\psi$ decay, the full available information is used to create the Ξ_b^- decay vertex and, thus, the related variables are known with a higher precision. The different strategies are motivated by the fact that the $\Lambda_b^0 \to \Lambda J/\psi$ decay channel is also used to control angular variables for the photon polarization measurement, where a different vertex reconstruction could induce unexpected discrepancies. On the other hand, the $\Xi_b^- \to \Xi^- J/\psi$ decay is used as normalization channel solely for the branching ratio measurement. It has been checked that using the full information to reconstruct the Λ_b^0 decay vertex for the $\Lambda_b^0 \to \Lambda J/\psi$ mode produces compatible results for the $\mathcal{B}(\Lambda_b^0 \to \Lambda\gamma)$ measurement.

6.2.2 Background description

The dominant background source in these analyses is the random combination of tracks, and photons, if applicable, from several decays. Particularly, for the radiative decays, this background is produced mainly by the combination of a real Λ or Ξ^- and a random photon, as it can be concluded observing the purity of the Λ and Ξ^- invariant mass distributions. This source of background is known as combinatorial background, and it is modeled by an exponential distribution:

$$\mathrm{Exp}(m;\tau) = \frac{1}{\tau} e^{\tau m}\,, \tag{6.4}$$

where τ is a free parameter.

Additionally, any decay with the same number of tracks as the analyzed channel and a high-E_T neutral particle in the final state is a potential candidate to be reconstructed as signal. This kind of background is referred as physical background and can be classified as:

- **Misidentified background**: produced by decay channels in which

one or more particles are misidentified as other particle type.

- **Partially reconstructed background**: this contamination is produced by decays wherein one or more particles in the final state have not been reconstructed and, therefore, they mimic the signal and produce peaks at lower invariant mass with a tail extending below the signal region.

The only potential source of physical background for the $\Lambda_b^0 \to \Lambda\gamma$ decay channel is found to be from $\Lambda_b^0 \to \Lambda\eta$ with $\eta \to \gamma\gamma$ decays. However, its contribution has been found to be compatible with zero [40]. Therefore, no source of physical background is considered for the $\Lambda_b^0 \to \Lambda\gamma$ decay channel. Similarly, the study of several sources of physical background for the $\Lambda_b^0 \to \Lambda J/\psi$ and $\Xi_b^- \to \Xi^- J/\psi$ decays has concluded that they are expected to be negligible [45, 102]. The physical background contributions for the $\Xi_b^- \to \Xi^-\gamma$ decay are evaluated using the simulated samples in the LHCb framework. For decay modes without available generated samples, the fast standalone MC generator RapidSim [113] is used to generate the kinematics of the decay, including the momentum smearing. The expected contamination from a given decay channel follows:

$$C_{\mathrm{H}_b\to X} = \frac{N(\mathrm{H}_b \to X)}{N(\Xi_b^- \to \Xi^-\gamma)} = \frac{f_{\mathrm{H}_b}\,\mathcal{B}_{\mathrm{total}}(\mathrm{H}_b \to X)}{f_{\Xi_b}\,\mathcal{B}_{\mathrm{total}}(\Xi_b^- \to \Xi^-\gamma)} \frac{\epsilon(\mathrm{H}_b \to X)}{\epsilon(\Xi_b^- \to \Xi^-\gamma)}\,, \tag{6.5}$$

where N refers to the expected yield, f_{H_b} is the hadronization fraction for the considered H_b hadron, $\mathcal{B}_{\mathrm{total}}$ is the product of branching ratios for the full decay chain, and ϵ is the efficiency extracted from the simulated sample. A background is considered to contribute if its contamination is above 10^{-6}, as $\mathcal{B}(\Xi_b^- \to \Xi^-\gamma)$ is expected to be of order 10^{-5}. Each of the analyzed samples is reconstructed and selected as the $\Xi_b^- \to \Xi^-\gamma$ candidates to extract the efficiency. When no events are retained after applying a selection step due to the limited statistics, the worst-case scenario is taken for the remaining steps considering that the efficiency for those is the same as for the radiative decay. For RapidSim samples, only kinematic criteria can be applied. The full list of decay channels considered for the background study along with their expected contamination is shown in Table 6.3.

The $\Omega_b^- \to \Omega^-\gamma$ decay (where $\Omega^- \to \Lambda K^-$ and $\Lambda \to p\pi$) is a potential source of misidentified background. However, it is not considered since it

Decay mode	Simulation type	Expected contamination
$\Xi_b^- \to \Xi^- J/\psi$	2016	$< 2.8 \times 10^{-7}$
$\Xi_b^- \to \Xi^- \eta$, $\eta \to \gamma\gamma$	RapidSim	$< 2.2 \times 10^{-5}$
$\Xi_b^- \to \Lambda K^- J/\psi$	2018	$< 1.6 \times 10^{-8}$
$\Lambda_b^0 \to \Lambda\gamma$	2015	$< 4.6 \times 10^{-7}$
$\Lambda_b^0 \to \Lambda\pi^-\pi^+$	2018	$< 1.7 \times 10^{-7}$
$\Lambda_b^0 \to \Lambda K^+\pi^-$	2018	$< 1.3 \times 10^{-7}$
$\Lambda_b^0 \to \Lambda K^+ K^-$	2018	$< 3.2 \times 10^{-7}$

Table 6.3: Potential sources of physical background studied for the $\Xi_b^- \to \Xi^-\gamma$ decay channel along with their expected contamination.

is highly suppressed and, thus, its branching ratio is expected to be much lower than that of the $\Xi_b^- \to \Xi^-\gamma$ decay.

The only potential contamination is due to the $\Xi_b^- \to \Xi^-\eta$ decay with $\eta \to \gamma\gamma$. This channel is simulated using RapidSim and, thus, the result does not reflect the low HLT1 and HLT2 efficiencies on Downstream tracks. Therefore, a deeper study of this channel, using a simulated sample in the LHCb framework, is needed. However, for this thesis, it is assumed that the efficiency is the same as for the radiative channel and $\mathcal{B}(\Xi_b^- \to \Xi^-\eta) = (2.5 \pm 0.7) \times 10^{-5}$ [114], which is one order of magnitude below the expected $\Xi_b^- \to \Xi^-\gamma$ branching ratio. As a consequence, the expected contamination would be one order of magnitude below the expected yield. Additionally, the $\mathcal{B}(\eta \to \gamma\gamma) = 0.394 \pm 0.002$ [43] further lowers the expected contamination.

There are no theoretical predictions for Ξ_b^- baryons decaying to π^0 mesons in the final state that could contaminate the sample. This contamination would fall below the signal peak making impossible to distinguish.

6.2.3 Ratio of branching ratios

The expected yield for the $\Lambda_b^0 \to \Lambda\gamma$ decay, described latter in Equation 6.14, uses inputs from several sources with high uncertainties, such as the recorded luminosity and the hadronization fraction. The use of these inputs in the measurement of the branching ratio would contain high systematic uncertainties as well. To cope with this issue, the branching ratio is measured with respect to the quite similar $\Lambda_b^0 \to \Lambda J/\psi$ decay. This method cancels out

some of the terms and, thus, their uncertainties, as shown in the following equation:

$$\frac{N(\Lambda_b^0 \to \Lambda\gamma)}{N(\Lambda_b^0 \to \Lambda J/\psi)} = \frac{\mathcal{B}(\Lambda_b^0 \to \Lambda\gamma)}{\mathcal{B}(\Lambda_b^0 \to \Lambda J/\psi)} \frac{1}{\mathcal{B}(J/\psi \to \mu^+\mu^-)} \frac{\epsilon_{sel}(\Lambda_b^0 \to \Lambda\gamma)}{\epsilon_{sel}(\Lambda_b^0 \to \Lambda J/\psi)} . \quad (6.6)$$

The normalization channel has been chosen for its similar topology with the radiative decay, to cancel as many contributions as possible. The branching ratio is obtained as:

$$\begin{aligned} \mathcal{B}(\Lambda_b^0 \to \Lambda\gamma) = \mathcal{B}(\Lambda_b^0 \to \Lambda J/\psi) \frac{N(\Lambda_b^0 \to \Lambda\gamma)}{N(\Lambda_b^0 \to \Lambda J/\psi)} \\ \times \mathcal{B}(J/\psi \to \mu^+\mu^-) \frac{\epsilon_{sel}(\Lambda_b^0 \to \Lambda J/\psi)}{\epsilon_{sel}(\Lambda_b^0 \to \Lambda\gamma)} . \end{aligned} \quad (6.7)$$

A similar procedure is applied to the $\Xi_b^- \to \Xi^-\gamma$ decay channel, wherein the following expression is used to determine its branching ratio:

$$\begin{aligned} \mathcal{B}(\Xi_b^- \to \Xi^-\gamma) = \mathcal{B}(\Xi_b^- \to \Xi^- J/\psi) \frac{N(\Xi_b^- \to \Xi^-\gamma)}{N(\Xi_b^- \to \Xi^- J/\psi)} \\ \times \mathcal{B}(J/\psi \to \mu^+\mu^-) \frac{\epsilon_{sel}(\Xi_b^- \to \Xi^- J/\psi)}{\epsilon_{sel}(\Xi_b^- \to \Xi^-\gamma)} . \end{aligned} \quad (6.8)$$

The relevant observable for these analyses is the ratio of branching ratios, defined as:

$$\begin{aligned} \sigma_{\text{rel}}^{\text{H}_b} &= \frac{\mathcal{B}(\text{H}_b \to \text{H}\gamma)}{\mathcal{B}(\text{H}_b \to \text{H}J/\psi)} \frac{1}{\mathcal{B}(J/\psi \to \mu^+\mu^-)} \\ &= \frac{N(\text{H}_b \to \text{H}\gamma)}{N(\text{H}_b \to \text{H}J/\psi))} \frac{\epsilon_{sel}(\text{H}_b \to \text{H}J/\psi))}{\epsilon_{sel}(\text{H}_b \to \text{H}\gamma))} , \end{aligned} \quad (6.9)$$

where H refers to the Λ or Ξ^- baryons. The $\sigma_{\text{rel}}^{\text{H}_b}$ observable depends exclusively on quantities obtained in the analyses (yields and efficiencies) and, thus, it is not affected by external measurements. Moreover, the extracted radiative branching ratios can be easily updated with new measurements of the branching ratio of the normalization channels.

6.2.4 Branching ratios for normalization channels

The signal yield extracted from the mass fit in the $\Lambda_b^0 \to \Lambda\gamma$ and $\Xi_b^- \to \Xi^-\gamma$ analyses are translated to branching ratios using Equations 6.7 and 6.8, respectively. The values needed for this are extracted from Tables 4.19, 4.20 and 6.5. In addition, the branching ratios for the normalization channels and the $J/\psi \to \mu^+\mu^-$ decay channel are used, which appears in Table 6.4.

Parameter	Branching ratio
$f_{\Lambda_b}\,\mathcal{B}(\Lambda_b^0 \to \Lambda J/\psi)$	$(5.8 \pm 0.8) \times 10^{-5}$
$f_{\Xi_b}\,\mathcal{B}(\Xi_b^- \to \Xi^- J/\psi)$	$(1.02 \pm 0.26) \times 10^{-5}$
$\mathcal{B}(J/\psi \to \mu^+\mu^-)$	0.0596 ± 0.0003

Table 6.4: Branching ratio values for the $\Lambda_b^0 \to \Lambda J/\psi$, $\Xi_b^- \to \Xi^- J/\psi$ and $J/\psi \to \mu^+\mu^-$ decays used for computing the $\Lambda_b^0 \to \Lambda\gamma$ and $\Xi_b^- \to \Xi^-\gamma$ branching ratios. These values are taken from the PDG [43].

The branching ratios of the normalization channels appear in the PDG multiplied by the hadronization fraction, which itself depends on the production energy. These measurements were performed at the Tevatron accelerator [115] using pp collisions at a center-of-mass energy of 1.96 TeV, which is very different from that at LHC. Therefore, it is needed to disentangle the branching ratio measurement from the hadronization fraction in order to eliminate the energy dependence. Double counting of the uncertainty is avoided by using the observable σ_{rel} from the $f_{\Lambda_b}\,\mathcal{B}(\Lambda_b^0 \to \Lambda J/\psi)$ analysis [116], which is:

$$\sigma_{\text{rel}} = \frac{f_{\Lambda_b}}{f_B}\frac{\mathcal{B}(\Lambda_b^0 \to \Lambda J/\psi)}{\mathcal{B}(B \to J/\psi K_S)} = 0.345 \pm 0.047\,. \tag{6.10}$$

The value $\mathcal{B}(B \to J/\psi K_S) = (4.36 \pm 0.64) \times 10^{-4}$ [43] is used, where the assumption $\mathcal{B}(B \to J/\psi K_S) = \frac{1}{2}\mathcal{B}(B \to J/\psi K)$ (ignoring CP violation terms of order 10^{-3}) is made to account for the not considered K_L. The fraction $\frac{f_{\Lambda_b}}{f_B}$ at the CDF energy is computed using the following relation:

$$\frac{f_{\Lambda_b}}{f_B} = \frac{\frac{f_{\Lambda_b}}{(f_u+f_d)}\,(f_u+f_d)}{f_B} \simeq \frac{\frac{f_{\Lambda_b}}{f_u+f_d}\,2f_u}{f_u} = 2\frac{f_{\Lambda_b}}{f_u+f_d}\,. \tag{6.11}$$

Using the result $\frac{f_{\Lambda_b}}{f_u+f_d} = 0.229 \pm 0.062$ and the assumption $f_u = f_d = 0.340 \pm 0.021$ [117] by CDF, the value $\frac{f_{\Lambda_b}}{f_B} = 0.458 \pm 0.124$ is obtained. Entering all this in Equation 6.10 results in:

$$\mathcal{B}(\Lambda_b^0 \to \Lambda J/\psi) = \sigma_{\text{rel}}\frac{f_B}{f_{\Lambda_b}}\mathcal{B}(B \to J/\psi K_S) = (3.29 \pm 1.11) \times 10^{-4}\,. \tag{6.12}$$

Equivalently, the PDG provides the hadronization fraction (at Tevatron energy) times the branching ratio of the $\Xi_b^- \to \Xi^- J/\psi$ decay channel. The latter is disentangled from the former following a similar procedure. The

relevant observable for the $\Xi_b^- \to \Xi^- J/\psi$ analysis [118] is:

$$\sigma_{\text{rel}} = \frac{f_{\Xi_b}}{f_{\Lambda_b}} \frac{\mathcal{B}(\Xi_b^- \to \Xi^- J/\psi)}{\mathcal{B}(\Lambda_b^0 \to \Lambda J/\psi)} = 0.167 \pm 0.033\,. \tag{6.13}$$

Using $f_{\Xi_b}/f_{\Lambda_b} = 0.11 \pm 0.03$ obtained by CDF [119, 120], and $\mathcal{B}(\Lambda_b^0 \to \Lambda J/\psi) = (3.29 \pm 1.11) \times 10^{-4}$ from the previous result, as inputs to Equation 6.13, the value $\mathcal{B}(\Xi_b^- \to \Xi^- J/\psi) = (5.0 \pm 2.4) \times 10^{-4}$ is obtained.

The computed branching ratio for the $\Lambda_b^0 \to \Lambda J/\psi$ and $\Xi_b^- \to \Xi^- J/\psi$ decay channels are in agreement with those provided in [120], and have a lower uncertainty due to the use of updated and more precise measurements.

6.2.5 Expected signal yields

The number of expected events after the reconstruction and selection chain depends on the integrated luminosity $\mathcal{L}$ (*i.e.* the number of pp collisions), the production cross-section of $b\bar{b}$ pairs ($\sigma_{b\bar{b}}$), the probability that a b-quark hadronizes into the hadron of interest H_b, called hadronization fraction (f_{H_b}), the probability of the subsequent decays, named branching ratios ($\mathcal{B}$), and the reconstruction and selection efficiencies. A factor of two is applied in order to consider both, the particle and the antiparticle. The expected signal yield for $\Lambda_b^0 \to \Lambda\gamma$ channel is then obtained from:

$$N(\Lambda_b^0 \to \Lambda\gamma) = 2\mathcal{L}\, \sigma_{b\bar{b}}\, f_{\Lambda_b^0}\, \mathcal{B}(\Lambda_b^0 \to \Lambda\gamma)\, \mathcal{B}(\Lambda \to p\pi)\, \epsilon_{sel}(\Lambda_b^0 \to \Lambda\gamma)\,. \tag{6.14}$$

On the other hand, for $\Xi_b^- \to \Xi^-\gamma$ candidates, the expected yield is given by:

$$\begin{aligned} N(\Xi_b^- \to \Xi^-\gamma) = 2\mathcal{L}\, \sigma_{b\bar{b}}\, f_{\Xi_b^-}\, \mathcal{B}(\Xi_b^- \to \Xi^-\gamma)\, \mathcal{B}(\Xi^- \to \Lambda\pi^-) \\ \times \mathcal{B}(\Lambda \to p\pi)\, \epsilon_{sel}(\Xi_b^- \to \Xi^-\gamma)\,. \end{aligned} \tag{6.15}$$

Table 6.5 contains the values of the different quantities entering in these expressions. Since the data sets for the two decays are different (2016 for $\Lambda_b^0 \to \Lambda\gamma$ and 2018 for $\Xi_b^- \to \Xi^-\gamma$), the integrated luminosity $\mathcal{L}$ is different as well. Moreover, there are no previous measurement of the branching ratio for the radiative decay $\Xi_b^- \to \Xi^-\gamma$, thus it is considered to be $\frac{3}{2}\,\mathcal{B}(\Lambda_b^0 \to \Lambda\gamma)$ by considering that the decay rates are related by SU(3) flavor symmetry [119, 120, 123]. The relation $\frac{f_{\Xi_b^-}}{f_{\Lambda_b}} = (8.2 \pm 2.7) \times 10^{-2}$ by LHCb [122, 124] was obtained under this assumption. Its main purpose is to serve as input

	$\Lambda_b^0 \to \Lambda\gamma$	$\Xi_b^- \to \Xi^-\gamma$
$\mathcal{L}$ [fb^{-1}] [53]	1.67	2.19
$\sigma_{b\bar{b}}$ [μb] [121]	~ 600	
f_{H_b} [%]	0.259 ± 0.018 [39]	0.021 ± 0.007
$\mathcal{B}(\mathrm{H}_b \to \mathrm{H}\gamma)$	$(7.1 \pm 1.8) \times 10^{-6}$ [40]	$(1.1 \pm 0.3) \times 10^{-5}$
$\mathcal{B}(\Xi^- \to \Lambda\pi^-)$ [%] [43]	-	99.887 ± 0.035
$\mathcal{B}(\Lambda \to p\pi)$ [%] [43]	63.9 ± 0.5	
ϵ_{sel}	$(7.0 \pm 0.1) \times 10^{-5}$	$(1.76 \pm 0.03) \times 10^{-5}$
Expected yield	82 ± 18	3 ± 1

Table 6.5: Relevant parameter values for obtaining the expected signal yield for the $\Lambda_b^0 \to \Lambda\gamma$ and $\Xi_b^- \to \Xi^-\gamma$ decay channels. Since the $\Xi_b^- \to \Xi^-\gamma$ channel has not been observed, its BR is assumed to be $\frac{3}{2}\,\mathcal{B}(\Lambda_b^0 \to \Lambda\gamma)$ [122].

for sensitivity studies. The strategy of using the ratio of branching ratios removes the dependence on f_{H_b}, as explained in Section 6.2.3.

6.2.6 Validation of the mass fit model

The fit model is validated using pseudo-experiments, as those described in Section 5.2. The generation uses the value of the mass model parameters extracted from the data mass fit. Since the analysis is blinded, the signal contribution for the radiative channel is extracted from the simulated samples. For the $\Lambda_b^0 \to \Lambda\gamma$ analysis, 1000 pseudo-experiments are generated using $\mathcal{B}(\Lambda_b^0 \to \Lambda\gamma) = (7.1 \pm 1.8) \times 10^{-6}$, as previously measured. The pull distribution for the $\Lambda_b^0 \to \Lambda\gamma$ signal yield is shown in Figure 6.3.

The probability to achieve an evidence ($\sigma \geq 3$) or an observation ($\sigma \geq 5$) can be obtained from pseudo-experiments. For this purpose, the statistical significance is computed using the Wilks' theorem [125],

$$\sigma = \sqrt{2 \times \left[\log\left(\mathcal{L}(H_1)\right) - \log\left(\mathcal{L}(H_0)\right)\right]}\,, \tag{6.16}$$

where $\mathcal{L}(H_0)$ is the likelihood value obtained from the null hypothesis (fixing the signal yield to zero) and $\mathcal{L}(H_1)$ is for the alternative hypothesis (letting the signal yield to float). For the assumed $\mathcal{B}(\Lambda_b^0 \to \Lambda\gamma)$, the probability of performing an observation is 48.0%, while the probability to find an evidence is 97.6%, for the considered data sample size.

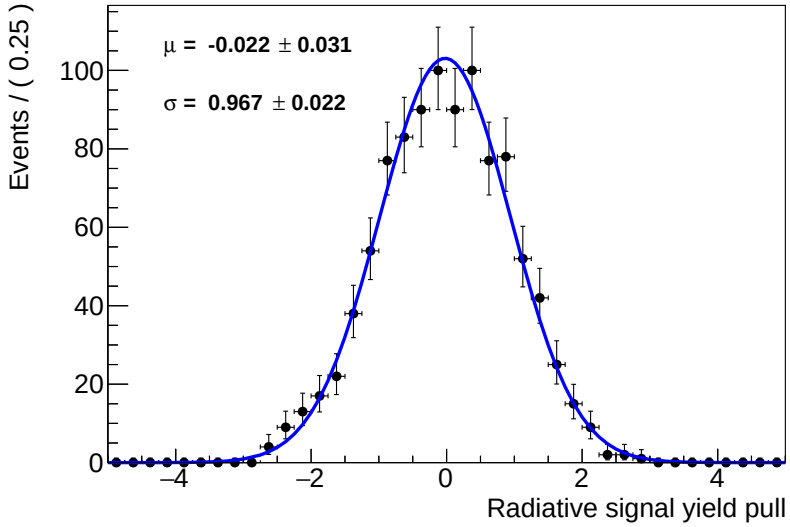

Figure 6.3: Pull distributions for the $\Lambda_b^0 \to \Lambda\gamma$ signal yields generated with the $\mathcal{B}(\Lambda_b^0 \to \Lambda\gamma) = 7.1 \times 10^{-6}$ hypothesis.

Similarly, several sets of pseudo-experiments are performed changing the assumption on the $\mathcal{B}(\Xi_b^- \to \Xi^-\gamma)$ to be $(1 \times 10^{-3}, 5 \times 10^{-4}, 1 \times 10^{-4}, 1.1 \times 10^{-5})$. Each of these sets consists of 1000 datasets, wherein the corresponding background and signal yield are generated and fitted to the full mass model. The resulting pull distributions show the expected shape for a well-behaved fit: no biases or over/under-estimation of the fitting uncertainties. The pulls for the $\Xi_b^- \to \Xi^-\gamma$ yields are shown in Figure 6.4.

The results provided by the Wilks theorem for the different $\mathcal{B}(\Xi_b^- \to \Xi^-\gamma)$ values are shown in Table 6.6. In case of no signal evidence, the CL

$\mathcal{B}(\Xi_b^- \to \Xi^-\gamma)$	Evidence Prob [%] ($\sigma \geq 3$)	Observation Prob [%] ($\sigma \geq 5$)
1×10^{-3}	100.0	100.0
5×10^{-4}	97.5	56.1
1×10^{-4}	2.4	0.0
1.1×10^{-5}	0.4	0.0

Table 6.6: Probability to achieve an evidence or an observation obtained from the pseudo-experiments as a function of several $\mathcal{B}(\Xi_b^- \to \Xi^-\gamma)$ hypotheses.

technique [126] can be used to set an upper limit to the $\mathcal{B}(\Xi_b^- \to \Xi^-\gamma)$.

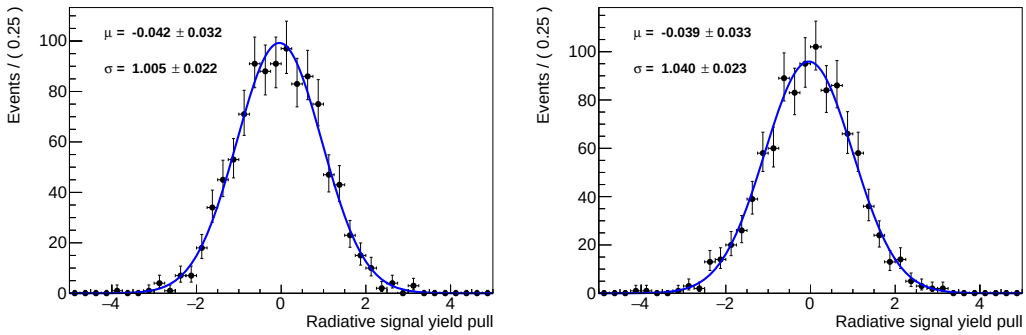

(a)

(b)

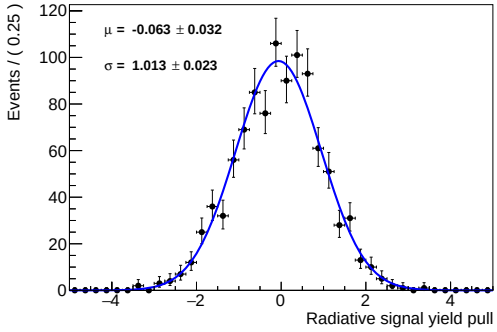

(c)

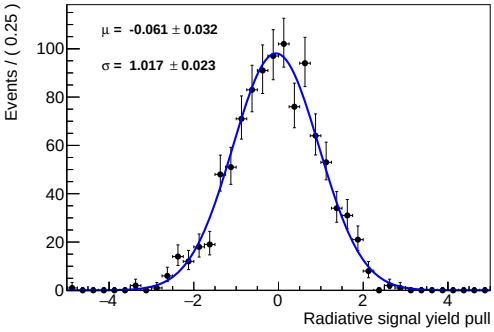

(d)

Figure 6.4: Pull distributions for the $\Xi_b^- \to \Xi^-\gamma$ signal yields generated with the $\mathcal{B}(\Xi_b^- \to \Xi^-\gamma) =$ (a) 1×10^{-3} , (b) 5×10^{-4}, (c) 1×10^{-4}, (d) 1.1×10^{-5} (d) hypotheses.

6.2.7 Blinded mass fit

The mass signal regions for the $\Lambda_b^0 \to \Lambda\gamma$ and $\Xi_b^- \to \Xi^-\gamma$ decay channels remain blinded until the selection criteria are fixed and the fit strategy is validated. This means that the signal regions of the $\Lambda_b^0 \to \Lambda\gamma$ and $\Xi_b^- \to \Xi^-\gamma$ candidates are excluded from the fit and, thus, only the background PDFs are included on the simultaneous fit. On the other hand, the full mass range and all the components of the fit model (signal and background) are included for the normalization channels. As described in the previous sections, the tail parameters of the DSCB function are fixed by the simulation. The rest of the parameters of the model are left free in the fit. The results of the simultaneous fit are shown in Figures 6.5 and 6.6, and the extracted values of the parameters are listed in Tables 6.7 and 6.8, for $\Lambda_b^0 \to \Lambda\gamma$ and $\Xi_b^- \to \Xi^-\gamma$ analyses respectively.

Parameter	$\Lambda_b^0 \to \Lambda\gamma$	$\Lambda_b^0 \to \Lambda J/\psi$	Units
N_{signal}	-	1884 ± 56	
μ_{signal}	-	5619.8 ± 0.6	MeV/c^2
σ_{signal}	-	18.6 ± 0.6	MeV/c^2
N_{comb}	465 ± 26	3863 ± 72	
τ_{comb}	$(-9.3 \pm 1.0) \times 10^{-4}$	$(-6.8 \pm 1.0)) \times 10^{-4}$	MeV/c^2

Table 6.7: Fitted parameters obtained in the simultaneous mass fit to blinded $\Lambda_b^0 \to \Lambda\gamma$ and $\Lambda_b^0 \to \Lambda J/\psi$ selected candidates from the 2016 data sample.

Parameter	$\Xi_b^- \to \Xi^-\gamma$	$\Xi_b^- \to \Xi^- J/\psi$	Units
N_{signal}	-	578 ± 35	
μ_{signal}	-	5797.2 ± 0.5	MeV/c^2
σ_{signal}	-	8.2 ± 0.5	MeV/c^2
N_{comb}	2472 ± 63	3290 ± 63	
τ_{comb}	$(-1.29 \pm 0.05) \times 10^{-3}$	$(-5.1 \pm 1.9) \times 10^{-4}$	MeV/c^2

Table 6.8: Fitted parameters obtained in the simultaneous mass fit to blinded $\Xi_b^- \to \Xi^-\gamma$ and $\Xi_b^- \to \Xi^- J/\psi$ selected candidates from the 2018 data sample.

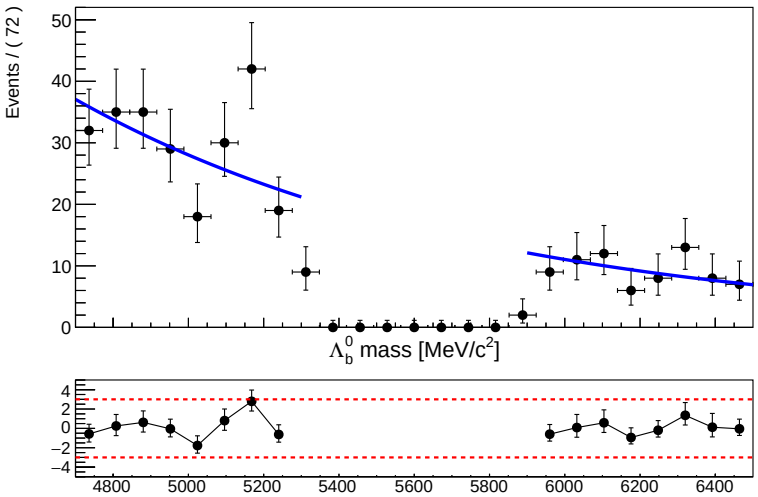

(a)

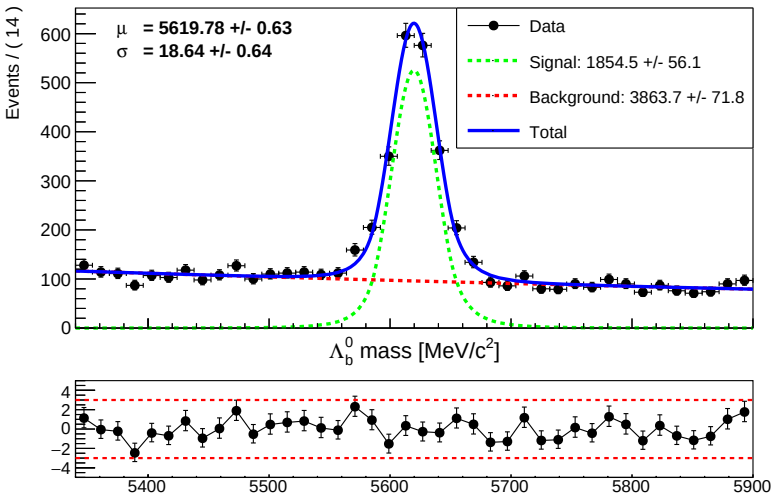

(b)

Figure 6.5: Projections of the simultaneous fit to the Λ_b^0 invariant mass distributions of (a) blinded $\Lambda_b^0 \to \Lambda\gamma$ and (b) $\Lambda_b^0 \to \Lambda J/\psi$ selected candidates from the 2016 data sample.

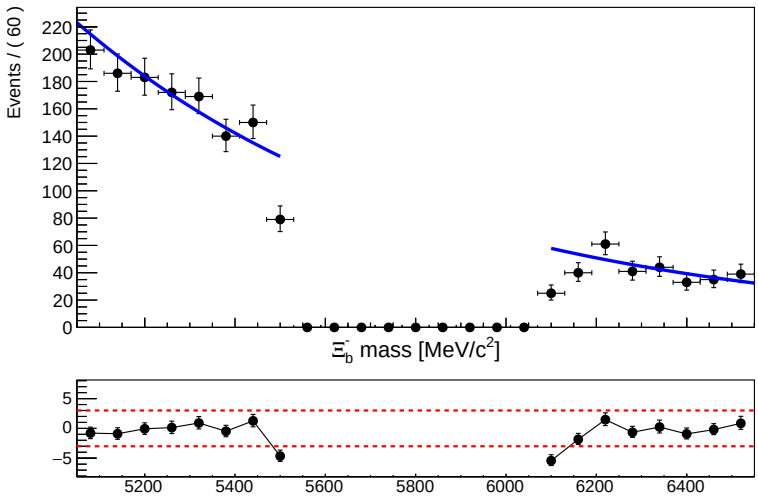

(a)

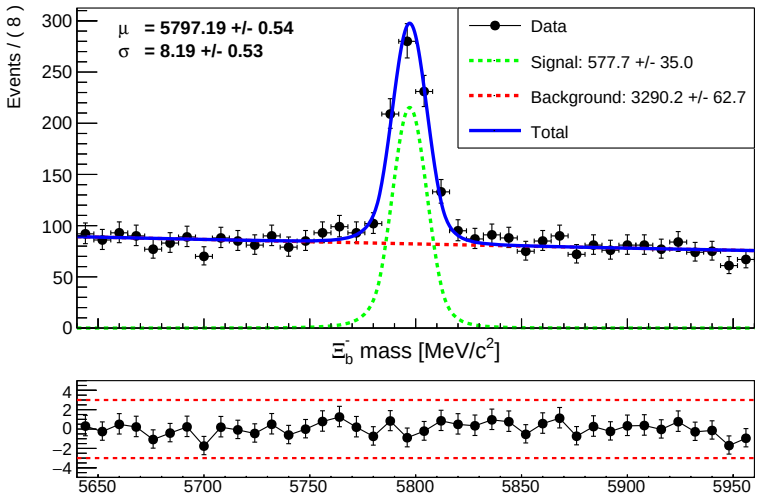

(b)

Figure 6.6: Projections of the simultaneous fit to the Ξ_b^- invariant mass distributions of (a) blinded $\Xi_b^- \to \Xi^-\gamma$ and (b) $\Xi_b^- \to \Xi^- J/\psi$ selected candidates from the 2018 data sample.

6.2.8 Unblinded results

Once the analysis fully validated and frozen, the simultaneous fit to the data candidates is performed in the full mass range for both radiative and normalization channels. The projections of the fits for the $\Lambda_b^0 \to \Lambda\gamma$ and $\Xi_b^- \to \Xi^-\gamma$ analyses can be seen in Figures 6.7 and 6.8 respectively, while the values of the parameters are listed in Tables 6.9 and 6.10.

Parameter	$\Lambda_b^0 \to \Lambda\gamma$	$\Lambda_b^0 \to \Lambda J/\psi$	Units
N_{signal}	71 ± 14	1849 ± 56	
μ_{signal}	5619.8 ± 0.6		MeV/c^2
σ_{signal}	108.4 ± 3.7	18.5 ± 0.6	MeV/c^2
N_{comb}	451 ± 24	3869 ± 72	
τ_{comb}	$(-9.8 \pm 1.0) \times 10^{-4}$	$(-6.8 \pm 1.0) \times 10^{-4}$	MeV/c^2

Table 6.9: Fitted parameters obtained in the simultaneous mass fit to unblinded $\Lambda_b^0 \to \Lambda\gamma$ and $\Lambda_b^0 \to \Lambda J/\psi$ for selected candidates from the 2016 data sample.

Parameter	$\Xi_b^- \to \Xi^-\gamma$	$\Xi_b^- \to \Xi^- J/\psi$	Units
N_{signal}	56 ± 29	577 ± 35	
μ_{signal}	5797.2 ± 0.5		MeV/c^2
σ_{signal}	98.2 ± 6.3	8.2 ± 0.5	MeV/c^2
N_{comb}	2463 ± 57	3291 ± 63	
τ_{comb}	$(-1.30 \pm 0.05) \times 10^{-3}$	$(-5.2 \pm 1.9) \times 10^{-4}$	MeV/c^2

Table 6.10: Fitted parameters obtained in the simultaneous mass fit to unblinded $\Xi_b^- \to \Xi^-\gamma$ and $\Xi_b^- \to \Xi^- J/\psi$ for selected candidates from 2018 data sample.

The mass fit shows a peak with 71 ± 14 $\Lambda_b^0 \to \Lambda\gamma$ signal candidates with a statistical significance, following the Wilks theorem, of 5.6σ. Analogously, a $\Xi_b^- \to \Xi^-\gamma$ peak with 57 ± 29 candidates is extracted. The statistical significance for the $\Xi_b^- \to \Xi^-\gamma$ events is 2σ, below the threshold for evidence.

The measured signal over background ratio is observed to be higher for $\Lambda_b^0 \to \Lambda\gamma$ and $\Lambda_b^0 \to \Lambda J/\psi$ than for $\Xi_b^- \to \Xi^-\gamma$ and $\Xi_b^- \to \Xi^- J/\psi$. This is

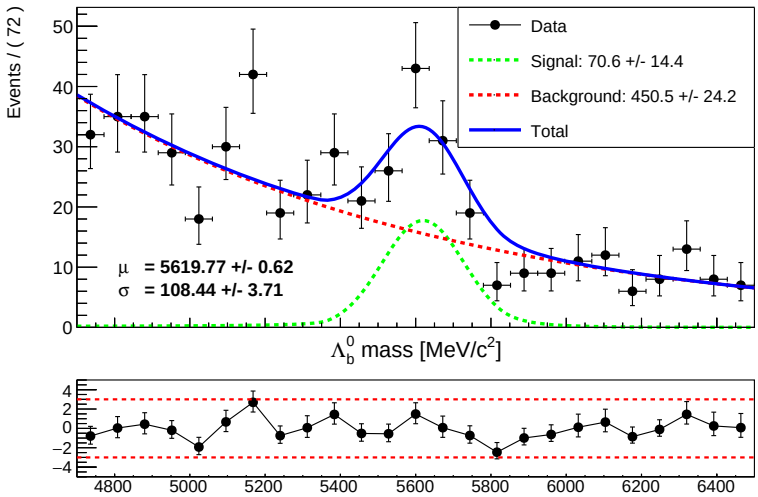

(a)

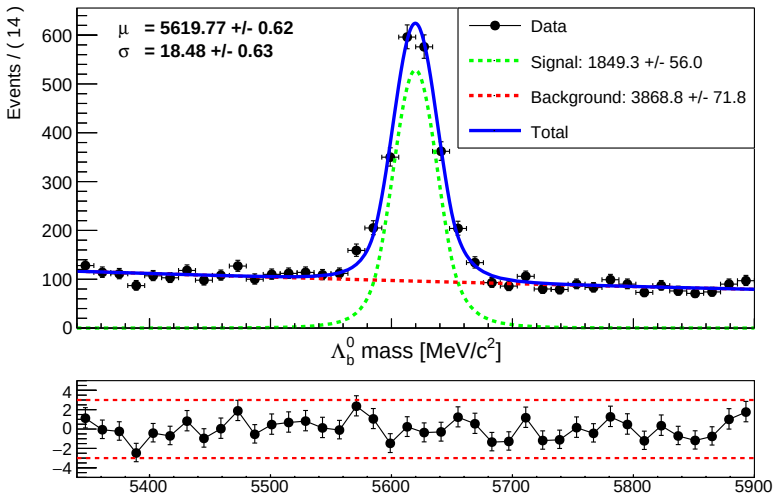

(b)

Figure 6.7: Projections of the simultaneous fit to the Λ_b^0 invariant mass distributions of (a) unblinded $\Lambda_b^0 \to \Lambda\gamma$ and (b) $\Lambda_b^0 \to \Lambda J/\psi$ (b) selected candidates from the 2016 data sample.

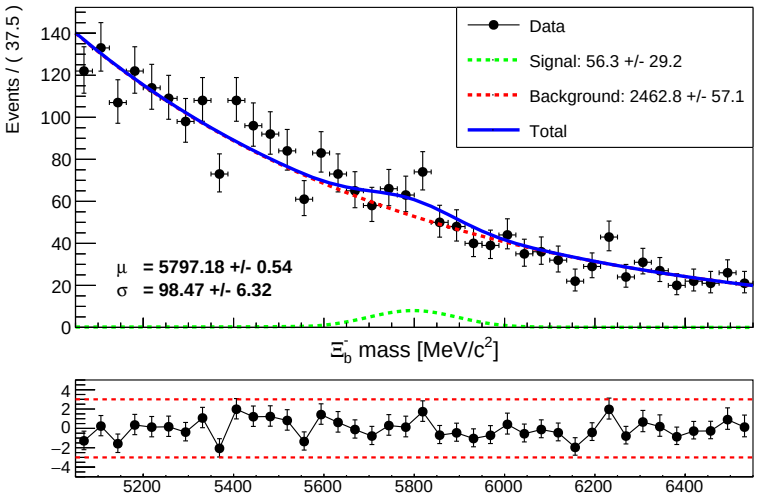

(a)

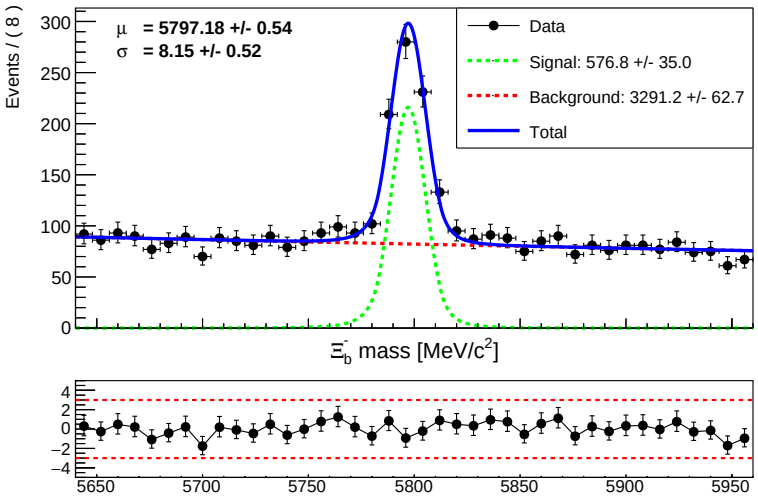

(b)

Figure 6.8: Projections of the simultaneous fit to the Ξ_b^- invariant mass distributions of (a) unblinded $\Xi_b^- \to \Xi^-\gamma$ and (b) $\Xi_b^- \to \Xi^- J/\psi$ selected candidates from the 2018 data sample.

due to the inclusion of Long tracks only for the former, while for the latter the topologies LLL, DDL and DDD are combined.

The measurement is repeated for the $\Xi_b^- \to \Xi^-\gamma$ decay channel considering each of its track topologies separately. For simplicity, only the unblinded mass fit to the data is shown here. Since the $\Xi_b^- \to \Xi^- J/\psi$ data sample is the same for all cases (all track topologies combined), only the projection of the simultaneous mass fit to the $\Xi_b^- \to \Xi^-\gamma$ data set is presented.

The $\Xi_b^- \to \Xi^-\gamma$ mass projections of the simultaneous fit with LLL, DDL and DDD only track topologies are shown in Figures 6.9, 6.10 and 6.11,, respectively. The values of the fitted parameters are listed in Tables 6.11, 6.12 and 6.13. Signal yields of -2 ± 3, 25 ± 14 and 35 ± 26, with significances 0.7σ, 2.1σ and 1.2σ, respectively, are obtained.

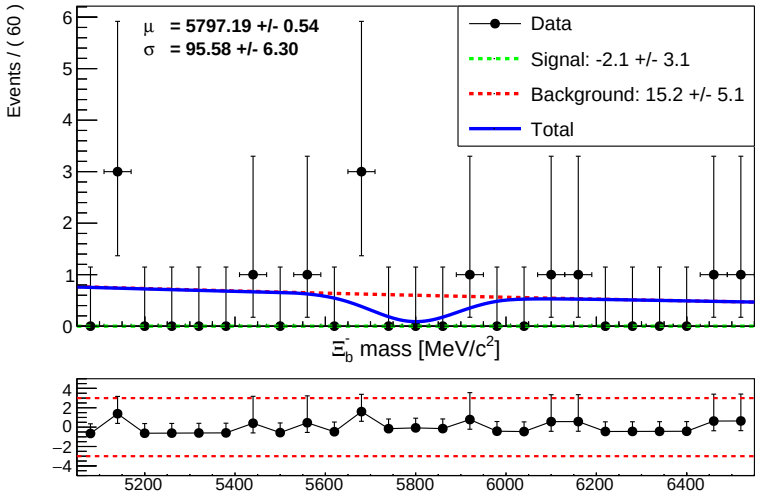

Figure 6.9: Projection to the $\Xi_b^- \to \Xi^-\gamma$ mass of the simultaneous fit to the Ξ_b^- invariant mass distributions of $\Xi_b^- \to \Xi^-\gamma$ and $\Xi_b^- \to \Xi^- J/\psi$ selected candidates with track topology LLL from the 2018 data sample.

The significance of the mass fit performed to the $\Xi_b^- \to \Xi^-\gamma$ decay channel is well below 3σ for each track topology (LLL, DDL and DDD) and also for the combination of these three categories. Therefore, no signal $\Xi_b^- \to \Xi^-\gamma$ is found and an upper bound for the branching ratio can be set using the CL method [127] (see Section 6.2.12).

Parameter	$\Xi_b^- \to \Xi^-\gamma$	$\Xi_b^- \to \Xi^- J/\psi$	Units
N_{signal}	-2.2 ± 3.1	576 ± 35	
μ	5797.2 ± 0.5		MeV/c^2
σ	95.6 ± 6.3	8.1 ± 0.5	MeV/c^2
N_{comb}	15 ± 5	3292 ± 63	
τ_{comb}	$(-3.3 \pm 5.9) \times 10^{-4}$	$(-5.2 \pm 1.9) \times 10^{-4}$	MeV/c^2

Table 6.11: Fitted parameters obtained in the simultaneous mass fit to unblinded $\Xi_b^- \to \Xi^-\gamma$ and $\Xi_b^- \to \Xi^- J/\psi$ selected candidates with topology LLL from the 2018 data sample.

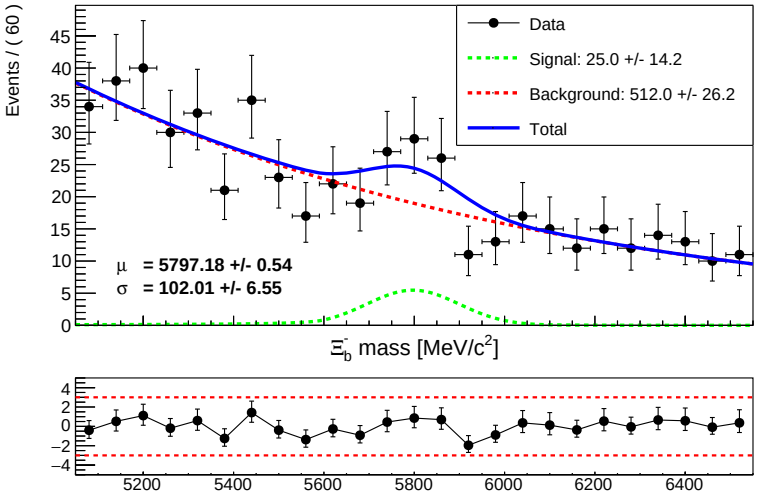

Figure 6.10: Projection to the $\Xi_b^- \to \Xi^-\gamma$ mass of the simultaneous fit to the Ξ_b^- invariant mass distributions of $\Xi_b^- \to \Xi^-\gamma$ and $\Xi_b^- \to \Xi^- J/\psi$ selected candidates with track topology DDL from the 2018 data sample.

Parameter	$\Xi_b^- \to \Xi^-\gamma$	$\Xi_b^- \to \Xi^- J/\psi$	Units
N_{signal}	25 ± 14	577 ± 35	
μ	5797.2 ± 0.5		MeV/c^2
σ	102.0 ± 6.6	8.1 ± 0.5	MeV/c^2
N_{comb}	512 ± 26	3291 ± 63	
τ_{comb}	$(-9.2 \pm 1.1) \times 10^{-4}$	$(-5.2 \pm 1.9) \times 10^{-4}$	MeV/c^2

Table 6.12: Fitted parameters obtained in the simultaneous mass fit to unblinded $\Xi_b^- \to \Xi^-\gamma$ and $\Xi_b^- \to \Xi^- J/\psi$ selected candidates with topology DDL from the 2018 data sample.

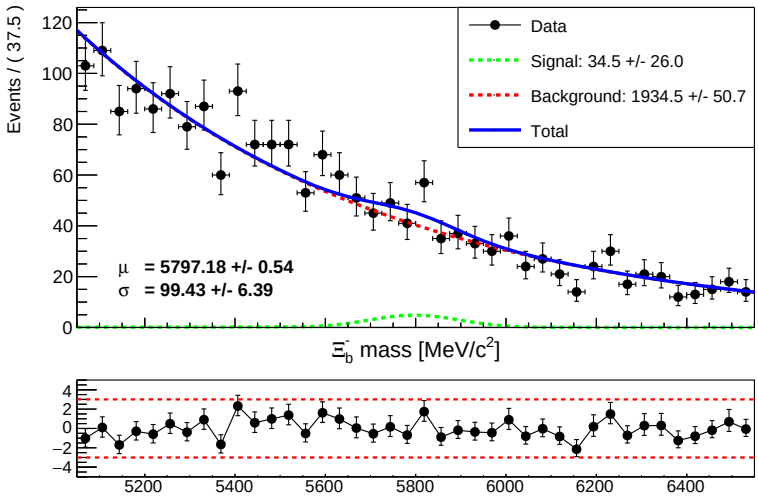

Figure 6.11: Projection to the $\Xi_b^- \to \Xi^-\gamma$ mass of the simultaneous fit to the Ξ_b^- invariant mass distributions of $\Xi_b^- \to \Xi^-\gamma$ and $\Xi_b^- \to \Xi^- J/\psi$ selected candidates with track topology DDD from the 2018 data sample.

Parameter	$\Xi_b^- \to \Xi^-\gamma$	$\Xi_b^- \to \Xi^- J/\psi$	Units
N_{signal}	35 ± 26	581 ± 35	
μ	5797.2 ± 0.5		MeV/c^2
σ	99.4 ± 6.4	8.2 ± 0.5	MeV/c^2
N_{comb}	1934 ± 51	3287 ± 63	
τ_{comb}	$(-1.42 \pm 0.06) \times 10^{-3}$	$(-5.2 \pm 1.9) \times 10^{-4}$	MeV/c^2

Table 6.13: Fitted parameters obtained in the simultaneous mass fit to unblinded $\Xi_b^- \to \Xi^-\gamma$ and $\Xi_b^- \to \Xi^- J/\psi$ selected candidates with topology DDD from the 2018 data sample.

6.2.9 Systematic uncertainties for the $\Lambda_b^0 \to \Lambda\gamma$ decay

Systematic uncertainties can arise from different sources, the most relevant ones are summarized in Table 6.14.

Mass fit model

Two sources of systematic effects are considered for the mass fit model. The first systematic uncertainty arises from the choice of the model describing the signal and background PDFs. It is computed as the deviation in the measured branching ratio using an alternative model compared to the nominal one. The alternative signal and background models are tested independently to avoid possible compensations. The alternative model for the signal is a double-sided crystal-ball with an asymmetric Apollonios [128] as a core, while the background is described with a second order Chebychev polynomial. Deviations of 3.4% and 9.6% are observed in the branching ratio for the alternative signal and background models respectively.

The second systematic uncertainty is produced from the tail parameters of the signal mass distribution and the scale factor relating the width of the signal and the normalization channels, which are fixed in the fit to the value obtained in MC. To account for possible differences between data and simulation, the fit is repeated letting float the tail parameters for the normalization mode. The value of the systematic uncertainty from this source is 5.3%.

Since these uncertainties are expected to be independent, they are added in quadrature. The combined mass fit model systematic accounts for 11.5%.

Simulation/Data differences

Section 4.6 describes the process whereby the modeling of the b-baryon p and p_T are corrected to match the data distributions. The limited amount of events and the kinematics of the chosen channel can produce deviations in the extracted weights. This effect is accounted by using the $\Lambda_b^0 \to \Lambda J/\psi$ decay channel as alternative control channel to extract the weights. The branching ratio is recomputed with the alternative weights and a deviation of 3.8% is observed, which is assigned as systematic uncertainty.

Efficiency calculation

The finite size of the MC sample induces a systematic uncertainty in the estimation of the efficiency used to extract the branching ratio. The systematic uncertainties from this source is extracted using error propagation and a value of 1.9% is obtained. This is a conservative approach since some of the efficiency uncertainties are expected to cancel in the efficiency ratio.

Charged PID efficiency

The PID efficiency is obtained from data samples provided by the PID group at LHCb, as described in Section 4.9. They recommend to linearly add a 0.1% systematic effect per charged track from which the PID information have been used to subtract the background. Two charged tracks are present in the radiative and normalization mode and, thus, a 0.2% systematic per decay mode is considered. Since both channels share the same hadronic decay, the PID systematic is assumed to be correlated and a total 0.28% total effect is taken.

CALO L0 trigger

The ECAL subdetector is calibrated in order to provide accurate measurements of the transverse energy. This information is used by the `L0Photon` and `L0Electron` trigger lines. During the 2016 data-taking period, this calibration suffered from configuration issues. This produced up to 13 different thresholds for the photon E_T requirement depending on the trigger configuration, the tightest being $E_T > 2976\,\text{MeV/c}$. However, the simulated samples are generated using only one of these trigger configurations and, thus, the L0 trigger efficiency may not be perfectly reproduced by the simulation. This effect is mostly superseded by the preselection requirement $E_T > 3000\,\text{MeV/c}$. A discrepancy between the transverse energy measured at L0 and offline level is nevertheless expected, since the L0 decision uses 2x2 CALO clusters while the offline reconstruction uses 3x3 CALO clusters. A comparison between these two quantities reveals that the E_T measured at offline level can be up to $1\,\text{GeV/c}$ higher than that reconstructed at L0 level. This effect is taken into account by repeating the branching ratio measurement with a higher photon E_T requirement ($E_T > 4000\,\text{MeV/c}$), which totally superseds the L0

trigger requirement considering the observed trigger/offline bias. A deviation of 2.6% is measured and assigned as systematic uncertainty.

SPD multiplicity L0 trigger

The `L0Photon` and `L0Electron` lines, triggered by the radiative candidates, require a SPD multiplicity below 450. On the other hand, the trigger lines `L0Muon` and `L0DiMuon`, selecting the normalization channel, are fired by events with a SPD multiplicity below 450 and 900, respectively. Due to the this different criteria, the measurement is sensitive to discrepancies between simulation and data in the SPD multiplicity. In order to assess this effect, the branching ratio measurement is repeated applying SPD multiplicity < 450 as offline requirement to the control channel. A deviation of 13.4% deviation is observed and assigned as systematic uncertainty.

Branching ratios

The systematic uncertainty from the limited precision of the external branching ratio measurements for $\Lambda_b^0 \to \Lambda J/\psi$ and $J/\psi \to \mu^+\mu^-$ decays is computed using error propagation rules. A value of 33.4% is obtained as systematic uncertainty from external measurements. This uncertainty is dominated by the precision of the $\mathcal{B}(\Lambda_b^0 \to \Lambda J/\psi)$.

Summary of uncertainties for the $\Lambda_b^0 \to \Lambda\gamma$ decay

The uncertainties previously computed are summarized in Table 6.14. They are assumed to be independent and, thus, added in quadrature to provide a total value. Additionally, they are split in two categories, one analysis dependent, and other that depends exclusively on external measurements, which will be improved when new measurements are performed.

6.2.10 Cross-checks: Stability of the BDT

The optimal requirement on the BDT output is extracted using the Punzi figure of merit, ass explained in Section 4.7. This relies on well-simulated samples and it is affected by the limited number of selected events. These two effects are considered by changing the condition on the BDT output to an upper and lower values and re-extracting the branching ratio. The result

Systematic source		Value(%)
Mass fit model	Signal	3.4
	Background	9.6
	Fix parameters	5.3
Simulation/Data differences		3.8
Efficiencies	MC limited statistics	1.9
	Charged PID	0.3
L0 trigger	CALO	2.6
	SPD multiplicity	13.4
External measurements	Branching ratios	33.4
Total	$\sigma_{\text{syst.}}$	18.3
	$\sigma_{\text{ext.}}$	33.4

Table 6.14: Summary of the systematic uncertainties for the $\mathcal{B}(\Lambda_b^0 \to \Lambda\gamma)$ measurement.

of this study is shown in Figure 6.12. A deviation is observed, especially for a tighter BDT requirement, which can be considered derived from the reduction in the sample size (statistical nature). Nevertheless, these deviations are compatible to the measured branching ratio using the nominal requirement.

6.2.11 Systematic uncertainties for the $\Xi_b^- \to \Xi^-\gamma$ decay

The simultaneous mass fit on the $\Xi_b^- \to \Xi^-\gamma$ analysis has a significance below the evidence threshold. Besides, the large uncertainty in the $\mathcal{B}(\Xi_b^- \to \Xi^- J/\psi)$ value dominates the measurement. Therefore, only two sources of systematic uncertainties are considered for this measurement:

- The systematic uncertainty due to the limited size of the simulated and control samples. It accounts for 1.8% of the observed branching ratio.

- A 48.0% is assigned as systematic uncertainty due to precision on the $\mathcal{B}(\Xi_b^- \to \Xi^- J/\psi)$ and $\mathcal{B}(J/\psi \to \mu^+\mu^-)$.

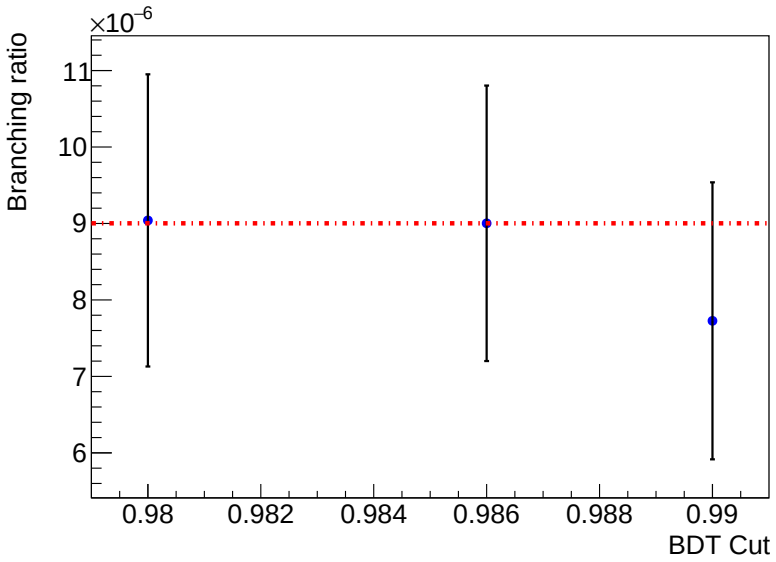

Figure 6.12: Measured value of $\mathcal{B}(\Lambda_b^0 \to \Lambda\gamma)$ with its statistical error as a function of the requirement on the BDT output.

6.2.12 Results

Combining the results presented in the previous sections, the $\Lambda_b^0 \to \Lambda\gamma$ ratio of branching ratios is measured to be

$$\sigma_{\text{rel}}^{\Lambda_b^0} = 0.46 \pm 0.09 \text{ (stat.)} \pm 0.08 \text{ (syst.)}\,, \tag{6.17}$$

where the first uncertainty is statistical and the second is systematic. Using the $\mathcal{B}(\Lambda_b^0 \to \Lambda J/\psi)$ value obtained in Section 6.2.4, the obtained branching ratio of the $\Lambda_b^0 \to \Lambda\gamma$ decay channel is:

$$\mathcal{B}(\Lambda_b^0 \to \Lambda\gamma) = \big(9.0 \pm 1.8 \text{ (stat.)} \pm 1.6 \text{ (syst.)} \pm 3.0 \text{ (ext.)}\big) \times 10^{-6}\,, \tag{6.18}$$

where the source of the first uncertainty is statistical, the second is due to systematic effects and the last is produced by the limited precision on the knowledge on external measurements.

As for the $\Xi_b^- \to \Xi^-\gamma$ analysis, the significance of the branching ratio measurement is below the evidence threshold and, thus, the CL method is used to set an upper bound on the $\mathcal{B}(\Xi_b^- \to \Xi^-\gamma)$. The CL method is applied to the combination of the three track topologies and to each one independently, and a different upper limit can be set regarding the used data sample. For simplicity, only the CL study setting the lower upper limit for the $\mathcal{B}(\Xi_b^- \to \Xi^-\gamma)$, from the LLL category, is reported here (see also

Figure 6.13):

$$\mathcal{B}(\Xi_b^- \to \Xi^-\gamma) < 1.7 \times 10^{-4}\ (95\%\ \mathrm{CL})\,. \tag{6.19}$$

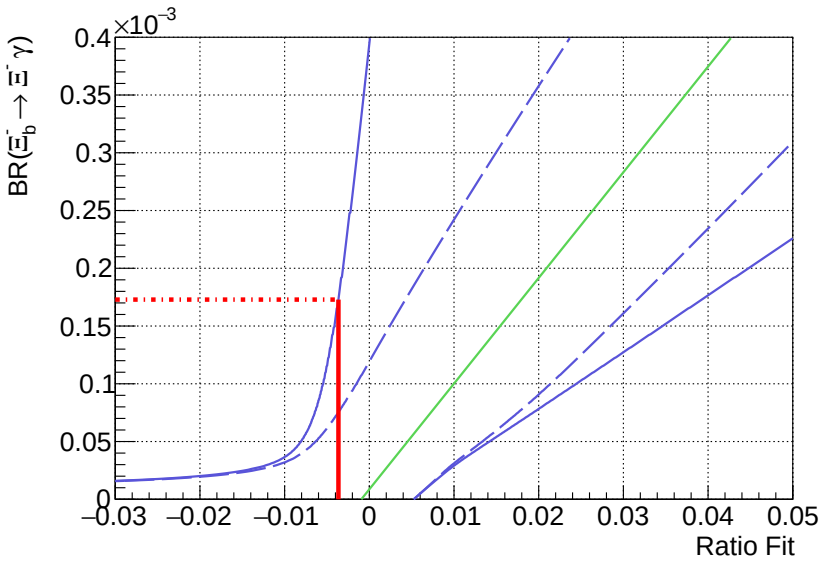

Figure 6.13: Neyman confidence belt showing the upper limit for $\mathcal{B}(\Xi_b^- \to \Xi^-\gamma)$ as a function of the $\frac{N(\Xi_b^- \to \Xi^-\gamma)}{N(\Xi_b^- \to \Xi^- J/\psi)}$ ratio, using only the LLL track topology. The green line represents the relation between the yield and the branching ratios, the dashed blue line is the Neyman belt considering only the statistical uncertainty, while the full blue line considers also the systematic effects. The red line corresponds to the actual measurement.

The background yield and shape are needed, amongst other variables, to use the CL method. However, due to the low amount of $\Xi_b^- \to \Xi^-\gamma$ candidates in the LLL data sample after the full selection, the background shape could not been accurately extracted. This effect is tested by repeating the CL method for the LLL category but using the background shape from the combination of the three categories. This study set the upper limit:

$$\mathcal{B}(\Xi_b^- \to \Xi^-\gamma) < 2.1 \times 10^{-4}\ (95\%\ \mathrm{CL})\,, \tag{6.20}$$

as it can be seen in Figure 6.14. Since no large deviation is observed using the alternative background shape, this effect will not be considered and the upper limit set for $\mathcal{B}(\Xi_b^- \to \Xi^-\gamma)$ is that reported in Equation 6.19.

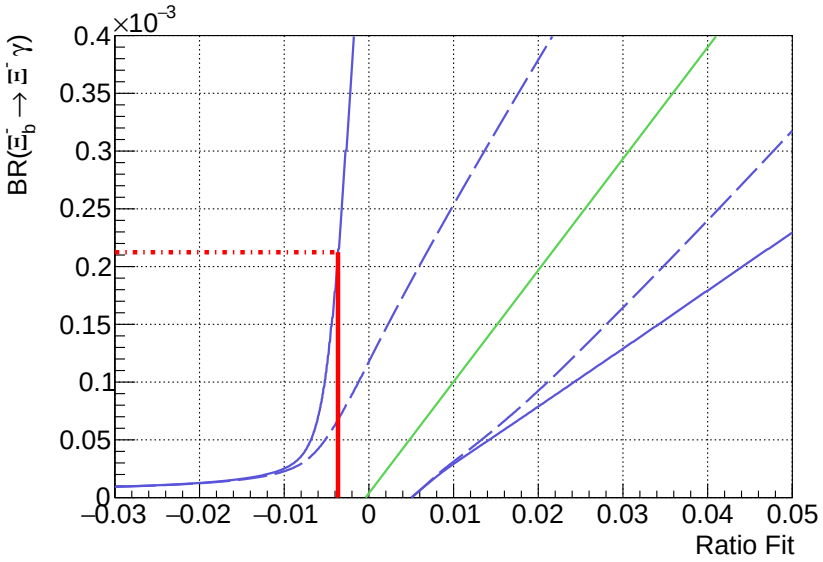

Figure 6.14: Neyman confidence belt showing the upper limit for $\mathcal{B}(\Xi_b^- \to \Xi^-\gamma)$ as a function of the $\frac{N(\Xi_b^- \to \Xi^-\gamma)}{N(\Xi_b^- \to \Xi^- J/\psi)}$ ratio, using only the LLL track topology and the background shape extracted from the combination of the three track topologies. The green line represents the relation between the yield and the branching ratios, the dashed blue line is the Neyman belt considering only the statistical uncertainty, while the full blue line consider also the systematic effects. The red line corresponds to the actual measurement.

6.3 Measurement of the photon polarization

The photon polarization is measured using the angular distribution in radiative $\Lambda_b^0 \to \Lambda\gamma$ decays. The signal fraction in the angular distribution fit is maximized by considering candidates with a reconstructed mass within 1.5σ around the nominal Λ_b^0 mass ([5460, 5780] MeV/c^2). From the yields extracted in Section 6.2.8, and the integral of the signal and background functions within the considered mass range, a total of 57 ± 11 signal events and 70 ± 4 background events are expected. This is translated into a signal fraction of 0.45 ± 0.05 that is used in the angular fit as a constraint, as described in Section 6.3.1. The contribution to the photon polarization sensitivity due to reconstruction effects and backgrounds are described in Chapter 5. From this study, it was concluded that the angular resolution has a negligible impact and can be ignored. The acceptance and background distributions are modeled using third order polynomials.

As for the branching ratio measurement, the value of the photon polarization (α_γ) is kept blinded until the analysis procedure and fit strategy are validated.

6.3.1 Angular fit strategy

The $\Lambda_b^0 \to \Lambda\gamma$ angular distribution is modeled by multiplying the theoretical distribution, described in Section 1.4, by an acceptance function and adding a background contribution. The PDF is:

$$\Gamma_{\Lambda_b}(\theta_p; \alpha_\Lambda, \alpha_\gamma) = \frac{S}{S+B}\left(1 - \alpha_\gamma \alpha_\Lambda \cos\theta_p\right)\mathcal{A}(\theta_p) + \frac{B}{S+B} W_B(\theta_p)\,, \quad (6.21)$$

where $\mathcal{A}(\theta_p)$ is the acceptance function discussed in Section 5.2.3, and $W_B(\theta_p)$ is the function describing the background constructed in Section 5.2.4. The values of the parameters for the acceptance and background functions are extracted in Chapter 5. The initial b-baryon and the photon polarizations cannot be extracted simultaneously from the angular fit due to the signal yield of the 2016 data sample. Hence, the fit dimension is reduced by integrating out the terms related with the initial b-baryon polarization in Equation 1.14, obtaining Equation 1.15 used to construct the above PDF.

The value of α_γ is extracted from an unbinned maximum likelihood fit. The signal and background yields within the signal mass range are used in the fit as Gaussian constraints, while the rest of the parameters are fixed.

Gaussian constraints

It is possible to use prior information of the parameters in the maximum likelihood fit by adding constraints as extra terms to the likelihood. This is done by adding a penalty to the function that effectively constraints the parameter. Any kind of constraint can be chosen, but Gaussian constraints are widely used:

$$\mathcal{L}'(\theta) = \mathcal{L}(\theta)\, G(\mu_\theta, \sigma_\theta) \tag{6.22}$$

where $G(\mu_\theta, \sigma_\theta)$ is a Gaussian distribution of mean μ_θ (measured value of the parameter) and width σ_θ (uncertainty of the parameter). The correlation between different parameters is considered by the use of multivariate Gaussian functions. The Gaussian constraints allow a proper convergence of the fit to parameters with poor sensitivity.

In this analysis, the value of the signal fraction ($\frac{S}{S+B}$) is Gaussian constrained to the value extracted from the full mass fit scaled to the signal mass range ($\frac{S}{S+B} = 0.45 \pm 0.05$).

6.3.2 Angular acceptance

The $\Lambda_b^0 \to \Lambda J/\psi$ decay channel is used to control the angular acceptance extracted from MC, and ensure that it is compatible with the data. This decay shares the hadronic contribution with the radiative $\Lambda_b^0 \to \Lambda\gamma$ channel, used to compute the helicity angles. Moreover, the selection criteria for this control channel is aligned with that of the radiative decays, as explained in Section 4.3.2. As stated previously, data and simulation samples from the 2016 data-taking period are used for this channel. The theoretical helicity angular distribution for the $\Lambda_b^0 \to \Lambda J/\psi$ decay channel, needed to compute the angular acceptance, is taken from [45]. The azimuthal and polar helicity angles, except θ_p are, integrated out, and the angular distribution is

expressed as:

$$W_{\Lambda_b^0\to\Lambda J/\psi}(\theta_p; r_0, r_1, \alpha_b, \alpha_\Lambda) \propto 1 + \frac{3\pi-2}{8\pi}(1-3r_0) + \left((2r_1-\alpha_b) - \frac{3\pi-2}{8\pi}(\alpha_b+r_1)\right)\alpha_\Lambda \cos\theta_p\,, \tag{6.23}$$

where $r_0 = 0.58 \pm 0.02$, $r_1 = -0.56 \pm 0.11$ and $\alpha_b = 0.05 \pm 0.18$ are parameters related with the $\Lambda_b^0 \to \Lambda J/\psi$ helicity amplitudes, measured in [45].

The $\Lambda_b^0 \to \Lambda J/\psi$ decay is generated in the LHCb simulation with a flat angular distribution, which is quite different from the expected theoretical distribution. Nevertheless, the acceptance shape in MC and data is expected to be the same, if correctly evaluated. The acceptance distribution is extracted from MC as the ratio between the reconstructed angular distribution and the generated one (flat). In data, the ratio takes as input the reconstructed angular distribution and the theoretical one, defined in Equation 6.23. The comparisons between the acceptance distributions extracted from $\Lambda_b^0 \to \Lambda J/\psi$ MC and data, and $\Lambda_b^0 \to \Lambda\gamma$ MC are depicted in Figure 6.15. A good agreement is observed in all cases within the available

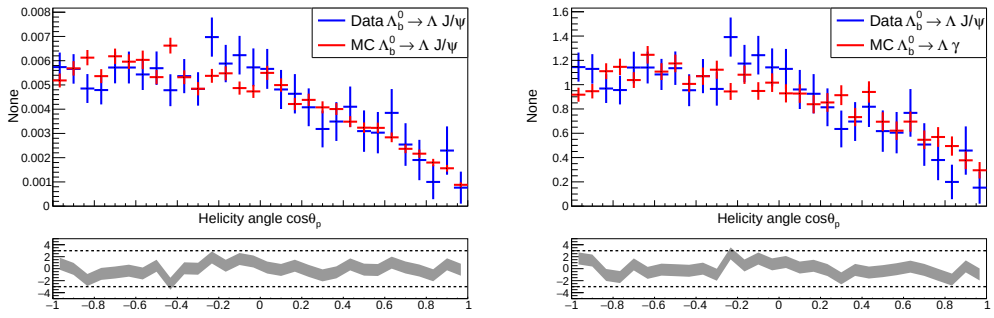

(a) (b)

Figure 6.15: Comparison between the acceptance extracted from MC and data in (a) $\Lambda_b^0 \to \Lambda J/\psi$ and (b) between simulated $\Lambda_b^0 \to \Lambda\gamma$ and data $\Lambda_b^0 \to \Lambda J/\psi$, after the full selection.

statistics. Hence, it is concluded that the acceptance due to the hadronic part of the decay is well reproduced by the simulation. An equivalent study for the radiative part is performed by comparing the helicity angle distribution between reweighted MC events and a sWeighted data sample of the $B_s \to \phi\gamma$ decay channel [129]. A good agreement of the aforementioned

distribution is observed in Figure 6.16 and, thus, it is concluded that the simulation also correctly reproduces the radiative part of the decay.

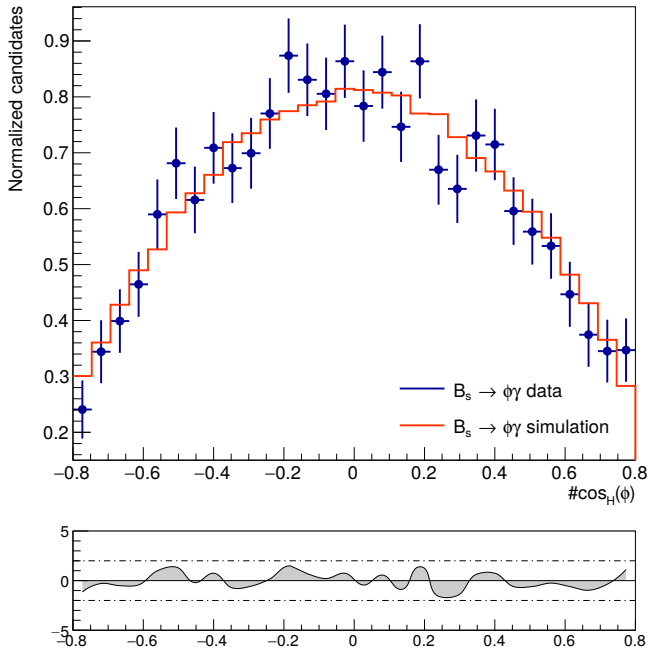

Figure 6.16: Comparison between the cosine of the helicity angle distribution from MC (blue) and data (red) for the $B_s^0 \to \phi\gamma$ candidates satisfying the trigger, stripping and preselection requirements defined for this decay channel. The shape is due to the theoretical angular distribution times the acceptance. This figure is taken from [129].

6.3.3 Background distribution

The background contribution has a significant impact on the sensitivity of the photon polarization measurement, as explained in Section 5.2.4. Furthermore, its correct modeling is crucial for the analysis in order to avoid any bias. The angular distribution of the background is extracted by applying an inverse BDT requirement (BDT output < 0.6) on candidates belonging to the signal region satisfying trigger, stripping and selection requirements. This procedure ensures that no signal events are present in the background shape extraction. In order to validate this procedure, the obtained shape is compared with the angular distribution of the background provided by other methods. Figure 6.17 shows the angular background shape obtained

by the described method. The background distribution for candidates in the signal region requiring only trigger, stripping and preselection is also added. Additionally, the background shape of candidates in the data mass sidebands satisfying the full selection appears for comparison. The results show

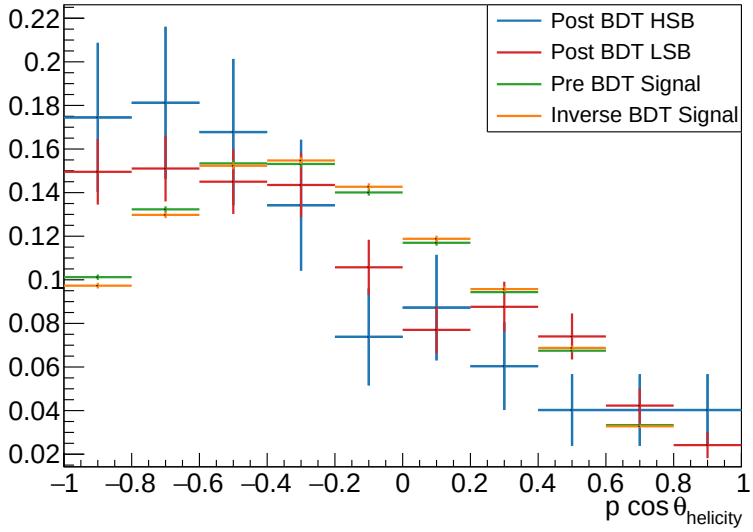

Figure 6.17: Angular distribution for $\Lambda_b^0 \to \Lambda\gamma$ background candidates satisfying the full selection in the high-mass sideband (blue) and low-mass sideband (red); and candidates in the signal region satisfying trigger, stripping and preselection (green), and the inverse BDT cut (orange).

a good agreement between the shapes with different requirements. Some discrepancies seem to arise in the borders ($\cos\theta_p = \pm 1$), Although they are consistent with statistical fluctuations. The inverse BDT method is chosen since it provides a large statistics sample and it grants a negligible signal event contribution.

6.3.4 Validation of the angular fit

The angular fit model is tested using simulation techniques. Sets of 10000 pseudo-experiments with the signal ($S = 57$) and background ($B = 70$) yields extracted from the mass fit (see Section 6.2.8) are produced. The generated value of the photon polarization matches the SM prediction ($\alpha_\gamma = 1$). The angular distribution is fitted according to the PDFs defined in Equation 6.21.

Figure 6.18 shows a pseudo-experiment with the generated angular distribution for $\Lambda_b^0 \to \Lambda\gamma$ including the acceptance effect and the background

contribution. The fit is validated in the full physical range of the photon

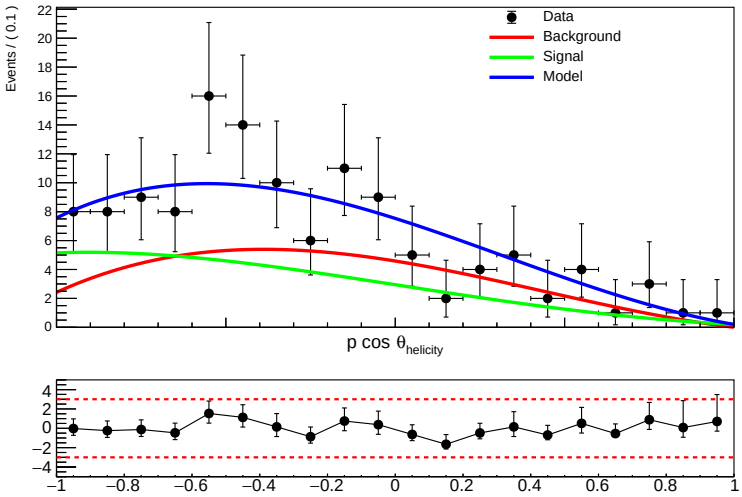

Figure 6.18: Angular distribution fit of pseudo-experiment for channel $\Lambda_b^0 \to \Lambda\gamma$, including acceptance and background effects.

polarization by repeating the MC study with generated values of the α_γ parameter between -1 and 1. The pull distribution shown in Figure 6.19 proves the goodness of the fit to the photon polarization. Additionally, the α_γ statistical uncertainty is extracted from the spread shown in the same figure. The α_γ dispersion and pull distribution are not defined for $\alpha_\gamma > \frac{1}{\alpha_\Lambda} \simeq 1.33$ since the signal PDF becomes negative for those values. The CL method will be used to correctly determine the photon polarization and its uncertainty in the case of a measurement outside the physical range.

As discussed in Section 5.2.4, the signal fraction has a Gaussian constraint in the fit procedure. This is considered in the pseudo-experiments by fluctuating the central value of the constraint, as if repeating the $\Lambda_b^0 \to \Lambda\gamma$ observation. Figure 6.20 shows the results of the MC study for the signal fraction parameter, where the pull distribution follows a normalized Gaussian distribution despite of the constraint on this parameter.

6.3.5 Systematic uncertainties

Systematic uncertainties ($\sigma_{\text{syst.}}$) arise from different sources and have been extracted before unblinding. Their contributions are extracted by means of 10000 pseudo-experiments for several values of the photon polarization. The

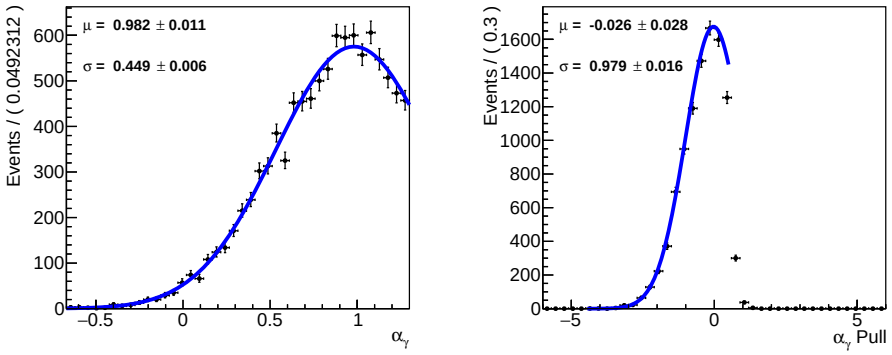

(a)

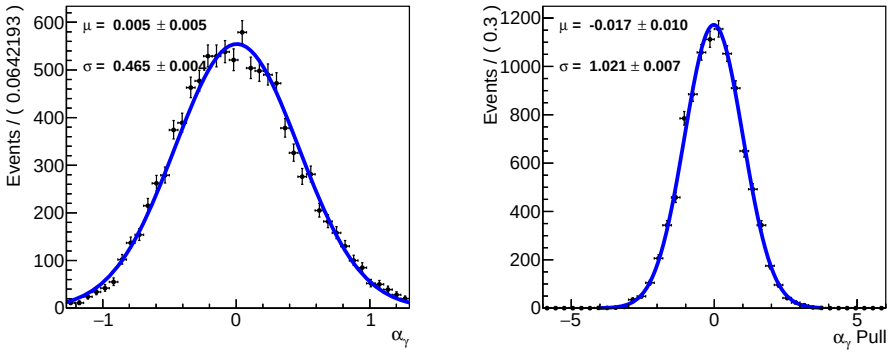

(b)

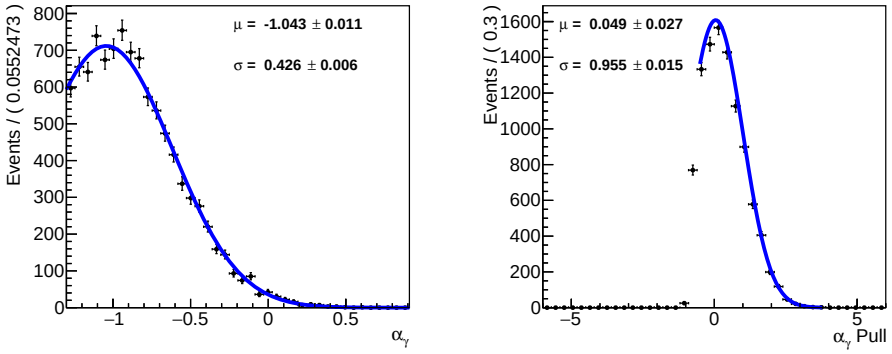

(c)

Figure 6.19: Dispersion (left) and pull distribution (right) for α_γ fitted values for the $\Lambda_b^0 \to \Lambda\gamma$ MC study, including acceptance and background effects, and generated with (a) $\alpha_\gamma = 1$, (b) $\alpha_\gamma = 0$ and (c) $\alpha_\gamma = 1$. A Gaussian fit is superimposed.

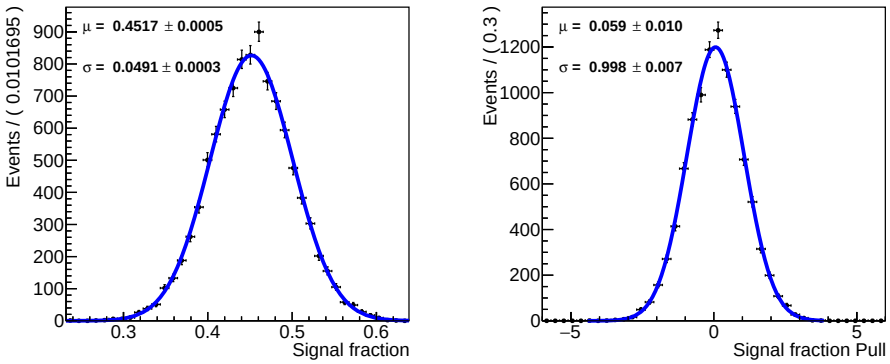

Figure 6.20: Dispersion (left) and pull distribution (right) for signal fraction fitted values from the MC study performed for $\Lambda_b^0 \to \Lambda\gamma$, including acceptance and background effects. A Gaussian fit is superimposed.

procedure to extract each systematic effect is explained in the following and their contributions are summarized in Table 6.15.

Acceptance

The angular acceptance is modeled by a third order polynomial extracted from a fit to simulated data (see Section 5.2.3). Data are generated varying the parameters of the polynomial within uncertainties, using the covariance matrix obtained from the polynomial fit, and then repeating the nominal fit to the generated data. The uncertainty due to the size of the MC sample is extracted as:

$$\sigma_{\text{syst.}} = \sqrt{\sigma^2_{\text{size}} - \sigma^2_{\text{nominal}}}\,, \tag{6.24}$$

where σ_{size} is determined from the dispersion of the α_γ fit values for the 10000 pseudo-experiments. The result of this study is shown in Figure 6.21 for different values of α_γ. No particular trend is observed. A mean systematic uncertainty of 0.068 is assigned to account for this systematic effect.

An additional contribution to the systematic uncertainty using a forth order polynomial as alternative model is considered. Figure 5.8 shows the fit to the acceptance using different models. The systematic uncertainty is taken as the deviation between the mean values (μ) for the nominal and the alternative model:

$$\sigma_{\text{syst.}} = \mu_{\text{nominal}} - \mu_{\text{alternative}}\,. \tag{6.25}$$

Figure 6.22 shows the uncertainty of the α_γ parameter with the alternative

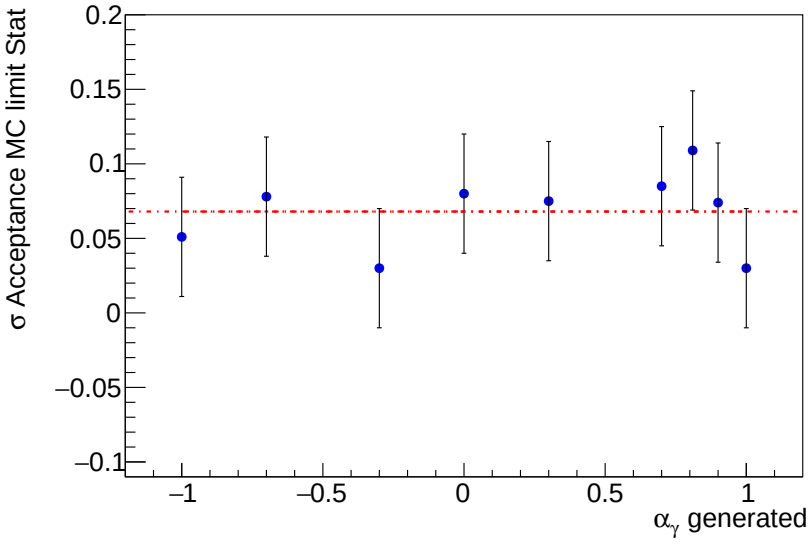

Figure 6.21: Systematic uncertainty as a function of the generated α_γ value in the $\Lambda_b^0 \to \Lambda\gamma$ MC study performed to account for the limited statistics on the acceptance parametrization.

acceptance model for several values of the photon polarization. Their mean values, 0.014, is assigned as systematic uncertainty.

Background

MC studies are performed varying the parameters of the background model within uncertainties following the corresponding covariance matrix. The results are shown in Figure 6.23. From this source, an uncertainty of 0.063 is taken.

The systematic error from the choice of the model is extracted using a forth order polynomial as alternative model. The result of the equivalent MC study can be seen in Figure 6.24 and an average deviation of 0.007 is considered.

Decay parameter

The uncertainty of the weak parameter α_Λ also affects the sensitivity of the photon polarization. The systematic effect on the measured α_γ is obtained by means of 10000 pseudo-experiments wherein the α_Λ value is varied in the generation using a Gaussian distribution with mean and width given by its measured value [43]. Figure 6.25 shows the result of this study. The

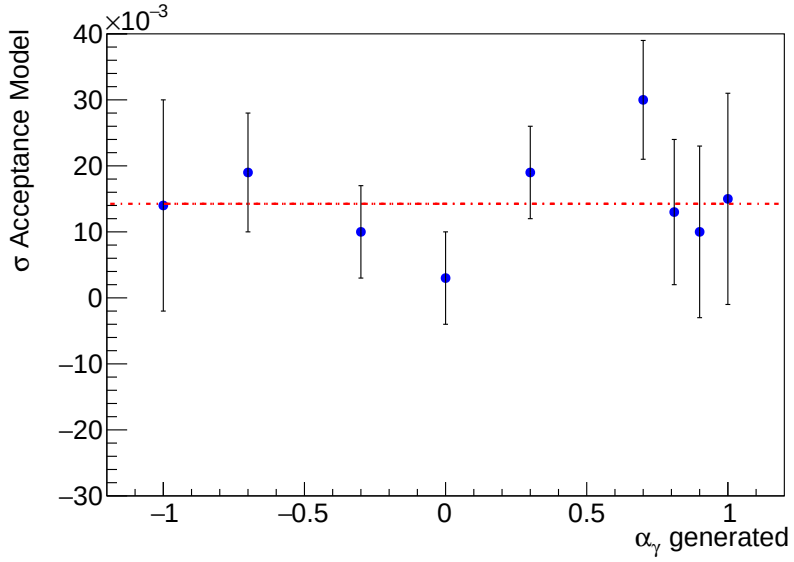

Figure 6.22: Systematic uncertainty for different generated values of α_γ using an alternative (Pol 4) acceptance model for the $\Lambda_b^0 \to \Lambda\gamma$ pseudo-experiments.

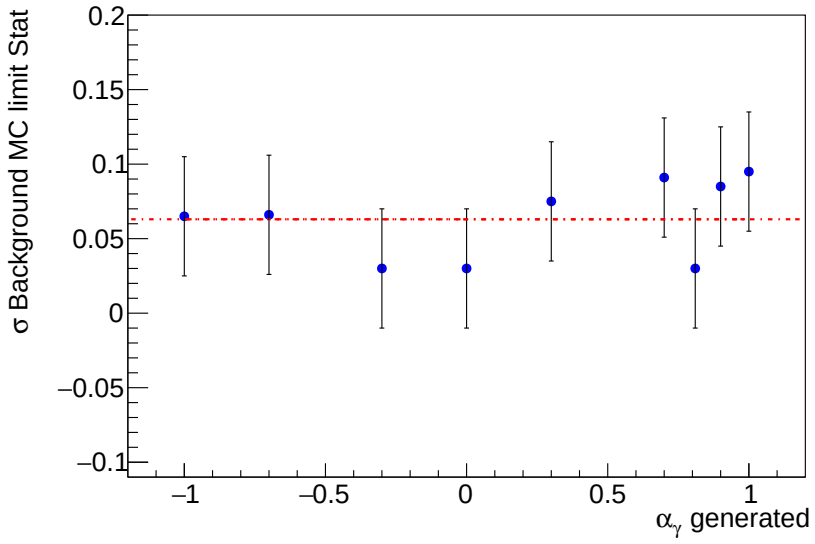

Figure 6.23: Systematic uncertainty for different generated values of α_γ in the $\Lambda_b^0 \to \Lambda\gamma$ MC study to account for the limited statistics on the background parametrization.

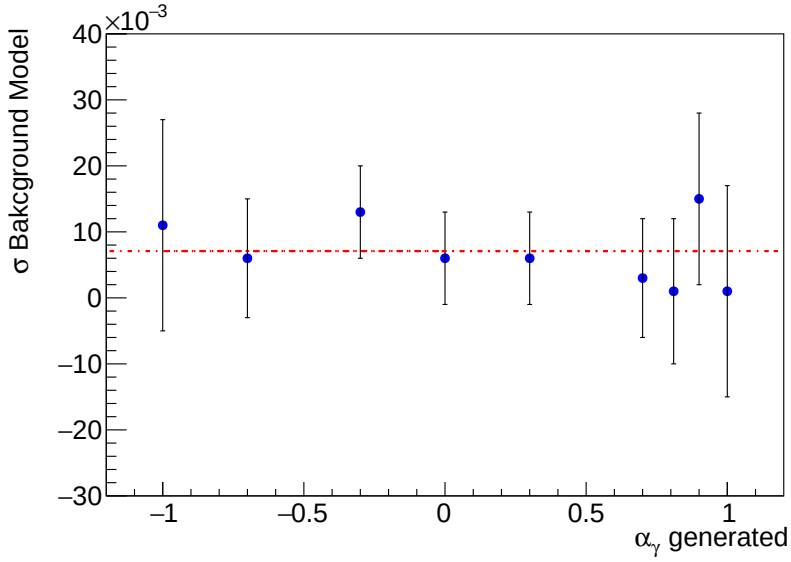

Figure 6.24: Systematic uncertainty for different generated values of α_γ using an alternative (Pol 4) background model for the $\Lambda_b^0 \to \Lambda\gamma$ pseudo-experiments.

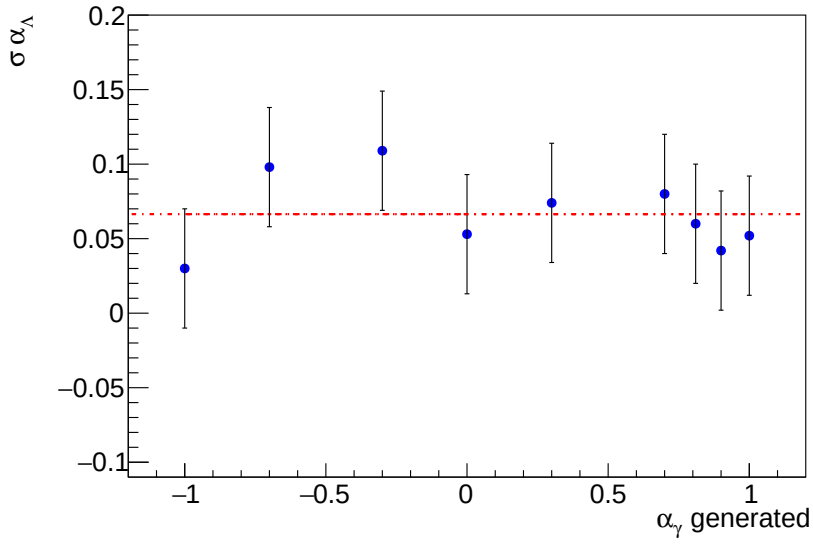

Figure 6.25: Systematic uncertainty for different generated values of α_γ for the $\Lambda_b^0 \to \Lambda\gamma$ MC study performed fluctuating the α_Λ parameter within its uncertainty.

systematic uncertainty is obtained using Equation 6.24 and it accounts for 0.066.

Summary of uncertainties

The summary of the systematic uncertainties for α_γ is listed in Table 6.15. The limited amount of pseudo-experiments also introduces a systematic effect, related to the statistical uncertainty in the estimation of μ in Equation 6.25. This is the error in the estimation of the μ parameter in the Gaussian fit to the α_γ distribution.

Systematic source		Value
Acceptance	Model	0.014
	MC limited statistics	0.068
Background	Model	0.007
	Limited statistics	0.063
Pseudo-experiments limited statistics		0.006
External measurement	α_Λ	0.066
Total	$\sigma_{\text{syst.}}$	0.094
	$\sigma_{\text{ext.}}$	0.066

Table 6.15: Summary of systematic uncertainties for the α_γ measurement.

6.3.6 Results

The fitted angular distribution from data in the signal region can be seen in Figure 6.26 for $\Lambda_b^0 \to \Lambda\gamma$.

Combining the results from these fits with the uncertainties obtained in the previous section, the photon polarization is measured to be:

$$\alpha_\gamma = 0.81 \pm 0.45 \text{ (stat.)} \pm 0.09 \text{ (syst.)} \pm 0.07 \text{ (ext.)} \quad . \tag{6.26}$$

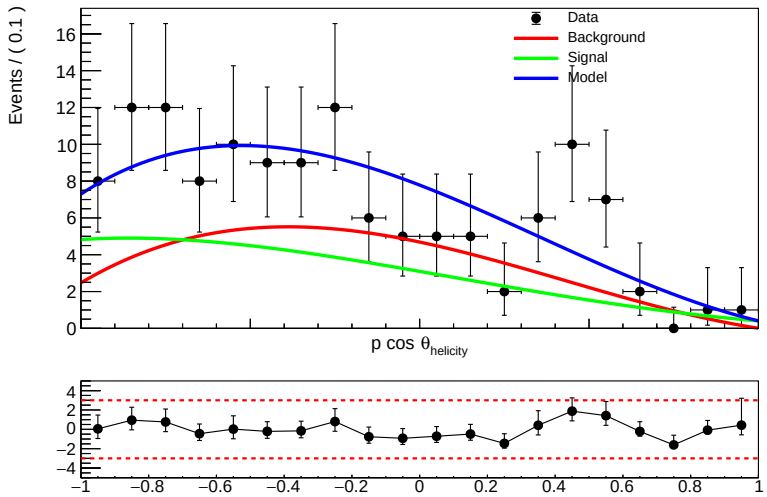

Figure 6.26: Fit to the angular distribution of $\Lambda_b^0 \to \Lambda\gamma$ data candidates in the signal region.

7 Conclusions and prospects

7.1 Conclusions

Two analyses are presented in this thesis, contributing to the expansion of the LHCb rare decays program in the area of radiative beauty decays: the measurement of the branching ratio and the photon polarization using the $\Lambda_b^0 \to \Lambda\gamma$ and $\Xi_b^- \to \Xi^-\gamma$ decay channels. These decays are mediated by FCNC which only appear at loop level in the SM and, thus, they are very sensitive to NP particles entering in the loop. Particularly, decays including the process $b \to s\gamma$ are sensitive to the Wilson coefficient C_7'. The SM prediction for this Wilson coefficient is very small, $C_7' \simeq \mathcal{O}(\frac{m_s}{m_b})$, since no right-handed currents are contributing.

The analysis of the $\Lambda_b^0 \to \Lambda\gamma$ decay uses data collected by the LHCb experiment in the 2016 data-taking period. The reconstruction and selection follows the one in [40], and it is further improved by reoptimizing the BDT and the inclusion of a new discriminant variable. In addition, the channel $\Lambda_b^0 \to \Lambda J/\psi$ is used as normalization channel to perform the measurement of the ratio of branching ratios. A total of 71 signal candidates are found and the ratio of branching ratio measurement is:

$$\sigma_{\text{rel}}^{\Lambda_b^0} = 0.46 \pm 0.09 \text{ (stat.)} \pm 0.08 \text{ (syst.)}\,. \tag{7.1}$$

Using the latest measurements for $\mathcal{B}(\Lambda_b^0 \to \Lambda J/\psi)$ and $\mathcal{B}(J/\psi \to \mu^+\mu^-)$, the obtained branching ratio for the $\Lambda_b^0 \to \Lambda\gamma$ decay channel is:

$$\mathcal{B}(\Lambda_b^0 \to \Lambda\gamma) = \big(9.0 \pm 1.8 \text{ (stat.)} \pm 1.6 \text{ (syst.)} \pm 3.0 \text{ (ext.)}\big) \times 10^{-6}\,. \tag{7.2}$$

Using these events, the photon polarization is extracted by means of a fit

to the angular distribution using the helicity formalism, wherein the effects of the acceptance and the background are considered. The signal candidates are taken withing 1.5σ of the Λ_b^0 invariant mass ([5460, 5780] MeV/c^2). Thereby, the angular fit is performed with 57 ± 11 signal candidates and 70 ± 4 background events. The photon polarization is measured for first time using a radiative b-baryon decay, providing a value of:

$$\alpha_\gamma = 0.81 \pm 0.45 \text{ (stat.)} \pm 0.09 \text{ (syst.)} \pm 0.07 \text{ (ext.)} \tag{7.3}$$

The analysis of the $\Xi_b^- \to \Xi^-\gamma$ decay is performed for first time. The whole selection criteria is defined from scratch, including the addition of trigger and stripping lines to the LHCb software. The $\Xi_b^- \to \Xi^- J/\psi$ is used as normalization and control channel, due to its similar hadronic decay with the signal channel. The data collected by LHCb during 2018 is used for this analysis. No signal is found with the available statistics. An upper bound is set for its branching ratio, with a value of:

$$\mathcal{B}(\Xi_b^- \to \Xi^-\gamma) < 1.7 \times 10^{-4} \text{ (95\% CL)}\,, \tag{7.4}$$

where the precision is mainly affected by the limited knowledge on the value of the $\mathcal{B}(\Xi_b^- \to \Xi^- J/\psi)$.

The current measurement of the photon polarization imposes new constraints on the value of the Wilson coefficient C_7'. The python package Flavio [130] is used to calculate these constraints in $C_7'^{NP}$, where, for simplicity, the SM contribution is subtracted ($C_7'^{NP} = C_7'$ - $C_7'^{SM}$). The constraints at 1σ from the current analysis, and from other radiative decay measurements, are presented in Figure 7.1. Additionally, the constraint imposed by the combination of the radiative measurement at 1σ and 2σ is shown. The following measurements are included in the plot:

- $BR(B \to X_s\gamma)$ refers to the inclusive branching ratios mediated by the process $b \to s\gamma$ [131]. They impose constraints of the kind:

$$\mathcal{B}(B \to X_s\gamma) \propto |C_7|^2 + |C_7'|^2\,. \tag{7.5}$$

  hence, the shape of the constraint in the $C_7'^{NP}$ complex plane is circular.

- $A_{\phi\gamma}^{\Delta}$ and $S_{\phi\gamma}$ are observables from the decay-rate time dependent analysis of $B_s^0 \to \phi\gamma$ [35]. These observables are related with the Wilson

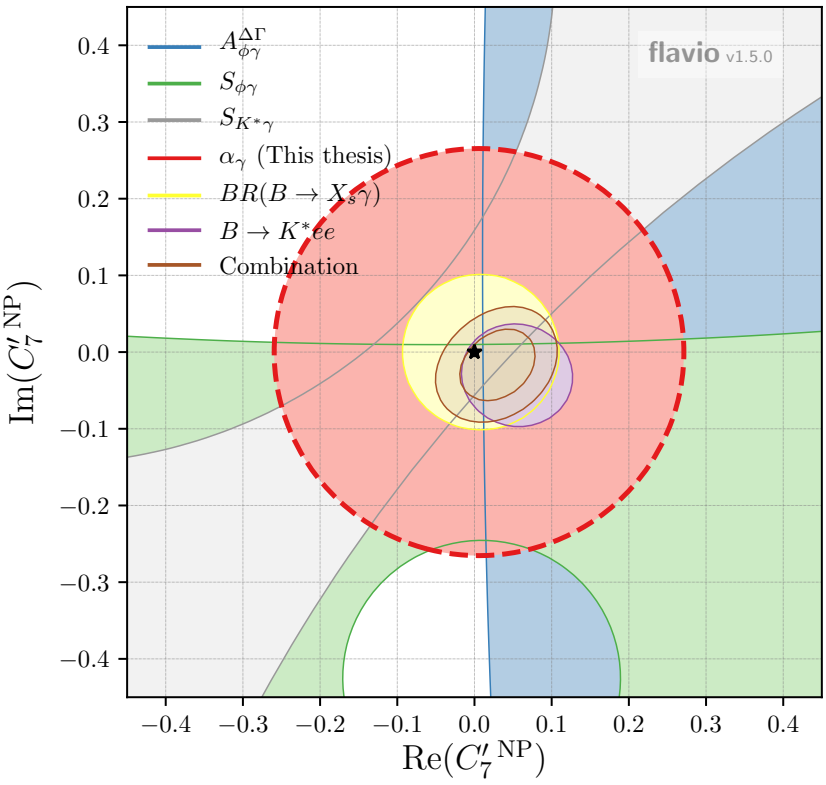

Figure 7.1: Constraints on the $C_7'^{NP}$ complex plane from all the radiative decay measurements, including those provided by this thesis.

coefficients as:

$$A_{\phi\gamma}^{\Delta} \simeq \frac{2\,\mathrm{Re}(e^{-i\phi}C_7C_7')}{|C_7|^2+|C_7'|^2}\,, \qquad S_{\phi\gamma} \simeq \frac{2\,\mathrm{Im}(e^{-i\phi}C_7C_7')}{|C_7|^2+|C_7'|^2}\,. \tag{7.6}$$

- $S_{K^*\gamma}$ corresponds to the observables from the mixing-induced CP asymmetry analysis of the $B^0 \to K^*\gamma$ decay channel. The imposed constraint is the combination of the measurement from the Belle [132] and BaBar [133] collaborations. The dependence of $S_{K^*\gamma}$ with the Wilson coefficients is the same as that for $S_{\phi\gamma}$, described in Equation 7.6.

- $B \to K^*ee$ makes reference to angular analysis of the $B \to K^*ee$ decay channel at $q^2 = 0$, performed by LHCb [36]. The transverse asymmetry is related with the Wilson coefficient as follows:

$$A_{\mathrm{T}}^{(2)}(q^2 \to 0) = \frac{2\,\mathrm{Re}(C_7C_7'^*)}{|C_7|^2+|C_7'|^2}\,, \qquad A_{\mathrm{T}}^{\mathrm{Im}}(q^2 \to 0) = \frac{2\,\mathrm{Im}(C_7C_7'^*)}{|C_7|^2+|C_7'|^2}\,. \tag{7.7}$$

The combination of the radiative measurements, including α_γ provided by this thesis, sets the best point for $C_7'^{\mathrm{NP}}$ at:

$$\left\{\mathrm{Re}\,C_7'^{\mathrm{NP}}, \mathrm{Im}\,C_7'^{\mathrm{NP}}\right\} = \{0.0306, -0.0170\}\,. \tag{7.8}$$

At present, the experimental value of C_7' is compatible with the SM prediction.

7.2 Prospects

In this work, the branching ratio measurement of the $\Lambda_b^0 \to \Lambda\gamma$ is completely dominated by the uncertainty from external measurements, particularly the $\mathcal{B}(\Lambda_b^0 \to \Lambda J/\psi)$ measurement. A measurement of the $\Lambda_b^0 \to \Lambda J/\psi$ decay channel by the LHCb will be more precise with respect to those performed by CDF and D0 experiments, reducing the statistical uncertainties. Moreover, the hadronization fraction (f_{Λ_b}), needed to compute $\mathcal{B}(\Lambda_b^0 \to \Lambda J/\psi)$, is known with better precision at LHCb conditions, which would further cut down uncertainties. On the other hand, the $\mathcal{B}(\Xi_b^- \to \Xi^- J/\psi)$ measurement used in the $\Xi_b^- \to \Xi^-\gamma$ analysis was performed by CDF and D0 experiments. A new measurement of the $\mathcal{B}(\Xi_b^- \to \Xi^- J/\psi)$ by the LHCb experiment would benefit in a equivalent way the search for the $\Xi_b^- \to \Xi^-\gamma$ decay channel. Besides, the $\mathcal{B}(\Lambda_b^0 \to \Lambda J/\psi)$ observable is used to compute the $\mathcal{B}(\Xi_b^- \to \Xi^- J/\psi)$ and, thus, the $\mathcal{B}(\Xi_b^- \to \Xi^-\gamma)$ measurement would also be improved from this update. The second major uncertainty is produced by the limited amount of signal candidates. For this thesis, only data from 2016 (for $\Lambda_b^0 \to \Lambda\gamma$ analysis) and 2018 (for $\Xi_b^- \to \Xi^-\gamma$ analysis) have been used. However, the data collected during the whole Run II data-taking period is available and its use will provide three times more signal events. The inclusion of this new data is currently in progress. The statistical uncertainty of the photon polarization measurement is expected to drop to 0.25 due to this inclusion.

The large amount of data expected in the next Run III, starting at 2021, could multiply the available statistics by a factor 10 with respect to the yield obtained in this thesis. The increase in the integrated luminosity is only one of the advantages of the Run III. The LHCb is receiving an upgrade on its system, which will provide more precise and cleaner measurement. This will lead in a better separation between the signal and the background, with higher selection efficiencies and, ultimately, in a reduction on the systematic and statistical uncertainties.

Appendix

A.1 Preselection plots

A.1.1 $\Lambda_b^0 \to \Lambda\gamma$

The comparison between the distributions of simulated signal and data mass side-band candidates for the $\Lambda_b^0 \to \Lambda\gamma$ decay can be seen in Figure A.1. The candidates are required to fulfill the stripping and trigger requirements.

A.1.2 $\Xi_b^- \to \Xi^-\gamma$ LLL

The comparison between the distributions of simulated signal and data mass side-band candidates for the $\Xi_b^- \to \Xi^-\gamma$ decay reconstructed exclusively with Long tracks (LLL) can be seen in Figure A.2. The candidates are required to fulfill the stripping and trigger requirements.

A.1.3 $\Xi_b^- \to \Xi^-\gamma$ DDL

The comparison between the distributions of simulated signal and data mass side-band candidates for the $\Xi_b^- \to \Xi^-\gamma$ decay reconstructed with Long and Downstream tracks (DDL) can be seen in Figure A.3. The candidates are required to fulfill the stripping and trigger requirements.

A.1.4 $\Xi_b^- \to \Xi^-\gamma$ DDD

The comparison between the distributions of simulated signal and data mass side-band candidates for the $\Xi_b^- \to \Xi^-\gamma$ decay reconstructed exclusively with

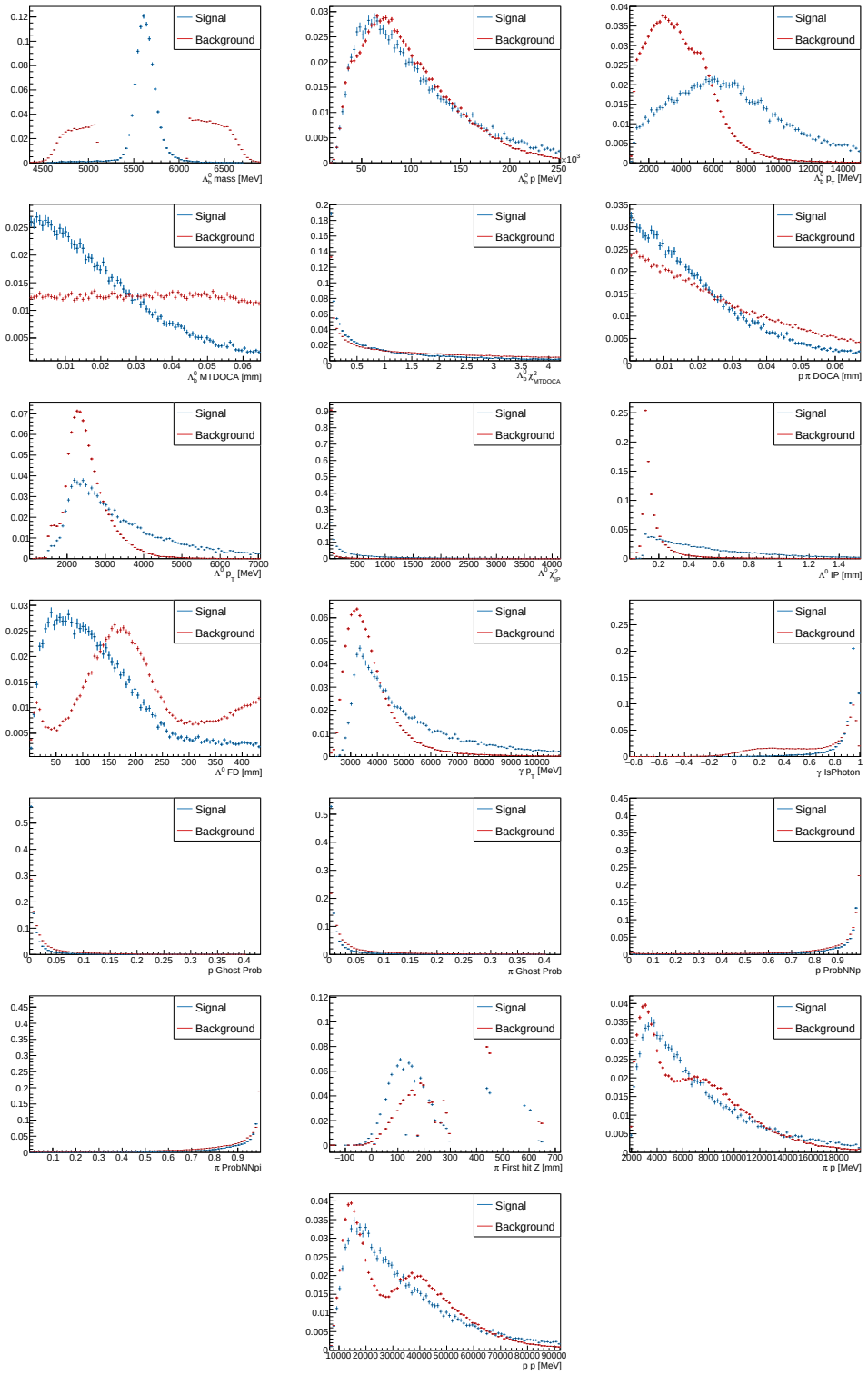

Figure A.1: Distribution of the $\Lambda_b^0 \to \Lambda\gamma$ candidates satisfying the stripping and trigger requirements for the variables used in the Preselection. The MC signal appears in blue, while the background from data side-bands is represented in red.

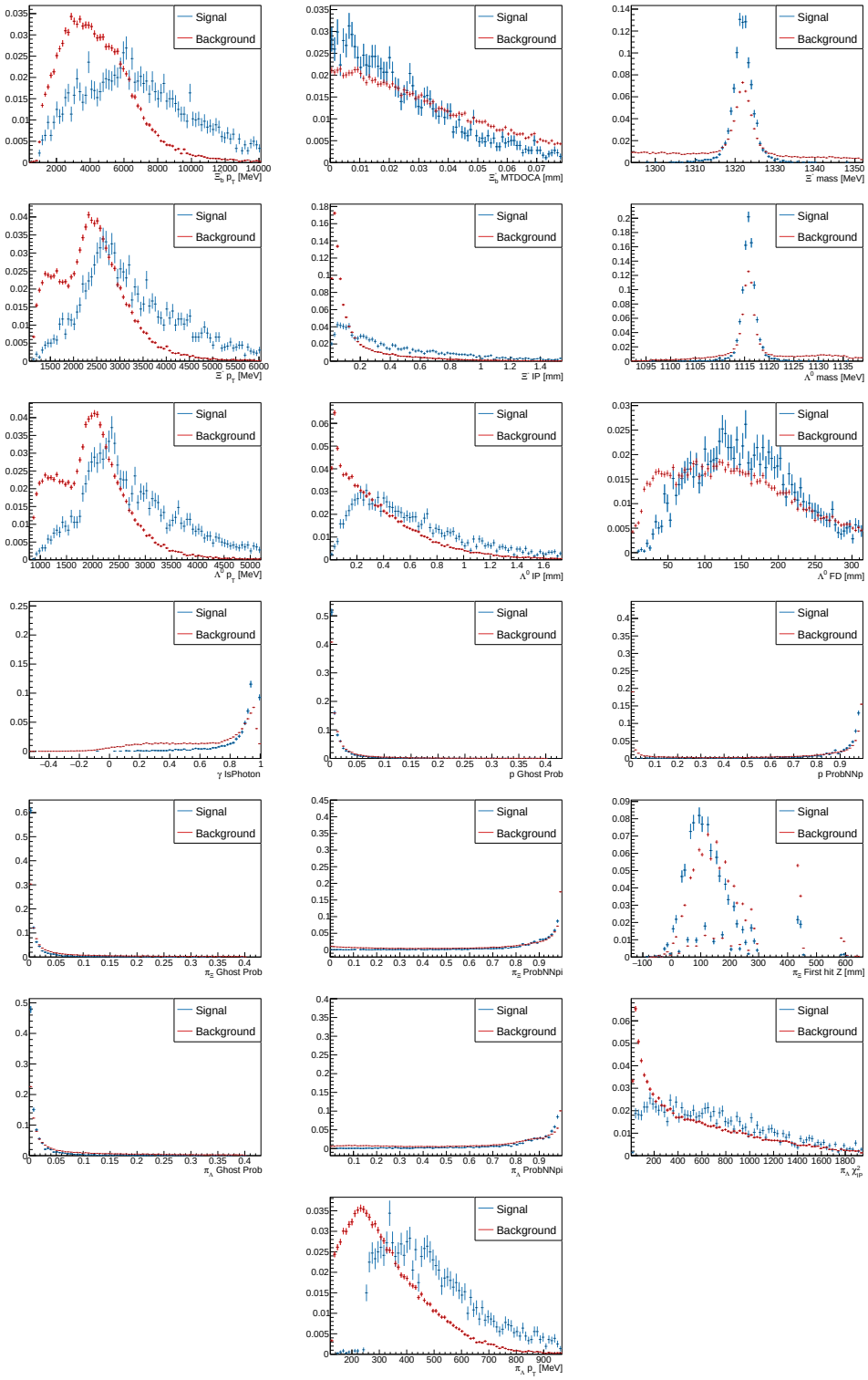

Figure A.2: Distribution of the $\Xi_b^- \to \Xi^-\gamma$ LLL candidates satisfying the stripping and trigger requirements for the variables used in the Preselection. The MC signal appears in blue, while the background from data side-bands is represented in red.

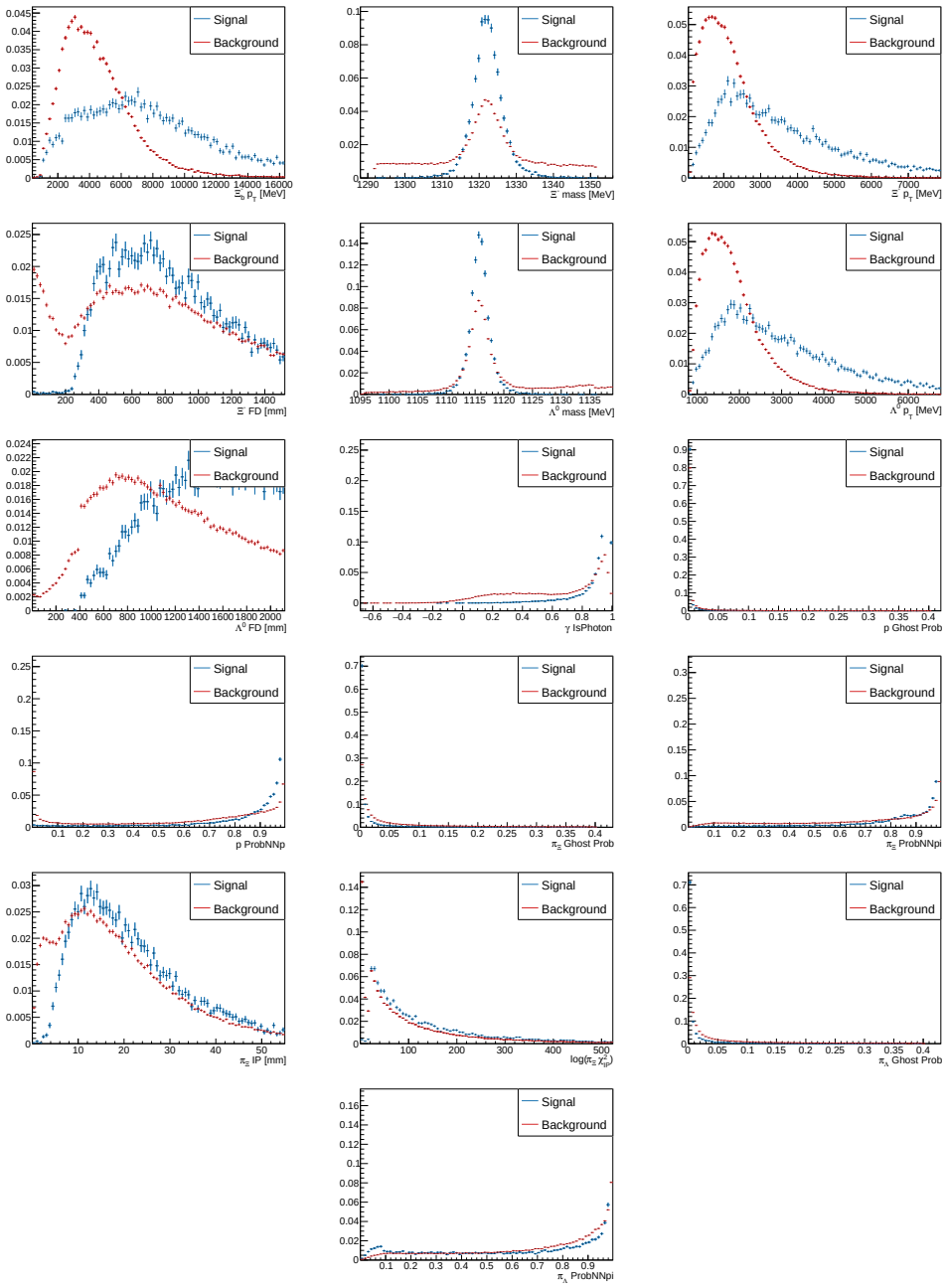

Figure A.3: Distribution of the $\Xi_b^- \to \Xi^-\gamma$ DDL candidates satisfying the stripping and trigger requirements for the variables used in the Preselection. The MC signal appears in blue, while the background from data side-bands is represented in red.

Downstream tracks (DDD) can be seen in Figure A.4. The candidates are required to fulfill the stripping and trigger requirements.

A.2 Agreement between simulation and data

A.2.1 $\Lambda_b^0 \to \Lambda\gamma$

The comparison between the distributions of simulated signal before and after the reweighting with the distribution of data s-weighted candidates for the $\Lambda_b^0 \to \Lambda J/\psi$ can be seen in Figure A.5.

A.2.2 Photon

The comparison between the distributions of simulated signal with the distribution of data s-weighted candidates for the $B^0 \to K^*\gamma$ can be seen in Figure A.6. Since the decay head is not a b-baryon, no reweighting is applied.

A.2.3 $\Xi_b^- \to \Xi^-\gamma$

The comparison between the distributions of simulated signal before and after the reweighting with the distribution of data s-weighted candidates for the $\Xi_b^- \to \Xi^- J/\psi$ can be seen in Figure A.7.

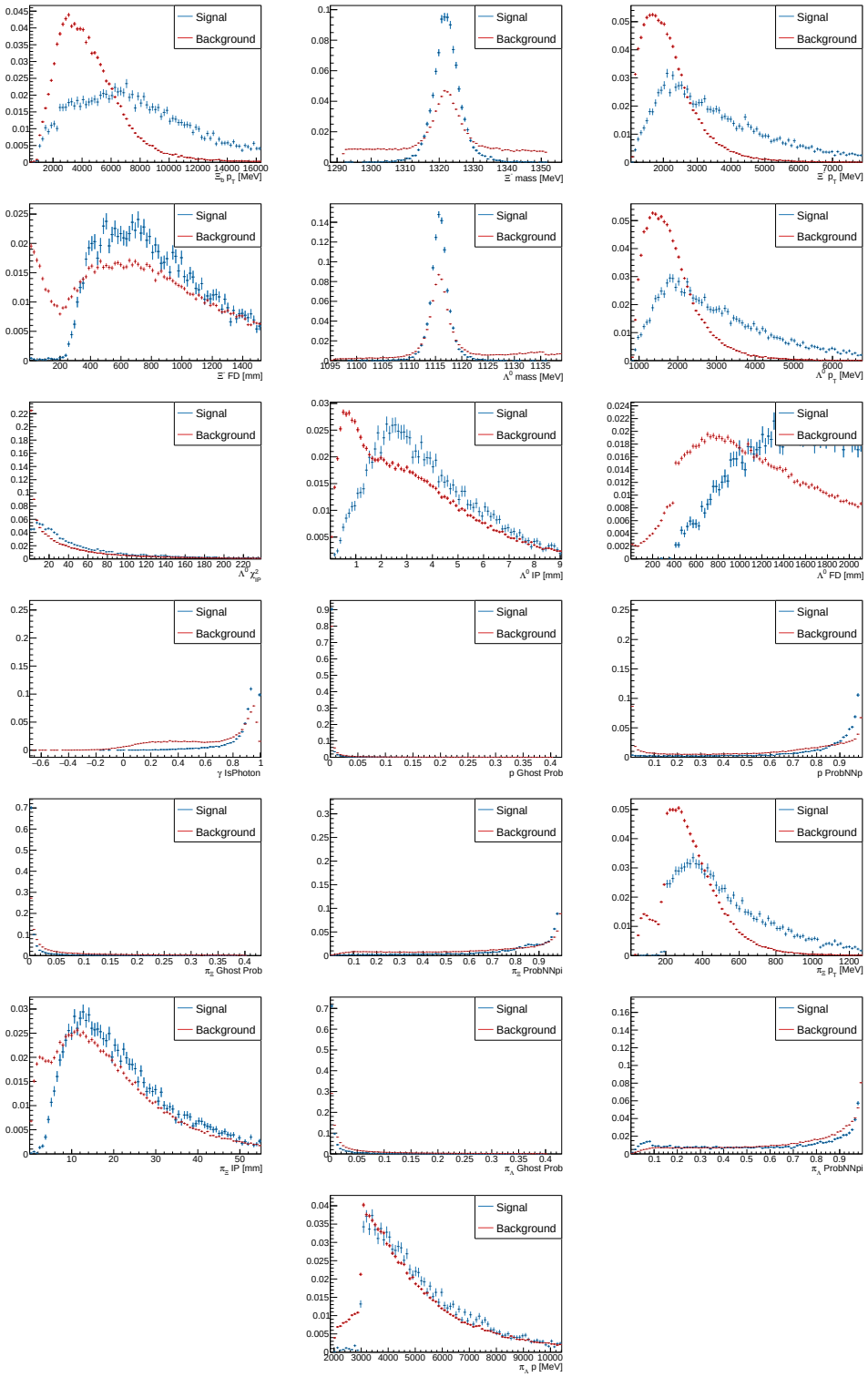

Figure A.4: Distribution of the $\Xi_b^- \to \Xi^-\gamma$ DDD candidates satisfying the stripping and trigger requirements for the variables used in the Preselection. The MC signal appears in blue, while the background from data side-bands is represented in red.

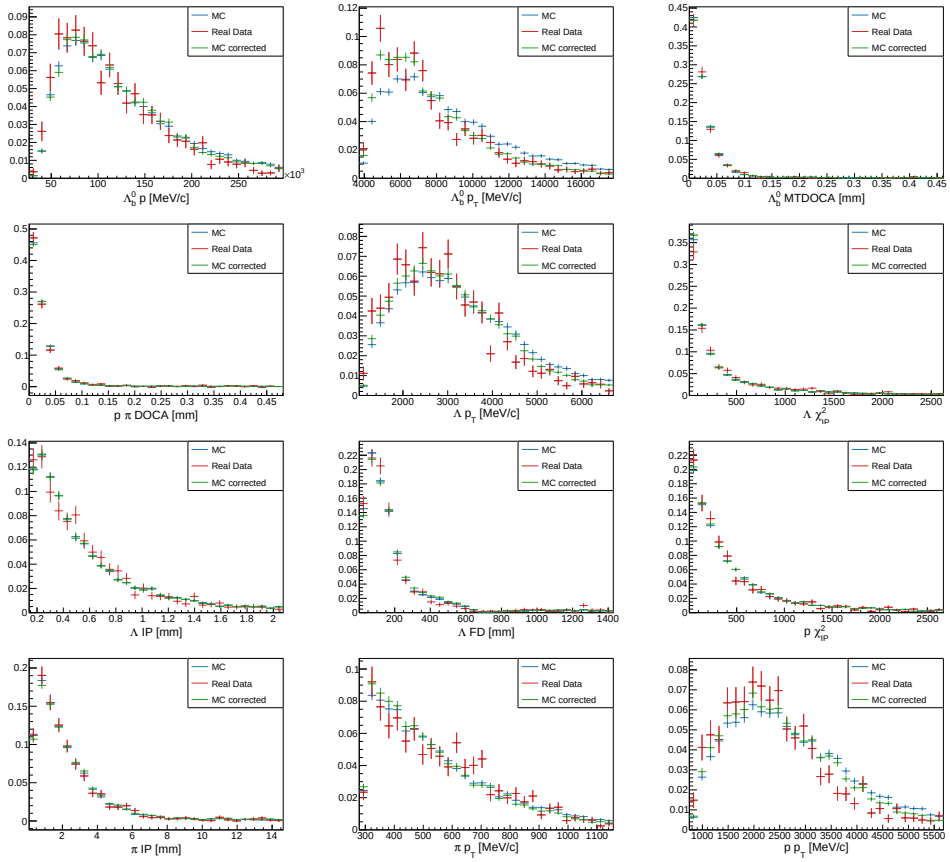

Figure A.5: Distributions from $\Lambda_b^0 \to \Lambda J/\psi$ s-weighted data (red), MC (blue) and corrected MC (green).

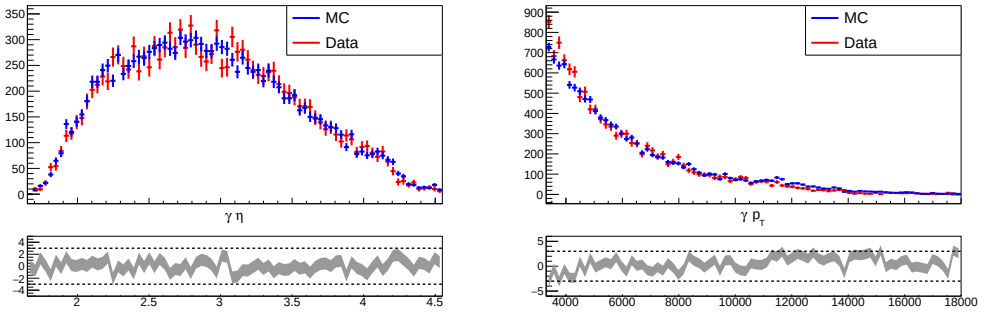

(a) (b)

Figure A.6: (a) Photon pseudorapidity and (b) transverse momentum distributions from $B^0 \to K^*\gamma$ s-weighted data (red) and MC (blue).

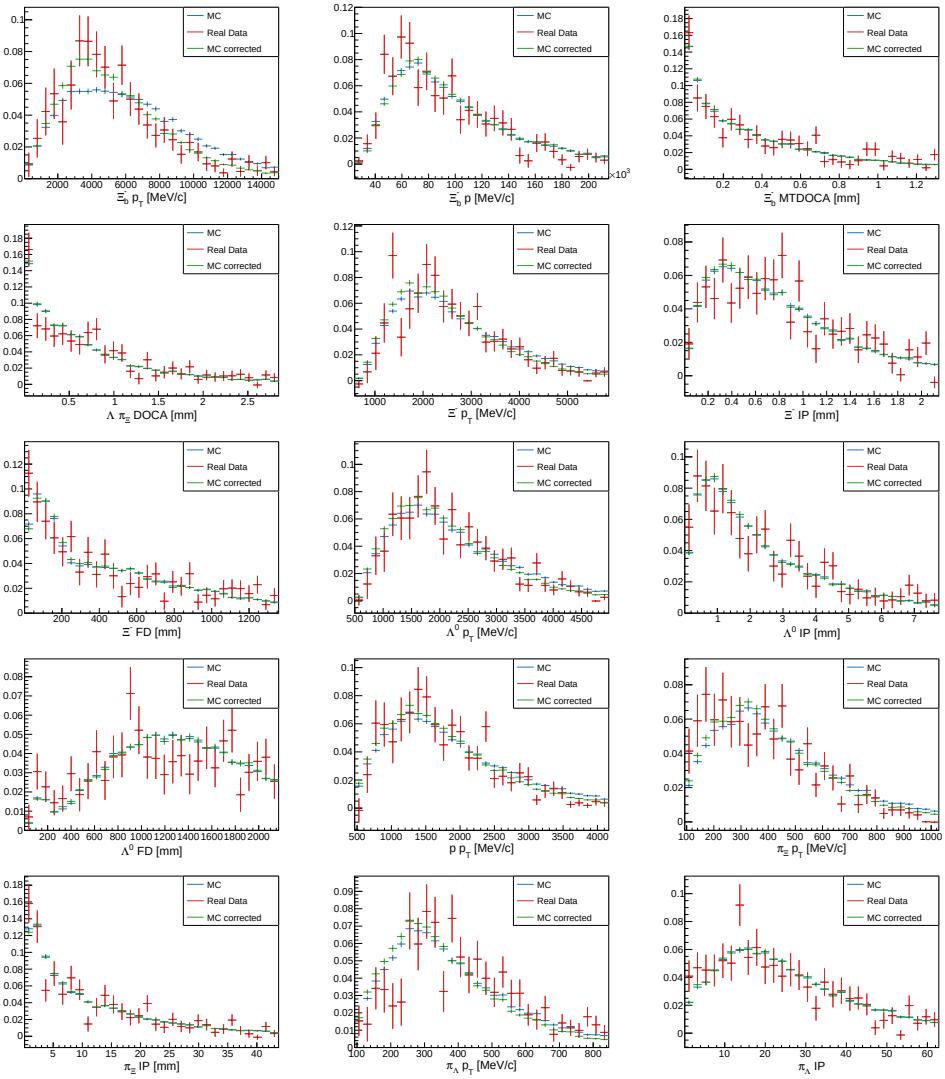

Figure A.7: Distributions from $\Xi_b^- \to \Xi^- J/\psi$ s-weighted data (red), MC (blue) and corrected MC (green).

Resumen

R.1 Introducción

El Modelo Estándar (ME) de la física de partículas es el marco teórico actual que describe la partículas elementales y su interacción con tres de las cuatro fuerzas fundamentales. El éxito del ME radica en que ha sido capaz de explicar la mayor parte de los fenómenos físicos observados hasta la fecha, e incluso ha hecho predicciones muy precisas que han concordado con los resultados de medidas posteriores. Sin embargo, el ME falla al incorporar algunos fenómenos observados, como la oscilación de neutrinos, la gravedad, la materia oscura y la energía oscura, entre otros. Debido a esto, los esfuerzos actuales de los experimentos de física de partículas se centran en encontrar desviaciones de la predicciones del ME, lo cuál sería una pista de las piezas que faltan para completarlo. Este tipo desviaciones se conocen como Nueva Física (NF). Una forma de búsqueda consiste en el estudio de procesos de interacción electrodébil que ocurren a nivel bucle. Dentro de este bucle podrían aparecer nuevas partículas virtuales a escalas de energía menores de su umbral de producción. De especial interés son los procesos que involucran corrientes neutras con cambio de sabor (FCNC[1]), que están Cabibo suprimidas y sólo ocurren a nivel bucle. Esto elimina las contribuciones del ME a nivel árbol, haciendo que los posibles efectos de NF sean comparables a los del ME.

El trabajo realizado en esta tesis se centra entorno a la transición $b \to s\gamma$, siendo una FCNC mediada por el bosón W, como muestra la Figura R.1 (iz-

[1]Por sus siglas en inglés, provenientes de *Flavor Changing Neutral Current*.

quierda). El ME predice que el fotón producido en esta transición tendrá una polarización principalmente levógira. Sin embargo, partículas de NF podrían entrar en el bucle y alterar la dinámica del proceso, como se ve en la Figura R.1 (derecha), cambiando la polarización del fotón.

La polarización del fotón de esta transición ha sido medida anteriormente usando desintegraciones de mesones compuestos por un quark b (b-mesones). Por otro lado, aún no se ha realizado ninguna medida de este tipo usando bariones compuestos por un quark b (b-bariones), los cuales proporcionan un acceso limpio a la estructura de helicidad del proceso de interés. Los canales de desintegración $\Lambda_b^0 \to \Lambda\gamma$ y $\Xi_b^- \to \Xi^-\gamma$ se explotan en esta tesis para realizar la medida. El primero fue la primera desintegración radiativa de un b-barion observada, la cuál se produjo recientemente. La desintegración $\Xi_b^- \to \Xi^-\gamma$ aún no ha sido observada, por lo que este es el primer objetivo.

El formalismo de helicidad brinda acceso a la polarización del fotón a través de la distribución angular. Para el caso del canal desintegración $\Lambda_b^0 \to \Lambda\gamma$ esta es:

$$W(\theta_p) \propto 1 - \alpha_\gamma \alpha_\Lambda \cos\theta_p \,, \tag{R.1}$$

donde α_Λ es el parámetro de la desintegración débil $\Lambda \to p\pi$ y $\cos\theta_p$ es el ángulo de helicidad de la distribución. La polarización del fotón (α_γ) esta definida como la diferencia normalizada de las polarizaciones levógira y dextrógira:

$$\alpha_\gamma = \frac{\Gamma(b \to s\gamma_L) - \Gamma(b \to s\gamma_R)}{\Gamma(b \to s\gamma_L) + \Gamma(b \to s\gamma_R)} \tag{R.2}$$

Ya que el modelo estándar predice que los fotones en este proceso tendrán polarización levógira principalmente, se espera que $\alpha_\gamma \simeq 1$. De forma equivalente, la distribución angular del canal de desintegración $\Xi_b^- \to \Xi^-\gamma$ es:

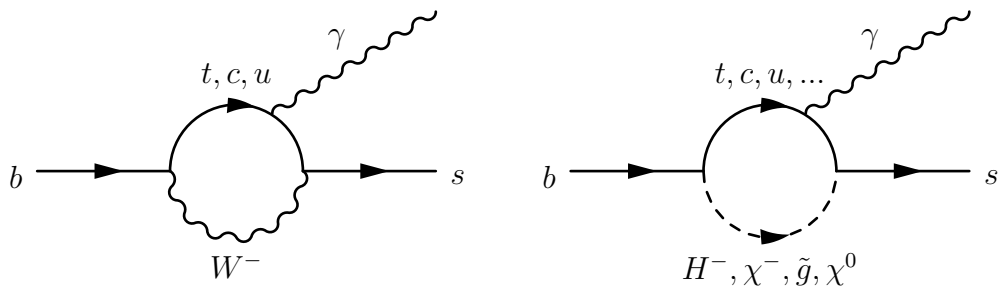

Figura R.1: Diagrama de la transición $b \to s\gamma$, mediado por partículas del Modelo Estándar (izquierda) y por nueva física (derecha).

$$W(\theta_\Lambda, \theta_p) \propto 1 + \alpha_\Lambda \alpha_\Xi \cos\theta_p + \alpha_\gamma \alpha_\Xi \cos\theta_\Lambda + \alpha_\Lambda \alpha_\gamma \cos\theta_p \cos\theta_\Lambda \,. \qquad \text{(R.3)}$$

R.2 El detector LHCb

Para producir los b-bariones descritos en la sección anterior se necesitan alcanzar una escalas de energía elevadas. Para esto, se utilizan grandes dispositivos que aceleran partículas a velocidad cercanas a las de la luz para luego hacerlas colisionar. A día de hoy, el mayor de estos dispositivos del mundo es el Gran Colisionador de Hadrones (LHC[2]), un anillo de 27 km de perímetro, situado a 100 m en el subsuelo en frontera Fraco-Suiza. El LHC ha sido diseñado para colisionar dos haces de protones a una energía nominal de 14 TeV.

Los datos usados en esta tesis han sido recogidos por el detector LHCb, expuesto en la Figura R.2, el cuál es uno de los cuatro experimentos principales del LHC. El LHCb es un espectrómetro frontal de un sólo brazo, optimizado para estudiar desintegraciones de b-hadrones con gran precisión. Los subsistemas que forman el detector LHCb son:

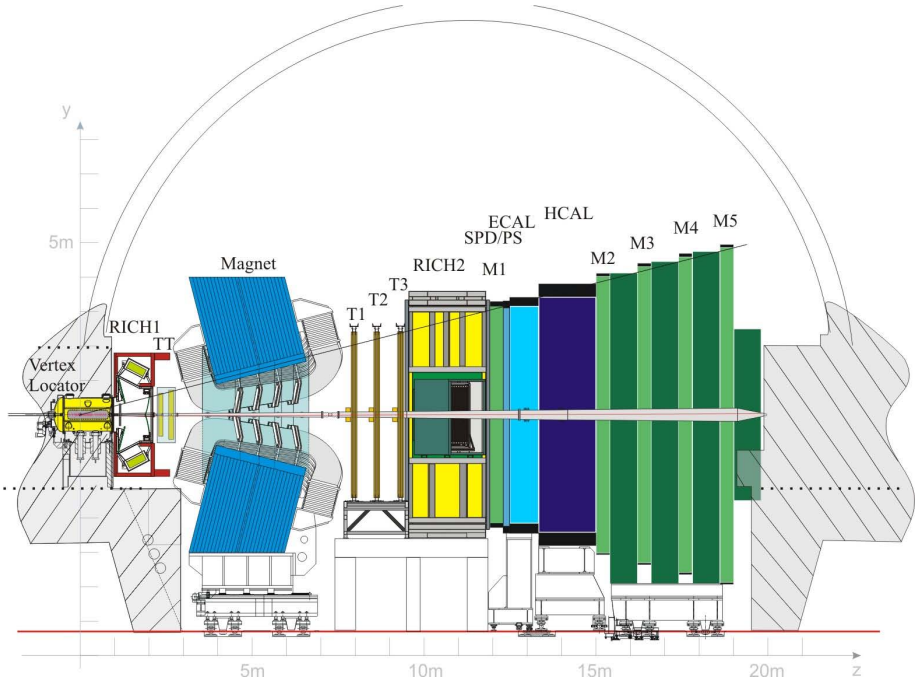

Figura R.2: Esquema de la vista lateral del detector LHCb.

[2]Por sus siglas en ingles, provenientes de *Large Hadron Collider*.

- El **sistema de trazas** sirve para detectar y reconstruir el camino que han seguido las particulas cargadas dentro del detector. Esta compuesto por un detector muy denso cerca del punto de colisión protón-protón (VELO), un potente imán que curva la trayectoria de las partículas en función de su momento, una estación de rastreo antes del imán (TT) y un grupo de tres estaciones después del imán (T Stations). La tecnología usada por la mayor parte del sistemas de trazas consiste en tiras de silicio.

- Dos subdetectores de radiación Cherenkov situados antes del imán (**RICH1**) y después de él (**RICH2**). Estos detectores proporcionan información de la velocidad de una partícula cargada. Esto, en combinación con la información del momento obtenida por el sistema de trazas, permite obtener la masa de una partícula y, por tanto, identificarla.

- Los calorímetros electromagético (**ECAL**) y hadrónico (**HCAL**) miden la energía de partículas electromagnéticas (fotones y electrones) y hadrónicas (piones, protones y kaones), respectivamente. El sistema calorimétrico también está formado por los subdetectores **SPD** y **PS**, separados por una placa de plomo, que aportan mayor grado de diferenciación entre fotones, electrones y piones neutros, ayudando a la identificación.

- Las **cámaras de muones** son estaciones de rastreo situadas en la parte más alejada al punto de colisión protón-protón. Debido a su baja interacción con la materia, únicamente los muones llegarán a las cámaras de muones. Estas permiten identificar con gran precisión a los muones, y aportan mayor resolución a la medida de su momento.

Existe una clasificación para las trayectorias reconstruidas de partículas cargadas en función de los subdetectores del sistema de trazas usados. Los dos tipos más relevantes para el trabajo realizada en esta tesis son:

- **Long**: trayectorias de partículas reconstruidas usando la información de todo el sistema de trazas. Son producidas por partículas originadas dentro del VELO y que recorren todo el detector LHCb.

- **Downstream**: trazas de partículas para las que se ha usado solamente el TT y las T stations para reconstruirla. Son causadas por los productos de desintegración de partículas con larga vida media y que, por tanto, se desintegran despues del VELO.

El funcionamiento del LHCb durante los periodos de toma de datos 2011-2012 (Run I) y 2015-2018 (Run II) ha sido excepcional. Para continuar con esta dinámica, el detector LHCb sufrirá una actualización (Upgrade) en la que se reemplazarán la mayoría de sus componentes por otros más precisos y resistentes a la radiación. Esto permitirá hacer frente al incremento en el número de colisiones protón-protón previstas para el Run III (2021-2024).

R.3 Eficiencias de los algoritmos de reconstrucción de trazas

Los algoritmos de reconstrucción de trazas toman la señal eléctrica de los diferentes subdetectores que conforman el sistema de trazas del LHCb para reconstruir la trayectoria de las partículas que han atravesado el LHCb. Estos algoritmos de reconstrucción de trazas utilizan la técnica del filtro de Kalman y de eliminación de clones. Todo esto proporciona trayectorias reconstruidas únicas y producidas por partículas reales y con una gran resolución espacial y de momento.

La correcta estimación de la eficiencia de estos algoritmos es fundamental para análisis centrados en el cálculo del *branching ratio* (como el presentado en esta tesis). La eficiencia de reconstrucción de trazas puede extraerse usando datos simulados. Sin embargo, la eficiencia calculada de este método es susceptible a errores en el modelado de la simulación, causando discrepancias entre datos reales y simulados. Para identificar y corregir estas diferencias, se recurre a métodos que usan únicamente datos reales. La muestra de datos reales debe ser debidamente seleccionada para obtener una muestra tan pura en señal como sea posible. Como trabajo de esta tesis, se ha desarrollado y usado un método para calcular la eficiencia de reconstrucción de trazas para los productos de desintegración de partículas de larga vida media.

El método desarrollado por el autor de esta tesis se basa en el uso de trazas Long como muestra de calibración para los algoritmos de reconstruc-

ción de trazas Downstream. El método consiste en ejecutar los algoritmos de reconstrucción de trazas Long y Downstream, permitiendo la existencia de duplicados (trazas reconstruidas como Long y como Downstream). Las trazas Downstream no duplicadas se les llama Downstream "realesz son descartadas, mientras que a las duplicadas se las conoce como Downstream "falsas". Una aplicación de este método a un caso particular puede verse en la Figura R.3. De esta forma, la eficiencia de los algoritmos de reconstrucción de

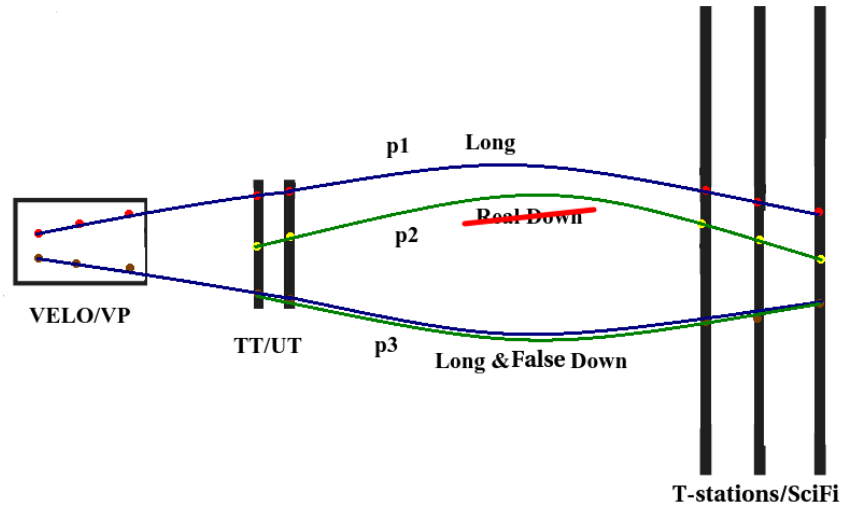

Figura R.3: Esquema del método en el que se muestra una traza Long, una traza Downstream "realz una traza Downstream "falsa."sociada a la traza Long.

trazas Downstream se extrae como:

$$\epsilon = \frac{N_{FD}}{N_L}\,, \tag{R.4}$$

donde N_{FD} es el número de trazas Downstream "falsas"(trazas Downstream que son subtrazas de una traza Long) y N_L es el número de trazas reconstruidas como Long. En el caso ideal de que los algoritmos fuesen perfectos, cualquier traza Long debería poder ser reconstruida también como Downstream, ya que cuenta con la información necesaria para ello.

Este método se ha usado con varias muestras de datos simulados y reales con diferentes condiciones. Los resultados pueden verse reflejados en la tabla R.1.

	Efficiencia (%)	
	Este método	Método de simulación
Simulación Run II	**77,4 ± 0,8**	74,5 ± 0,3
Datos reales Run II	**76,3 ± 0,5**	-
Datos reales Upgrade	**89,4 ± 0,2**	89,7 ± 0,1 [89]

Cuadro R.1: Eficiencia calculada usando este método para los algoritmos de reconstrucción de trazas Downstream usando datos reales y simulados, en condiciones del Run II y Upgrade. Los resultados se comparan con la eficiencia calculada usando el método tradicional en simulación.

R.4 Reconstrucción de desintegraciones de b-bariones radiativos

Las medidas realizadas en esta tesis utilizan dos canales de desintegración. Por un lado, se estudia el canal $\Lambda_b^0 \to \Lambda\gamma$, con $\Lambda \to p\pi$, mostrado en la Figura R.4. Por otro lado, se utiliza el canal de desintegración $\Xi_b^- \to \Xi^-\gamma$,

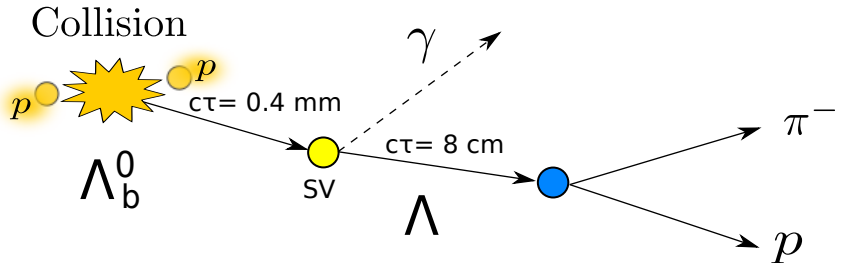

Figura R.4: Topología del canal de desintegración $\Lambda_b^0 \to \Lambda\gamma$.

con $\Xi^- \to \Lambda\pi^-$ y $\Lambda \to p\pi$, como puede verse en la Figura R.5.

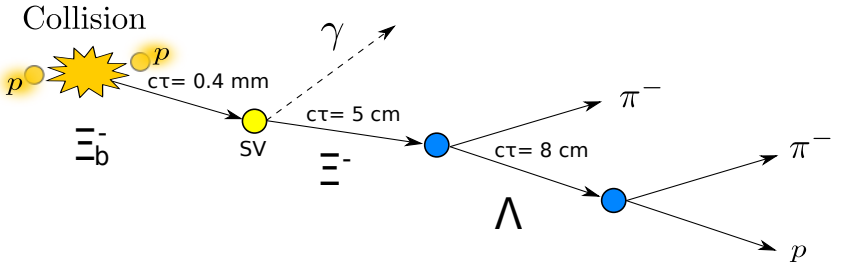

Figura R.5: Topología del canal de desintegración $\Xi_b^- \to \Xi^-\gamma$.

En ambos casos, su reconstrucción se basa en la búsqueda de dos hadrones

compatible con la hipótesis de masa de un pión y un protón que apunten a un vértice común desplazado del punto de colisión protón-protón. Esto forma un candidato a Λ que, en la caso de la desintegración $\Xi_b^- \to \Xi^-\gamma$, se combina con un hadrón compatible con la hipotesis de pión en otro vértice desplazado para formar un candidato a Ξ^-. Finalmente, el candidato a Λ o Ξ^- se combina con un fotón de alta energía para proporcionar un candidato a Λ_b^0 o Ξ_b^0, respectivamente. Cabe resaltar que la reconstrucción del canal de desintegración $\Lambda_b^0 \to \Lambda\gamma$ utiliza únicamente trazas Long debido a limitaciones de procesamiento. Por otro lado, todas las combinaciones de trazas Long y Downstream se tienen en cuenta para reconstruir el canal de desintegración $\Xi_b^- \to \Xi^-\gamma$.

La reconstrucción y selección tiene lugar en tres etapas separadas: trigger, stripping y selección offline. El trigger selecciona los eventos potencialmente interesantes al mismo tiempo que los datos son tomados por el detector LHCb. El stripping utiliza los datos ya almacenados y reconstruye el canal de desintegración y lo filtra más aún para disponer de una muestra de datos más manejable. La selección offline es el último paso de filtrado y, al contrario que las anteriores, no está centralizada por el marco del LHCb, sino que es el analista el encargado de desarrollarla y aplicarla.

Como parte del trabajo de la tesis, se desarrollaron estrategias de trigger y stripping para el canal de desintegración $\Xi_b^- \to \Xi^-\gamma$. Estas no existían con anterioridad dado que es la primera vez que se estudia dicho canal. En este análisis, la selección offline se divide en dos etapas: una preselección en la que se aplican cortes rectangulares, y una selección en la que se usa un método multivariado llamado *boosted decision tree* (BDT).

Los canales de desintegración $\Lambda_b^0 \to \Lambda J/\psi$, $\Xi_b^- \to \Xi^- J/\psi$ y $\Lambda_b^0 \to pK^- J/\psi$ también se utilizan para control y normalización. El proceso de control se refiere a buscar y, en caso de ser necesario, corregir diferencias entre las distribuciones de datos reales y simulados. Estas discrepancias pueden ser producidas por imprecisiones en el modelo de simulación. Por otro lado, el proceso de normalización hace referencia a la toma de medidas relativas. En un experimento como el LHCb, en el que no todo el evento originado por la colisión protón-protón es reconstruido, no pueden hacerse medidas absolutas debido a la falta de información. Esto se soluciona efectuando medidas relativas. Los canales de desintegración $\Lambda_b^0 \to \Lambda J/\psi$ y $\Xi_b^- \to \Xi^- J/\psi$ se han

tomado como canales de control debido a la gran similitud con los canales de interés. Esta similitud repercute en cancelaciones en las medidas que reducen la incertidumbre del resultado final. La reconstrucción y selección de los canales de control y normalización sigue el mismo esquema descrito anteriormente. La única diferencia radica en que, para estos canales, la selección offline se limita a una preselección. Debido a la pureza de las muestras, no es necesario la utilización del método multivariado.

R.5 Estudios de sensibilidad a la polarización del fotón

Uno de los objetivos de esta tesis es el de realizar la primera medida de la polarización del fotón (α_γ) en desintegraciones de b-bariones radiativos. Previamente es necesario realizar un estudio de la viabilidad de dicha medida usando los datos recogidos por el detector LHCb. Dicho estudio compara la sensibilidad de una medida simultánea de la polarización del fotón y del b-barión, con la precisión de extraer únicamente la polarización del fotón. El estudio de sensibilidad también considera de forma independiente el efecto del tamaño finito de la muestra de señal, la resolución del detector, la aceptancia de la selección y la contribución del fondo. El método usado para calcular la sensibilidad consiste en la generación de 1000 muestras de datos con 1000 eventos de señal cada una salvo contraindicación. A cada una de estas muestras se le realiza un ajuste de la distribución angular teórica considerando los efectos estudiados.

El estudio de la sensibilidad concluye que puede extraerse simultáneamente la polarización del fotón y del b-barion sin que esto suponga un deterioro de la medida del primer observable. La mayor precisión de la polarización del b-barión se alcanza para valores de α_γ cercanos a +1 ó -1. Este hecho sólo se ha comprobado para muestras de 1000 eventos de señal, se espera que la adicción de un observable si suponga un deterioro de la medida global para el caso de muestras pequeñas.

La Figura R.6 muestra la precisión con la que puede medirse la polarización del fotón en función del número de eventos de señal. Dicha precisión es muy similar para los canales de desintegración $\Lambda_b^0 \to \Lambda\gamma$ y $\Xi_b^- \to \Xi^-\gamma$. Unos

1000 eventos de señal para cualquiera de estos canales serían suficientes para realizar un medida competitiva con aquellas producidas por b-factorías.

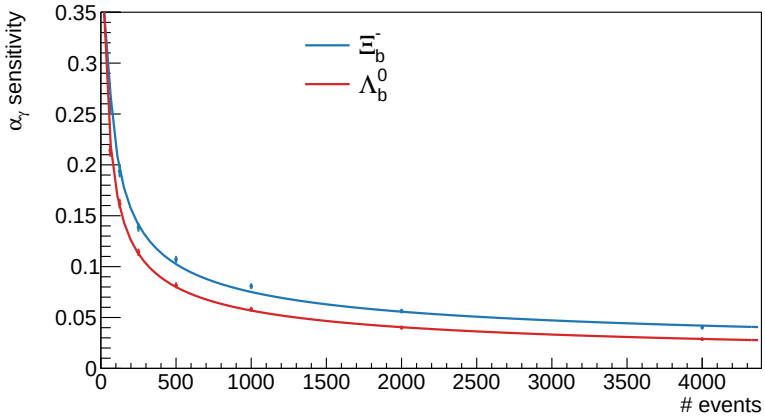

Figura R.6: Sensibilidad a la medida de la polarización del fotón en función del número de eventos de señal para los canales de desintegración $\Lambda_b^0 \to \Lambda\gamma$ (rojo) y $\Xi_b^- \to \Xi^-\gamma$ (azul). La distribución se ajusta a la función $1/\sqrt{N}$ para ver mejor su tendencia.

Los efectos de la resolución del detector y la aceptancia de la selección sobre la sensibilidad a la polarización del fotón pueden verse en la Figura R.7, la sensibilidad estadística también se dibuja para comparar. Este estudio de Monte Carlo concluye que el efecto de la resolución es despreciable en comparación con el efecto del tamaño finito de la muestra y, por lo tanto, el efecto estudiado puede ser despreciado. El efecto de la aceptancia tiene una dependencia asimétrica con α_γ. El caso de una polarización del fotón con un valor cercano al predicho por el ME ($\alpha_\gamma = 1$) es el que aporta mayor sensibilidad a la polarización del fotón debido a la aceptancia para el canal de desintegración $\Xi_b^- \to \Xi^-\gamma$. Por contra, la situación más favorable para esta medida usando el canal de desintegración $\Lambda_b^0 \to \Lambda\gamma$ es $\alpha_\gamma = -1$.

La contribución del fondo se estudia en función de la relación entre el número de eventos de señal y fondo (S/B). Para esto se recurre a la generación y ajuste de 1000 muestras, cada una con 1000 eventos de señal y un número variable de eventos de fondo, dependiendo del S/B estudiado. Este estudio remarca la importancia de obtener una muestra tan pura como sea posible para evitar una degradación severa de la precisión en la medida de la polarización del fotón debido al fondo.

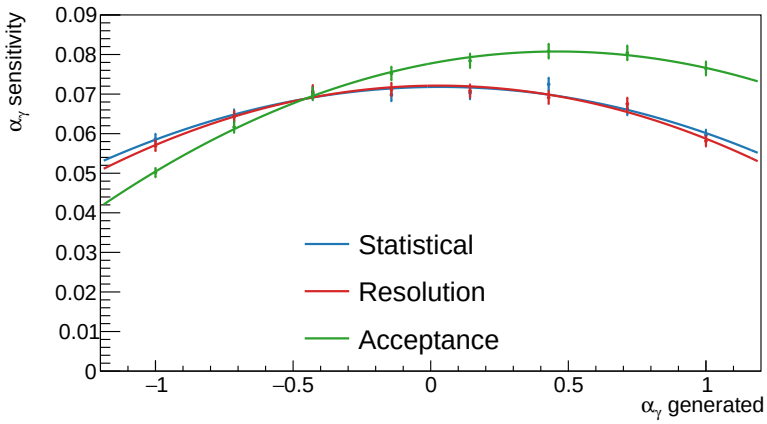

(a)

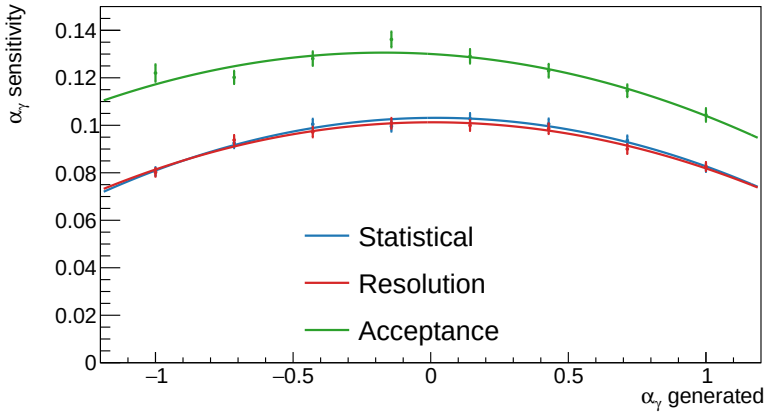

(b)

Figura R.7: Sensibilidad a la medida de la polarización del fotón en función de su valor para los canales de desintegración (a) $\Lambda_b^0 \to \Lambda\gamma$ y (b) $\Xi_b^- \to \Xi^-\gamma$. Se incluyen los efectos de la estadística, la resolución y la aceptancia. Para un mejor entendimiento de la tendencia de estas distribuciones, se añade un polinomio de segundo orden a cada efecto.

R.6 Medida de la fracción de desintegración de canales con b-bariones

Una vez han sido seleccionados los sucesos de interés es posible realizar la medida de la fracción de desintegración de los canales radiativos con b-bariones. En esta tesis, esta medida se realiza mediante un ajuste de masa simultáneo con el canal de interés y el canal de normalización, como se menciona en la sección R.4. El ajuste de masa proporciona el número de eventos de señal en ambos canales, y su fracción esta relacionada con la fracción de fracciones de desintegración de la siguiente forma:

$$\begin{aligned}\mathcal{B}(H_b \to H\gamma) =& \mathcal{B}(H_b \to HJ/\psi) \times \frac{N(H_b \to H\gamma)}{N(H_b \to HJ/\psi)} \\ & \times \mathcal{B}(J/\psi \to \mu^+\mu^-) \times \frac{\epsilon_{sel}(H_b \to HJ/\psi)}{\epsilon_{sel}(H_b \to H\gamma)}\,,\end{aligned} \tag{R.5}$$

donde $\mathcal{B}$ es la fracción de desintegración, N es número de eventos de señal extraídos del ajuste de masa, ϵ_{sel} es la eficiencia de la selección y H hace referencia a Ξ^- o Λ.

Las potenciales fuentes de fondo físico del canal de desintegración $\Xi_b^- \to \Xi^-\gamma$ han sido estudiadas en esta tesis, mientras que para el resto de canales de desintegración dicho estudio se ha tomado de la literatura. Para los cuatro canales no se ha encontrado ninguna fuente de fondo físico relevante. Por lo tanto, la única contribución de fondo que se tiene en cuenta para el ajuste de masas es el combinatorial, principalmente debido a la combinación aleatoria de fotones y bariones del evento subyacente.

El ajuste de masa se valida a través de conjuntos de 1000 pseudo-experimentos, obteniéndose las distribuciones esperadas para los parámetros de ajuste. Una vez validado, el ajuste de masa se realiza a las muestras de datos recogidas por el detector LHCb. Como resultado de dicho ajuste se obtienen 70 eventos del canal de desintegración $\Lambda_b^0 \to \Lambda\gamma$ con 5.6σ de significancia, como puede verse en la Figura R.8. Usando la Ecuación R.5, este resultado se traduce a una fracción de desintegración de $\Lambda_b^0 \to \Lambda\gamma$ de:

$$\mathcal{B}(\Lambda_b^0 \to \Lambda\gamma) = (9{,}0 \pm 1{,}8) \times 10^{-6}\ (\text{stat.})\ \pm 1{,}6\ (\text{syst.}) \pm 3{,}0\ (\text{ext.})\,, \tag{R.6}$$

donde el primer error es estadístico, el segundo es sistemático y el tercero es debido a medidas externas. Para la incertidumbre sistemática se han evalua-

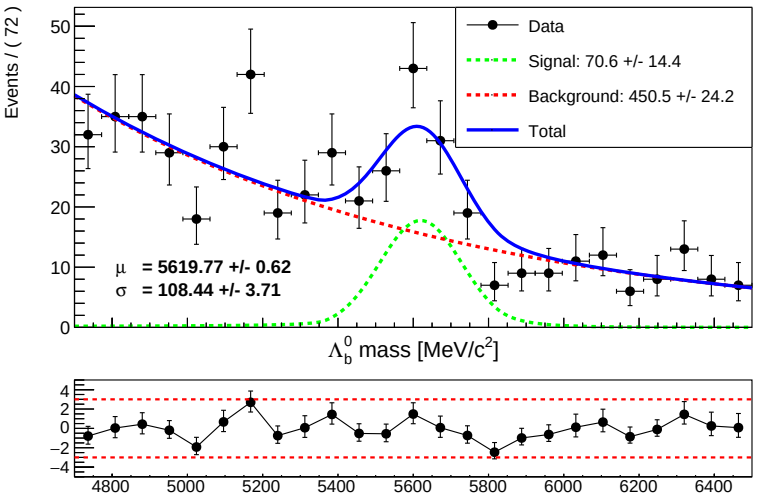

(a)

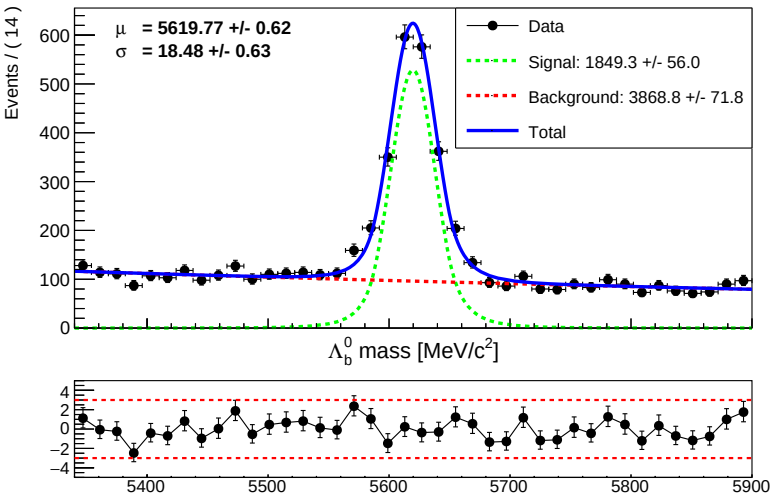

(b)

Figura R.8: Ajuste simultáneo a la distribución masa invariante Λ_b^0 de los canales de desintegración (a) $\Lambda_b^0 \to \Lambda\gamma$ y (b) $\Lambda_b^0 \to \Lambda J/\psi$ para los eventos de datos seleccionados.

do los efectos de elección del modelo para la señal y el fondo, las posibles discrepancias entre simulación de datos y el tamaño finito de las muestras usadas para extraer la eficiencia. La incertidumbre debida a medidas externas está dominada por el error de la medida de la fracción de desintegración del canal $\Lambda_b^0 \to \Lambda\gamma$, medida por los experimentos CDF y D0. Este último error domina actualmente la medida, por lo que este análisis se vería ampliamente beneficiado de una nueva medida de $\mathcal{B}(\Lambda_b^0 \to \Lambda J/\psi)$ realizada por la colaboración LHCb, con más estadística y similares condiciones a las de la medida de $\mathcal{B}(\Lambda_b^0 \to \Lambda\gamma)$.

El ajuste de masa se realiza para el canal de desintegración $\Xi_b^- \to \Xi^-\gamma$ para cada una de las posibles combinaciones de trazas Long y Downstream, y también el conjunto de todas ellas. La Figura R.9 muestra el resultado para la muestra con únicamente trazas Long. La significancia de los ajustes de masa no supera las 3σ para ninguna topología de trazas, por lo tanto no se ha realizado una observación ni existen evidencias de ello. El método del nivel de confianza (CL[3]) se usa para establecer un límite superior a la fracción de desintegración del canal $\Xi_b^- \to \Xi^-\gamma$. La Figura R.10 muestra la aplicación del método CL al caso del canal de desintegración $\Xi_b^- \to \Xi^-\gamma$ reconstruido solamente con trazas Long.

Debido a la baja presencia de fondo, esta muestra es la que permite establecer el límite superior más bajo, con un valor de:

$$\mathcal{B}(\Xi_b^- \to \Xi^-\gamma) < 1{,}7 \times 10^{-4}\ (95\,\%\ \mathrm{CL}) \tag{R.7}$$

Las incertidumbres consideradas para el método CL son la estadística, la sistemática debido al tamaño finito de las muestras empleadas para calcular la eficiencia de la selección, y la debida a medidas externas. La incertidumbre dominante es debida a la precisión con la que se conoce $\mathcal{B}(\Xi_b^- \to \Xi^- J/\psi)$. Esta medida fue realizada por las colaboraciones CDF y D0, una actualización de dicho valor por la colaboración LHCb mejoraría el límite superior establecido en esta tesis.

Esta tesis es la primera que realiza el análisis del canal de desintegración $\Xi_b^- \to \Xi^-\gamma$ y contribuye a extender el programa de física de la colaboración LHCb. Además, este resultado constituye el primer límite superior establecido para la fracción de desintegración del canal $\Xi_b^- \to \Xi^-\gamma$.

[3]Por sus siglas en ingles, provenientes de *confidence level*.

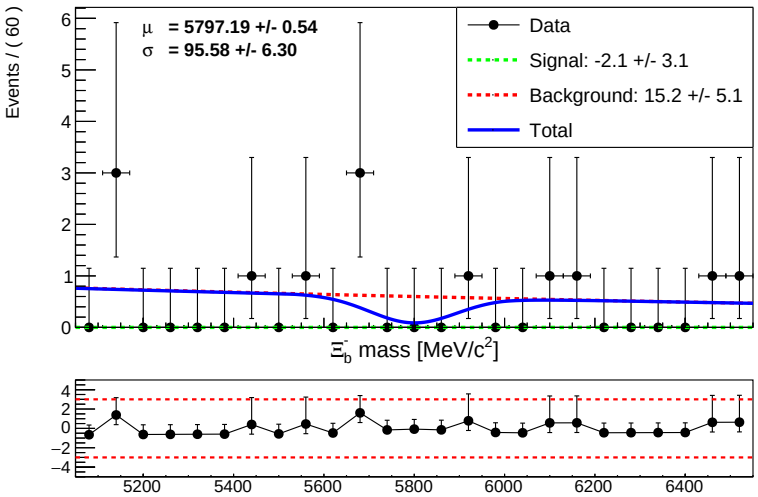

(a)

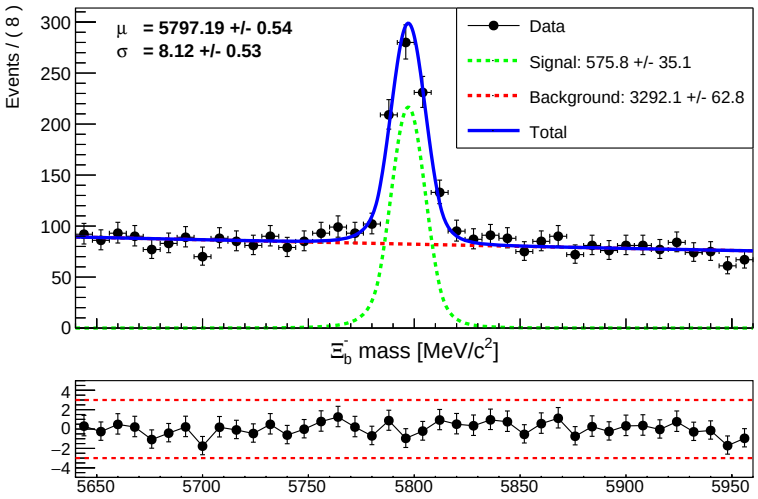

(b)

Figura R.9: Ajuste simultáneo a la distribución masa invariante Ξ_b^- de los canales de desintegración (a) $\Xi_b^- \to \Xi^-\gamma$ and (b) $\Xi_b^- \to \Xi^- J/\psi$ para los eventos de datos seleccionados con trazas Long.

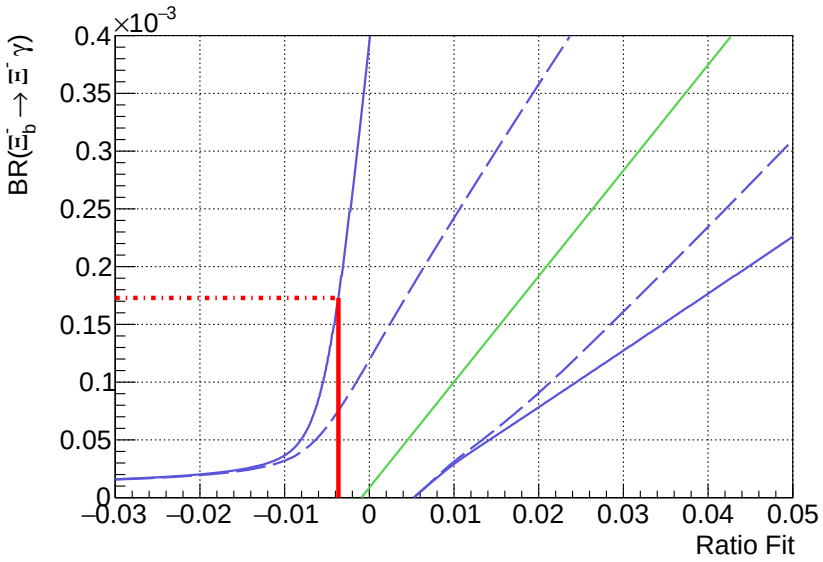

Figura R.10: Cinturón de confianza de Neyman mostrando el límite superior para $\mathcal{B}(\Xi_b^- \to \Xi^-\gamma)$ en función de la fracción $\frac{N(\Xi_b^- \to \Xi^-\gamma)}{N(\Xi_b^- \to \Xi^- J/\psi)}$ medida, donde el canal de desintegración $\Xi_b^- \to \Xi^-\gamma$ se ha reconstruido usando únicamente trazas Long. La línea verde relaciona el valor de la fracción de eventos medida y la fracción de desintegración, la línea azul punteada es el cinturón de Neyman considerando sólo la incertidumbre estadística, mientras que para la líea azul continua se consideran también los errores sistemáticos y de medidas externas. La linea roja se corresponde con la medida realizada en esta tesis.

R.7 Medida de la polarización del fotón en el canal $\Lambda_b^0 \to \Lambda\gamma$

La polarización del fotón se mide usando los eventos de señal hallados en la muestra de datos del canal de desintegración $\Lambda_b^0 \to \Lambda\gamma$. Para maximizar la pureza de la muestra, se consideran sólo aquellos eventos con una masa invariante reconstruida en el rango [5460, 5780] Mev/c^2. Este rango corresponde a 1.5 veces la anchura de la distribución gausiana obtenida en el ajuste de masa, y cuenta con 57 ± 11 eventos de señal y 70 ± 4 eventos de fondo.

La medida de la polarización del fotón se extrae de un ajuste a la distribución angular de helicidad con el siguiente modelo:

$$\Gamma_{\Lambda_b}(\theta_p; \boldsymbol{\alpha_\gamma}) = \frac{S}{S+B} \times \Big(1 - \boldsymbol{\alpha_\gamma}\alpha_\Lambda \cos\theta_p\Big) \times \mathcal{A}(\theta_p) + \frac{B}{S+B} \times f_B(\theta_p)\,, \quad \text{(R.8)}$$

donde $\mathcal{A}$ es la función que describe la aceptancia angular, f_B es la función que modeliza la distribución angular del fondo, y $\frac{S}{S+B}$ y $\frac{B}{S+B}$ son las fracciones de señal y fondo respectivamente. El modelo de la aceptancia angular se extrae de la simulación. La bondad del modelo de la aceptancia en simulación se comprueba comparándolo con la aceptancia de datos usando los canales $\Lambda_b^0 \to \Lambda J/\psi$, para la parte hadrónica de la desintegración, y $B_s^0 \to \phi\gamma$, para la parte radiativa. Se encuentra un buen acuerdo entre las distribuciones angulares usando datos y simulación, por lo que se asume que la aceptancia está bien reproducida. La distribución angular del fondo se obtiene de candidatos en la región de señal ([5460, 5780] Mev/c^2) de la muestra de datos, que cumplan los requisitos de *trigger*, *stripping* y preselección. Las contribuciones de señal en esta muestra se eliminan imponiendo un corte inverso en la BDT, es decir, que el candidato tiene mayor probabilidad de ser fondo que señal según el método multivariado. Este modelo se compara con la distribución obtenida excluyendo la región de señal para candidatos cumpliendo la selección completa. Ambas distribuciones son compatibles entre sí considerando los errores estadísticos. La información de número de eventos de señal y fondo procedente del ajuste de masa se usa imponiendo una restricción gausiana a la fracción de señal en el ajuste angular.

El ajuste angular se valida para varios valores la polarización del fotón en su rango físico [-1, 1] usando conjuntos de 10000 pseudo-experimentos.

El resultado del ajuste a la muestra de datos del canal de desintegración $\Lambda_b^0 \to \Lambda\gamma$ puede verse en la Figura R.11. De este ajuste, se obtiene el

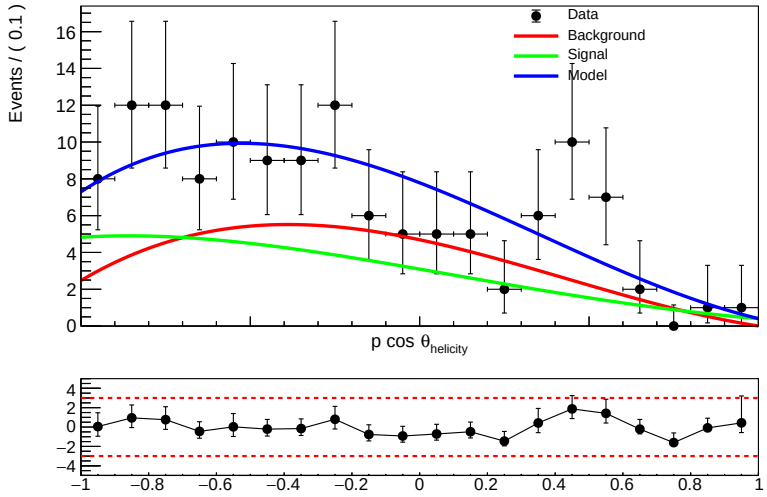

Figura R.11: Ajuste a la distribución angular de helicidad para los candidatos seleccionados del canal de desintegración $\Lambda_b^0 \to \Lambda\gamma$ en la región de señal.

siguiente valor para la polarización del fotón:

$$\alpha_\gamma = 0{,}81 \pm 0{,}45 \text{ (stat.)} \pm 0{,}09 \text{ (syst.)} \pm 0{,}07 \text{ (ext.)} \ , \qquad \text{(R.9)}$$

donde el primer error es estadístico, el segundo es sistemático y el tercero es debido a la medidas externas. Las fuentes de incertidumbre sistemática que se han tenido en cuenta son la elección del modelo de la aceptancia y el fondo, el tamaño finito de la muestra para determinar los parámetros del modelo de la aceptancia y el fondo, y el número finito de pseudo-experimentos realizados. Las fuentes de incertidumbre externas se reducen a la precisión con que se conoce el parámetro de desintegración débil α_Λ.

Este resultado constituye la primera medida de la polarización del fotón usando desintegraciones radiativas de b-bariones. Las medidas usando b-bariones en lugar de b-mesones se ven afectadas por distintos factores de forma, por lo que aportan restricciones independientes al parámetro $C_7^{\prime NP}$. Las restricciones a dicho parámetro usando medidas anteriores y las realizadas en esta tesis pueden verse en la Figura R.12.

El análisis de la polarización del fotón realizado en esta tesis usa datos tomados por el detector LHCb durante el 2016. Recientemente pasaron a

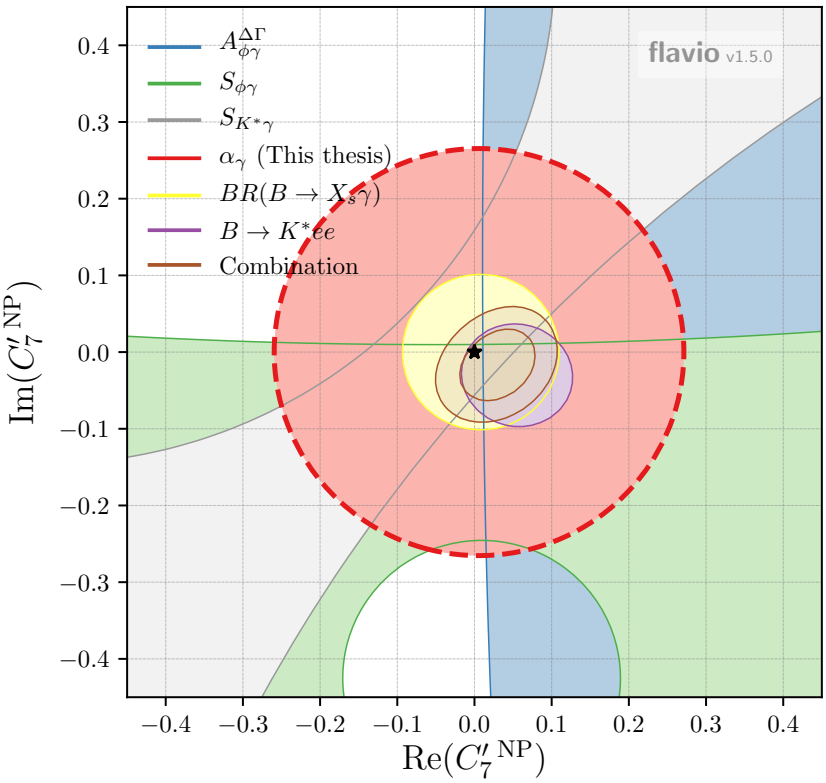

Figura R.12: Restricciones en el plano complejo del parámetro $C_7'^{NP}$ para todas las medidas de desintegraciones radiativas, incluyendo los resultados de esta tesis.

estar disponibles los datos tomados durante todo el Run II (2015-2018). El uso de dichos datos con las estrategias descritas en esta tesis permitirían reducir la incertidumbre estadística, y aportar medidas competitivas de la polarización del fotón. El programa del LHCb se extiende más allá, y se realizará una nueva toma de datos durante el Run III para la cuál el detector LHCb será actualizado, como se describe en la sección R.2. Durante el Run III no sólo aumentará el tamaño de la muestra de datos, sino que los nuevos y mejorados subsistemas del LHCb serán más precisos, reduciendo también la incertidumbre estadística de la medida.

Bibliography

[1] W. N. Cottingham and D. A. Greenwood. "An Introduction to the Standard Model of Particle Physics", 2nd ed. Cambridge University Press, 2007 (Cited on page 1).

[2] ATLAS Collaboration, G. Aad et al. "Observation of a new particle in the search for the Standard Model Higgs boson with the ATLAS detector at the LHC", *Phys. Lett.* B716 (2012), pp. 1–29. arXiv: 1207.7214 [hep-ex] (Cited on page 1).

[3] CMS Collaboration, S. Chatrchyan et al. "Observation of a new boson at a mass of 125 GeV with the CMS experiment at the LHC", *Phys. Lett.* B716 (2012), pp. 30–61. arXiv: 1207.7235 [hep-ex] (Cited on page 1).

[4] M. E. Peskin and D. V. Schroeder. "An introduction to quantum field theory", Boulder, CO: Westview, 1995. URL: https://cds.cern.ch/record/257493 (Cited on page 1).

[5] Wikimedia Commons. *File:Standard Model of Elementary Particles.svg*. 2006. URL: https://commons.wikimedia.org/wiki/File:Standard_Model_of_Elementary_Particles.svg (Cited on page 2).

[6] P. A. M. Dirac. "The Quantum Theory of the Emission and Absorption of Radiation", *Proceedings of the Royal Society of London. Series A, Containing Papers of a Mathematical and Physical Character* 114.767 (1927), pp. 243–265. URL: https://doi.org/10.1098/rspa.1927.0039 (Cited on page 2).

[7] C. Quigg. "The Electroweak Theory", (2002). eprint: arXiv:hep-ph/0204104 (Cited on page 3).

[8] A. Salam and J. C. Ward. "Electromagnetic and weak interactions", *Phys. Lett.* 13 (1964), pp. 168–171 (Cited on page 3).

[9] S. Weinberg. "A Model of Leptons", *Phys. Rev. Lett.* 19 (1967), pp. 1264–1266 (Cited on page 3).

[10] S. L. Glashow. "Partial-symmetries of weak interactions", *Nuclear Physics* 22.4 (1961), pp. 579–588. URL: http://www.sciencedirect.com/science/article/pii/0029558261904692 (Cited on page 3).

[11] V. Barger and R. J. N. Phillips. *Collider Physics 1993*. 1993. eprint: arXiv:hep-ph/9309250 (Cited on page 3).

[12] J. Greensite. "An introduction to the confinement problem", *Lect. Notes Phys.* 821 (2011), pp. 1–211 (Cited on page 3).

[13] LHCb Collaboration. "Observation of $J/\psi\phi$ Structures Consistent with Exotic States from Amplitude Analysis of $B^+ \to J/\psi\phi K^+$ Decays", *Phys. Rev. Lett.* 118 (2 Jan. 2017), p. 022003. URL: https://link.aps.org/doi/10.1103/PhysRevLett.118.022003 (Cited on page 3).

[14] LHCb Collaboration. "Observation of a Narrow Pentaquark State, $P_c(4312)^+$, and of the Two-Peak Structure of the $P_c(4450)^+$", *Phys. Rev. Lett.* 122 (22 June 2019), p. 222001. URL: https://link.aps.org/doi/10.1103/PhysRevLett.122.222001 (Cited on page 3).

[15] P. W. Higgs. "Broken Symmetries and the Masses of Gauge Bosons", *Phys. Rev. Lett.* 13 (1964), pp. 508–509 (Cited on page 3).

[16] F. Englert and R. Brout. "Broken Symmetry and the Mass of Gauge Vector Mesons", *Phys. Rev. Lett.* 13 (1964), pp. 321–323 (Cited on page 3).

[17] C. Quigg. "Gauge Theories Of The Strong, Weak And Electromagnetic Interactions", *Front. Phys.* 56 (1983), pp. 1–334 (Cited on page 4).

[18] Planck Collaboration. "Planck 2013 results. I. Overview of products and scientific results", *A&A* 571 (2014), A1. URL: https://doi.org/10.1051/0004-6361/201321529 (Cited on page 4).

[19] N. Cabibbo. "Unitary Symmetry and Leptonic Decays", *Phys. Rev. Lett.* 10 (12 June 1963), pp. 531–533 (Cited on page 5).

[20] M. Kobayashi and T. Maskawa. "CP-Violation in the Renormalizable Theory of Weak Interaction", *Progress of Theoretical Physics* 49.2 (1973), p. 652 (Cited on page 5).

[21] L. Wolfenstein. "Parametrization of the Kobayashi-Maskawa Matrix", *Phys. Rev. Lett.* 51 (21 Nov. 1983), pp. 1945–1947 (Cited on page 6).

[22] S. Descotes-Genon and P. Koppenburg. "The CKM Parameters", *Annual Review of Nuclear and Particle Science* 67.1 (2017), pp. 97–127. eprint: https://doi.org/10.1146/annurev-nucl-101916-123109. URL: https://doi.org/10.1146/annurev-nucl-101916-123109 (Cited on page 6).

[23] "Roadmap for selected key measurements of LHCb", (2009). arXiv: 0912.4179 [hep-ex] (Cited on page 6).

[24] CKMfitter Group. *Global CKM fit as of Summer 2018*. URL: http://ckmfitter.in2p3.fr/www/html/ckm_results.html (Cited on page 7).

[25] B. Pontecorvo. "Inverse beta processes and nonconservation of lepton charge", *Sov. Phys. JETP* 7 (1958). [Zh. Eksp. Teor. Fiz. 34, 247 (1957)], pp. 172–173 (Cited on page 6).

[26] Z. Maki, M. Nakagawa, and S. Sakata. "Remarks on the unified model of elementary particles", *Prog. Theor. Phys.* 28 (1962), pp. 870–880 (Cited on page 6).

[27] S. L. Glashow, J. Iliopoulos, and L. Maiani. "Weak Interactions with Lepton-Hadron Symmetry", *Phys. Rev. D* 2 (7 Oct. 1970), pp. 1285–1292. URL: https://link.aps.org/doi/10.1103/PhysRevD.2.1285 (Cited on page 8).

[28] K. G. Wilson. "Non-Lagrangian Models of Current Algebra", *Phys. Rev.* 179 (5 Mar. 1969), pp. 1499–1512. URL: https://link.aps.org/doi/10.1103/PhysRev.179.1499 (Cited on page 8).

[29] B. Grinstein et al. "Photon polarization in $B \to X\gamma$ in the standard model", *Phys. Rev. D* 71 (1 Jan. 2005), p. 011504. URL: https://link.aps.org/doi/10.1103/PhysRevD.71.011504 (Cited on page 10).

[30] F.-S. Yu, E. Kou, and C.-D. Lü. "Photon polarization in the $b \to s\gamma$ processes in the left-right symmetric model", *Journal of High Energy Physics* 2013.12 (Dec. 2013), p. 102. URL: https://doi.org/10.1007/JHEP12(2013)102 (Cited on page 10).

[31] L. Everett et al. "Alternative approach to $b \to s\gamma$ in the uMSSM", *Journal of High Energy Physics* 2002.01 (Jan. 2002), pp. 022–022. URL: https://doi.org/10.1088%2F1126-6708%2F2002%2F01%2F022 (Cited on page 10).

[32] D. Atwood, M. Gronau, and A. Soni. "Mixing-Induced CP Asymmetries in Radiative B Decays in and beyond the Standard Model", *Phys. Rev. Lett.* 79 (2 July 1997), pp. 185–188. URL: https://link.aps.org/doi/10.1103/PhysRevLett.79.185 (Cited on page 10).

[33] LHCb Collaboration, R. Aaij et al. "Observation of photon polarization in the $b \to s\gamma$ transition", *Phys. Rev. Lett.* 112.16 (2014), p. 161801. arXiv: 1402.6852 [hep-ex] (Cited on page 11).

[34] LHCb Collaboration, R. Aaij et al. "First experimental study of photon polarization in radiative B_s^0 decays", *Phys. Rev. Lett.* 118.2 (2017). [Addendum: *Phys. Rev. Lett.* 118.10, p.109901 (2017)], p. 021801. arXiv: 1609.02032 [hep-ex] (Cited on page 11).

[35] LHCb Collaboration, R. Aaij et al. "Measurement of CP-Violating and Mixing-Induced Observables in $B_s^0 \to \phi\gamma$ Decays", *Phys. Rev. Lett.* 123 (8 Aug. 2019), p. 081802. URL: https://link.aps.org/doi/10.1103/PhysRevLett.123.081802 (Cited on pages 11, 162).

[36] LHCb Collaboration, R. Aaij et al. "Angular analysis of the $B^0 \to K^{*0}e^+e^-$ decay in the low-q^2 region", *JHEP* 04 (2015), p. 064. arXiv: 1501.03038 [hep-ex] (Cited on pages 11, 163).

[37] Belle Collaboration. "Search for $B_s^0 \to \gamma\gamma$ and a measurement of the branching fraction for $B_s^0 \to \phi\gamma$", *Phys. Rev. D* 91 (1 Jan. 2015),

p. 011101. URL: https://link.aps.org/doi/10.1103/PhysRevD.91.011101 (Cited on page 11).

[38] C. Sanchez Mayordomo. "Measurement of the mixing-induced and CP-violating parameters of $B_s^0 \to \phi\gamma$ decays at LHCb". Presented 02 Jul 2018. June 2018. URL: https://cds.cern.ch/record/2678950 (Cited on page 12).

[39] LHCb Collaboration. "Measurement of b hadron fractions in 13 TeV pp collisions", *Phys. Rev. D* 100 (3 Aug. 2019), p. 031102. URL: https://link.aps.org/doi/10.1103/PhysRevD.100.031102 (Cited on pages 11, 129).

[40] LHCb Collaboration. "First observation of the radiative decay $\Lambda_b^0 \to \Lambda^0\gamma$", *Phys. Rev. Lett.* 123 (3 July 2019), p. 031801. URL: https://link.aps.org/doi/10.1103/PhysRevLett.123.031801 (Cited on pages 11, 58, 66, 117, 124, 129, 161).

[41] A. D. Martin and T. D. Spearman. "Elementary-particle theory", Amsterdam: North-Holland, 1970. URL: https://cds.cern.ch/record/102663 (Cited on page 13).

[42] L. M. García Martín et al. "Radiative b-baryon decays to measure the photon and b-baryon polarization", *The European Physical Journal C* 79.7 (July 2019), p. 634. URL: https://doi.org/10.1140/epjc/s10052-019-7123-7 (Cited on pages 13, 14).

[43] Particle Data Group Collaboration, M. Tanabashi et al. "Review of Particle Physics", *Phys. Rev. D* 98 (3 Aug. 2018), p. 030001. URL: https://link.aps.org/doi/10.1103/PhysRevD.98.030001 (Cited on pages 13, 16, 125, 127, 129, 156).

[44] CMS Collaboration, "Measurement of Λ_b^0 polarization and the angular parameters of the decay $\Lambda_b^0 \to J/\psi\Lambda^0$ ", tech. rep. CMS-PAS-BPH-15-002. Geneva: CERN, 2016. URL: https://cds.cern.ch/record/2204914 (Cited on page 14).

[45] LHCb Collaboration. "Measurements of the $\Lambda_b^0 \to J/\psi\Lambda^0$ decay amplitudes and the Λ_b^0 polarisation in pp collisions at s=7 TeV", *Physics Letters B* 724.1 (2013), pp. 27–35. URL: http://www.sciencedirect.

com/science/article/pii/S0370269313004231 (Cited on pages 14, 79, 101, 124, 149, 150).

[46] L. Evans and P. Bryant. "LHC Machine", *JINST* 3 (2008), S08001 (Cited on page 19).

[47] T. C. accelerator complex. *Facts and figures about the LHC*. URL: https://home.cern/resources/faqs/facts-and-figures-about-lhc (Cited on page 19).

[48] E. Mobs. "The CERN accelerator complex - August 2018. Complexe des accélérateurs du CERN - Août 2018", (Aug. 2018). General Photo. URL: http://cds.cern.ch/record/2636343 (Cited on page 20).

[49] R. Jacobsson. "Future wishes and constraints from the experiments at the LHC for the proton-proton programme. LHC, Large Hadron Collider", arXiv:1410.3663. CERN-LHCb-PROC-2013-029. CERN-ATS-Note-2013-030 PERF. LHCb-PROC-2013-029 (May 2013). ICFA Mini-Workshop on Beam-Beam Effects in Hadron Colliders (BB2013), Cern, Switzerland, 18 - 22 Mar 2013, 167–176. 10 p. URL: http://cds.cern.ch/record/1550768 (Cited on page 21).

[50] LHCb Collaboration. *LHCb Operations Plots Webpage*. URL: https://lbgroups.cern.ch/online/OperationsPlots/index.htm (Cited on page 22).

[51] LHCb Collaboration, C. Elsässer. *$\bar{b}b$ production angle plots*. URL: https://lhcb.web.cern.ch/lhcb/speakersbureau/html/bb%5C_ProductionAngles.html (Cited on page 23).

[52] LHCb Collaboration. "The LHCb Detector at the LHC", *JINST* 3.LHCb-DP-2008-001. CERN-LHCb-DP-2008-001 (2008). Also published by CERN Geneva in 2010, S08005. URL: https://cds.cern.ch/record/1129809 (Cited on pages 23, 33).

[53] LHCb collaboration. *Standard set of performance numbers*. URL: https://lhcb.web.cern.ch/lhcb/speakersbureau/html/PerformanceNumbers.html (Cited on pages 24, 32, 129).

[54] LHCb Collaboration. *VELO Approved Conference Plots*. URL: https://lbtwiki.cern.ch/bin/view/VELO/VELOConferencePlots (Cited on page 25).

[55] LHCb Collaboration. *LHCb Silicon Tracker - Material for Publications*. URL: https://www.physik.uzh.ch/groups/lhcb/public/material/ (Cited on page 27).

[56] LHCb Collaboration. *LHCb magnet: Technical Design Report*. Geneva, 2000. URL: https://cds.cern.ch/record/424338 (Cited on page 28).

[57] LHCb Collaboration. "LHCb inner tracker: Technical Design Report", Technical Design Report LHCb. revised version number 1 submitted on 2002-11-13 14:14:34. Geneva: CERN, 2002. URL: https://cds.cern.ch/record/582793 (Cited on page 29).

[58] The LHCb Outer Tracker group. "Performance of the LHCb Outer Tracker", *Journal of Instrumentation* 9.01 (Jan. 2014), P01002–P01002. URL: https://doi.org/10.1088%2F1748-0221%2F9%2F01%2Fp01002 (Cited on page 29).

[59] LHCb Collaboration, J. C. *ANN PID Retuning*. URL: %7B%5Chref%7Bhttps://indico.cern.ch/event/508832/contributions/2030857/attachments/1249785/1842643/ANNPID-2015TuneV1-30032016.pdf%7D%7D (Cited on page 29).

[60] LHCb Collaboration, M. Adinolfi et al. "Performance of the LHCb RICH detector at the LHC", *Eur. Phys. J. C* 73.arXiv:1211.6759. CERN-LHCb-DP-2012-003. LHCb-DP-2012-003 (Nov. 2012), 2431. 25 p. URL: http://cds.cern.ch/record/1495721 (Cited on page 31).

[61] The LHCb RICH Collaboration et al. "Performance of the LHCb RICH detector at the LHC", *The European Physical Journal C* 73.5 (May 2013), p. 2431. URL: https://doi.org/10.1140/epjc/s10052-013-2431-9 (Cited on page 30).

[62] LHCb Collaboration. "LHCb RICH: Technical Design Report", Technical Design Report LHCb. Geneva: CERN, 2000. URL: https://cds.cern.ch/record/494263 (Cited on page 32).

[63] LHCb Collaboration. "LHCb calorimeters: Technical Design Report", Technical Design Report LHCb. Geneva: CERN, 2000. URL: https://cds.cern.ch/record/494264 (Cited on page 33).

[64] LHCb Collaboration. "LHCb muon system: Technical Design Report", Technical Design Report LHCb. Geneva: CERN, 2001. URL: https://cds.cern.ch/record/504326 (Cited on page 35).

[65] LHCb collaboration. *Trigger Schemes*. URL: http://lhcb.web.cern.ch/lhcb/speakersbureau/html/TriggerScheme.html (Cited on page 36).

[66] G. Corti et al. "Software for the LHCb experiment", *IEEE Transactions on Nuclear Science* 53.3 (June 2006), pp. 1323–1328 (Cited on page 37).

[67] G. Barrand et al. "GAUDI - A software architecture and framework for building HEP data processing applications", *Comput. Phys. Commun.* 140 (2001), pp. 45–55 (Cited on page 37).

[68] LHCb Collaboration, M. Clemencic et al. "The LHCb simulation application, Gauss: Design, evolution and experience", *J. Phys. Conf. Ser.* 331 (2011), p. 032023 (Cited on page 37).

[69] LHCb Collaboration. *The GAUSS project*. URL: http://lhcb-release-area.web.cern.ch/LHCb-release-area/DOC/gauss/ (Cited on page 37).

[70] T. Sjöstrand, S. Mrenna, and P. Skands. "A brief introduction to PYTHIA 8.1", *Computer Physics Communications* 178.11 (2008), pp. 852–867. URL: http://www.sciencedirect.com/science/article/pii/S0010465508000441 (Cited on pages 37, 46).

[71] D. J. Lange. "The EvtGen particle decay simulation package", *Nucl. Instrum. Meth.* A462 (2001), pp. 152–155 (Cited on page 37).

[72] GEANT4 Collaboration, S. Agostinelli et al. "GEANT4: A Simulation toolkit", *Nucl. Instrum. Meth.* A506 (2003), pp. 250–303 (Cited on page 38).

[73] LHCb Collaboration. *The BOOLE project*. URL: http://lhcb-release-area.web.cern.ch/LHCb-release-area/DOC/boole/ (Cited on page 38).

[74] LHCb Collaboration. *The BRUNEL project*. URL: http://lhcb-release-area.web.cern.ch/LHCb-release-area/DOC/brunel/ (Cited on page 38).

[75] LHCb Collaboration. *The MOORE project*. URL: http://lhcb-release-area.web.cern.ch/LHCb-release-area/DOC/moore/ (Cited on page 38).

[76] LHCb Collaboration. *The DAVINCI project*. URL: http://lhcb-release-area.web.cern.ch/LHCb-release-area/DOC/davinci/ (Cited on page 38).

[77] LHCb Collaboration. *The LHCb Public results*. URL: http://lhcbproject.web.cern.ch/lhcbproject/Publications/LHCbProjectPublic/Summary_all.html (Cited on page 39).

[78] LHCb Collaboration. "Framework TDR for the LHCb Upgrade: Technical Design Report", tech. rep. CERN-LHCC-2012-007. LHCb-TDR-12. Apr. 2012. URL: https://cds.cern.ch/record/1443882 (Cited on page 39).

[79] LHCb Collaboration. "LHCb VELO Upgrade Technical Design Report", tech. rep. CERN-LHCC-2013-021. LHCB-TDR-013. Nov. 2013. URL: https://cds.cern.ch/record/1624070 (Cited on page 39).

[80] LHCb Collaboration. "LHCb Tracker Upgrade Technical Design Report", tech. rep. CERN-LHCC-2014-001. LHCB-TDR-015. Feb. 2014. URL: https://cds.cern.ch/record/1647400 (Cited on page 40).

[81] LHCb Collaboration. "LHCb PID Upgrade Technical Design Report", tech. rep. CERN-LHCC-2013-022. LHCB-TDR-014. Nov. 2013. URL: https://cds.cern.ch/record/1624074 (Cited on pages 40, 41).

[82] "LHCb Trigger and Online Upgrade Technical Design Report", tech. rep. CERN-LHCC-2014-016. LHCB-TDR-016. May 2014. URL: https://cds.cern.ch/record/1701361 (Cited on page 41).

[83] J. Albrecht et al. "The upgrade of the LHCb trigger system", *Journal of Instrumentation* 9.10 (Oct. 2014), pp. C10026–C10026. URL: https://doi.org/10.1088%2F1748-0221%2F9%2F10%2Fc10026 (Cited on page 42).

[84] LHCb Collaboration, L. M. Garcia et al. "Tracking performance for long-lived particles at LHCb", *Connecting the Dots and Workshop on Intelligent Trackers*. arXiv: 1910.06171 [hep-ex] (Cited on page 43).

[85] O. Callot. "FastVelo, a fast and efficient pattern recognition package for the Velo", tech. rep. LHCb-PUB-2011-001. CERN-LHCb-PUB-2011-001. LHCb. Geneva: CERN, Jan. 2011. URL: https://cds.cern.ch/record/1322644 (Cited on page 44).

[86] O. Callot and S. Hansmann-Menzemer. "The Forward Tracking: Algorithm and Performance Studies", tech. rep. LHCb-2007-015. CERN-LHCb-2007-015. Geneva: CERN, May 2007. URL: https://cds.cern.ch/record/1033584 (Cited on page 44).

[87] M. De Cian. "Revision of Adding TT Hits to Long Tracks", tech. rep. LHCb-INT-2010-020. CERN-LHCb-INT-2010-020. Geneva: CERN, Apr. 2010. URL: https://cds.cern.ch/record/1259672 (Cited on page 44).

[88] O. Callot and M. Schiller. "PatSeeding: A Standalone Track Reconstruction Algorithm", tech. rep. LHCb-2008-042. CERN-LHCb-2008-042. Geneva: CERN, Aug. 2008. URL: https://cds.cern.ch/record/1119095 (Cited on page 44).

[89] R. Quagliani. "Study of double charm B decays with the LHCb experiment at CERN and track reconstruction for the LHCb upgrade". Presented 06 Oct 2017. Oct. 2017. URL: https://cds.cern.ch/record/2296404 (Cited on pages 44, 55, 179).

[90] M. Needham. "Performance of the Track Matching", tech. rep. LHCb-2007-129. CERN-LHCb-2007-129. Geneva: CERN, Oct. 2007. URL: http://cds.cern.ch/record/1060807 (Cited on page 44).

[91] A. Davis et al. "PatLongLivedTracking: a tracking algorithm for the reconstruction of the daughters of long-lived particles in LHCb", tech. rep. LHCb-PUB-2017-001. CERN-LHCb-PUB-2017-001. Geneva: CERN, Jan. 2017. URL: https://cds.cern.ch/record/2240723 (Cited on page 44).

[92] E. E. Bowen, B. Storaci, and M. Tresch. "VeloTT tracking for LHCb Run II", tech. rep. LHCb-PUB-2015-024. CERN-LHCb-PUB-2015-024. LHCb-INT-2014-040. Geneva: CERN, Apr. 2016. URL: https://cds.cern.ch/record/2105078 (Cited on page 45).

[93] R. E. Kalman. "A New Approach to Linear Filtering and Prediction Problems", *Journal of Basic Engineering* 82.1 (Mar. 1960), pp. 35–45. URL: http://dx.doi.org/10.1115/1.3662552 (Cited on page 45).

[94] P. Billoir. "Track fitting with multiple scattering: A new method", *Nuclear Instruments and Methods in Physics Research* 225.2 (1984), pp. 352–366. URL: http://www.sciencedirect.com/science/article/pii/0167508784902746 (Cited on page 45).

[95] R. Frühwirth. "Application of Kalman filtering to track and vertex fitting", *Nuclear Instruments and Methods in Physics Research Section A: Accelerators, Spectrometers, Detectors and Associated Equipment* 262.2 (1987), pp. 444–450. URL: http://www.sciencedirect.com/science/article/pii/0168900287908874 (Cited on page 45).

[96] LHCb collaboration. "Measurement of the track reconstruction efficiency at LHCb", *Journal of Instrumentation* 10.02 (Feb. 2015), P02007–P02007. URL: https://doi.org/10.1088%2F1748-0221%2F10%2F02%2Fp02007 (Cited on page 46).

[97] M. Bähr et al. "Herwig++ physics and manual", *The European Physical Journal C* 58.4 (Dec. 2008), pp. 639–707. URL: https://doi.org/10.1140/epjc/s10052-008-0798-9 (Cited on page 46).

[98] T. Gleisberg et al. "Event generation with SHERPA 1.1", *JHEP* 02 (2009), p. 007. arXiv: 0811.4622 [hep-ph] (Cited on page 46).

[99] O. Lupton et al. "Calibration samples for particle identification at LHCb in Run 2", tech. rep. LHCb-PUB-2016-005. CERN-LHCb-PUB-2016-005. Geneva: CERN, Mar. 2016. URL: https://cds.cern.ch/record/2134057 (Cited on page 49).

[100] I. M. Belyaev et al. "The calibration of an LHCb electromagnetic calorimeter by recovering the invariant mass of neutral pions", *Moscow University Physics Bulletin* 68.5 (2013), pp. 360–366. URL: https://doi.org/10.3103/S0027134913050032 (Cited on page 59).

[101] LHCb collaboration. "Observation of the suppressed decay $\Lambda_b^0 \to p\pi^-\mu^+\mu^-$", *Journal of High Energy Physics* 2017.4 (Apr. 2017), p. 29. URL: https://doi.org/10.1007/JHEP04(2017)029 (Cited on pages 75, 79).

[102] LHCb Collaboration. "Measurement of the Ξ_b^- and Ω_b^- baryon lifetimes", *Physics Letters B* 736 (2014), pp. 154–162. URL: http://www.sciencedirect.com/science/article/pii/S0370269314004699 (Cited on pages 79, 124).

[103] M. Pivk and F. L. Diberder. "Plots: A statistical tool to unfold data distributions", *Nuclear Instruments and Methods in Physics Research Section A: Accelerators, Spectrometers, Detectors and Associated Equipment* 555.1 (2005), pp. 356–369. URL: http://www.sciencedirect.com/science/article/pii/S0168900205018024 (Cited on page 80).

[104] T. Skwarnicki. "A study of the radiative CASCADE transitions between the Upsilon-Prime and Upsilon resonances". PhD thesis. Cracow, INP, 1986. URL: http://www-library.desy.de/cgi-bin/showprep.pl?DESY-F31-86-02 (Cited on pages 80, 119).

[105] P. C. Bhat. "Multivariate Analysis Methods in Particle Physics", *Annual Review of Nuclear and Particle Science* 61.1 (2011), pp. 281–309. eprint: https://doi.org/10.1146/annurev.nucl.012809.104427. URL: https://doi.org/10.1146/annurev.nucl.012809.104427 (Cited on page 84).

[106] T. Chen and C. Guestrin. "XGBoost: A Scalable Tree Boosting System", *Proceedings of the 22Nd ACM SIGKDD International Conference on Knowledge Discovery and Data Mining*. KDD '16. San Francisco, California, USA: ACM, 2016, pp. 785–794. URL: http://doi.acm.org/10.1145/2939672.2939785 (Cited on page 84).

[107] A. Hocker et al. "TMVA - Toolkit for Multivariate Data Analysis with ROOT: Users guide. TMVA - Toolkit for Multivariate Data Analysis", tech. rep. physics/0703039. TMVA-v4 Users Guide: 135 pages, 19 figures, numerous code examples and references. Geneva: CERN, Mar. 2007. URL: https://cds.cern.ch/record/1019880 (Cited on page 88).

[108] M. W. Browne. "Cross-Validation Methods", *Journal of Mathematical Psychology* 44.1 (2000), pp. 108–132. URL: http://www.sciencedirect.com/science/article/pii/S0022249699912798 (Cited on page 89).

[109] G. Punzi. *Sensitivity of searches for new signals and its optimization*. 2003. eprint: arXiv:physics/0308063 (Cited on page 89).

[110] M. Calvo Gomez et al. "A tool for γ/π^0 separation at high energies", tech. rep. LHCb-PUB-2015-016. CERN-LHCb-PUB-2015-016. Geneva: CERN, Aug. 2015. URL: https://cds.cern.ch/record/2042173 (Cited on page 92).

[111] L. Anderlini et al. "The PIDCalib package", tech. rep. LHCb-PUB-2016-021. CERN-LHCb-PUB-2016-021. Geneva: CERN, July 2016. URL: https://cds.cern.ch/record/2202412 (Cited on page 94).

[112] L. Moneta et al. "The RooStats Project", *PoS* ACAT2010.arXiv:1009.1003 (Sept. 2010). Comments: 11 pages, 3 figures, ACAT2010 Conference Proceedings, p. 057. URL: https://cds.cern.ch/record/1289965 (Cited on page 100).

[113] G. Cowan, D. Craik, and M. Needham. "RapidSim: An application for the fast simulation of heavy-quark hadron decays", *Computer Physics Communications* 214 (2017), pp. 239–246. URL: http://www.sciencedirect.com/science/article/pii/S0010465517300413 (Cited on page 124).

[114] Y. K. Hsiao, Y. Yao, and C. Q. Geng. "Charmless two-body antitriplet b-baryon decays", *Phys. Rev. D* 95 (9 May 2017), p. 093001. URL: https://link.aps.org/doi/10.1103/PhysRevD.95.093001 (Cited on page 125).

[115] V. Lebedev and V. Shiltsev. "Accelerator physics at the Tevatron collider", Particle Acceleration and Detection. New York, NY: Springer, 2014. URL: http://cds.cern.ch/record/1707550 (Cited on page 127).

[116] D0 Collaboration. "Measurement of the production fraction times branching fraction $f(b \to \Lambda_b) \cdot \mathcal{B}(\Lambda_b \to J/\psi\Lambda)$", *Phys. Rev. D* 84 (3 Aug. 2011), p. 031102. URL: https://link.aps.org/doi/10.1103/PhysRevD.84.031102 (Cited on page 127).

[117] HFLAV Group, "Averages of b-hadron, c-hadron, and τ-lepton properties as of 2018", (2019). arXiv: 1909.12524 [hep-ex] (Cited on page 127).

[118] CDF Collaboration, T. Aaltonen et al. "Observation of the Ω_b^- and Measurement of the Properties of the Ξ_b^- and Ω_b^-", *Phys. Rev.* D80 (2009), p. 072003. arXiv: 0905.3123 [hep-ex] (Cited on page 128).

[119] M. B. Voloshin. *Remarks on measurement of the decay* $\Xi_b^- \to \Lambda_b \pi^-$. 2015. eprint: arXiv:1510.05568 (Cited on page 128).

[120] Y. Hsiao et al. "Fragmentation fractions of two-body b-baryon decays", *Physics Letters B* 751 (2015), pp. 127–130. URL: http://www.sciencedirect.com/science/article/pii/S0370269315007649 (Cited on page 128).

[121] LHCb Collaboration. "Measurement of the b-Quark Production Cross Section in 7 and 13 TeV pp Collisions", *Phys. Rev. Lett.* 118 (5 Feb. 2017), p. 052002. URL: https://link.aps.org/doi/10.1103/PhysRevLett.118.052002 (Cited on page 129).

[122] LHCb Collaboration. "Measurement of the mass and production rate of Ξ_b^- baryons", *Phys. Rev. D* 99 (5 Mar. 2019), p. 052006. URL: https://link.aps.org/doi/10.1103/PhysRevD.99.052006 (Cited on pages 128, 129).

[123] M. J. Savage and M. B. Wise. "SU(3) predictions for nonleptonic B meson decays to charmed baryons", *Nuclear Physics B* 326.1 (1989), pp. 15–30. URL: http://www.sciencedirect.com/science/article/pii/055032138990432X (Cited on page 128).

[124] H.-Y. Jiang and F.-S. Yu. "Fragmentation-fraction ratio $f_{\Xi_b}/f_{\Lambda_b^0}$ in b- and c-baryon decays", *The European Physical Journal C* 78.3 (Mar. 2018), p. 224. URL: https://doi.org/10.1140/epjc/s10052-018-5704-5 (Cited on page 128).

[125] S. S. Wilks. "The Large-Sample Distribution of the Likelihood Ratio for Testing Composite Hypotheses", *Ann. Math. Statist.* 9.1 (Mar. 1938), pp. 60–62. URL: https://doi.org/10.1214/aoms/1177732360 (Cited on page 129).

[126] A. L. Read. "Presentation of search results: The CL(s) technique", *J. Phys.* G28 (2002). [,11(2002)], pp. 2693–2704 (Cited on page 130).

[127] G. J. Feldman and R. D. Cousins. "Unified approach to the classical statistical analysis of small signals", *Phys. Rev. D* 57 (7 Apr. 1998), pp. 3873–3889. URL: https://link.aps.org/doi/10.1103/PhysRevD.57.3873 (Cited on page 138).

[128] D. M. Santos and F. Dupertuis. "Mass distributions marginalized over per-event errors", *Nuclear Instruments and Methods in Physics Research Section A: Accelerators, Spectrometers, Detectors and Associated Equipment* 764 (2014), pp. 150–155. URL: http://www.sciencedirect.com/science/article/pii/S0168900214008353 (Cited on page 141).

[129] M. Calvo Gomez et al. "Measurement of the mixing-induced CP-violating observables in $B_s^0 \to \phi\gamma$ decays", (June 2018). URL: https://cds.cern.ch/record/2622145 (Cited on pages 150, 151).

[130] D. Straub et al. *flav-io/flavio v0.28*. Apr. 2018. URL: https://doi.org/10.5281/zenodo.1218732 (Cited on page 162).

[131] M. Misiak and M. Steinhauser. "Weak radiative decays of the B meson and bounds on $M_{H^\pm}$ in the Two-Higgs-Doublet Model", *Eur. Phys. J.* C77.3 (2017), p. 201. arXiv: 1702.04571 [hep-ph] (Cited on page 162).

[132] Belle Collaboration, Y. Ushiroda et al. "Time-dependent CP asymmetries in $B^0 \to K_S^0\pi^0\gamma$ transitions", *Phys. Rev.* D74 (2006), p. 111104. arXiv: hep-ex/0608017 [hep-ex] (Cited on page 163).

[133] BaBar Collaboration, B. Aubert et al. "Measurement of time-dependent CP asymmetry in $B^0 \to K_S^0\pi^0\gamma$ decays", *Phys. Rev.* D78 (2008), p. 071102. arXiv: 0807.3103 [hep-ex] (Cited on page 163).